Swansea University
Prifysgol Abertawe

Scandium metal processing for aerospace application

Sephira Riva

Submitted to Swansea University in fulfilment
of the requirements for the Degree of Doctor of Philosophy

2017

DECLARATION

This work has not previously been accepted in substance for any degree and is not being concurrently submitted in candidature for any degree.

Signed: [redacted]

Date: 1 March 2018

STATEMENT 1

This thesis is the result of my own investigations, except where otherwise stated.
Where correction services have been used, the extent and nature of the correction is clearly marked in a footnote(s).
Other sources are acknowledged by footnotes giving explicit references.
A bibliography is appended.

Signed: [redacted]

Date: 1 March 2018

STATEMENT 2

I hereby give consent for my thesis, if accepted, to be available for photocopying and for inter-library loan, and for the title and summary to be made available to outside organisations.

Signed: [redacted]

Date: 1 March 2018

There are more things in heaven and earth, Horatio,
Than are dreamt of in your philosophy.
– Shakespeare, 'Hamlet'
(1.5.167-8), Hamlet to Horatio

Qu'il regarde cette éclatante lumière mise comme une lampe éternelle pour éclairer l'univers, que la terre lui paraisse comme un point au prix du vaste tour que cet astre décrit et qu'il s'étonne de ce que ce vaste tour lui-même n'est qu'une pointe très délicate à l'égard de celui que ces astres, qui roulent dans le firmament, embrassent.
Mais si notre vue s'arrête là que l'imagination passe outre, elle se lassera plutôt de concevoir que la nature de fournir.
Tout ce monde visible n'est qu'un trait imperceptible dans l'ample sein de la nature. Nulle idée n'en approche, nous avons beau enfler nos conceptions au-delà des espaces imaginables, nous n'enfantons que des atomes au prix de la réalité des choses. C'est une sphère infinie dont le centre est partout, la circonférence nulle part.
– Blaise Pascal, 'Pensees'

Acknowledgements

First and foremost, I would like to express my deepest gratitude to Prof Stephen Brown and Dr Nicholas Lavery for their unwavering support, guidance, encouragement and patience. Moreover, I surely would not have made it this far without the guidance of Dr Kirill Yusenko, a strict but just teacher and an extraordinary man of science and culture. To these people I own a great debt.

I wish to acknowledge several other individuals who have greatly assisted me in conducting my research. I am very grateful to Dr Shahin Mehraban, without whose expertise this work would have remained a theory; to Dr David Jarvis, Dr Wayne Voice and Dr Wim Sillekens of the European Space Agency, for strongly believing in this project as well as providing the necessary material. For their support in funding the communication side of this project, I would like to thank the National Research Network of Wales, and especially Claudia and Ruth, for being kind and welcoming and patient with the inpatient me.

Finally, none of this would have been possible without the emotional support given me by my family spread all over the world, my lovely boyfriend, my dearest friends, my humming house mate, my PhD colleagues and all the amazing people I had the honour to meet during this journey.

Summary

The use of scandium has been conventionally restricted to minor additions in alloys for structural applications. The term 'scandium effect' came thus to indicate the properties improvements caused by the precipitation of scandium intermetallics in the matrix.

The development of High-Entropy Alloys (HEA, multi-principal component alloys combining compositional complexity with simple crystal structures) opened the door for the development of new systems, and therefore for new applications for lightweight metals such as scandium.

This work is a thorough investigation of the potential of scandium-based intermetallics in the growing field of HEAs.

The synthesis and characterisation of multi-principal component alloys containing scandium as active alloying element illustrate the compound-forming ability of this element. The high mixing entropy of the studied systems (comprising alloys of scandium with first raw metals or with *hcp*-structured elements) cannot efficiently inhibit the precipitation of stable intermetallic compounds. Among them, of interest is the so-called W-phase, so-far only reported for Al-based Cu-containing commercial alloys.

Small scandium additions to $Al_2CoCrFeNi$, $Al_{0.5}CoCrCuFeNi$ and $AlCoCrCu_{0.5}FeNi$ cause the segregation of a secondary phase along grain boundaries. This hexagonal Laves phase, formed by scandium in combination with Al, Co, Cr, Cu, Fe and Ni, does not disrupt the HEA matrix and is extremely stable. Moreover, it deeply affects microstructure and mechanical properties – for example, by enhancing the HEA stability with the postponement of a T-dependent phase exsolution by roughly 150 °C. Furthermore, a synergistic effect in the main phase stabilisation takes place when the Sc-doped sample is pressed at 9.5 GPa: no transition occurs and the intermetallic dissolves in the matrix.

Preliminary investigations performed by spark-plasma sintering of different additives (among which Sc_2O_3, used as a source of scandium metal) in combination with the $Al_2CoCrFeNi$ alloy led to the discovery of a promising nanodiamond HEA composite.

Contents

Nomenclature

A, B, α_0, α_1, β_0, β_1, δ	Fitting parameters.
a, b, c and α, β, γ	Length of the unit cell vectors along the x, y and z axes and angles between them (unit cell parameters).
c_P	Specific heat capacity.
D	Diffusion.
D_0	Pre-exponential coefficient in the Arrhenius equation of thermal diffusion.
D_{AB}	Interatomic distance.
d_{AB}	Distance between atoms in the compound.
d_{hkl}	Distance between neighbouring parallel, equally spaced, planes in a crystal lattice.
e/a	Electron concentration, corresponding to the ratio between the number of valence electrons and the total number of atoms in the unit cell.
E	Young's modulus.
F	Degrees of freedom in a system (*variance*).
f'_j	Atomic scattering factor.
$F(hkl)$	Structure factor function describing the scattering of X-rays by the crystal.
H	Enthalpy.
$\overline{H}$	Hardness.
k_{tot}	Thermal conductivity.
K	Thermal diffusivity.
L	Lorentz number ($2.44 \cdot 10^{-8}$ WK^{-2}).

m	Mass.
N	Number of components in a system.
P	Pressure.
Q	Number of phases in thermodynamic equilibrium.
Q_a	Activation energy.
R	Gas constant (8.3144598(48) $\mathrm{Jmol^{-1}K^{-1}}$).
S	Entropy *or* Seebeck coefficient.
T	Temperature.
T_g	Glass transition temperature.
T_m	Melting temperature.
V	Volume (or volume fraction).
ZT	Thermoelectric figure of merit.

α_T	Coefficient of linear thermal expansion (thermal expansivity).
$\alpha_{T,m}$	Average coefficient of linear thermal expansion.
β	Heating rate of the sample.
β_T	Coefficient of volumetric thermal expansion.
κ_e	Electronic contribution to thermal conductivity.
κ_{ph}	Phononic contribution to thermal conductivity.
ρ	Density.
σ	Electrical conductivity.
Φ	Heat flow rate.
χ_i	Atomic percentage.

List of Figures

List of Tables

Chapter 1

Literature review

Since the first days of powered flight, aircraft designers have focused on achieving minimum weight, both in air-frames and in propulsion systems. From 1903 to 1930, the selection of materials was driven mostly by strength/weight ratio considerations. In the 1920s, the designers Junkers, Dornier and Rohrbach experimented with aircraft made from 'duralumin', an age-hardenable aluminium alloy containing magnesium, copper and manganese [1]. Since 'duralumin' suffered from exfoliation corrosion when exposed to air, it was only after a new method of cladding aluminium alloys with pure aluminium (not susceptible to exfoliation corrosion and thus protecting the alloy in aggressive environments) and the first anodized protective films were discovered and implemented; that aluminium alloys became commonplace in load-bearing components of aircraft [2]. From 1930 through the 1960s, improved performance was the goal and reduced weight a principal contributor. While materials development continued to focus on aluminium, the requirements of the construction of supersonic commercial aircraft designed to fly at Mach2 (in the frame of Soviet and English-French programs) led to the creation of more complex alloys, such as the 2618 alloy. Several Al–Li alloys containing about 2 wt.% Li were developed in the early 70s and found application for secondary structure in aircraft ever since [3].

However, current design criteria have strict requirements for processing methods, safety and materials specifics [2]. The Al–Li alloys (1420 alloys) and Al–Be alloys are indeed affordable alternatives to decrease aircraft mass up to 20%, but the danger involved in applying such reactive materials limits their active use [4]. Although polymer matrix composites (PMCs) are being used in modern commercial aircraft, aluminium alloys continue to be the primary material of choice for airframes. The current challenge is to develop alloys with improvements in both structural performance and life cycle cost. Aluminium alloys serve in many types of rockets, seagoing craft and riverboats, cars, and carriages of high-speed trains. In order to provide good weight efficiency as well as long-term life and service reliability, new alloys should possess high strength, good corrosion resistance, high resistance to repeated loads and low rate of fatigue-crack propagation [5, 6]. The introduction of scandium into the 1420 alloy in the early 1960s, leading to an increase in yield strength of 20-25% while decreasing rocket bodies mass by 10-15%, put the metal in the limelight and opened the doors for its wider

application in the aerospace industry. At the time of the Soviet Union break-up, scandium alloys were on the verge of major application in MIG 29 fighters because of their advantages over the low density and high strength of Al-Mg, Al-Li, and other recent alloys [7]. Indeed, historically the progress in scandium-aluminium metallurgy has been driven by its major producer - Soviet Russia - and will be briefly reviewed in Section 1.2.1.
However, more applications for scandium-containing alloys have been proposed following the development of the Al–Sc alloy by Ashurst Technology Corporation for the construction of lightweight high-strength bicycle frames [8]. Eventually, scandium gained popularity as a small addition to ceramic materials (as Sc_2O_3) and alloys, interest culminating in the development by Airbus of a new generation of Al–Mg–Sc alloys with the trademark Scalmalloy®.

The last ten years have brought about a renewed interest in scandium as a key element for the development of lighter materials for aerospace applications. A recent NASA report describes the use of Al–Sc-based alloys for fuel tanks and air frames, applications in which low weight and chemical stability to hydrogen peroxide are critical [9]. Moreover, the recent ESA Grand Challenge, identified by FTAP in 2012, states that lightweight, stable and high-stiffness structures are a top priority for the Agency [9].

As such, high-performance scandium alloys could find numerous applications in primary satellite structures, cryogenic tanks, solar panel substrates, rocket nozzles and thrusters, reentry hot structures, Mars rovers, electronic packages and optical benches, as well as in armour development [10].

1.1 Background

1.1.1 Scandium properties and natural abundance

Scandium was first discovered in 1879 by Lars F. Nilson in Uppsala, Sweden. However, the intrinsic difficulties in its extraction delayed its study until 50 years later, and it was only in 1937 that the first pound of pure elemental scandium metal was produced (Figure 1.1). Preliminary investigations of scandium compounds were published only in the early 1960s.

Figure 1.1: Ultrapure crystalline scandium, 5 g (Courtesy of the European Space Agency).

From the early days of its discovery, specialists have been divided on whether scandium should be considered a rare earth element (RE), lanthanide, pre-lanthanon triad (together with yttrium and lanthanum), transition element, disperse element, ultra-trace element, non-essential element, or as the biological non-entity for group III of the elements [11]. In fact, scandium occupies an intermediate position between the typical REs and other light elements, being the first of the transition elements. Arguments favouring the inclusion of scandium among RE were mostly linked to its production from RE-containing minerals, while arguments opposed to its inclusion highlighted its low weight and the chemical similarity with beryllium.

Today scandium is generally grouped together with Light Rare-Earth Elements (LREE) – Sc, La, Ce, Pr, Nd, Pm, Sm and Eu; also known as the cerium group, - whereas the chemically similar ytterbium is part of the Heavy Rare-Earth elements (HREE) – Y, Gd, Tb, Dy, Ho, Er, Tm, Yb, and Lu; also known as the yttrium group.

According to data published by the Scandium International Mining Corporation in 2015, scandium occurrence in minerals is around 22 ppm, making it more abundant than lead, mercury and precious metals. However, scandium rarely concentrates in nature over 100 ppm. The only known concentrated sources of this element are the following minerals [12]:

- Allendeite $[Sc_4Zr_3O_{12}]$
- Bazzite $[Be_3(Sc,Al)_2Si_6O_{18}]$
- Cascandite $[Ca(Sc,Fe^{2+})Si_3O_8(OH)]$
- Davisite $[Ca(Sc,Ti^{3+},Mg,Ti^{4+})AlSiO_6]$
- Heftetjernite $[ScTaO_4]$
- Jervisite $[(Na,Ca,Fe^{2+})(Sc,Mg,Fe^{2+}Si_2O_6]$
- Juonniite $[CaMgSc(PO_4)_2OH \cdot 4H_2O]$
- Kolbeckite $[ScPO_4 \cdot 2H_2O]$
- Kristiansenite $[Ca_2 - ScSn(Si_2O_7)(Si_2O_6OH)]$
- Magbasite $[KBa(Al,Sc)(Mg,Fe^{2+})_6Si_6O_{20}F_2]$
- Oftedalite $[(Sc,Ca)_2KBe_3Si_{12}O_{30}]$
- Pretulite $[ScPO_4]$
- Scandiobabingtonite $[Ca_2(Fe^{2+},Mn)ScSi_5O_{14}(OH)]$
- Thortveitite $[(Sc,Y)_2Si_2O_7]$
- Titanowodginite $[Mn^{2+}(Ti,Ta,Sc)_2O_8]$

The following mineral species, on the other hand, contain less than 1 at.% Sc:

Property	**Value**
Electronic configuration	$[Ar]3d^14s^2$
Atomic number	21
Standard atomic weight	44.955908(5) $gmol^{-1}$
Atomic radius	162 pm
Oxidation states	**+3**, +2, +1
Crystal structure	*hcp* (α) below 1337 °C; *bcc* (β) between 1337-1541 °C
Density at room temperature	2.985 gcm^{-3}
Melting point	1814 K (1541 °C)
Boiling point	3109 K (2836 °C)

Table 1.1: Selected physical properties of elemental scandium [13].

- Stavelotite-(La) $[La_3Mn_3^{2+}Cu^{2+}(Mn^{3+}, Fe^{3+}, Mn^{4+})_{26}(Si_2O_7)_6O_{30}]$
- Lakargiite $CaZrO_3$
- Samarskite-(Yb) $[(Yb, Y, REE, U, Th, Ca, Fe^{2+})(Nb, Ta, Ti)O_4]$
- Arrojadite-(SrFe) $[SrFe^{2+}Na_2Ca(Fe^{2+}, Mn, Mg)_{13}Al(PO_4)_{11}(PO_3OH)(OH, F)_2]$
- Dissakisite-(La) $[(Ca, Fe^{2+}, Th, La)(La, REE, Ca)(Al, Cr, Ti)_2(Mg, Fe, Al)Si_3O_{12}(OH, F)]$ with La > Ce[1]

The concentration of scandium in carbonates, silicates and phosphates can be ascribed to its lipophilic character, which associates scandium with HREE. More information about existing mines and costs are provided in section 1.2.2.

Selected physical properties of elemental scandium are reported in Table 1.1 [13].

1.1.2 Elemental scandium under high temperature and high pressure

At ambient pressure Sc has two forms: the low-temperature (α) *hcp* form, stable below 1337 °C, transforms into a high-temperature (β) *bcc* structure with a melting temperature of 1541 °C. Transition between α and β phases have been investigated *in situ* using time-of-flight neutron diffraction [14].

The high-pressure behaviour of elemental scandium has been intensively investigated during the last two decades using diffraction and magnetometry in diamond anvil cells up to 297 and 74 GPa respectively [15]. Under compression Sc shows five high-pressure modifications. None of these can be recovered after decompression. Schematically, high-pressure properties of Sc can be summarised as follows:

$$\begin{aligned} \frac{hcp - Sc(I)}{amb.phase} \xrightarrow{17\ \text{GPa}} \frac{Sc(II)}{I'4/mmc(00\gamma)} \xrightarrow{104\ \text{GPa}} Sc(III) \\ \xrightarrow{140\ \text{GPa}} Sc(IV) \xrightarrow{239\ \text{GPa}} \frac{Sc(V)}{P6_122 or P6_522} \end{aligned} \tag{1.1}$$

[1]Part of this list can be found online at the webmineral.org Mineralogy Database.

The crystal structures of Sc-II and Sc-V have been solved and refined using high-pressure powder X-ray diffraction. Both structures are quite complex. The crystal structure characteristic for Sc-II (Figure 1.2) can only be described using incommensurate crystallography. In the structure, tetragonal host channels along the c-axis include incommensurate guest chains within the host lattice. The structural parameters for the host lattice were refined as a_1=7.550 Å, c_1=3.439 Å and those for the guest lattice as $a_2 = a_1$, $c_2 = 2.281$ Å. The crystal structure can be solved in the $I'4/mcm(00\gamma)$ four dimensional space group with incommensurability γ, defined by c_1/c_2: its corresponding value has been refined as 1.508.

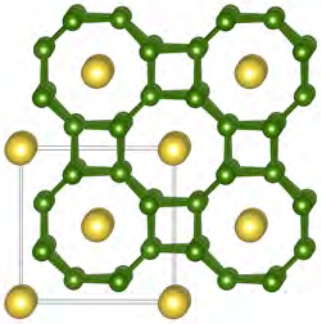

Figure 1.2: Crystal structure of the high-pressure tetragonal incommensurate Sc-II phase along the c-axis. Two crystallographically independent Sc atoms form host frameworks (*yellow*) and guest atoms (*green*) [14].

The hexagonal Sc-V crystal structure (Figure 1.3) can be derived from modulations of the inter-plane stacking of the (111) planes in an *fcc* arrangement. Both crystal structures are unique among all elements investigated under high-pressure. The crystal structures of phases Sc-III and Sc-IV seem to be quite complex and can probably be solved in low symmetry space groups, since diffraction patterns show many diffraction lines. These crystal structures are still unknown.

(a) Along the a-axis. (b) Along the c-axis.

Figure 1.3: Crystal structure of the high-pressure hexagonal Sc-V phase [14].

The ambient phase Sc-I does not show a superconducting transition. In contrast, Sc-II

shows a superconducting transition below 5 K at 50 GPa. Critical temperature increases with pressure and reaches 19.7 K at 107 GPa. 19.7 K is the second highest superconducting temperature observed for pure elements investigated under pressure. The value reported is slightly lower in comparison with the maximum temperature of 25 K obtained for Ca compressed up to 161 GPa. The critical temperature observed for the Sc-II phase drops sharply to 8 K at the Sc-II → Sc-III boundary (107 GPa) and then rises slightly when pressure is increased. Electronic properties, as well as the nature of the superconducting state in Sc-II, have been theoretically investigated. In particular, recent studies highlighted the important role played by *d*-electrons in phase transitions under pressure [16].

1.1.3 Binary phase diagrams and intermetallic compounds

The performance of scandium in combination with other metals or semi-metallic elements has been object of study ever since the 1960s and has led to the production of an extensive literature of binary and ternary phase diagrams. However, the lack of a consistent approach resulted in knowledge of scandium binary and multicomponent phase diagrams actually being fragmented: several phase diagrams were covered only partially, others have been investigated only as part of ternary phase diagrams, others are still completely unknown. Nevertheless, the critical systematisation of scandium-based binary phase diagrams makes it possible to identify regularities and common trends [17].

Figure 1.4: Scandium phase diagrams state of the art. In *red* are presented phase diagrams studied over the whole composition rage; in *blue* are binary phase diagrams covered only partially; in *green* are systems where information comes only from ternary phase diagrams; in *white* are currently unknown phase diagrams [17]. Currently reported phase diagrams can be traced back to the four reported at the top of the figure, namely Sc–Hf, Sc–Li, Sc–Ce and Sc–Pd.

As highlighted in Figure 1.4, the currently reported binary phase diagrams can be divided into four types:

- Systems with complete mutual solubility in liquid and solid phase, in which no compounds occur (Type I : Y, Zr, Hf, Nd, Gd and Tb);
- Systems with miscibility gaps in liquid state, in which no compounds occur (Type II: Li, Ca, Sr, Ba, Eu, Yb and U);
- System dominated by an eutectic, with low mutual solubility in the solid phase and in which no compounds occur (Type III: Ti, V, Cr, Mo, Ta, La, Ce, Er and Th);
- Systems with at least one binary compound, with low mutual solubility in the solid phase (Type IV).

Type IV systems are by far the most common: in some cases (e.g. Hg, Os, Tc, As, Sb and Se) the existence of intermetallic compounds is known despite the phase diagrams not being investigated. A total of 170 scandium binary compounds are known, most of them occurring at constant compositions. Noticeable exceptions are ScPd, Sc_5Tl_3, ScMg and ScC_{1-x}, which have variable composition. Homogeneity ranges are reported for Co_2Sc, Ni_2Sc, Ru_2Sc, RuSc, RhSc, Rh_3Sc, CdSc, IrSc, Ir_2Sc, $IrSc_2$ and Sc_2Ir_3.

Scandium intermetallics with a given element E often occur at stoichiometries ScE, ScE_2, ScE_3, Sc_2E and Sc_5E_3.

The most common crystal structures for ScE are $Pm\overline{3}m$ and $Fm\overline{3}m$ (if E is a metal); or $Fm\overline{3}m$ (if E is a non-metal). Elements that form this phase are distributed almost symmetrically with respect to the Cr group (whose elements do no participate in the formation of such compounds). The stability of these compounds is correlated to the difference between interatomic distance (D_{ScE}, the sum of Sc and E radii) and distance between atoms in the compound ($d_{ScE} = a_o\sqrt{3/2}$, where a_o is the lattice period), therefore it increases along a group and decreases along a period. The electron concentration (defined as the ratio between the number of valence electrons and the total number of atoms in the unit cell e/a, see Section 1.3.2) also plays a role. The optimal e/a interval for the formation of the $Pm\overline{3}m$ (CsCl-type) phase has been calculated as 5.5-7.0 [18, 19].

The most common crystal types for ScE_2 compounds (also known as Laves phases) are the close-packed $MgZn_2$, $MgNi_2$ (both belonging to the $P6_3/mmc$ space group) and $MgCu_2$ ($Fd\overline{3}m$). It is worth noting that most of the scandium compounds of these classes have the same syngony as the starting E element: $Fd\overline{3}m$ is preferred by originally *fcc* metals, whereas *hcp* metals crystallise in $P6_3/mmc$. Both structures can be described as ordered cubic or hexagonal closed-packing of Sc and E atoms, with each Sc atom being surrounded by 12 neighbouring atoms. However, the two elements can form partially disordered phases depending on temperature and composition. Extensive efforts towards the prediction of Laves phases precipitation in complex multi-component system have been made and have ultimately led to the use of atomic size mismatch and Allen electronegativity difference parameters. The

criterion of $\delta_r > 5.0\%$ and $\Delta_{\chi Allen} > 7.0\%$ [2] has proven successful in predicting the formation of Laves phases in *bcc*-structured HEAs based on 4-6 groups elements [20]. A more in depth review of these parameters can be find in section 1.3.2.

ScE_3 compounds crystallise as $AuCu_3$ or $SnNi_3$ ($Pm\bar{3}m$). The formation of this phase is favoured when the size factor (r_{Sc}/r_E) is in the range 1.00-1.21. Electron concentration also plays a role, since this structure type principally arises when a group III-VI element is combined a group VIII element [19].

Several scandium binary compounds crystallise in the Sc_2E stoichiometry, mainly as Ti_2Ni ($Fd\bar{3}m$) and Al_2Cu types ($I4/mcm$). Finally, Sc_5E_3 picnide compounds crystallise as Mn_5Si_3 and Yb_5Sb_3 structure types ($P6_3/mcm$) [21].

Scandium intermetallics and oxides under high pressure

Scandium oxides and intermetallics have been sporadically studied under medium or high–pressure. Already in the late '60s, $\mathbf{Sc_2O_3}$ was investigated up to 13 GPa, following the transformation from open C–rare-earth structure type to monoclinic B–rare-earth form. The corresponding 8.3% density increase reflects the increase in coordination from six to seven fold for 2/3 of the scandium atoms of the structure [22].

$\mathbf{Sc_2(WO_4)_3}$ and $\mathbf{Sc_2(MoO_4)_3}$ have been shown to undergo several pressure-induced transition prior to becoming amorphous. In $Sc_2(WO_4)_3$, the initial compound undergoes a reversible structural phase transition at 0.6 GPa, going from orthorhombic to monoclinic ($P2_1/a$ symmetry). $Sc_2(MoO_4)_3$, on the other hand, shows two reversible phase transitions at 0.6 and 1.6 GPa, and becomes disordered over 6.5 GPa. The disorder progressively and irreversibly grows into an amorphous phase [23].

ScZn and **ScGa** binary compounds were thoroughly investigated under moderate pressure. Three intermediate phases were found in the reaction between elemental Sc and Ga at 7.7 GPa in the temperature range 200 to 1000 °C: Sc_5Ga_3 (Mn_5Si_3 structure type), $ScGa_2$ ($ZrGa_2$ structure type), and $ScGa_3$ (Cu_3Au structure type) have been characterised. Only Sc_5Ga_3 is stable under ambient pressure. It has been noted that the ScGa phase diagram becomes more complicated with increasing pressure. $ScGa_2$ exists as an ambient pressure phase with an $Imma$ space group and the high-pressure phase crystallizes as a $Cmmm$ space group [24].

[2] The definition of electronegativity according to Allen (χ_{Allen})is the following:

$$\chi_{Allen} = \frac{n_s\epsilon_s + n_p\epsilon_p}{n_s + n_p} \tag{1.2}$$

where $\epsilon_{s,p}$ are the one-electron energies of the *s*- and *p*- electrons in the atom, whereas $n_{s,p}$ are the number of *s*- and *p*- electrons in the atom's valence shell.

(a) At ambient pressure. (b) At high pressure.

Figure 1.5: Crystal structure of $ScGa_2$ viewed along the *b*-axis [24]. Scandium and gallium atoms are reported in *orange* and *green* respectively.

The ambient pressure phase can be described as a Ga framework with hexagonal channels along the *b*-axis filled by Sc atoms (Figure 1.5). The high-pressure phase can be described as two-layered close packing along the *a*-axis. Pure Ga layers follow sequentially mixed Sc and Ga (1:1) layers.

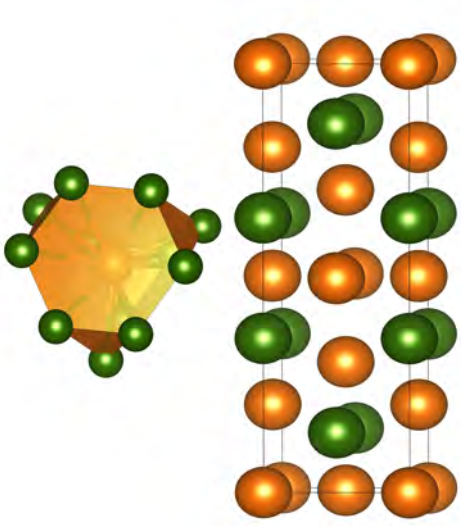

Figure 1.6: $ScZn_{12}$ coordination polyhedron (left) and high-pressure crystal structure of $ScZn_2$ (right) [25]. Scandium and zinc atoms are reported in *orange* and *green* respectively.

The reaction between elemental Sc and Zn at 4 GPa and 1900 °C results in the formation of hexagonal closed packed $ScZn_2$ phase (Figure 1.6, a $MgZn_2$ structural type similar to many other ScE_2 intermetallics) which can be recovered after cooling the reaction apparatus and decompressing. $ScZn_2$ phase does not exist under ambient pressure (only ScZn, $ScZn_{12}$, and Sc_3Zn_{12} have been described in the literature) [25].

Finally, Grewe and coworkers discovered a dependence of the superconducting transition temperature from applied hydrostatic pressure in **Sc_3In** from ambient conditions to 600 MPa [26].

1.1.4 Ternary intermetallic compounds

In the past ten years the number of known scandium-containing ternary systems has almost doubled. Particular importance has been given to the Al–Sc–*E* (33 investigated systems), Si–Sc–*E* (24), B–Sc–*E* (10), Ge–Sc–*E* (9), Fe–Sc–*E* (7) and C–Sc–*E* (6) systems. Simultaneously, the number of synthesised ternary compounds has doubled, reaching over a thousand.

A large number of compounds occur on some characteristic cross-sections of ternary phase diagrams [27]. For example, considering the cited Sc–*M*–*E* systems (where *M* = Al, Si, B, Ge or C), ternary intermetallics occurs at the following stechiometries: $Sc/M = 1/1$, $Sc/E = 1/1$, $M/E = 1/1$, $Sc/M = 1/2$ and $Sc/E = 1/2$. Therefore, the great majority of scandium ternary compounds have stoichiometry ScME, ScME_2, ScM_2E and ScM_2E_2. These simple structures are favoured by metallic bonding, whereas higher complexity appear in compounds with covalent bonding.

Scandium ternary compounds generally occur in the ternary phase diagram region where scandium content is equal to or lower than 50 at.%. In this respect, the behaviour of scandium differs from the one of RE, and resembles that of *d*-metals.

The peculiar features of scandium in the framework of compound formation can be ascribed to the atomic size factors (r_{Sc}/r_M, r_E/r_M), which play an important role in the distribution of atoms in the ternary phase. In particular, the larger atoms of the compound usually occupy sites with larger coordination numbers and vice versa. Scandium is generally the largest atom in the structures, unless other RE metals are included [21].

Ternary systems of industrial importance

In the present section, emphasis is put on ternary phase diagrams of Al–Sc with elements that are technologically important for multi-principal components systems (see section 1.3). Some general categories can be drawn [28]:

- Ternary phase diagrams with precipitate-forming elements; namely with Mg, Cu, Li, Si, Sn, Zn.
- Ternary phase diagrams with dispersoid-forming elements, whose function is to control grain size, grain orientation and degree of recrystallisation (with Cr, Fe, Mn, Zr).
- Other ternary phase diagrams (*i.e.* with Ba, Be, Co, Mo, N, Sr, Ti, V).

In this section a few systems falling under the scope of lightweight multiprinciple component alloys will be reviewed. A considerable part of the literature relevant for scandium in aluminium alloys was reviewed in 2005 [29], where the authors covered the precipitation pathways of Al_3Sc, the compound responsible for the improved mechanical features of the

Al-based alloys, as well as the macroscopic influence of scandium on microstructure and properties (grain refinement, strengthening effect and corrosion resistance) of Al-based alloys.

Al–Cu–Sc The Al–Cu–Sc system was primarily investigated to develop hard and heat-treatable Al alloys [30]. Nine ternary compounds have been reported in the phase diagram, three of those located at the Al-rich corner (AlCuSc, $AlCu_2Sc$ and $Al_{5.4-8}Cu_{6.6-4}Sc$) [31].

AlCuSc has $MgZn_2$ structure ($P6_3/mmc$, $a = 5.04$ Å and $c = 8.24$ Å). $Al_{5.4-8}Cu_{6.6-4}Sc$ has $MnTh_{12}$-type crystal structure ($a = 8.63$ Å and $c = 5.10$ Å). The difficulties encountered in the characterisation of these phases reside in the stability range broadening of the three-phase areas while decreasing temperature [32].

More recently, several authors have noted that the formation of these intermetallics (going under the name W-phase) strongly influences the properties of the alloy. The W-phase can be detected with optical microscopy as relatively small inclusions, which are light after polishing and dark after chemical etching. The phase displays no particular morphology and is usually detected after heat-treatment of the as-cast alloy [33]. Various compositions have been proposed for the W-phase: $Al_{5-8}Cu_{7-4}Sc$, $Al_{5.4-8}Cu_{6.6-4}Sc$ and $Al_{8-x}Cu_{4+x}Sc$, with a possible $I4/mcm$ crystal structure similar to Al_2Cu. In general, the formation of the W-phase is considered unfavourable, because it consumes part of the Sc and Cu atoms embedded in the Al matrix. As a consequence, both the precipitation of Al_3Sc and the occurrence of Cu strengthening phases are reduced, minimizing the positive effect of Sc on the mechanical properties of the alloy.

Two pathways for the formation of the W-phase have been proposed, springing from the dissolution of the Al_2Cu θ-phase (Figure 1.7) [34].

In particular, the W-phase nucleation mechanism is supposed to involve either (i) its growth on an existing θ-phase particle or (ii) the transformation of the θ-phase into the W-phase due to the diffusion of scandium in the θ-phase from the Al matrix. In the first case, the W-phase constituents must already be in the Al matrix in order to form a nucleus at the interface between Al matrix and θ-phase. The low interfacial energy associated with this interface would make it a preferred nucleation site. In order for the W-phase to grow, Sc and Cu would diffuse from the θ-phase, thereby consuming it. The W-phase/θ-phase interface would remain unchanged until the θ-phase had been completely dissolved [34].

Al–Co–Sc and Al–Ni–Sc Following the development of bulk-metallic glasses (BMG), pioneering studies have been performed on RE–Co and RE–Ni alloys quenched into metallic glass ribbons. Moreover, following the discovery that Al and Y additions greatly enhance manufacturability and glass-forming ability, a series of Al–Co–Sc BGMs was developed [35].

Three ternary compounds have been reported in the Al–Co–Sc system, namely AlCoSc, $Al_{15}Co_8Sc_6$ ($Mn_{23}Th_6$-type) and $Al_9Co_3Sc_2$ ($Cmcm$, $Ga_9Co_3Y_2$-type). AlCoSc ($P6_3/mmc$, $MgZn_2$) has a wide homogeneity range (33-45 at.% Al and 28-37 at.% Sc) [36, 37].

Compared with Sc, the solubility of Ni in Al is very limited. Under equilibrium conditions and room temperature, only up to 0.023 at.% Ni is soluble in Al. Further Ni addition results

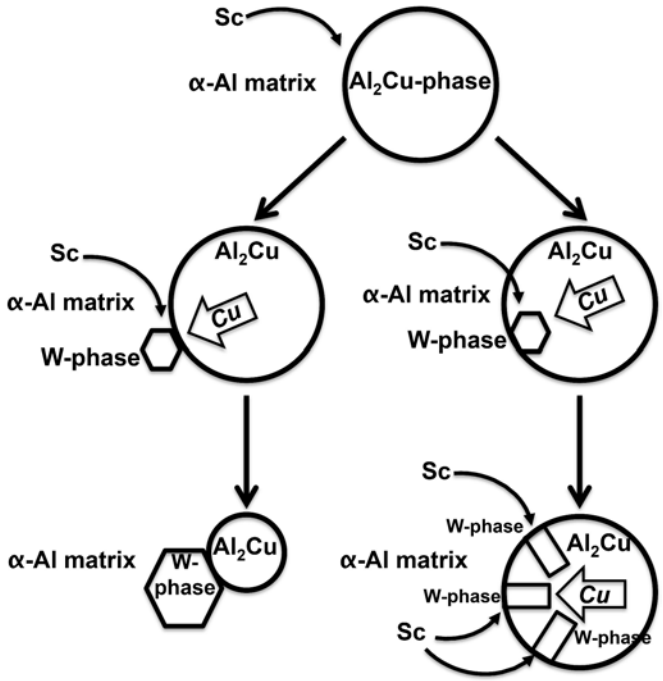

Figure 1.7: Formation of the W-phase by nucleation on the Al_2Cu-phase a (*left*) and by transformation from the θ-phase to the W-phase (*right*). Redrawn from [34].

in the formation of an eutectic between α-Al and the Al_3Ni intermetallic. The Al–Ni–Sc ternary system comprises five ternary compounds: AlNiSc ($MgZn_2$-type), Al_2NiSc ($MgCuAl_2$-type), $AlNi_2Sc$ (Cu_2MnAl-type), $Al_6Ni_2Sc_{0.67}$ ($Al_6Ni_2Y_{0.67}$-type) and $Al_{16}Ni_7Sc_6$ (Th_6Mn_{23}-type) [38]. $AlNi_2Sc$ and Al_9Ni_2 have been reported to precipitate along grain boundaries and improve hardness and tensile properties respectively [39].

1.2 The 'scandium effect'

1.2.1 The 'scandium effect' in Al–based alloys

Micro-alloying elements in Al alter properties by changing the morphology, chemistry, structure, spatial distribution, and size of precipitates. Pioneer studies of Al–Sc alloys were performed in the early '70s in order to gain better theoretical understanding of the relative changes in the lattice parameters of Al–3d alloys. However, those investigations were hampered by the low equilibrium solid solubility at room temperature of 3d-metals in aluminium [40]. Follow-up experiments highlighted a trend in the modifying capability of 3d metals with respect to Al, with scandium displaying the highest effect. Moreover, Sc was reported to act as an Al-modifier even at concentrations lower than the eutectic composition (< 0.3 at.%), above which it precipitates as Al_3Sc aluminide [41].

Studies aiming to uncover the modification mechanism found that additives can affect the state of aluminium melts by changing the distribution, amount and size of its structural

constituents. However, the only additives that have a modifying capability are those forming in melt clusters with similar syngony as the structure of growing crystals, because these groups can act as nucleation centres of a new phase on supercooling [42]. The same holds true when a high-melting point master alloy is added to aluminium. Along with the basic structural components of the melt having composition close to that of the aluminium matrix, micro-regions occur whose short-range order resembles the aluminides' structure, but in which the content of additive is much higher [43, 44]. In other words, the addition of high-melting additives (such as Sc, Ti and Zr) results in an increase in the matrix micro-heterogeneity. Upon heating above the liquidus temperature, the aluminides in the matrix melt, giving rise to complexes with short-range order inheriting the structure of the initial intermetallics. At definite temperature and additive's concentration, particles' dispergation occurs in the melt, resulting in an increase in the number of nucleation sites during the subsequent solidification [43, 44].

In more recent years, new Al–Mg-based alloys alloyed with Sc were developed. The ultrafine microstructure obtained was found to be remarkably stable; moreover, the alloy displayed high superplasticity [45, 46]. Alloying with Zr enhanced grain stability due to the presence of $Al_3(Zr_xSc_{1-x})$ precipitates, whose stability at high temperature (773 K) resulted in turn in a further superplasticity increase [47]. The addition of scandium to Al–Zn–Mg weldable alloys made it possible to create materials with high mechanical and anti-corrosion properties [48]. The formation of sub-microcrystalline and nano-structured states in Al–Mg–Mn alloys with scandium and zirconium additions was studied during shear at a high hydrostatic pressure by Brodova and co-workers [49]. Their studies highlighted that the most favourable conditions for the formation of super-saturated solid solutions containing refractory metals (Mn, Zr, and Sc) include overheating of the melt and its subsequent fast solidification. The cause for such abrupt structural refinement consists in the formation of the multi-component Al based solid solution, which is more resistant to decomposition, as well as in the precipitation of individual primary aluminides [49]. Furthermore, the effect of minor additions of Sc and Zr was studied to several rapidly solidified Al-transition metals alloys, namely Al–8Fe, Al–4Fe–4Ni, Al–8Mn, Al–8Mn–2Cr (all wt.%). All systems reported the presence of a fine uniform distribution of $Al_3(Zr_xSc_{1-x})$ particles [50].

Al_3Sc possesses a strong seeding capacity in the melt, causing crashing of the ingot's grain structure. It can form in the alloy through different routes [51, 43]:

- In primary crystallisation of a melt of hypereutectic alloy: $L \rightarrow Al_3Sc$;
- In eutectic crystallisation: $L \rightarrow \alpha_{Al} + Al_3Sc$;
- In decomposition of a supersaturated solid solution, with segregation of secondary Al_3Sc particles: $\alpha^1_{Al} \rightarrow \alpha^2_{Al} + Al_3Sc$.

The industrial issues arising from the high growth rate of secondary Al_3Sc particles (increase in recrystallisation temperature, decrease in strengthening effect) are in fact solved by the introduction of Zr into the alloying set. Zirconium dissolves in the aluminide without

altering its $L1_2$ lattice and influences only slightly the parameters, retaining all its valuable properties - grain refinement, precipitation hardening, enhanced superplasticity and corrosion resistance [52]. The effects of Sc and Zr additions to aluminium alloys demonstrated that the effect of different impurities to a metal does not equate to the summed effect of each of them [53].

While the effects of scandium had been known for decades, the definition '**scandium effect**' was coined only in 2000 to indicate the positive influence of small scandium additions to the chemical and mechanical properties of aluminium alloys [54].

Following up on the renewed centrality of scandium, other alloying elements were divided in classes depending on the nature of their physico-chemical interactions with Al and Sc [55]:

(i) Elements which do not significantly influence the solidus temperature of the alloy and do not form stable intermetallic compounds with Sc (Ti, Hf, V, Nb, Ta, Mn, Cr, Mo, W, Re);

(ii) Elements which lower the solidus temperature of the alloy, but are highly soluble in it at 300 °C (Zn, Mg, Li);

(iii) Elements which form stable intermetallics with Sc, removing it from the hardening process (Fe, Co, Ni, Cu, Si);

(iv) Elements which partially substitute Sc in Al_3Sc compound, lowering Sc consumption and therefore preserving the hardening effect (Zr, Y).

While generally consistent with phase diagrams and experimental results in Al-based alloys, this classification should be considered very qualitative for more complex systems. For example, the formation enthalpy values of scandium binary compounds with non-metals are very low, favouring their precipitation with respect to metallic binary compounds (a trend consistent with the formation of of Al_3Sc in Al-containing alloys and of Sc_2O_3 when non-metal impurities are present in the bulk alloy, as well as with the formation of the $AlSc_2Si_2$ V-phase in Al–Si alloys). Whenever Al is not present, scandium forms stable oxides or intermetallic compounds (e.g. Mn_2Sc, Sc_2O_3) [17, 29, 56, 57, 58].

1.2.2 The 'scandium effect' in multicomponent alloys

I previously mentioned that the positive effect of scandium additions to multicomponent alloys can be ascribable to the precipitation of its intermetallics in the alloy matrix. Scandium has been added to most commercially available Al- and Mg-based alloys as well as steel. In all cases, scandium led to enhanced mechanical properties, in particular grain refinement and precipitation hardening (Table 1.2).

Original alloy	**Effect of Sc addition**	**Responsible compound**
Al	Grain refinement	Al_3Sc
	Precipitation hardening	
	Increased superplasticity	
	Recrystallisation resistance	
	Corrosion resistance	
Al–Ni	Increased hardness	$AlNi_2Sc$, Al_9Ni_2
	Increased tensile properties	
Al–Si	Grain refinement	$AlSi_2Sc_2$ (V-phase)
	Precipitation hardening	
	Si eutectic modification	
	Increased fluidity	
	Increased tensile strength	
Al–Ti	Grain refinement	$Ti_3(Al,Sc)$, Al_3Sc
	Precipitation hardening	
	Increased ductility	
	Increased compressive strength	
Al–Mg	Precipitation hardening	Al_3Sc
	Corrosion resistance	
	Increased electrical/thermal conductivity	
Mg–Mn	Grain refinement	Mn_2Sc
	Increased creep resistance	
	Increased ductility	
	Increased fatigue resistance	
Steel	Increased homogeneity	Sc_2O_3
	Decreased viscosity	
	Decreased surface tension	

Table 1.2: Effect of Sc additions on the properties of multicomponent alloys, [17, 29, 56, 57, 58].

While these features could be obtained with the addition of less expensive elements, scandium often improves ductility, viscosity, creep, fatigue and corrosion resistance. Moreover, the high stability of scandium intermetallic compounds makes them resistant to recrystallisation.

Recent progress in scandium metallurgy

While scandium has long been recognised as a valuable commodity, its economic concentrations are rare. Scandium is typically produced today from low-grade mineral waste stockpiles or as a by-product from other mineral processing operations. These limited supply sources

(virtually entirely sourced from Russia and China) have kept prices high (Figure 1.8) and volumes inadequate for wide-scale adoption.

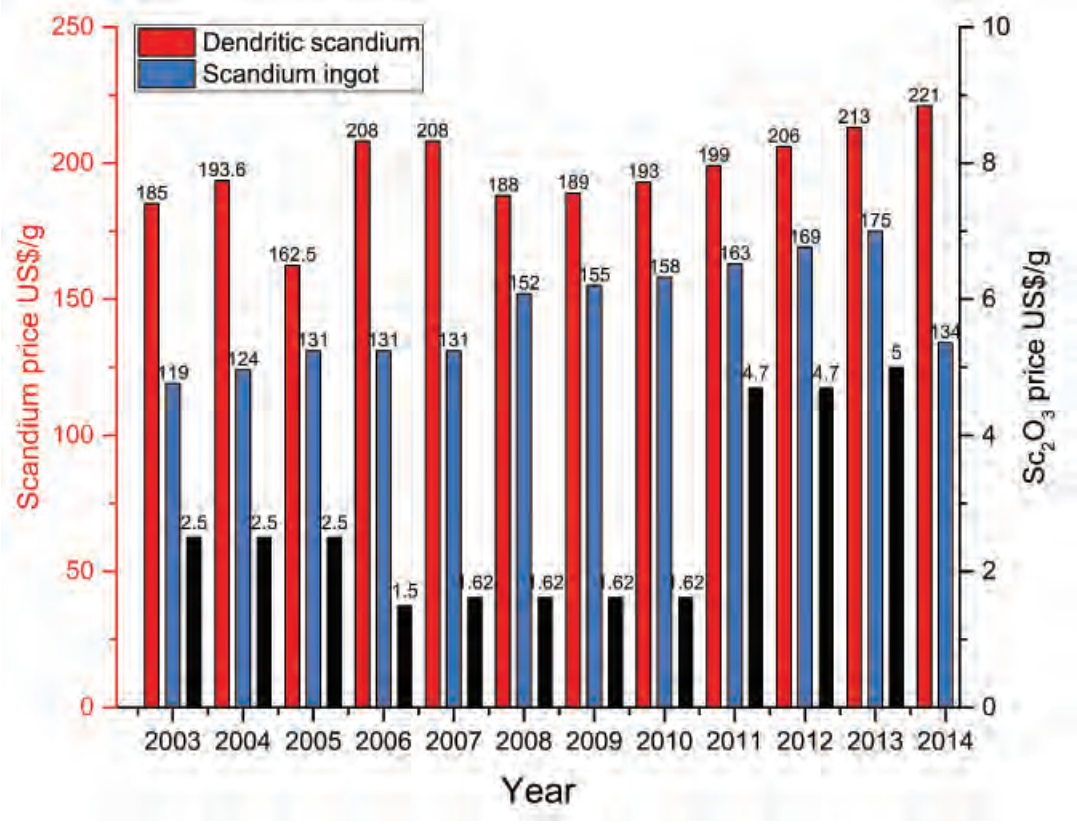

Figure 1.8: Dendritic (*red*) and ingot (*blue*) scandium (*left axis*) and S_2O_3 (99.99% purity, *black, right axis*) price in US$ per gram. Courtesy of U.S. geological Survey, Mineral Commodity Summaries, years 2003-14 [17].

Currently, the primary production is of circa 400 kg, while the rest comes from Russian stockpiles created during the Cold War. As such, the most widespread uses of the metal were related to aircraft production and space programs based in the Soviet Union and modern Russia. Since the deposits of Madagascar and Norway (rich in thortveitite and kolbeckite) are not exploited, in year 2003 only three mines actively produced scandium [59]:

- The uranium and iron mines in Zhovti Vody, Ukraine;
- The rare earth mines in Bayan Obo, China;
- The apatite mines in the Kola peninsula, Russia.

In each case, scandium was a by-product from the extraction of other elements.

Recent studies, however, have shown a close genetic and spatial association of scandium with high-magnesian ultramafic-maficigneous rocks [60]. The element is thus coupled with nickel and cobalt in Phanerozoic laterites. Such scandium deposits are rare: most of them are located in Australia (Queensland, New South Wales, Greenvale Province) and Africa (Cote

d'Ivoire, Republic of Guinea). The New South Wales lateritic clay belt represents a recent discovery of scandium at grades approximately four times the grade of existing sources. These resources are surface-mineable and could deliver scandium at large enough scale to promote much wider use of the metal, thus opening a new age for scandium exploitation.

In this framework, the investigation of compound-forming systems such as Al–Cu–Sc, Al–Co–Sc and Al–Ni–Sc might prove to be the key for a drastic improvement in manufacturing and casting routes.

With its price decreasing, eventually scandium will not only be considered as a 'spice metal' (a term coined to describe its major effect when added in very small amounts to Al–based alloys), but also as an active alloying element. Pioneering works performed in the field of High-Entropy Alloys (HEAs) and BMGs highlight the high potential of scandium for the development of novel systems tackling specific technological needs. For example, Al–Co–Y–Sc BMGs exhibit outstanding values of elastic moduli (e.g. Young's modulus E= 85 GPa; bulk modulus B= 77.5 GPa), glass transition temperature (T_g= 662 K) and crystallisation temperature (T_x= 760 K), combined with a large region of supercooled liquid (dT= 98 K) [61, 62, 63, 64, 65]. On the other hand, the recently synthesised $Al_{20}Li_{20}Mg_{20}Sc_{20}Ti_{30}$ *fcc*-structured HEA combines extremely low density (2.67 g cm^{-3}) with high hardness, and its estimated strength-to-weight ratio is significantly higher than other nano-crystalline alloys, almost comparable with ceramic materials [66].

1.3 Multi-principal components alloys: High-Entropy Alloys

High-Entropy Alloys (HEAs) are defined according to the atomic percentage of their principal elements, 5 at.% $\leqslant \chi_1 \leqslant$ 35 at.%, or according to their configurational entropy at random state, $\Delta S_{conf} > 1.5$ R (R= 8.314 J K^{-1} mol^{-1}) [67]. High Entropy Alloys present a formidable array of compositional complexity and rich microstructural variation. The unexplored central regions of the hyper-dimensional composition space of multicomponent alloys, away from the edges, faces and vertices, can reveal new alloys of scientific and practical significance.

Following their discovery in 2004 by Yeh [67] and Cantor [68], HEAs have attracted growing research interest due to their outstanding mechanical and thermal properties at extreme conditions, including high compression yield [69], fracture strength [70], ductility [71, 72] and toughness [73, 74], as well as extreme corrosion [75, 76], wear [77] and fatigue [78] resistance. Moreover, HEAs have been proposed as candidates for applications in which high temperature stability is pivotal, and their phase evolution has been extensively studied both *ex situ* and *in situ* [79, 80, 81].

Systematic investigation of different alloy compositions is one avenue of research where the use of high-throughput experimental methods and predictive numerical modelling is increasingly being exploited, because HEA studies emphasize the search for single-phase solid solutions. In fact, in early works HEAs have been reported to crystallize as ideal regular solid solutions, where atoms are randomly distributed [82], and the study of HEAs was mostly driven by the search of new single-phase systems. However, the formation of single-phase

systems is opposed by the diverse mixing enthalpies, atomic size and valence electron concentration of the constituent elements. Single-phase HEAs are actually rare, whereas more common are systems consisting of multiple solid solutions and ordered intermetallic phases [83]. The later discovery of sub-ordered solutions and intermetallic compounds displaying long-range order challenged the traditional definitions of HEAs and opened the road for the rationalisation and control of mechanical and functional properties [84].

The most widely studied *bcc* and *fcc* single-phase HEAs consist of first-row metals (Al, Co, Cr, Fe, Ni) or of refractory elements (Mo, Nb, Ta, W, Zr). Recently, several works were performed to develop *hcp*-structured single-phase HEAs [85]. In the 4f transition metal alloy family, GdHoLaTbY, DyGdLuTbTm and DyGdLuTbY were found to contain a mixture of *hcp* alloy and unknown admixture phases [86, 87]; whereas $AlLiMg_{0.5}ScTi_{1.5}$ was reported to be mainly *hcp* after heat treatment of mechanically-alloyed powders [66]. The senary ScYLaTiZrHf alloy, designed taking into account the constituent binary phase diagrams, was found to form dual *hcp* structures and cannot be considered a HEAs due to the significant difference in composition between its phases [88]. Finally, the melting of hexagonal metals leads only to 3– or 4–component *hcp* alloys, which are normally in equilibrium with ordered phases or quasicrystals, as in $AlCuMg_xMnZn$ [86, 89]. The first family of *hcp*-structured single-phase HEAs was recently obtained by thermal decomposition of single-source precursors. It shows exceptional pressure and temperature stability as well as pronounced electro-catalytic activity in methanol oxidation in acidic media [90].

1.3.1 'Core effects' of HEAs

The following effects are often cited to describe the peculiar features of HEA:

- The *high entropy* effect;
- The *lattice distortion* effect;
- The *sluggish diffusion* effect.

A forth phrase, *cocktail effect*, came to describe a synergistic mixture whose unexpected result is greater than the sum of the parts [91].

The high entropy effect is a pivotal concept in the design of HEAs, and claims that the increased configurational entropy in multi-principal components alloys may favour the formation of solid solutions over competing intermetallic compounds. Severe lattice distortion comes from the different size and type of the atoms occupying each position, and their local environment. Finally, diffusion is proposed to be sluggish in HEAs, because of the formation of nanocrystals and amorphous phases upon solidification.

In order to validate these claims, it is first necessary to discuss the thermodynamic figures of merit of HEAs.

The early HEA literature focuses on the configurational entropy of ideal solid solutions, in which atoms are randomly distributed. In such an ideal and regular solid solution, the

probability of finding an atom i on a given lattice site equals the atom fraction of the element, χ_i. However, even in binary solid solutions, atoms have the tendency to form sub-regular solid solutions and thus to distribute non-randomly ($\approx$ 85 % of solid solutions presents sub-regular features, Figure 1.9) [92, 93].

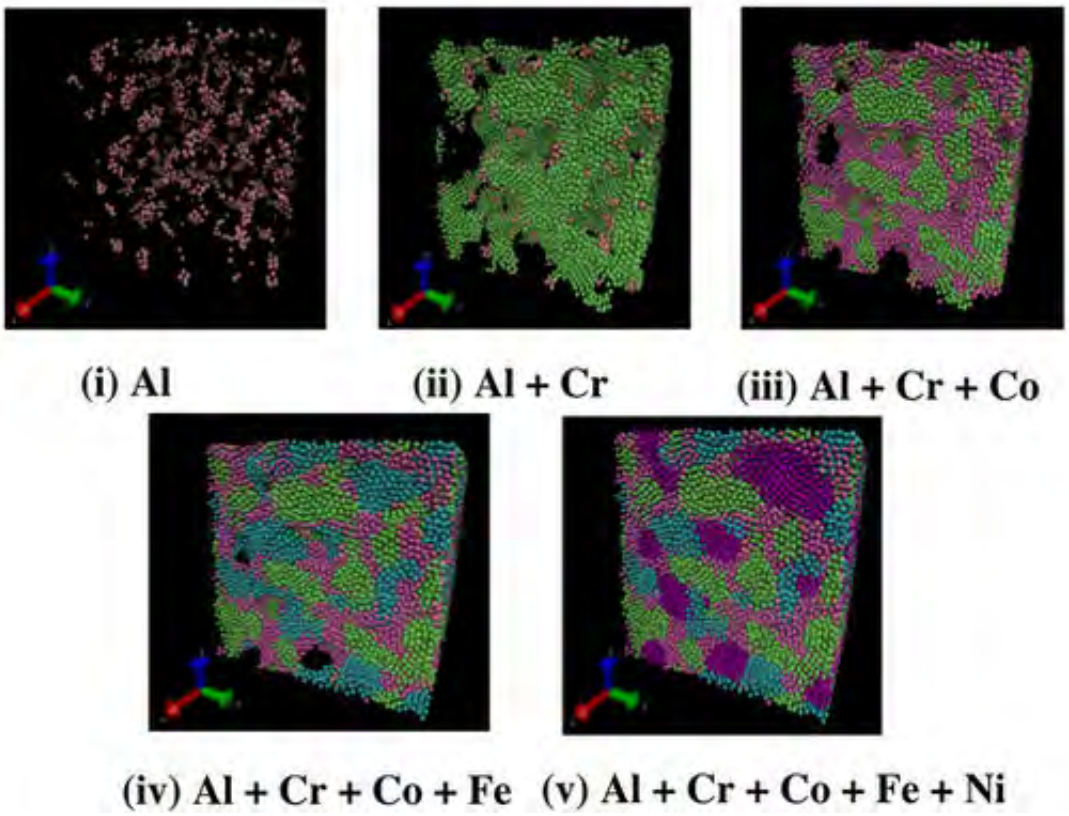

Figure 1.9: Atomistic representation of the $Al_{0.1}$CrCoFeNi HEA high-entropy alloy for different elements on lattice. Al, Cr, Co, Fe, and Ni are combined in an *fcc* lattice. Quenching of the HEA causes the high temperature solid solution disordered phase to shift to the phase-separated regions of (Al, Cr, Co, Fe, and Ni) at T = 300 K, as shown in (v) [93].

In sub-regular solid solutions, atoms are not random but their probability of occupying a specific lattice site does not vary dramatically from χ_i. This is not the case for intermetallic compounds, which display long-range ordering. The probability of finding an atom i on a given sub-lattice in a binary intermetallic phase is thus typically close to 0 or 1. This fundamental structural diversity between solid solutions and intermetallics requires different thermodynamic treatment.

If we consider the free Gibb's energy (G^{SS}) of a solid solution as being:

$$G^{SS} = H^{SS} - T(S^{SS}) \tag{1.3}$$

At fixed entropy (S^{SS}), a positive enthalpy ($H^{SS} > 0$) would favour phase separation, whereas a negative enthalpy deviation ($H^{SS} < 0$) would give a tendency to chemical short-

range ordering.

The same thermodynamical relationship can be drawn for intermetallics. For an ideal binary compound, in which each lattice site is occupied by a single element, the entropic contribution approaches zero [94]. However, complex, concentrated alloys usually have more constituents than sub-lattices. In this case, two or more elements will occupy each sub-lattice, increasing disorder in the structure and ultimately configurational entropy. As far as enthalpy is concerned, its value can be determined as the sum of the bond enthalpies between each atom i and its nearest neighbour atoms j (ϵ_{ij}), and of the number and type of first-neighbours bonds per atom (n_{ij}). Since, in general, compounds have more stable bonds than solid solutions of the same composition, usually $H^{IM} < H^{SS}$ [82].

Gibbs phase rule and High-Entropy effect

We consider a system consisting of N constituents types in a heterogeneous state with Q existing phases; values of pressure, temperature and chemical potential (μ_i) are common to all phases as they exist in mutual stable equilibrium. Two neighbouring Q-phase states will thus differ by $dT, dP, d\mu_1, d\mu_4, ...d\mu_N$ and each phase should satisfy a Gibbs-Duhem equation:

$$\sum_{i=1}^{N} n_i d\mu_i = -SdT + VdP \tag{1.4}$$

Where n_i is the number of moles of component i, $d\mu_i$ is the infinitesimal increase in chemical potential for this component and S is the entropy. Therefore, for the 1, 2, ... N constituents of the (I), (II), ... (Q) phases:

$$\begin{aligned} S^{(I)}dT - V^{(I)}dP + n_1^{(I)}d\mu_1 + n_2^{(I)}d\mu_2 + ... + n_N^{(I)}d\mu_N = 0 \\ S^{(II)}dT - V^{(II)}dP + n_1^{(II)}d\mu_1 + n_2^{(II)}d\mu_2 + ... + n_N^{(II)}d\mu_N = 0 \\ ... \\ S^{(Q)}dT - V^{(Q)}dP + n_1^{(Q)}d\mu_1 + n_2^{(Q)}d\mu_2 + ... + n_N^{(Q)}d\mu_N = 0 \end{aligned} \tag{1.5}$$

Since there are Q Gibbs-Duhem equations to be satisfied, only *N+2-Q* of the *N+2* differences $dT, dP, d\mu_1, d\mu_2, ...d\mu_N$ are independent. It follows that only *N+2-Q* of the intensive properties $T, P, \mu_1, \mu_2, ...\mu_N$ can be varied independently. Thus *N+2-Q* equals F, the number of intensive variables that can be changed independently without affecting the equilibrium [95]. At constant pressure, the Gibbs rule takes the form:

$$Q = N - F + 1 \tag{1.6}$$

Since, as shown previously, the system has one degree of freedom for T and *(N-1)* compositional degrees of freedom (as follows from the definition of μ_i), the maximum value of F is *N*. A discrete point on a phase diagram presenting the maximum number of phases *(N+1)* implies $F = 0$; any compositional or temperature deviation from this point turns into

a decrease in the number of equilibrium phases Q, reaching a minimum of 1 when $F = N$.

The Gibbs phase rule has many practical implications, but it cannot be used as a predictive tool to determine how many phases are to be expected in a given system at a specified T and P. Any number of phases can exist in an N-component system, without violating the Gibbs phase rule. The fact that HEAs, consisting of at least five components, display less than the maximum available phase value has been used to support the entropy effect [96, 97, 98, 99].

However, not only is concrete evidence of this link still missing, the concepts herein described apply to system at thermodynamic equilibrium - whereas the great majority of investigations have so far been performed on as-cast materials.

The lattice distortion effect

Real solid solutions consist of atoms of different sizes, leading to uncertainty in atom locations and an excess configurational entropy term. This effect is small in dilute solutions, where the location of the minority atoms is constrained by the surrounding majority atoms, but its importance increases with size differences and concentrations [100].

Since, as previously mentioned, the total enthalpy of a system can be determined from the number and energy of atomic bonds, difference in neighbouring atoms affect its value. Small atoms favour low (< 12) coordination numbers, whereas coordination numbers > 12 are common around larger atoms. *Fcc* and *hcp* elemental metals typically have a coordination number of 12, rising to 14 in *bcc* crystals; but coordination numbers in systems of differently-sized atoms can significantly differ from these values.

In HEAs, the lattice is thus expected to be highly strained and atoms to be displaced with respect to their average lattice sites. Recently, a model to address the lattice distortion of crystalline lattices in HEAs was developed [101].

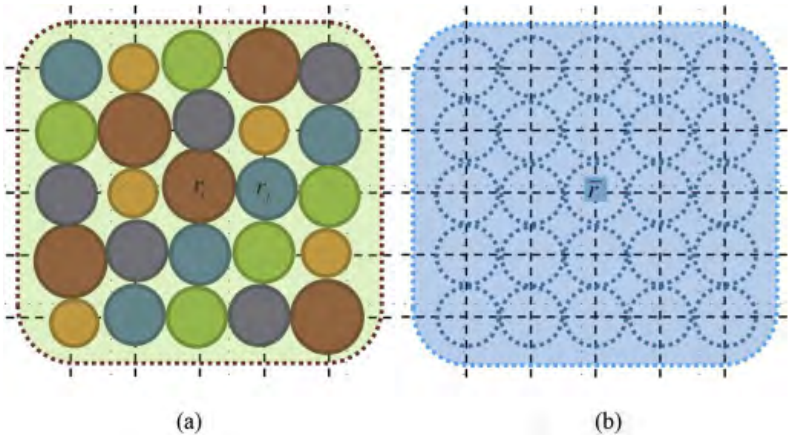

Figure 1.10: Sketch of the random occupation of atoms with different atomic sizes in the crystalline lattice of a HEA (a). The referenced ideal lattice, where dotted circles represent the virtual atoms with average atomic size $\overline{r}$ (b) [101].

By comparing the local lattice distortion with its ideal counterpart (characterised by the

average radius value $\overline{r}$, Figure 1.10), the dimensionless displacement of an atom from its ideal position will be $\frac{|r_i-\overline{r}|}{\overline{r}}$, and the total displacement:

$$\alpha_1 = \sum_{i}^{n} \frac{c_i|r_i - \overline{r}|}{\overline{r}} \tag{1.7}$$

Analogously, by defining as $\frac{|r_i+r_j-2\overline{r}|}{2\overline{r}}$ the dimensionless displacement between an atomic pair and its counterpart pair, we can define the parameter α_2 to represent a local atomic distortion:

$$\alpha_2 = \sum_{j \geqslant i}^{n} \frac{c_i c_j|r_i + r_j - 2\overline{r}|}{2\overline{r}} \tag{1.8}$$

The α_2 parameter shows a strong correlation with excess entropy and intrinsic strain energy.

Apart from being sensitive to local atoms arrangements, the lattice parameter was also found to correlate with the magnetic momentum of atoms. Lattice distortion has thus a significant effect on magnetic interactions [102].

Diffusion

The great variety in the nature of the atoms surrounding each lattice site in HEAs has a deep impact on diffusion. In fact, due to their near-equimolarity and compositional complexity, in HEAs there is no solvent element dominating the composition of the solid solution. The local atomic interactions, including vacancy formation and migration (Section 1.3.1), affect local enthalpy and thus diffusion kinetics.

Diffusion following thermal activation can be described by an Arrhenius-type equation:

$$D = D_0 exp\left(\frac{-Q_a}{RT}\right) \tag{1.9}$$

where the pre-exponential term D_0 and the activation energy Q_a are determined experimentally, R represent the perfect gas constant and Q_a the normalized activation energy.

The measurement of diffusion is made difficult by compositional complexity. In the only experimental study addressing the issue, the diffusion coefficients are determined after normalizing activation energies for the melting temperature (or solidus temperatures for alloys). This is based on the assumption that diffusion coefficients at melting temperature are roughly equal for metals and alloys displaying the same crystal structure and bonding type, and that the pre-exponential term D_0 is constant at melting temperature. The normalized activation energy Q_a obtained for the $CoCrFeMn_{0.5}Ni$ HEA is lower than the one of pure *fcc* metals [103]. The result is ascribed to lattice potential energy fluctuation between different sites and confirms the sluggish diffusion effect in HEAs.

1.3.2 Phase classification

Phase classification in HEAs should address whether a phase is (*i*) ordered or disordered, (*ii*) if it is a solid solution, (*iii*) if it is simple or complex. A recent work expanded the criteria used for conventional alloys (*i.e.* terminal phases, intermetallic compounds and solution phases [3]), to present the following taxonomy [104]:

- Terminal solid solutions, intermetallic compounds restricted to a stoichiometric ratio of constituent atoms and intermediate solutions;
- Random solid solutions, ordered solid solutions and intermetallic phases;
- Structures which can be characterised as simple–complex and ordered–disordered (*i.e.* simple disordered, simple ordered or complex ordered phases).

Disordered solid solutions have a single crystal lattice and do not display long-range order. If the solid solution phase is contiguous with one pure element, the phase can be defined a terminal solid solution, without the need for a single element to dominate over the others. Simple phases are defined as identical or derived from *fcc*, *bcc* and *hcp* structures (e.g. B2, $L1_2$ and B4). The phase is considered complex if atom positions in the crystal lattice are different from the aforementioned simple structures (e.g. σ-phase, Laves phase).

Analogously, microstructures can be classified as [105]:

- SS: microstructure (or alloy) containing one or more solid solutions;
- IM: microstructure (or alloy) with one or more intermetallic phases;
- SS+IM: microstructure (or alloy) containing a mixture of solid solution and intermetallic phases.

The most common crystalline phases found in HEAs are reported in Table 1.3.

Disordered *fcc* (56 %) and *bcc* (43 %) are the most common phases, whereas less than a dozen *hcp* alloys are known (1 %). All reported *bcc* HEAs from 3d transition metals contain Al, Cr and Fe (sometimes also Si, Ti and *bcc*-refractory elements). All these elements are known as *bcc*-stabilisers in steels [106, 96, 85]. All reported duplex *fcc*+*bcc* HEAs belong to the 3d transition metal family and consist of a combination of *fcc* and *bcc* stabilising elements.

Common intermetallic phases include B2, σ, the hexagonal Laves phase C14 and $L1_2$. The first and latter phases are common in Al-containing alloys, but B2 appears in microstructures in combination with a *bcc* phase, whereas $L1_2$ is generally seen with an *fcc* phase. The σ phase always forms in first-raw transition metals alloys containing Co, Cr and/or V, Fe and Ni. Alloys containing a Laves phase always have Cr and either Nb or Ti, and often Co, Fe and Ni (see Section 1.1.3).

[3] Corresponding respectively to phases based on a dominating element; compounds having stoichiometric, fixed compositional ratio; solid solution based on simple or complex crystal structures.

Strukturbericht notation	Pearson symbol	Prototype phase
A1 (*fcc*)	cF4	Cu
A2 (*bcc*)	cI2	W
A3 (*hcp*)	hP2	Mg
A5	tI4	β-Sn
A9	hP4	graphite
A12	cI58	α-Mn
B2	cP2	ClCs (or AlNi)
C14 (hexagonal Laves phase)	hP12	$MgZn_2$ (or Fe_2Ti)
C15 (cubic Laves phase)	cF24	Cu_2Mg
C16	tI12	Al_2Cu
$D0_2$	cF16	BiF_3 (or Li_2MgSn)
$D0_{11}$	oP16	Ni_3Si
$D0_{22}$	tI8	Al_3Ti
$D0_{24}$	hP16	Ni_3Ti
$D2_b$	tI26	$Mn_{12}Th$ (or $AlFe_3Zr$)
$D8_b$ (σ)	tP30	σ-CrFe
$D8_5$	hR13	Fe_7W_6 (or Co-Mo or Fe-Mo)
$D8_m$	tI32	W_5Si_3 (or Mo_5Si_3)
$E9_3$	cF96	Fe_3W_3C (or Fe-Ti)
$L1_0$	tP2	AuCu
$L1_2$	cP4	$AuCu_3$
$L2_1$ (Heusler phase)	cF16	$AlCu_2Mn$

Table 1.3: Crystal structures appearing in HEAs listed by Strukturbericht notation: A (elements), B (AB compounds), C (AB_2 compounds), D (A_mB_n compounds), E (more complex compounds), L (alloys) [82].

Empirical predictive approaches: the Hume-Rothery rules

Efforts have been made to develop methods able to identify desired or undesired phases and ultimately predict compositions which might favour solid solutions. While thermodynamic and atomistic models have been created, a considerable number of studies has focused on empirical approaches.

Hume-Rothery rules have been widely exploited to guide the investigation of the HEAs' hypermetric space. The foundations of these studies were laid by Hume-Rothery as early as the 1920s and promote the existence of a link between the stability of solid solutions, intermetallic compounds and liquidus temperature in metals and alloys, and the electron concentration parameter [107, 108].

The theoretical foundation of the rules, as set from Mott and Jones in 1936, is that the critical electron concentration (*i.e.* the number of free electrons per atom) is determined

from the condition that a spherical Fermi surface[4] touches the Brillouin zone[5] of relevant phases [110]. Subsequent development and applications of the Hume-Rothery rules have been extensively reviewed [111, 82].

Several authors have reported the usefulness of the electron concentration parameter in designing and classifying alloys, but it has also been noted that alloys and compounds obeying the rules were restricted to those whose electronic structure could be described within the nearly-free electron (NFE) model and discussed in terms of interaction between Fermi surface and Brillouin zone [112]. To overcome this limitation and extend the Hume-Rothery concentration rules to quasi-crystals, new electron concentration values were proposed as derived from Full-Potential Linearized Augmented Plane Wave (FLAPW) band calculations.

The Hume-Rothery rules state that the formation of solid solutions is favoured in alloys whose elements have similar atom size, electronegativity, crystal structure and valence. Atomic size is difficult to define in complex systems, as it is affected by the coordination's sphere [113]. Moreover, two definitions of electron concentration exist, and are to be considered depending on the studied material: the first is the valence electron concentration (VEC), according to which all electrons - including those accommodated in the valence band - should be counted; the second is e/a, the number of itinerant electrons per atom calculated as per:

$$e/a(A_mB_n) = \frac{v_A m + v_B n}{m+n} \tag{1.10}$$

Where v_A and v_B are the valence electrons of A and B respectively [114]. To address these issues, the HEAs community has developed composition-weighted definitions for differences in atomic radii (δr, also referred to as *atomic size mismatch*) and electronegativity ($\delta\chi$), whereas thermodynamical considerations have been taken into account through the mixing enthalpy (ΔH_{mix}) and through an Ω term combining ΔH_{mix}, entropy of mixing (ΔS_{mix}) and melting temperature (T_m) [115]:

$$\begin{aligned}
\delta r &= \sqrt{\sum_{1=1}^{n} c_i \left(1 - \frac{r_i}{\sum_{j=1}^{n} c_j r_j}\right)} \\
\delta\chi &= \sqrt{\sum_{i=1}^{n} c_i \left(1 - \frac{\chi_i}{\overline{\chi}}\right)^2} \\
\Delta H_{mix} &= \sum_{i=1, i<j}^{n} 4\Delta H_{ij}^{mix} c_i c_j \\
\Omega &= \left(\sum_{1=1}^{n} c_i T_{m,i}\right) \frac{\Delta S_{mix}}{|\Delta H_{mix}|}
\end{aligned} \tag{1.11}$$

[4]The Fermi level (corresponding to the total chemical potential for electrons) is the energy level which has a 50% probability of being occupied by any electron at any temperature. At absolute zero, it is the lower available energy state for electrons.

[5]A Brillouin zone is a particular choice of the unit cell of the reciprocal lattice (see Section 2.3.2). It is defined as the set of points closer to the origin than to any other reciprocal lattice point. The whole reciprocal space may be covered without overlap with copies of such a Brillouin zone [109].

where r_i and r_j are the atomic radii of atoms i and j; c_i and c_j are the atom fractions of atoms i and j; $\overline{\chi}$ is the average electronegativity; ΔH_{ij}^{mix} is the enthalpy of mixing of elements i and j at the equimolar concentration in regular binary solutions [116].

Most empirical approaches draw from δr and ΔH_{mix} or Ω to predict the formation of single solutions or intermetallics [117, 118, 119, 120, 121, 122]. Nevertheless, it was recently highlighted that e/a and average radius offer a valid methodology to estimate the phases that might occur in a multi-principal component alloy [113]:

- $e/a < 1.65$: *fcc*;
- $1.65 < e/a < 2.05$: mixed phases, and in particular σ;
- $e/a > 2.05$: *bcc*.

Other predictive approaches are based on CALPHAD calculations and modelling, and are most reliable when interpolating between compositions used to build the phase-diagrams database.

1.3.3 Phase transformations in HEAs

The 'core effects' reported in Section 1.3.1 play an important role in the phase transformations undergone by HEAs. In particular, the high mixing entropy of HEAs compared with conventional alloys is at the basement of the formation of simple solid solutions phases at high temperature. During the subsequent cooling, however, mixing entropy loses importance, and short-range ordering, long-range ordering or precipitation of secondary phases might occur. This phenomenon might be affected by sluggish diffusion, and either yield fine precipitates, or even inhibit the formation of competitive phases. On the other hand, if HEAs did not have high ΔS_{mix} at high temperature, intermetallic phases would form upon heating, and cooling would bring about very complex microstructures [123, 124, 84].

This observations led to the hypothesis of HEAs' phase diagrams being actually quite simple. In fact, due to high-entropy affect, regions of the compositional hyperspace characterised by single-, duplex and three-phases regions might exist, each delimited by specific concentration, temperature and pressure requirements. By knowing the phase diagram of a HEA, it would be thus possible to predict the stability range of each phase, and the equilibrium phases of a composition in a system [125]. Such approximate phase diagram are usually drawn from binary and ternary experimental data, but make use of computational software and ultimately rely on experimental validation. Among the most studied systems are Al–Co–Cr–Fe–Ni, Co–Cr–Fe–Mn–Ni (Figure 1.11) and Al–Co–Cr–Fe–Mo–Ni [85, 126].

Two types of phase transformations are known to occur in alloys: the diffusional type and the diffusionless type. The first includes solidification, precipitation, eutectic and eutectoid reactions, spinodal decomposition, ordering transformations and dissolution. Grain coarsening and Oswald ripening of second phase particles as consequence of annealing are also considered diffusional type phase transformations. Diffusionless transformation include

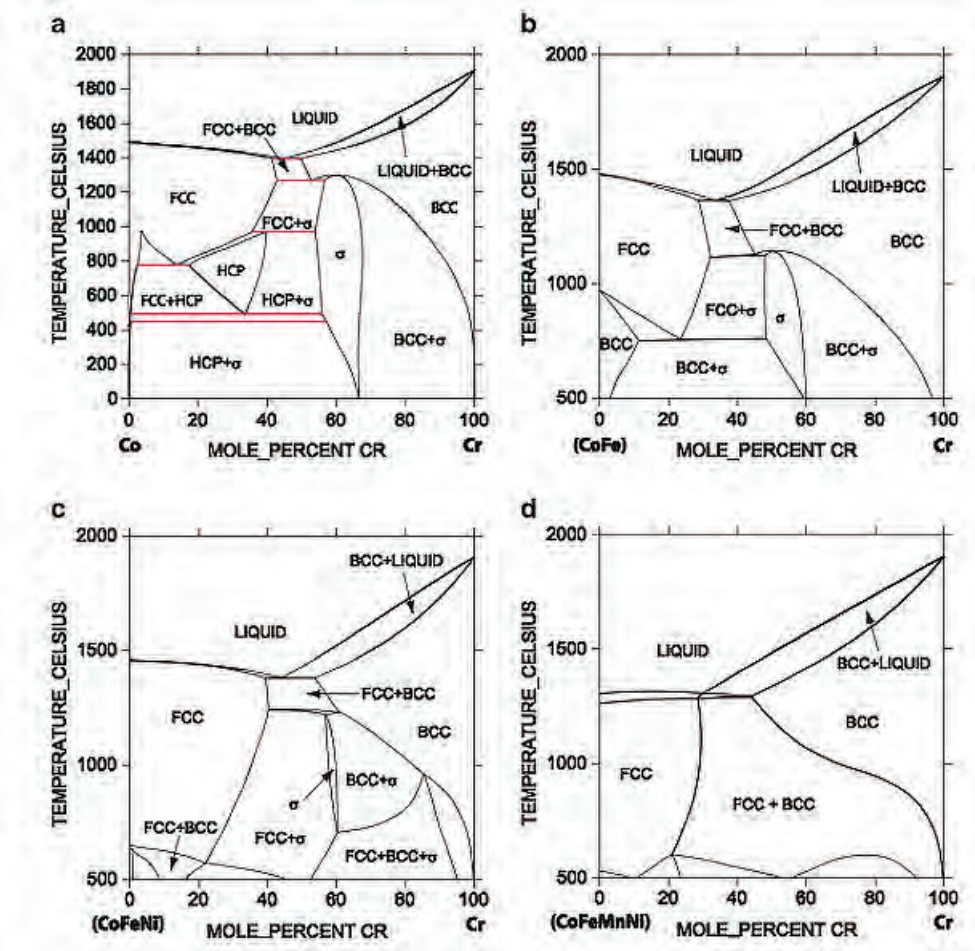

Figure 1.11: (*a*) Co–Cr binary and pseudo-binary systems, (*b*) CoFe–Cr, (*c*) CoFeNi–Cr, and (*d*) CoFeMnNi–Cr phase diagrams calculated using the TCNI7 database [85].

martensitic transitions, which have been reported only once in HEAs literature [127]: the CoCrFeMnNi HEA was reported to undergo an *fcc-hcp* transition beginning at 14 GPa and attributed to the suppression of local magnetic moments. The two closed-packed structures differ only in the stacking sequence of their close-packed planes: the energy required by the transformation is low and promoted by the formation of stacking faults during compression.

Diffusional type transformations are by far the most common in HEAs, and in particular nucleation and growth and spinodal decomposition. The driving force for the transformation to occur is provided by the Gibbs free energy difference between new and old phases. However, interfacial energy relates to lattice distortion, and nucleation and growth rate are influenced by sluggish diffusion. It is possible to completely inhibit long-range diffusion, and thus obtain non-equilibrium simple solid solutions and eventually amorphous structures: this is achieved by using mechanical alloying [128, 86], melt spinning [129] or sputtering deposition [130, 131, 132], because the atomic size difference required to form amorphous structures is smaller than the one required by the solidification route [85].

Few recent works have also focused on determining the equation of state of HEAs, a

pressure-volume relationships at constant temperature from which the bulk modulus of the material can be calculated (see section 2.3.5). The HoDyYGdTb HEA was synthesised and compressed up to 60 GPa at room temperature: three transformations were identified, as following [133]:

$$hcp \xrightarrow{4.4\ \text{GPa}} Sm-type \xrightarrow{26.7\ \text{GPa}} double-hcp \xrightarrow{40.2\ \text{GPa}} distorted-fcc \tag{1.12}$$

Conversely, investigation of the AlCoCrCuFeNi HEA from ambient pressure to 24 GPa highlighted that the alloy maintains its original *fcc*+*bcc* structure [134].

The *hcp*-structured $Ir_{0.19}Os_{0.22}Re_{0.21}Rh_{0.20}Ru_{0.19}$ was also reported to be stable between ambient pressure and 45 GPa [90].

1.3.4 Effect of intermetallic phases in HEAs

As in many of the most advanced structural alloys, the properties of HEAs can be further tuned by proper control of the size, shape, volume fraction and distribution of intermetallic phases [82, 135].

Precipitation hardening represents an effective strengthening mechanism, as reported by several papers for the Al–Co–Cr–Cu–Fe–Ni and Al–Cr–Fe–Mn–Ni [136, 137] systems. Further introduction of ordered nano-precipitates as pinning centres [138] can be achieved either by selective annealing [139, 140] or by the addition of alloying elements [98]. Importantly, these compounds require stabilisation to maintain coherence without disrupting the matrix [141, 142].

Following a traditional trend in alloy development, HEAs have thus seen the addition of selected secondary phases to further tune their mechanical properties. The addition of alloying elements in low concentrations, on the other hand, has resulted in the precipitation of intermetallic compounds in the alloy matrix. However, while intermetallics deeply affect yield strength, hardness, tensile properties and matrix stabilisation – due to the competition between mixing enthalpy of atom pairs and mixing entropy–, their proper distribution, size, shape and volume fraction represent a cause for concern [82]. The creation of precipitation-hardened HEAs following intermetallic introduction has proven largely unsuccessful when binary compounds are concerned, and no studies have been performed on the formation of stable ternary inclusions as pinning centres in complex multi-principal component alloys [142, 141]. This is mostly due to the difficulties in choosing an appropriate alloying element. The selection should be guided by the following considerations: miscibility for most or all HEA constitutive elements in liquid state, low formation enthalpy for ternary compounds and crystallisation in common structure-types.

The importance of atomic size in the selection of major intermetallic phase types has recently been highlighted. CoCrFeNiX was systematically alloyed with X = Y, Ti, Zr, Hf, V, Nb, Ta, Cr, Mo, W, resulting in the formation of intermetallics related to the so-called Topologically Closed-Packed (TCP) phase. Each TCP has its own allowable range of atomic

size ratio r_X/r_A, therefore a particular intermetallic phase will form only if the atomic radii of A (corresponding to Co, Cr, Fe or Ni) and X is adequate [143].

1.3.5 HEA–based Composites

Metal matrix composites (MMC) are a class of materials often displaying properties unattainable with conventional alloys. Their features entail tunable thermal and mechanical properties, thus MMCs are frequently implemented for the thermal management of electronic components and for applications in which high hardness, yield and tensile strength are pivotal. MMCs rely on the addition of a reinforcing material to a metal matrix. For the additive to be effective, a careful balance of wettability and chemical affinity is essential, and the new phase should be homogeneously distributed [144]. These requirements are difficult to satisfy with complex multi-component alloy matrices. The development of HEA composites (HEACs) is thus still at its early stages, and medium-entropy alloys consisting of four components are more often exploited. HEACs containing oxides [145], silicon carbide [146] or nano-diamonds [147] have been so far reported.

Unlike the pure sintering of metal powders, the preparation of HEACs might be opposed by low densification. The incomplete densification of large elemental clusters during SPS has been reported as the result of entrapped gases and/or localized increase in electrical resistivity [145]. Furthermore, the limited electrical conductivity of certain additives or their low homogeneity can hinder the formation of bonds between reinforcing material and matrix. These results have been reported for the addition of hexagonal and cubic boron nitride, silicon carbide and functionalised carbon nano-tubes to the $Al_2CoCrFeNi$ HEA [147] (Section 3.3.1).

The Rule of Mixtures

Many composites materials consist of two phases: a continuous matrix surrounding a dispersed phase. The properties of composites are a function of the properties of the constituent phases, their relative amounts and the geometry of the disperse phase (*i.e.* particles' shape, size, distribution and orientation). On the basis of microstructure, three types of microscopic composites can be distinguished [148]:

- Dispersion strengthened, consisting of a matrix in which particles with diameter 10-100 nm are dispersed.
- Particle reinforced, containing 20-40 vol.% particles of diameter > 1 μm.
- Fiber reinforced, in which the dispersed phase has a large length-to-diameter ratio, and whose concentration may range from several percent to 70 vol.%.

Predicting the overall mechanical properties of the composite is very important for material design and applications. Many models attempting to correlate the overall mechanical properties of the composite and the properties of its constitutes have been proposed: for example, the self-consistent variation methods, mean-field theories, shear-lag theory, finite element method

(FEM) and a rule of mixtures (ROM). Although the FEM gives satisfactory results for problems with complex geometry, the ROM is a more intuitive and fast solution for estimating the effective mechanical properties of a composite in terms of its constitutes [149].

The Rule of Mixtures in particle-reinforced composites Generally, properties that obey the ROM can be calculated as the sum of the value of the property of each constituent multiplied by its respective volume fraction or weight fraction in the mixture [150]. Density and heat capacity are accurately predicted by simple rule of mixture (ROM) models. For example, the **density** of a composite (ρ_c) can be calculated from the density and volume fraction (or weight fraction w) of the matrix (ρ_m and V_m) and the additive (ρ_a and V_a) as follows [150]:

$$\rho_c = \rho_m V_m + \rho_a V_a = \frac{1}{\frac{w_m}{\rho_m} + \frac{w_a}{\rho_a}} \tag{1.13}$$

Numerous models have been proposed for the description of thermal behaviour of composites [151]. The first model to predict the **thermal expansion** of a particle-reinforced composite was proposed by Kerner as follows [152]:

$$\alpha_{T,c} = \overline{\alpha_T} + \frac{V_a(1-V_a)(\alpha_a - \alpha_m)(K_a - K_m)}{K_m(1-V_a) + K_a V_a + (\frac{3K_a V_m}{4G_m})} \tag{1.14}$$

Where $\alpha_{T,c}$ is the composite coefficient of thermal expansion (CTE), $\overline{\alpha_T}$ is the linear ROM CTE, V_a is the volume fraction of additive reinforcement, K_m and K_a are the bulk moduli of the matrix and additive, and G_m is the shear modulus of the matrix. Under the assumption that the composite is a simple mixture of two phases, with each phase exhibiting physical behaviours which are not influenced by their presence in the mixture, the second term is negligible in comparison to the first. The Kerner model can thus be reduced to the more general linear ROM form for a two-phase composite, known as the Voigt approximation [153]:

$$\alpha_{T,c} = \alpha_1 + V_2(\alpha_2 - \alpha_1) \tag{1.15}$$

Where α_1 and α_2 are the CTEs of the first and second phase, respectively. In this model the effects of microstructure, plasticity, and thermal softening are not considered [153]. An equation for spherical reinforcement particles, which considers only isostatic stress, was derived by Turner [154]:

$$\alpha_{T,c} = \frac{\alpha_m V_m K_m + \alpha_a V_a K_a}{V_m K_m + V_a K_a} \tag{1.16}$$

The ROM formulation developed by Schapery, on the other hand, can be used to account for the effects of damage on the thermal expansion behaviour of particle-reinforced composites [155].

$$\alpha_{T,c} = \alpha_a + (\alpha_m - \alpha_a)\left[\frac{\frac{1}{K_c} - \frac{1}{K_a}}{\frac{1}{K_m} - \frac{1}{K_p}}\right] \tag{1.17}$$

Electrical conductivity of composites (σ_c) was also extensively modelled. For metal-

matrix composites with small volume fractions of approximately spherical reinforcement, the Rayleigh-Maxwell equation gives accurate results [150]:

$$\sigma_c = \sigma_m \frac{1 + 2V_a \left[\frac{1-(\sigma_m/\sigma_a)}{1+(2\sigma_m/\sigma_a)}\right]}{1 - V_a \left[\frac{1-(\sigma_m/\sigma_a)}{1+(2\sigma_m/\sigma_a)}\right]} \tag{1.18}$$

Where σ_m and σ_a are the electrical conductivity of the matrix and the reinforcement, respectively. For this calculation, Rayleigh considered material in the form of spherical inclusions arranged in a simple cubic array, embedded in a continuous matrix [156].

Young's modulus (E_c) is an elastic property which is well bracketed by two models, one for axial loading (Voigt model, equal stress), and one for transverse loading (Reuss model, equal strain) [150, 157]. For a composite material made up of continuous and unidirectional fibers, the upper-bound modulus corresponds thus to loading parallel to the fibers; while the lower-bound modulus corresponds to a transverse loading. The linear upper bound (E_c^{up}) is defined by the rule of mixtures as [150]:

$$E_c^{up} = \frac{E_m V_m + E_a V_a}{V_m + V_a} \tag{1.19}$$

Whereas the non-linear lower bound (E_c^{low}) is defined through a more complex expression for materials containing spherical particles, which can be simplified by assuming Poisson's ratio to be a universal constant with value 0.2:

$$E_c^{low} = \frac{E_m V_m + E_a (V_a + 1)}{E_a V_m + E_m (V_a + 1)} \tag{1.20}$$

The equal strain treatment (upper bound) and the equal stress treatment (lower bound), can be used for modelling the effective **hardness** $\overline{H_c}$ of the composite as in elasticity analysis [149]. In the case of a soft matrix containing a hard additive, the upper and lower bounds take the form of, respectively:

$$\begin{aligned} \overline{H_c^{up}} &= V_a \overline{H_a} + V_m \overline{H_m} \\ \overline{H_c^{low}} &= \frac{1}{\frac{V_a}{H_a} + \frac{V_m}{H_m}} \end{aligned} \tag{1.21}$$

1.4 Potential of scandium in the developing field of HEAs

New low-density multi-principal component alloys.

As previously mentioned, outstanding mechanical and structural features, coupled with simple crystal structures, make HEAs promising as materials for high-temperature applications, in which high hardness should be coupled with high chemical and mechanical stability [79]. The design of new HEAs is driven by the principle of configurational entropy maximization, with consequent Gibb's free energy reduction. This is mostly achieved by combining at least five

principal elements at 5–35 at.% concentrations. However, the relative affinities of metals, synthetic route and mechanical treatments also play a role in the formation of single-phase HEAs. Therefore, trials have often led to the development of equimolar multicomponent alloys consisting of intermetallic compounds and solid solutions of different space groups [158, 159]. While models based exclusively on ternary phase diagrams fail to predict the formation of single phase HEAs, the information extracted from simple systems can certainly prove useful in directing new synthetic approaches.

According to their density, melting point and hardness, HEAs can be classified as heavy–light, refractory, and soft–hard materials. In many cases, refractory (with melting point above 2000 °C) HEAs are characterised by high hardness (600–900 HV): however, since their main components are Mo, Nb, Ta or Zr, their density equals or surpasses 10 $g \cdot cm^{-3}$ [160, 161], which limits their application. Conversely, only few alloys display micro-hardness values of 800 HV or more. Such hardness values have usually been obtained for refractory HEAs (such as MoTiVFeNiZrCoCr) or for light Al-based HEAs with moderate density (3–5 $g \cdot cm^{-3}$) through mechanical alloying [162]. Nevertheless, high-temperature applications demand a sensible balance between strength and tensile ductility, and no known single-phase HEA satisfies such requirements.

The low density and high hardness of scandium makes it a promising candidate for creating multi-principal components alloys which are both light and strong. The trials and steps forward made in this direction are reported in Section 3.1.1.

New *hcp*-structured multi-principal component alloys.

As highlighted in Section 1.3, *hcp*-structured HEAs a growing field. This is partly because previous research has tackled only a small portion of the compositional space, focusing mostly on some transition or refractory metals. The preparation of *hcp*-structured HEAs has been mostly driven by uncommon elements, especially those belonging to the lanthanides series. DyGdLuTbY and DyGbLuTbTm HEA consist of an *hcp* alloy plus an unknown phase [87]. Two-phase *hcp* structures were reported in the six-component HfLaScTiYZr alloy [88]; one of these was isolated as the equiatomic HfScTiZr [163]. Exceptions are the CoFeNiTi alloy [164], which is a mixture of *hcp* and *fcc* phases, and the predicted CoOsReRu alloy [165]. $AlLi_{0.5}MgScTi_{1.5}$, produced via mechanical milling followed by high temperature annealing [66], and DyGdHoTbY, synthesized via arc melting from pure metals [166] were reported to be purely *hcp*-structured. Phase pure three- and four-component alloys have also been reported (MoRhRu and MoPdRhRu). However, using the composition definition from [82], they cannot be considered HEAs, but rather medium-entropy alloys [167].

A new family of *hcp*-structured HEAs was recently prepared by thermal decomposition of single-source precursor. The forefather of this new class of alloys is $Ir_{0.19}Os_{0.22}Re_{0.21}Rh_{0.20}Ru_{0.19}$ and springs from the combination of Ir–Os–Pt–Re–Rh–Ru phase diagrams. The 6 metals have 15 binary phase diagrams, including 3 *fcc–fcc* and 3 *hcp–hcp* diagrams with complete solubility in solidus at high temperatures, as well as 9 *fcc–hcp* peritectic diagrams with a miscibility

gap between *fcc*- and *hcp* alloys. The system can thus be constructed from the two ternary sub-systems Os–Re–Ru and Ir–Pt–Rh with complete solubility in the solid state, and 5- and 6-component alloys can be classified by their ratio between *fcc* (Rh, Ir, Pt) and *hcp* (Ru, Re, Os) metals [90].

The idea of combining *hcp*-structured elements to investigate the formation of *hcp* alloys in multi-principal component alloys may seem naïve, but the state of the art of *hcp* HEA highlights that even pan-hexagonal metallic compositions usually form poly-phase mixtures of *hcp*-alloys or intermetallic compounds. The melting of hexagonal metals leads only to 3- or 4-component *hcp* alloys, which are normally in equilibrium with ordered phases or quasicrystals, as in $AlCuMg_xMnZn$ [96]. Furthermore, as in the case of $AlLi_{0.5}MgScTi_{1.5}$, melting temperatures of individual metals might be so different that mechanical alloying substitutes more traditional synthesis routes.

The results obtained by combining scandium with other *hcp*-structured metals are reported in Section 3.1.2.

Small scandium additions to HEAs

The mechanical properties of multi-principal component alloys heavily depend on their microstructure and composition. The latter influences dislocation behaviours by setting atomic interactions and elastic properties, and is determinant in defining the existing phases and their volume fraction. Microstructural features such as distribution, shape and size of the phases or the presence of defects influence mechanical properties just as profoundly [82]. Both parameters are strictly connected to the thermodynamic of the system, as well as to synthetic conditions and post-synthetic mechanical and/or heat treatments [168].

As previously mentioned, scandium forms over three hundred binary and ternary phases with most elements of the periodic table, many of which showing simple recurring structures and low formation enthalpy. Moreover, scandium-based intermetallics (*i.e.* Al_3Sc, *V*- and *W*-phases) deeply affect the properties of commercial aluminium alloys and newly developed multicomponent systems [17].

While the compound-forming ability of scandium might be a drawback for its use in large quantities to develop new single-phase HEAs, these very same features make it a perfect candidate to achieve precipitation-hardened HEAs. Moreover, its low density makes it ideal in combination with HEA based on first-raw metals, which make up to 85% of the known systems [82].

The thoroughly-investigated $Al_xCoCrCu_yFeNi_z$ HEA can be considered a model alloy, whose solid solution nature can be tuned by changing the amount of aluminium and copper content (since Al and Cu act as *bcc*- and *fcc*-stabilizers respectively) [169, 170]. Computational studies on AlCoCrFeNi and $Al_{1.25}CoCrFeCuNi$ at 800 °C have highlighted the existence of short-range interactions for both systems: for the first, the most preferred pair is AlNi, followed by AlCo and CrFe. For the latter, the preferred pair interactions are CrFe, AlNi and CuCu. This suggests the existence of short-range ordering of AlNi, CoCr and CrFe pairs in

the liquid state for both alloys and the segregation of copper in $Al_{1.25}CoCrFeCuNi$ [170].

Experimental observations have confirmed these results. Several $Al_xCoCrFeNi$ investigations report the presence of a B2 sublattice (AlNi), whereas $Al_xCoCrCu_yFeNi$ generally show a mixture of *bcc* and *fcc* solid solutions (corresponding respectively to Cr–Co–Fe-rich and Cu-rich areas) [84, 171, 172, 173]. Consistently, the reported single-phase *fcc*-structured HEAs belonging to this family contain low amounts of Al; in particular $Al_xCoCrFeNi$ (for $0 \leqslant x \leqslant 0.3$) and CoCrCuFeNi [174, 175, 176, 177]. A mixture of *fcc* and B2 phases has been obtained in the as-cast $AlCoCrFeNi_{2.1}$ eutectic HEA [178]. Nevertheless, $AlCoCrCu_yFeNi$ HEAs are still widely reported as being single-phase solid solutions [82].

Results obtained when scandium was alloyed to HEAs in small quantities are reported in Section 3.2.1.

Since HEAs have been proposed for applications in extreme environments, their phase evolution upon heating has been extensively studied, both *in situ* and *ex situ* [84]. On the other hand, the exploration of the hyper-dimensional stability space of HEAs systems at different pressure and temperature conditions has barely been tackled. Even for sintering (a common processing route for manufacturing bulk polycrystalline materials), the effect of pressure – rather than temperature – has rarely been studied [179, 180, 181].

A commonly used field-assisted technique is Spark Plasma Sintering (SPS), which provides fast densification of powder-based precursor materials due to highly localized temperature increases caused by the application of pulsed current. The pulsed current has a cleansing effect on particle surfaces, which results in very low or zero oxygen concentration at grain boundaries. Feedstock particle size and morphology have little influence on the resulting material [182]. While several HEAs have been consolidated or synthesized by SPS, the results give only a partial overview of the phase stability or the equation of state of the respective systems [183, 184, 185].

On the other hand, preliminary work performed on CoCrFeNiMn highlight the extraordinary potentials hidden in the pressure-dependent phase diagrams of multicomponent alloys [127]. The role of pressure in the phase stability of phase pure and intermetallic containing HEAs is a promising avenue of research which has barely been tackled.

Part of the current work has focused on investigating the effect of pressure on pristine and Sc-containing HEAs. The results are reported in Section 3.2.2.

High-Entropy Alloy Composite materials

Metal matrix composites (MMCs) represent a class of materials often displaying properties unattainable within conventional alloys systems. With their inherent features being deeply influenced by the nature of the metal matrix and by the type and amount of secondary phase herein contained, MMCs are typically implemented for the thermal management of electronic components and for applications requiring high hardness, yield and tensile strength [186, 144]. The wide variety of reinforcing materials used, ranging from carbides (SiC, B_4C

and WC) to oxides (Al_2O_3 and SiO_2) to carbon nanotubes and graphite, is matched by the diversity of metal matrices [187]. Commonly used metal systems include light metal alloys (Al, Mg and Ti), Zn- and Cu-based alloys and stainless steel, but Al remains by far the most exploited matrix material for the development of new MMCs [188]. Thus, most work reported in the literature refers to the A357, A359, 2618, 2214, 6061, 6063 and 7075 aluminium alloys [189, 190, 191].

Considering that the attractive properties of MMCs often entail tuneable thermal and mechanical properties, the absence of MMCs based on multicomponent alloys might appear surprising. However, a homogeneous distribution of the strengthening phase requires a careful balance of wettability and chemical affinity, which would be extremely difficult to achieve with complex multi-phase systems. An answer to this issue can come from High-Entropy Alloys (HEAs), which combine high chemical complexity with simple, single-phase crystal structures and that have been proposed for applications in which high thermal and mechanical stabilities are pivotal.

The results obtained by introducing several commercially available additives to the $Al_2CoCrFeNi$ HEA are reported in Section 3.3.

1.5 Outline of the work

In the 'Introduction' section, I explored the nature of scandium and its behaviour when combined with different elements of the periodic table. I highlighted that, even though knowledge about scandium metallurgy is fragmentary, this metal has been widely exploited as a small addition to many commercial alloys. The formation of stable scandium-based intermetallics in multicomponent alloys always led to enhanced properties, thus sealing the role of scandium as a 'spice metal'.

The appearance of a new class of alloys based on a high number of principal components (the so-called High-Entropy Alloys) challenged traditional approaches in metallurgy and opened the door for the utilisation of scandium as active alloying element. In the current work I will investigate the role which scandium might acquire in the growing field of HEAs.

In section 3.1, I report two pilot studies concerning the use of scandium as active alloying element in the development of a multi-principal component alloy. In the first study, scandium is combined with other first-raw metals (Al, Cr, Cu and Ti); whereas in the latter, it is alloyed with other *hcp*-structured elements (Co, Gd, Ti, Y and Zr).

In section 3.2, I highlight the effect of small scandium additions to single- or duplex-HEAs. The resulting alloys are thoroughly characterised as per their microstructures, mechanical properties and phase stability. In the light of the enhanced phase stability upon temperature, I explore a section of the hyper-dimensional space of the doped $Al_2CoCrFeNi$ HEAs upon extreme conditions of pressure and temperature.

Finally, in section 3.3 I present our efforts in obtaining a scandium metal-doped HEA starting from the commercially available scandium master alloy Scalmalloy® and from the cheaper Sc_2O_3. Unlike Scalmalloy®, the low electric conductivity of Sc_2O_3 makes it unsuitable for our regular melting route. I thus study its behaviour as additive to a ready-made HEA in a spark-plasma sintering process. Coincidentally, I investigate the performances of several additives traditionally used for the development of Metal Matrix Composites.

The rationale behind the current work is schematically presented in Figure 1.12.

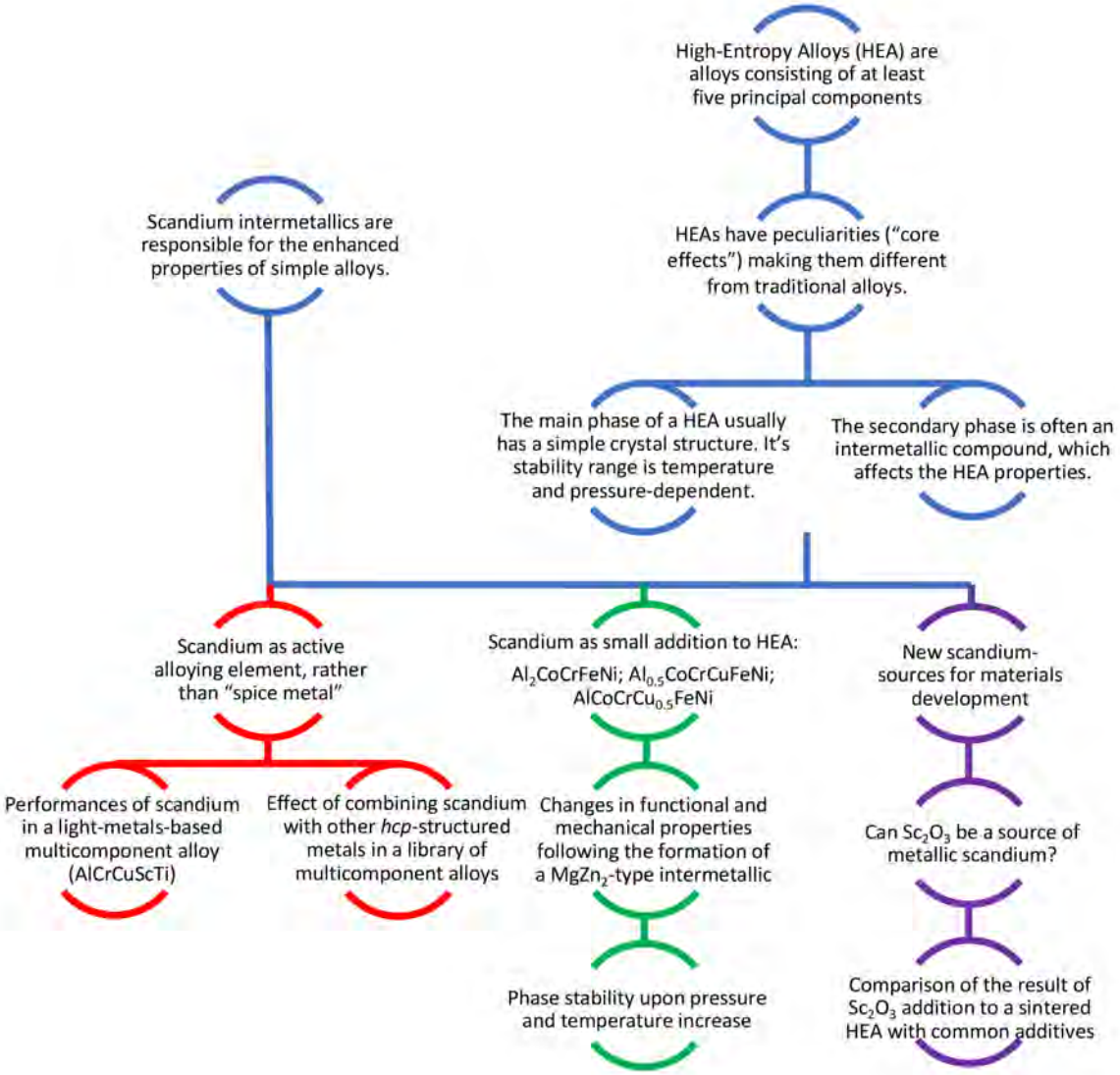

Figure 1.12: Infographic presenting the rationale behind the current work. In *blue* is outlined the Introduction; in *red*, *green* and *purple* the three main sections of the Results and Discussion chapter.

The scope of the study does not extend to a consideration of computational modelling, due to lack of time and resources.

1.6 Aims and objectives

In conclusion, the aim of this work is to explore the potential of scandium in the growing field of High-Entropy Alloys; with special attention to structure-properties relationships, behaviour in extreme conditions of temperature and pressure, and scaling-up feasibility.

In order to achieve this aim, I will:

- Produce and test multi-principal component alloys containing scandium as active alloying element;
- Produce and characterise scandium-doped HEAs displaying simple crystal structures;
- Analyse *in situ* the phase stability of promising scandium-containing HEA candidates in extreme pressure and temperature conditions;
- Test the potentiality of different resources as scandium metal sources.

Chapter 2

Methods

The experimental techniques used to synthesise and characterise the materials investigated in this work are herein described.

All studied specimens have been prepared via induction melting, and either investigated as pellets or crushed into powder and processed further with mechanical alloying or spark-plasma sintering. PXRD highlighted no difference between crushed samples and original pellets.

The sample morphology and composition were investigated with Scanning Electron Microscopy (SEM) equipped with Energy-Dispersive X-ray (EDX) analyser or with AFM-SKP. Phase identification was performed on the powered samples with Powder X-ray Diffraction (PXRD) on in-site equipment or at synchrotron radiation facilities. The occurrence of phase transition upon heating was estimated from Differential Scanning Calorimetry (DSC).

The most promising specimens were characterised according to their mechanical and functional properties for Vicker's hardness, ductility (disk-punch test), thermal expansion (dilatometry) and thermo-electric properties (Laser Flash Analysis (LFA), Seebeck coefficient).

2.1 Synthesis

2.1.1 Induction melting

Thermal treatment is a common procedure for achieving or speeding up a reaction between solid or liquid reactants. Depending on the reactivity of reagents and products, as well as on the temperature required by the process, several furnaces types are available. In general, each of them contains a temperature measuring device and a control device. The most common laboratory furnaces are:

- Electric resistance furnace. It consists of an electrical resistance heating coil and is useful for both preparatory purposes and long heat treatments; it usually operates up until 1700 °C and under inert atmosphere.
- Induction furnace. It utilises the electro-magnetic field produced by current flowing though a copper coil (inductor coil, Fig. 2.1).

- Arc furnace. It consists of a copper block, acting as the positive electrode, and a tungsten wire, acting as negative electrode: when the melting generator has been turned on, the electric arc can melt the sample. Due to its high operating temperatures, the system requires a vacuum chamber and a water-cooling system. Several re-meltings may be necessary to obtain a homogeneous specimen.

Equal importance should be given to the choice of crucibles, in order to avoid side-reactions and prevent sample contamination. Crucibles can be made from several different materials:

- Metals. They have to be used in inert or reducing atmosphere to avoid oxidation; the most common are W, Mo, Fe (for alkaline/alkaline earth metals), Ni, Cu, Ag, Au, Pt (for metalloids).
- Ceramics. They can be used in air and at very high temperatures, but their performances drop in oxidizing atmosphere. Most common ceramic materials include porcelain, alumina, stabilized zirconia, silicon nitride, graphite, and others: between them, thorium oxide (ThO_2) has the higher melting point and can be processed to obtain a high-density ceramic body.

Boron nitride crucibles represent a valid alternative to the traditionally used Al_2O_3 and graphite ones, due to its high temperature conductivity and electrical resistivity, its thermochemical stability and its non-wetting properties. In fact, boron nitride can withstand higher melting temperatures and aggressive melts (e.g. steel, molten sodium carbonate, Al–Li and Cu–Ti alloys) [192].

Figure 2.1: Induction melting of the $Al_2CoCrFeNi$ HEA in a boron nitride crucible. The synthesis is performed in an Ar-filled glove box.

Although simple, melting has some limitations: if an alloy was to be cooled too fast, a non-equilibrium phase would be created - requiring more treatments to achieve homogeneity [193, 148]. Moreover, some alloys may be difficult or impossible to synthesise with this method, because the melting temperature of one component is higher than the boiling point of the

other. In this case, it may be worth considering less invasive approaches, such as mechanical alloying or interface diffusion. During interface diffusion processes, two metals are placed in contact with one another and heated up to the melting temperature of the lower-melting species. The melted metal will slowly diffuse through the interface and react with the higher-melting one: several re-meltings are necessary to obtain a homogeneous sample. Nevertheless, the method has gained popularity in the frame of high-throughput analysis (Diffusion-Multiple Approach) [194, 195].

2.1.2 Mechanical alloying

While melting from powders remains the easiest route for new alloys development, it is hardly applicable to systems consisting of metals of very different melting points. In such cases, mechanical alloying (MA) - a powder processing technique that allows production of homogeneous materials starting from blended elemental powder mixtures - is usually preferable. MA is normally a dry, high-energy ball milling technique and has been employed to produce a variety of powder materials, ranging from amorphous to metastable phases, to intermetallics, to nanocomposites [196].

A second term is commonly used to denote the processing of powder particles in high-energy ball mills: mechanical milling (MM). Contrary to MA, in MM the powders are already alloyed and only a reduction in particle size need to be induced mechanically. Since the time required for processing is shorter, MM of powders reduces oxidation of the constituent powders [197].

The feedstock material generally used for MA is in powder form (*i.e.* pure metals, master alloys, prealloyed powders, refractory compounds) that have particle sizes in the range of 1-200 μm. As long as it is smaller than the grinding ball size, however, the powder particle size is not critical. In fact, it decreases exponentially with time, reaching a few microns only after a few minutes of milling [198].

Since MA is a complex process, several parameters affect the final constitution of the powder. Some of the variables to be taken into consideration are: type of mill; milling container; milling speed; milling time; type, size, and size distribution of the grinding medium; ball-to-powder weight ratio; extent of vial filling; milling atmosphere; process control agent; temperature of milling. These process variables are not completely independent. Some of them will be reviewed in the following pages.

A suitable mill has to be chosen depending on the type, quantity and required final constitution of the powder. Different types of high-energy milling equipment are used to produce mechanically alloyed powders. These mills differ in their capacity, speed of operation, and their ability to control the operation by varying the temperature of milling and the extent of minimising the contamination of the powders. The two most common types are [198]:

- Shaker mills (used for screening purposes). This mill commonly has one or two secured

vials which are swung energetically back and forth several thousand times a minute. The back-and-forth shaking motion is combined with lateral movements of the ends of the vial, so that the vial appears to be describing an infinity sign as it moves. Since with each swing of the vial the balls impact against the sample and the end of the vial, both milling and mixing occur in the sample.

- Planetary ball mills (used to produce large quantities of milled powder). In this instrument, vials are arranged on a rotating support disk. A special drive mechanism also causes them to rotate around their own axes, so that vials and the supporting disk rotate in opposite directions. The centrifugal force produced by the vials as well as by the rotating support disk both act alternately on the contained powder. This causes the grinding balls to run down the inside wall of the vial (friction effect), followed by the material being ground and grinding balls colliding against the opposing inside wall (the impact effect).

The material used for the milling container vial is important, because the impact of grinding balls on the inner walls of the container may result in some material being dislodged and incorporated into the powder. This can contaminate the powder or alter its chemistry. The most common types of materials used for grinding vessels are steel, WC-Co, WC- lined steel. Other specific materials (e.g. sintered corundum, yttria-stabilized zirconia, sapphire...) are used for specialized purposes. To avoid cross-contamination, the same materials used for the containers are employed for the grinding medium, whose density should be high enough so that the balls create enough impact force on the powder. Following the same reasoning, a large size of the grinding balls is often preferred [199].

Milling speed and time also affect the final result of MA. Increasing the speed of rotation will increase the speed of balls' movement. However, above a critical speed, the balls will be pinned to the inner walls of the vial and will not exert any impact force upon falling. The maximum speed should therefore be just below this critical value: this way, the balls will fall down from the maximum height and produce the maximum collision energy [199]. On the other hand, milling time is usually chosen as to achieve a steady state between the fracturing and cold welding of the powder particles. The choice of time varies depending on the type of mill used, the intensity of milling, the ball-to-powder ratio and the temperature of milling. However, if the powder is milled for times longer than required, the level of contamination increases and some undesirable phases might form [199].

During the milling process, powder particles are trapped between colliding balls and undergo severe plastic deformation. Figure 2.2 shows three examples of the manners in which flying balls could collide with the powders in the vials [196].

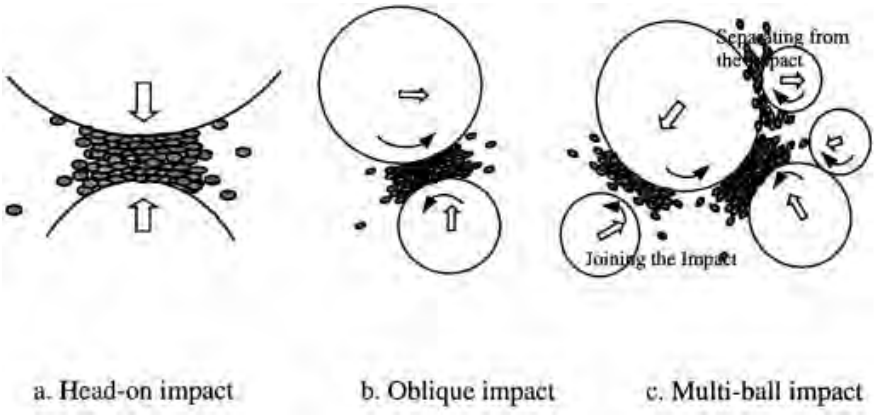

Figure 2.2: Schematic diagram showing the different forms of impact which might occur during high-energy ball milling [196].

In MA, ball-powder-ball collisions lead to the following events [200]:

a. Repeated cold welding and fracturing of particles, resulting in the mixing of constituents and the formation of composites of powders.

b. Creation of high density of lattice defects (e.g. point defects, dislocations, stacking faults) induced by severe plastic deformation.

c. Material transfer by diffusion of components. Diffusion during MA is significantly accelerated by lattice defects and by a momentary increase in temperature of particles trapped between colliding balls.

While MA is intrinsically difficult to scale up, ball-milling followed by annealing still represents a practical way to explore new metal combinations. Moreover, it is a powerful technique for alloying elements immiscible in liquid state [201]. The recently reported synthesis of the $Al_{20}Li_{20}Mg_{20}Sc_{20}Ti_{20}$ HEA, highlighting its promising features of a Sc-containing HEAs for aerospace applications, is one such example. Scandium has a miscibility gap in liquid state with lithium; moreover, elements have very different melting points. Other researchers have thus used ball-milling to combine low-density metals, finally achieving an outstanding density to hardness ratio [66].

In the current work, ball-milling equipment has been used to perform mechanical milling (MM) so as to crush prealloyed pellets. Even though vials and balls were made of steel, no carbon or carbide contamination was visible from EDX and PXRD. Moreover, since all ground samples already contained about 20 wt.% Fe, small fluctuations in composition due to contamination went unnoticed.

2.1.3 Spark-Plasma Sintering

A commonly used field-assisted technique is Spark Plasma Sintering (SPS), which provides fast densification of powder-based precursor materials due to highly localized temperature

increases caused by the application of pulsed current. The main advantage of Spark-Plasma Sintering (SPS) is to achieve very high heating rates on materials where a fine grain size is desirable. SPS is comparable with Hot Pressing, but the mechanism for heating differs: while SPS provides a direct current through the powder, in Hot Pressing heating is typically achieved via radiation to the external surface of a container and hence the heating rate is relatively slow.

It has been suggested that SPS direct current application enhances densification by promoting diffusion mechanisms over grain growth. Furthermore, the process is characterised by short process timescales, which are preferred over slow and energy intensive processes. Moreover, the direct current or, more specifically, the pulsed current has a cleaning effect on particle surfaces, which in turn results in very low or absence of oxygen at grain boundaries [202]. There is no evidence so far on whether 'plasma' is evident during SPS processing; however, the 'cleaning' suggestion lends itself well to this idea.

Previous works on Ti based alloys have indicated that higher sintering temperatures and pressures have the most significant influence on the final density [182]. The feedstock particle size and morphology have little if any influence on resulting material. The rate at which sintering occurs is mainly dependent on the heating rate, although this is independent of the duration spent at the dwell temperature. Final grain size is also influenced by this factor. The spark plasma sintering field assisted technique (SPS/FAST) process currently has limitations, including tool size, scale up limitations, graphite tooling. However, for bespoke materials and parts, this is outweighed by the uniformity of the grain structure and the process speed. Several HEAs have been consolidated or synthesised by SPS [203, 184, 185].

Spark-plasma sintering was performed in collaboration with Kennametal Manufacturing (UK) Ltd. An FCT Systeme GmbH Spark Plasma Sintering Furnace type H-HP D 250 located at Newport (UK) was used. The tooling consists of graphite punch, ring elements and carbon-fibre resistance heating elements. 0.35 mm graphite foil is used for lining the graphite elements.

The powder under investigation is loaded into the mould so that only the graphite foil is in contact with the powder. To enable a DC current to pass through the tooling, water cooled rams are used, which clamps the tooling, apply a force during sintering and conduct current through the tool and powder. The load provided to the tool from the rams is increased during the processing cycle. The cycle used for processing can be summarised as:

a. Achieve vacuum (less than 1 mbar abs); contact load on rams of 10 MPa;

b. Heat tooling/powder at a uniform rate until 500 °C is reached;

c. Increase temperature at a ramp rate of 50 °C / min until 1123 K is reached; concurrent with this, the pressure on the powder is increased up to 50 MPa (approx. 7.8 MPa / min);

d. The tool set is held at 1123 K for 10 minutes;

e. Initial cooling phase for 1 minute during which time the load is removed; further cooling for 30 mins;

f. Throughout the heating phases, a repeating pulsed DC current scheme was used of '36 ms pulse on' and '8 ms pulse off'.

Throughout the cooling phases, the vacuum is maintained until a temperature of less than 100 °C is indicated, then vacuum is removed and the tooling retrieved.

Temperature and load are measured directly by the SPS equipment. For temperature, this is done via a pyrometer which works from 449 °C and higher - it is calibrated once a year and is no greater than ±10 °C in error. Uncertainty on pressure is measured from load cells calibrated once a year. The error is tighter than the temperature measurement and is ±1 kN. This figure has be converted into MPa depending on the diameter of the sample being pressed: for a specimen of 80 mm in size, 1 kN is about 0.2 MPa.

2.2 Microstructure and elemental composition

2.2.1 Scanning Electron Microscopy and X-Ray microanalysis

The Scanning Electron Microscopy (SEM) is a useful technique for the characterisation of the microstructural features of solid objects. SEM guarantee high spatial resolution under routine laboratory operating conditions. Moreover, SEM can provide very high magnification and three-dimensional specimen images, due to the large depth of field and shadow-relief effect of the secondary and backscattered electron contrast.

The SEM equipment comprises an electron gun, a set of reducing and magnetic lenses, a scanning circuit and a signal amplifier. The electron gun includes a hot tungsten filament as a source of electrons and a control grid, both connected to a negative high voltage. The produced electrons are accelerated through a central hole and then through the first reducing lens, aiming to reduce the size of the electron source in the electron gun. A magnetic lens produces further reduction and a very fine electron probe is created. The electron beam is scanned through the sample surface in the x and y direction by a single or double deflection field [204].

Backscattering and secondary electrons When the beam electrons encounter the specimen, they interact as negatively charged particles with the electric field of the specimen's atoms. This interaction can result in the deflection of the beam's electrons along a new trajectory (elastic scattering), causing them to spread laterally with respect to the original beam direction. Some electrons can undergo numerous elastic scattering events, accumulating enough deviation from the incident beam path to return to the surface (**backscattering**).

Large atoms have higher probability of producing elastic collisions, due to their higher cross-sectional area. Since the probability of elastic scattering and of backscattering increases

with atomic number, in low-atomic-number materials elastic scattering is less likely to occur and the trajectories deviate less from the initial beam path. This allows for deeper penetration into the solid and contributes to a larger interaction volume. Consequently, the number of backscattered electrons reaching a detector is proportional to the mean atomic number of the specimen: the corresponding scan is limited to a grayscale range, because the only recorded variable is the average atomic number Z (bright areas correlate with greater average Z, and viceversa).

The shape of the interaction volume also changes significantly as a function of atomic number: low-atomic-number materials display a dense pear-shaped region of trajectories; whereas high-atomic-number materials have a nearly hemispherical shape truncated by the plane of the surface [205]. Monte Carlo electron trajectory simulation can identify individual trajectories of backscattered electrons for which the beam electron actually penetrates to a significant fraction of the range, before reversing its course and returning to the surface to escape as a backscattered electron. Electrons that travel along such trajectories may be influenced by subsurface features of the specimen structure and can carry these structural information upon escaping. As such, the backscattered electron signal can respond to subsurface details of the specimen structure.

It is worth noting that the beam of electrons can interact in the same way with air, therefore it is necessary to evacuate the chamber before proceeding with the measurement. Conventional SEM operates at a pressure of 10^{-4} Pa [205].

At the same time as elastic scattering, inelastic scattering might also occur. During this interaction, the electron beam gradually transfers its energy to the sample's atoms, giving rise to secondary electrons, X-rays and Auger electrons. **Secondary electrons** (SE) are loosely bound outer-shell electrons from the specimen atoms. They receive sufficient kinetic energy during inelastic scattering to be ejected from the atom and set into motion, propagate through the solid, and eventually intersect the surface while escaping. The energy distribution of the SE emitted from the specimen is narrow and peaked at very low energy, generally in the range 2-5 eV. The secondary electrons emission is confined to a volume near the beam's impact area, thus contributing to the high spatial resolution of the technique [206].

The SEM image formation process can be summarised as a geometric mapping of information, collected when the beam is sequentially addressed to an x–y pattern of specific locations on the specimen. Since the number and trajectories of backscattered electrons and number of secondary electrons both depend on the angle of incidence between the beam and the specimen surface, the morphology of the surface can be imaged. The following factors contributes to topographic contrast [205]:

- The more highly inclined the local surface is to the incident beam, the higher is the backscatter coefficient.
- The angular distribution of backscattered electrons is strongly dependent on the local

surface tilt.

- The secondary electron coefficient varies with the specimen tilt angle in a monotonic fashion.

X-ray phonons generation As already anticipated, the electron beam generates **X-ray photons** in the interaction volume beneath the specimen surface. X-ray generation is a two-steps process: first, an electron from the beam collides with the specimen and removes a core electron from the target atom. Second, an electron in a higher energy state drops to fill the empty lower energy level, emitting an X-ray photon of energy equal to the difference between the upper and lower energy levels of the electron that filled the core hole. Since the energy difference between electronic shells is specific for each element, the X-ray photons can provide information about specimen's composition. However, the peaks characteristic of each atom are superimposed over a background whose intensity sets a limit to the amount of detectable element. The background (Bremsstrahlung radiation) is a result of the energy loss following the deceleration of beam electrons in the Coulombic field of the sample's atoms. The peak-to-background ratio (P/B) can thus be defined as follows [207]:

$$\frac{P}{B} = \frac{1}{Z}\Big(\frac{E_0 - E_c}{E_c}\Big)^{n-1} \tag{2.1}$$

Where Z is the atomic number, E_0 is the accelerating voltage, E_c is the critical ionization energy and n is a constant for each element and shell (it normal ranges between 1.5 and 2). From this equation, it would appear that the best P/B would occur at the highest accelerating voltages. However, while very high accelerating voltages decrease spatial resolution, they also increase the absorption of X-rays within the specimen before they reach the detector. The production of X-ray photons is further hindered by the creation of Auger electrons. In the Auger process, the difference in shell energies is transmitted to another outer shell electron, ejecting it from the atom as an electron with a specific kinetic energy [207].

The energy and intensity distribution of the X-ray signal generated by a focused electron beam can be measured by Energy Dispersive X-ray Spectroscopy (EDX), through an X-ray spectrometer provided with most modern SEM instruments [206]. While deviations from the ideal detection process results in modifications of the spectra (e.g. peak broadening and distortion, sum peaks), an accurate X-ray spectrum can provide both qualitative and quantitative information. Qualitative analysis involves the identification of the lines in the spectrum: in principle, all elements from atomic number 4 (Be) to 92 (U) can be detected, though not all instruments are equipped for elements with Z $<$ 10. Quantitative analysis entails measuring line intensities for each element in the sample referencing them to calibrated standards. Since X-ray intensities are measured by counting photons, the precision obtainable is limited by statistical error and can be biased by an intense background. EDX is thus often considered a semi-quantitative analysis. The constraint of the technique are summarised in Table 2.1 [205].

Constraint	**Value**
Energy resolution	130 eV at Mn Kα
Detection limit	1000-3000 ppm; >10% wt.%
Spatial resolution	Low atomic number (Z): 1-5 μm^3
	High atomic number (Z): 0.2-1 μm^3
Precision	circa $\pm$0.1%
Accuracy	Between $\pm$1% and $\pm$5%

Table 2.1: Constraints of the EDX technique [205].

It is worth noting that the relatively low resolution of the signal is due to the fact that X-rays photons generate from very deep in the interaction volume. In other words, the spatial resolution of the technique is governed by the penetration and spreading of the electron beam in the specimen. Since the electrons penetrate an approximately constant mass, spatial resolution is a function of density [205].

Sample preparation

Since most of the investigations carried out with the SEM are on the internal parts of specimens, this surface should be exposed. For this reason, samples might have to be cut to size (with either a sharp blade or a saw): cutting devices can be made of a variety of materials, including diamond, steel, sapphire, ceramics and glass. The cutting action of a saw completely removes part of the specimen but damages its surface, making it necessary to clear it prior to characterisation.

A common procedure to fix metallic and geological samples to the microscopy stage consists of mounting, the formation a tight bond between the exterior of a largely impermeable specimen and the embedding material. For samples unaffected by high pressures and temperatures, thermosetting materials are often used. These materials (e.g. phenol-formaldehyde resin) flow when heated under high pressure and polymerise to form a stable, conductive material. The resin is hard, and can be subsequently abraded during grinding and polishing.

Grinding and polishing are necessary steps to remove surface damages brought about by cutting and thus expose a clean surface. While very effective, they might cause mechanical and thermal damage to the sample. Mechanical grinding involves rubbing brittle hard samples against a grinding tool. An abrasive material is placed between the two surfaces: as the abrasive material moves, it creates microscopic conchoidal fractures. The grinding motion (usually carried out by a mechanically rotating abrasive disk) progressively removes the sample surface, the mounting resin and the abrasive lap. In mechanical polishing, a soft material containing a suspension of abrasive material is lapped against the harder sample. The abrasive material progressively cuts across the specimen. By using increasingly smaller abrasive particles, the sample becomes increasingly more polished. Both grinding and polishing depend on the choice and type of the abrasive material. Abrasive materials can be supplied as impregnated papers and cloths, powders or suspensions; and come in a wide range of hardness. Commonly used abrasives include diamond, quartz (SiO_2), corundum, aluminium oxide [208].

2.2.2 Atomic Force Microscopy

Atomic Force Microscopy (AFM) is a technique used to see the shape of a surface in three-dimensional detail down to the nanometric scale. AFM imaging can be performed on all organic and inorganic materials irrespective of their opaqueness, texture and conductivity. The sample is usually imaged in air, but analysis can be performed in liquid environments as well as in vacuum. Unlike optical or electron microscopes, an AFM does not form an image by focusing light or electrons onto a surface. Rather, it physically 'feels' the sample's surface with a sharp probe, building up a map of the height of the specimen's surface. By inheriting the features of traditional microscopes and mechanical profiles, AFM is able to make measurements in the X, Y and Z axes [209].

The main components of an AFM are the following [209]:

- Microscope stage, supported on a vibration isolated platform to reduce noise. It contains the scanner (the mechanism used for moving the AFM tip relative to the sample), a sample holder and a force sensor holding and monitoring the AFM tip. Usually, it also includes an integrated optical microscope to view the sample and tip.
- Control electronics. Used to generate the signals driving the motorised components in the microscope stage and to digitize the signals coming from the AFM (feedback), so that they can be displayed and recorded by the computer.
- Computer. It sets the parameters handled by the control electronics and is used by the operator to acquire and display AFM images.

AFM instruments are designed to operate into the following two configurations: sample-scanning (the sample is scanned and the force sensor is held in one place) or probe-scanning (the sample is held fixed and the probe is scanned). The first configuration gives limits on the specimen's dimensions and on the size of it to be probed. The latter, on the other hand, can be used on any size of sample and, since only the sample lies underneath the scanning probe, it is simple to accessorise [209].

At the basement of AFM operation are the piezoelectric scanners, force transducers (sensors) and feedback control. The piezoelectric scanner moves the tip over the sample surface in the X–Y axis; the force transducer senses the voltage changes between the tip and the surface; and the feedback control feeds the signal from the force transducer back to the piezoelectric, to maintain a set force between the probe and the sample [209]. Piezoelectric materials (naturally occurring crystals or polymers, or synthetic ceramics) are electromechanical transducers that convert electrical potential into a geometric change (*i.e.* a mechanical motion), or vice versa. Ideally, the piezoelectric would expand and contract in direct proportion to the driving voltage - but in reality, the piezoelectric ceramics commonly used for AFM display hysteresis and creep, two behaviours which are to be corrected to avoid images distortion. The first causes the ceramic to resist the change it is undergoing, for example

giving a negative shaped non-linearity. The latter is as a source of leftward or rightward drift of force-versus-Z curves, meaning a gradual offset of height with elapsed time, diminishing in time [210].

The force sensors in an AFM are typically a cantilever with integrated tip (the probe) and an optical lever. When the probe comes into contact with the surface, the voltage output from the transducer increases monotonically.

The control electronics take this signal, and uses it to drive the piezoelectrics so as to maintain the probe-sample distance. Thus, if the probe registers an increase in force (for instance, when the scanning tip encounters a hill on the surface), the feedback control causes the piezoelectrics to move the probe away from the surface [209].

AFM modes

The many modes of operation of AFM make it a very versatile technique. Some of the most common topographic and non-topographic modes will be herein briefly reviewed.

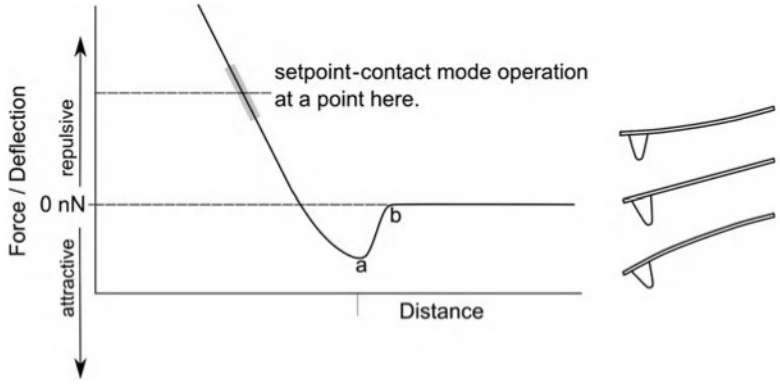

Figure 2.3: *Left*: Simplified force-distance curve showing contact scanning regime. The deflection-distance curve, from which a force-distance curve is measured, follows a very similar trend. *Right*: Probe bending in attractive and repulsive regime [209].

- Topographic modes [209]. As previously described, datasets generated by AFM are a map of height measurements, which can be later transformed into a more naturalistic image with light shades, perspective, etc. To create these topographic images, several modes were developed, whose differences lead to diverse information, data interpretation and sample suitability.

  a. **Contact mode**. In this mode, the cantilever tip is always in contact with the surface, as per the force-distance curve reported in Figure 2.3. As the tip approaches the surface, it feels an attractive force that makes it jumps into contact with it. As the instrument continues to push the cantilever towards the surface, the interaction moves into the 'repulsive' regime. In this regime, a combination of cantilever

bending and sample compression occur, leading to imaging. While this provides higher image resolution, the prolonged contact might also damage the sample and the tip [209].

b. **Oscillating modes.** The cantilever is oscillated at its resonant frequency, usually through an additional piezoelectric element. When the probe approaches the sample surface, its oscillation is damped due to its interaction with the sample's force field. The oscillation changes are monitored by the force transducer, and the scanner adjusts the height via the feedback loop, to maintain the probe at a fixed distance from the sample. By using a highly stiff cantilever and monitoring the change in the oscillation, it is possible to maintain the tip very close to the surface without jumping to the repulsive regime. This mode is named **Close-contact AFM**. Analogously, if the probe oscillates between attractive and repulsive regime, the technique is named **Tapping mode AFM**. Since it involves large probe tip-sample forces, the latter can be more destructive, but it is easier to implement [209].

- Non-topographic modes. These modes proceed in parallel with topographic imaging. Properties that can be revealed include elastic modulus, viscosity and visco-elasticity, frictional response, surface energy and potential, magnetisation.

  a. **Nanoindentation**. The recorded data are those measured as a very hard tip comes in contact with and presses onto the sample surface. The technique guarantees high load sensitivity, inherent ability to measure the created indents and high positioning resolution; but requires calibration to extract real forces and for the indenter to approach the sample perpendicularly (which is normally not the case for AFM). As such, this mode has been mostly used to look at relative hardness and softness [209].

  b. **Magnetic force microscopy**. The presence and distribution of magnetic fields is measured directly with a magnetic probe, consisting of standard silicon cantilevers coated with cobalt, cobalt-nickel or cobalt-chromium. Although it is relatively easy to obtain magnetic contrast at a high resolution, signals' quantification is complex, because the domains on the probe can cause a change in the magnetic domains on the surface of the material during the measurement [209].

  b. **Electric Force Microscopy and Scanning Kelvin Probe Microscopy.** When two different materials (*i.e.* sample and tip) that are not electrically grounded are brought together, their respective Fermi levels are different. Upon electrically connecting them, however, electron charges will flow to align the Fermi levels: this in turn produces an electric field between tip and sample, and thus a net force of attraction between opposite charges. The strength of the attraction and its variation along the sample can be enhanced by the application of an external bias, and is at the basement of Electric Force Microscopy (EFM) [210]. Conversely,

during Scanning Kelvin Probe Microscopy (SKPM) a DC potential bias is applied to the conductive probe, which is further modulated by an AC voltage oscillating at the resonant frequency of the cantilever. If the potential of the sample is not the same as the tip's, the difference will cause the cantilever to mechanically vibrate. The feedback circuit will thus register the frequency of the vibration and output a DC voltage aiming to minimise it. The voltage required to minimise the oscillation is digitised and displayed as the potential image of the surface. If the tip is first calibrated against a reference sample, SKPM can provide absolute values of the sample work function [210].

While obtaining AFM images at relatively low resolution (scan sizes > 1 μm, resolution of > 50 nm) is quite easy, very high-resolution images (resolution on the order of 5 nm or less) can be more challenging, since a large number of factors must be optimised. The probe tip must be clean and particularly sharp. The sample must be well fixed to the substrate, which should not be moving. Sources of external noise and the vibration isolation must be optimised. Finally, scanning parameters must be optimised [209].

2.3 Phase identification

2.3.1 Crystalline materials

Solid state crystalline materials are ordered arrays of regularly repeating structural units (atoms, molecules, group of atoms, molecules, ions). The periodic structure of an ideal crystal is best described by a lattice, which is the pattern resulting by representing each structural motif with a point. The simplest repeating unit in the lattice pattern is referred to as the unit cell. To fully describe a three-dimensional unit cell, three non-coplanar vectors are required, (**a**, **b**, **c**, lying along the x, y and z axes respectively) which coincide with the three independent edges of an imaginary parallelepiped. The angle between the unit cell vectors **b** and **c** is represented by α, whereas β is the angle between **a** and **c** and γ is the angle between **a** and **b**.

The crystal structure is completely described combining the geometry of the unit cell with the distribution of the atoms in one repeat unit. This is obtained by translating each point of the unit cell in three dimensions (stacking).

The presence of any rotation or reflection symmetry in a crystal structure leads to a corresponding symmetry of the lattice and of conventionally selected unit cells, the shapes of which are classified under seven crystal systems (Table 2.2). Each crystal system has characteristic symmetry and a corresponding set of restrictions on some or all of the six unit cell parameters (α, β, γ and the lengths of the unit cell vectors along the x, y and z axes, namely a, b and c).

Crystal system	Bravais Lattices	Unit cell dimensions
Triclinic	P	$a \neq b \neq c$; $\alpha \neq \beta \neq \gamma \neq 90°$
Monoclinic	P; C	$a \neq b \neq c$; $\alpha = \gamma = 90°$; $\beta \neq 90°$
Orthorhombic	P; C; I; F	$a \neq b \neq c$; $\alpha = \beta = \gamma = 90°$
Trigonal	P	$a = b = c$; $\alpha = \beta = \gamma \neq 90°$
Tetragonal	P; I	$a = b \neq c$; $\alpha = \beta = \gamma = 90°$
Hexagonal	P	$a = b \neq c$; $\alpha = \beta = 90°$; $\gamma = 120°$
Cubic	P; I, F	$a = b = c$; $\alpha = \beta = \gamma = 90°$

Table 2.2: The seven crystal lattice systems and corresponding symmetry restrictions.

Since the choice of the unit cell is arbitrary, certain conventions have been adopted to designate a standard choice dependent on the crystal system. The following unit cells are customarily used:

- Primitive (P). Lattice points are located in eight corners of the parallelepiped, but each corner is shared by eight neighbouring unit cells in three dimensions.
- Base-centered (A, B or C). With respect to the P lattice, it contains additional lattice points in the middle of the two opposite faces. The cell is termed A-type if the lattice point is located in the face defined by the b and c directions, B-type if in the face defined by the a and c directions, C-type if in the face defined by the a and b directions.
- Body-centered (I). With respect to the P lattice, it contains one additional lattice point in the middle of the body of the unit cell.
- Face-centered (F). With respect to the P lattice, it contains three additional lattice points, located in the middle of each face.
- Rhombohedral (R). Allowed only in a trigonal crystal system, it contains two additional lattice points, located at (1/3, 2/3, 2/3) and (2/3, 1/3, 1/3).

Considering seven crystal families and five types of lattices, it is possible to show that only 14 different types of unit cells are required to describe all lattices using conventional crystallographic symmetry. For example, in the triclinic crystal system any of the centered lattices is reduced to a primitive lattice with smaller volume of the unit cell. The 14 unit cell types are listed in Table 2.2 and are known as Bravais lattices [211].

For a single finite object such as a molecule or a crystal, all symmetry elements present must pass through a common central point. However, when translational symmetry is taken into consideration (screw axes and glide planes), symmetry elements do not pass though a point, but are rather arranged at regular intervals in space. Various combinations of symmetry elements plus allowed translation results in the so-called crystallographic space groups. The number of symmetry operation combinations is limited, therefore only 230 space groups exist.

The distribution of the different space groups across the seven crystal systems is not uniform, with some being extremely rare and others being very common.

Lattice points can be intersected by a set of planes (crystallographic planes), parallel to each other and equally spaced. The distance between neighbouring planes is called d-spacing. Each family of crystallographic planes is described using triplets of integers (h k l) labelled Miller indices. Miller indices indicate that the plane belonging to the (h k l) family divides the lattice vectors **a**, **b** and **c** into h, k and l equal parts, respectively.

The d-spacing is a function of the unit cell parameters and Miller indices which fully describe every set of of crystallographic planes. The corresponding formulae for the cubic (Eq. 2.2) and hexagonal (Eq. 2.3) crystal classes are:

$$\frac{1}{d^2} = \frac{h^2 + k^2 + l^2}{a^2} \tag{2.2}$$

$$\frac{1}{d^2} = \frac{3}{4}\frac{h^2 + hk + k^2}{a^2} + \frac{l^2}{c^2} \tag{2.3}$$

2.3.2 Fundamentals of X-ray diffraction

X-ray diffraction is an extremely powerful technique for the characterisation of polycrystalline materials, springing from the scattering interaction of X-rays with electrons bound to atoms. The scattering leads to the Fourier transform in the form of the structure factor equation (Eq. 2.4) [212]:

$$F(hkl) = \sum_{j=1}^{N} f_j exp[2\pi i(hx_j + ky_j + lz_j)] \tag{2.4}$$

where each atom j at a position (x_j, y_j, z_j) in the unit cell contribute with its atomic scattering factor f'_j, incorporating atomic displacement, to the whole crystal scattering.

As part of this treatment, the concept of reciprocal lattice is introduced, as a convenient representation of the geometrical basis of diffraction. Vectors normal to the planes of the direct lattice radiate from the lattice point taken as the origin, with each normal terminating at a point distant $1/\mathrm{d}_{hkl}$ from the origin. The resultant set of points comprises the reciprocal lattice. The following relationships exist between the reciprocal and real lattice parameters:

$$a^* = \frac{bc\sin\alpha}{V}$$
$$b^* = \frac{ac\sin\beta}{V}$$
$$c^* = \frac{ab\sin\gamma}{V}$$
$$\cos\alpha^* = \frac{(\cos\beta\cos\gamma - \cos\alpha)}{\sin\beta\sin\gamma}$$
$$\cos\beta^* = \frac{(\cos\alpha\cos\gamma - \cos\beta}{\sin\alpha\sin\gamma}$$
$$\cos\gamma^* = \frac{(\cos\alpha\cos\beta - \cos\gamma)}{\sin\alpha\sin\beta}$$

At the same time, Bragg's Law emerges as a single equation for the geometry governing each individual diffracted beam:

$$n\lambda = 2d_{hkl}\sin\theta_{hkl} \tag{2.5}$$

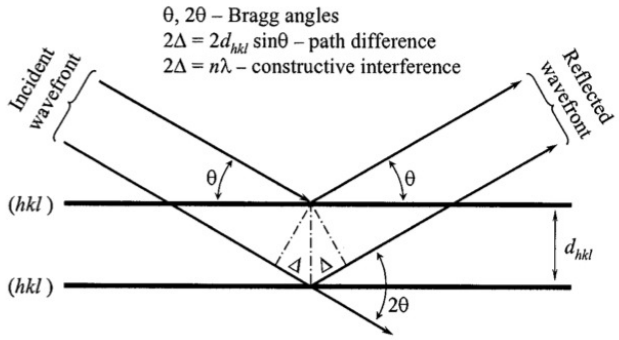

Figure 2.4: Illustration of the geometry used for the derivation of the Bragg's Law, depicting the diffraction of an incident wavefront by parallel (*hkl*) set of planes [212].

According to Bragg's Law, diffraction from a crystalline sample can be visualised as a mirror reflection of the incident X-ray beam from a series of crystallographic planes, with each plane in a set considered as a separate scattering object (Fig. 2.4). Considering an incident front of waves with parallel propagation vectors, which form an angle θ with the planes (*hkl*), the reflected wavefront will also consist of parallel waves forming the same θ angle with all planes. The path difference introduced between a pair of waves both before and after they are reflected by the neighbouring planes (Δ) can be geometrically determined by the interplanar distance as $\Delta = \mathrm{d}_{hkl}\sin\theta$. Since the total pair difference equals 2Δ and constructive interference is only observed when $2\Delta = n\lambda$ (where n is an integer known as the order of reflection and λ is the wavelength of the incident wavefront), interference maxima, observed as bright reflections, are only observed when θ satisfies Eq. 2.5.

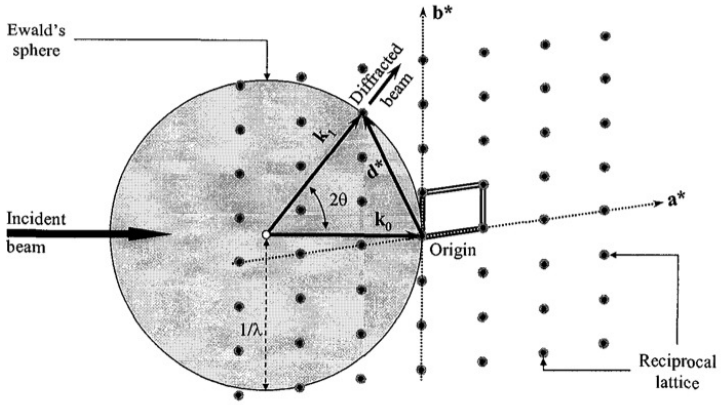

Figure 2.5: The visualisation of diffraction using the Ewald's sphere with radius $1/\lambda$ and two-dimensional reciprocal lattice with unit vectors $\mathbf{a}^*$ and $\mathbf{b}^*$. The origin of the reciprocal lattice is located on the sphere's surface at the end of $\mathbf{k}_0$ [212].

Another model that helps visualise the geometry of diffraction, particularly in showing how the Bragg's Law is satisfied for individual sets of lattice planes as a crystal is rotated in an X-ray beam, is the Ewald construction (Fig. 2.5). A sphere of radius $1/\lambda$ is centred on the crystal and the incident beam of wavelength λ forms one diameter. As the crystal is rotated, the reciprocal lattice rotates, while the sphere remains fixed. If the origin of the reciprocal lattice is placed on the surface of the sphere at the exit point of the incident beam, then rotation takes individual reciprocal lattice points through the sphere surface at different times. In the case of powder diffraction, each crystallite has its own reciprocal lattice orientation, and thus each reciprocal lattice point is smeared onto the spherical shell of the surface of the Ewald sphere due to the averaging of crystallite orientation. The appearance of the resulting reciprocal lattice is therefore that of a series of concentric shells (as opposed to the distinct array of spots observed in single crystal diffraction) [213].

2.3.3 Phase identification and Rietveld refinement

In a typical PXRD experiment, the intensity diffracted by a polycrystalline sample is measured as a function of Bragg angle (2θ). Hence, the resulting diffraction pattern is usually plotted as measured intensity *versus* 2θ.

The position of peaks is established from the Bragg's Law as a function of the wavelength λ and the interplanar distance d_{hkl}, which in turn relates to cell parameters (see section 2.3.1). The intensity of the diffraction maxima is a function of periodicity of the scattering centres, and is thus dependent of the position of the atoms in the cell and its geometry. The shape of Bragg's peaks is weakly dependent on the crystal structure and is the convolution of several parameters (including experimental set-up, instrument parameters and preparation method). An often satisfactory description of PXRD peaks can be achieved by the Pseudo-Voigt approximation of the Voigt function (pV) - a linear combination of Lorentzian (L) and

Gaussian (G) components weighted for the Voigt mixing parameter η as follows:

$$pV(x, \eta, W) = \eta L(x, W_L) + (1 - \eta)G(x, W_G) \tag{2.6}$$

where W_L and W_G are the full-width at half maxima of the Lorentzian and Gaussian functions respectively.

Each powder diffraction pattern is characterised by a unique distribution of peak position and intensity, which enables the utilization of the technique for phase identification. While qualitative analysis is generally quite straightforward (though still dependent on the quality of the diffraction pattern and on the nature of the material), to determine the concentration of various phases in a mixture after the nature of each has been established is a complex task. This holds even truer for powder diffraction data, which provide less information with respect to single crystals data due to the peak overlap occurring upon projection of the three-dimensional grid of lattice points on to the single-dimensional pattern.

The Rietveld method is a whole-pattern-fitting technique based on cycles of non-linear least squares, whose aim is to refine both structure and peak profiles and thus minimise the detrimental effect of overlapping peaks [214]. Let us consider the experimental profile $y_i(obs)$ and the calculated profile $y_i(calc)$, with $y_i(calc)$ being a function of n refinable parameters (unit cell parameters, atomic positions, thermal displacement values, background, absorption correction, site occupancies...). The objective of the Rietvield method is to obtain the best estimate of the refinable parameters x_j by minimising the following quantity via least-square technique:

$$S = \sum_i w_i[y_i(obs) - y_i(calc)]^2 \tag{2.7}$$

where $w_i = 1/y_i(obs)$, that is, the weigh associated to each observed count. The minimisation is carried out via subsequent iterations. Agreement between the experimental and calculated patterns is usually estimated by the weighted profile (R_{wp}) with the following relation [215]:

$$R_{wp} = \sqrt{\frac{\sum_i w_i[y_i(obs) - y_i(calc)]^2}{\sum_i w_i[y_i(obs)]^2}} \tag{2.8}$$

Through the refinement of each parameter, it is possible to obtain an estimation of the wt.% of each phase in a mixture. For this model to be applied to complex alloy systems such as HEAs, it is necessary to assume all components of the mixture to be perfect solutions (since the positions of their atoms are not known).

Due to the non-linearity of the relationship between calculated profile and refinable parameters, the starting model has to be close to the real one. If this condition is not satisfied, the refinement might diverge or converge to false minima. This is particularly critical for powder diffraction data, due to the aforementioned loss of information as well as the correlation between several refinable parameters (*i.e.* site occupancy and thermal factor).

Considering the wealth of structural information provided by the diffraction pattern, the

technique necessitates the use of crystallographic software packages. All analyses of the synchrotron X-ray diffraction profiles herein reported were performed with the Jana or the TOPAS programs [216, 217].

2.3.4 Instrumentation

Preliminary diffraction data were collected in trasmission mode from capillaries using a Bruker D8 Advance.

A copper filament bombarded with high energy electrons (thus undergoing multiple electronic transitions and X-rays emissions) acted as X-ray source. The resulting X-ray pattern shows sharp maxima correspondent to the electron transitions and labelled according to the electron shells involve in the X-ray production (in this case, K_{α_1} = 1.54056 Å). The single, collimated, wavelength required by the diffraction experiment is selected by means of a Ge single-crystal monochromator. A position sensitive detector (PSD) enables rapid acquisition.

Synchrotron radiation sources

Synchrotrons were developed in the 1960s and today represent the most powerful X-ray radiations sources. In the synchrotron ring, beams of accelerated electrons are moving in circular orbit: the acceleration of charged particles towards the beam centre produces electromagnetic radiation ranging from radio-frequency to short-wavelength X-rays. The velocity change at ESRF (European Synchrotron radiation Facility, Grenoble, France) is achieved by applying a magnetic field to electrons travelling at relativistic speed, forcing them to follow a curved trajectory. The synchrotron ring consists of alternating straight and curved sections, and electrons are guided from one to another by the bending magnets. The X-ray beam is thus emitted tangentially to the electron orbit.

Given the synchrotron size, the average beam consists of beams that can be considered nearly parallel at the distance typically used for powder diffraction: this enhances instrumental resolution. Moreover, the high intensity of the beam allows for easy selection of the desired wavelength [212].

High- and Low-Temperature experiments *In situ* high-temperature X-ray diffraction data for the powdered samples were collected at the I-11 beam-line at the DIAMOND light source located in Harwell, UK (λ = 0.494984 Å).

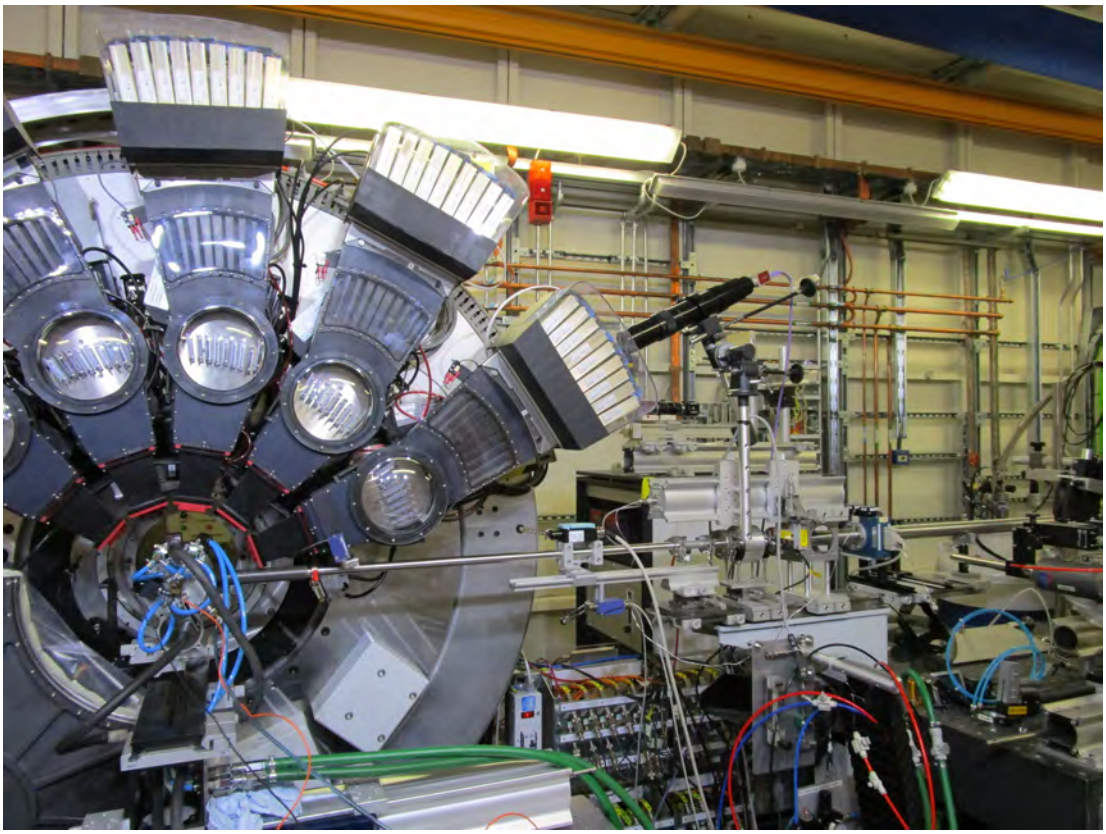

Figure 2.6: I-11 beamline at the DIAMOND Light Source (Harwell, UK).

LaB_6 (NIST SRM 660c) was used as external standard for calibration. A wide-angle position sensitive detector based on Mythen-2 Si strip modules was applied to collect the PXRD data (Figure 2.6). The detector was moved at constant angular speed with 10 s scan time at each temperature and 60 s waiting time in order to let the temperature stabilise. The powdered alloys were sealed in 0.5 mm quartz capillaries in vacuum, and heated in the capillary furnace from 300 to 1400 K with axial rotation [218]. In all samples, oxidation has been detected above 1000 °C, which can be due to the reaction of metallic alloy with quartz at high temperature, resulting in capillary destruction.

In situ low-temperature powder X-ray diffraction profiles for the powdered samples were collected at the PETRA III synchrotron (λ = 0.207150 Å). LaB_6 (NIST SRM 660c) was used as external standard for calibration. A wide-angle position sensitive detector based on Mythen-2 Si strip modules was used to collect the XRD data. The detector was moved at constant angular speed with 10 s scan time at each temperature and 60 s waiting time to let the temperature stabilise. The powdered alloys were sealed in a 0.5 mm quartz capillary in vacuum, and cooled in liquid nitrogen flow from 300 to 100 K. Temperature dependent PXRD patterns were plotted and analysed using Powder3D software [219]. Phase composition has been verified using the PDF database [1]. Parametric sequential refinements were performed

[1]PDF-2 Release 2012 (Database), ed. S. Kabekkodu, International Centre for Diffraction Data, Newtown

using the TOPAS software [2]. Profile parameters for the Lorentzian function, cell parameters, and phase fractions were refined simultaneously for all phases.

High Pressure–High Temperature experiments Experiments from ambient pressure to 9.5 GPa were performed on the large-volume press installed at the beam-line ID06-LVP, ESRF (Figure 2.7).

(a) Large-volume press.

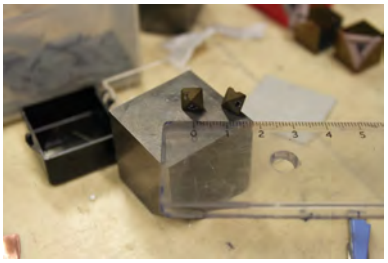

(b) Detail of the graphite furnace and ZrO_2 plugs used during the *in situ* experiment.

Figure 2.7: ID06-LVP at ESRF (Grenoble, France).

X-ray diffraction data were collected using a linear pixelated GOS detector from Detection Technology at monochromatic wavelengths of 0.22542 Å. Powdered alloy samples were loaded into *h*-BN capsules, before being introduced into the windowed 10/4 MgO:Cr octahedral high-pressure assembly, along with a graphite furnace and ZrO_2 plugs. Pressure was generated using the 2000 tons MAVO press in 6/8 (x32) mode with tungsten carbide (25 mm carbides) anvils [220]. Pressures were estimated using the equation of state of *h*-BN and temperatures were estimated using the equation of state of MgO (see Section 2.3.5). Samples were compressed up to 9.5 GPa and heated up to 1000 K (without *in situ* XRD monitoring) or 1500 K (with *in situ* XRD monitoring) under a constant pressure. Heating was performed using a Delta Elektronika SM6000 power supply, by regulating constant voltage.

Compressibility, heating, cooling and decompression curves were collected. The time resolution for PXRD patterns collected continuously on heating is 0.1 seconds, which are rebinned and written at 3.2 s interval and at 32 s interval on compression and decompression.

Square, PA, USA (2012).

[2]TOPAS v.4.0, Bruker-AXS 5465 East Cheryl Parkway – Bruker AXS – 2009.

2.3.5 Estimation of pressure and temperature using EoS

The standard method to determine pressure and temperature in a large-volume press with X-ray access is to measure temperature with a thermocouple, and then recalculate pressure using an internal standard. However, it is often impractical to use this system. In such cases it is still possible to estimate pressure and temperature by using two pressure standards simultaneously. MgO (periclase) and *h*-BN make for ideal pressure calibrants. MgO has low chemical reactivity and is stable in large temperature and pressure ranges [221]. *h*-BN has been widely used as sample container in PXRD experiments because it is transparent to X-rays, as well as being an excellent thermal conductor and electrical insulator [222].

Given an observed unit cell volume V, which can be calculated from the refined cell parameters, there is always an *isochoric* line in the $P-T$ space uniquely described by the thermoelastic equation of state of the given material. In the case of MgO and *h*-BN, their isochoric lines (with observed volumes V_{MgO} and V_{h-BN}) must have an interception point in the $P-T$ space, giving the experimental conditions of the sample mixture [223].

The calculation is not straightforward and requires several steps. First, it is necessary to identify the peaks corresponding to the two phases and index them. Once the Miller indices and the line *d*-spacing are known, it is possible to calculate the corresponding cell parameters using Eq. 2.2 and 2.3. Unlike the cubic MgO, whose only modifiable cell parameter is *a*, *h*-BN is hexagonal. Nevertheless, its cell parameter *a* is almost incompressible, and can thus be considered constant. Only the changes occurring in the *c* parameter are followed [222].

From cell parameters, the cell volume can be calculated. Since the Equation of State of both phases is known, the V_{MgO} and V_{h-BN} experimental values can be used to estimate the corresponding T and P. The EoS used in this work are modified isothermal Birch-Murnaghan equations; the corresponding fitted thermoelastic parameters used are presented in Table 2.3 [224, 225].

$$P_{MgO} = \frac{3A_0(T_0)e^{-(\alpha+\alpha_1 T)\delta T}}{2}\left[\left(\frac{V_0(T_0)e^{(\alpha_0+\alpha_1 T)T}}{V}\right)^{7/3} - \left(\frac{V_0(T_0)e^{(\alpha_0+\alpha_1 T)T}}{V}\right)^{5/3}\right]\cdot \cdot\left\{1+\frac{3(A'(T_0)-4}{4}\left[\left(\frac{V_0(T_0)e^{(\alpha_0+\alpha_1 T)T}}{V}\right)^{2/3}-1\right]\right\} \tag{2.9}$$

$$P_{h-BN} = \frac{3}{2}\left[B_0(T_0)+\beta_0(T-T_0)\right]\left[\left(\frac{V(T)}{V_0(T)}\right)^{-2/3}-1\right]\left\{1+\left[\left(\frac{V(T)}{V_0(T)}\right)^{-2/3}-1\right]\right\}^{5/2}\cdot \cdot\left\{1-\frac{3}{4}\left[\left(\frac{V(T)}{V_0(T)}\right)^{-2/3}-1\right]\left[4-\left(B'(T_0)+\beta_1(T-T_0)\right)\right]\right\} \tag{2.10}$$

From the methodology described above, it is clear that errors in the determination of P and T come from the combination of errors in the estimation of lattice parameters - which

Fitted thermoelastic parameters for MgO	Value	Fitted thermoelastic parameters for *h*-BN	Value
$A_0(T_0)$	163.59 GPa	$B_0(T_0)$	27.6 GPa
A'(T_0)	4.145	B'(T_0)	10.5 GPa
V_0	11.137 Å^3	V_0	24.2417 Å^3
α_0	$3.197 \cdot 10^{-5}$ K^{-1}	β_0	$-0.81 \cdot 10^{-2}$ GPa K^{-1}
α_1	$5.784 \cdot 10^{-9}$ K^{-1}	β_1	$0.16 \cdot 10^{-2}$ GPa K^{-1}
δ	3.690	T_0	298 K

Table 2.3: Thermoelastic parameters determined from fitting experimental data according to Eq.2.9 and 2.10 [224, 225].

include errors in wavelength, sample-detector distance, misfits to other detector calibrations, numerical errors (the ones in integration as well as those introduced at LSQ for lattice minimisation (e.g. bias from inclusion of other peaks into fit) - and errors in the original description of the two EoS used. The latter include errors on the fitting parameters and in comparing the two EoS, arising from the fact that it is impossible to fit a combination of two EoS descriptions by using one for T and one for P simultaneously, so their respective values are collected within a certain tolerance.

Since error propagation through all this is a daunting task, it has been seldom performed. Indeed, the large-volume cell is not the tool of choice for high-precision experimentation in P-T space: we do not anticipate high-accuracy output, rather about 5% errors in P and 15% in T [226].

In this work, determinations of pressure and temperature assume errors of X and Y according to those established by the method highlighted by Crichton and Mezouar, after rescaling for the differences in bulk modulus and thermal expansivity between the NaCl and Au standards used there and the MgO and BN used here. A $\pm 2\sigma$ error estimation (corresponding to uncertainties of 7% on P and 18% on T) was made for the technique, according to the following derivation:

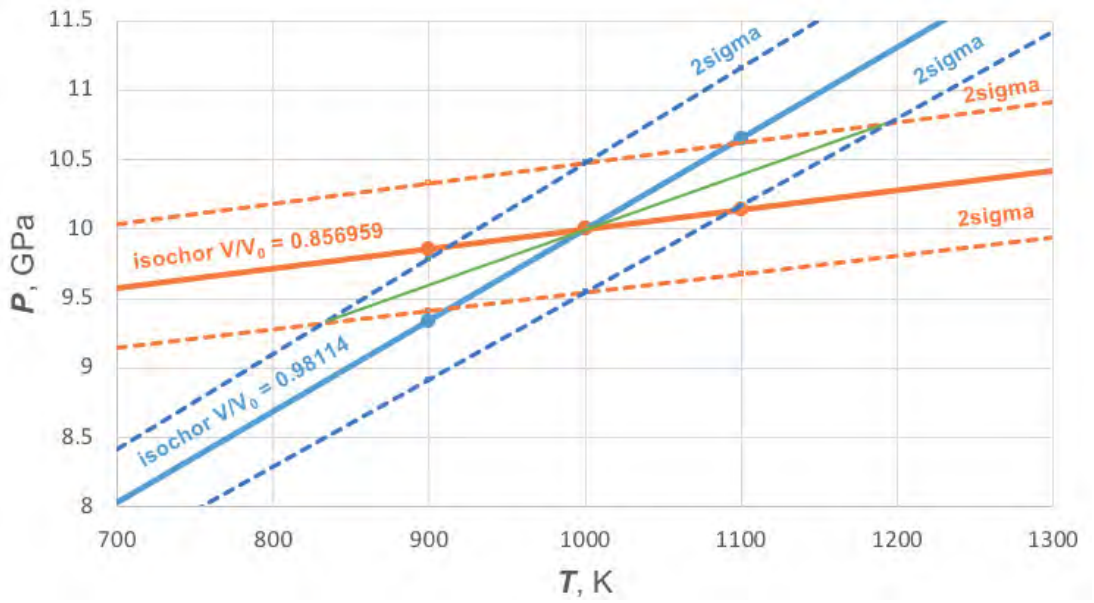

Figure 2.8: Calculation of ideal P,T trends for MgO (blue) and *h*-BN (orange). The respective 95% confidence lines ($\pm 2\sigma$) are reported as dashed lines. The green line indicates the maximum range of acceptable solutions (363 K), covering a maximum of 1.4 GPa.

1. Cell parameter a_{MgO} and c_{BN} are determined at 900, 1000 and 1100 K. The corresponding cell volume ratio V/V_0 is calculated assuming $V_{0,MgO}$ and $V_{0,BN}$ values at room temperature to be 60.379 Å^3 and 59.241 Å^3 respectively.

2. The corresponding pressures are estimated from the EoS 2.9 and 2.10. Plotting the calculated pressures *vs* temperature gives the ideal trends for MgO and BN (blue and orange full line in Figure 2.8).

3. A 95% confidence (2σ level) is added to the plot (dashed lines in Figure 2.8). This confidence level generously estimates for errors in lattice estimation, which can be determined with a 10^{-3}-10^{-4} certainty. The confidence limits are placed on isochoric trends in the P,T space defined by the used EoS and related to the product $\alpha \cdot K = \frac{dT}{dP}$ of each phase at the P,T point of interest (where α is the thermal expansivity and K the bulk modulus of the material).

4. The lozenge bound by the 2σ level lines is the locus of the 95% confidence solutions: the maximum T range of these solution is 363 K, spreading over a maximum range of 1.4 GPa (green line in Figure 2.8).

5. If systematic errors are present throughout the experiment, the fractional error in P (σ/P) decreases with increasing P, and σ_{V/V_0} scales with the volume ratio. The pressure estimation is thus better at higher P values. Since EoS equate for P, this in turn reduce the error on T.

2.4 Thermal behaviour

2.4.1 Differential Scanning Calorimetry

Differential Scanning Calorimetry (DSC) is the measurement of the change of the difference in the heat flow rate between the sample and a reference, while they are subjected to a controlled temperature programme. Thus the original quantities measured in a DSC are a temperature difference and the set value of the temperature of the furnace, which is electronically controlled to follow a certain temperature program. The temperature difference is internally transformed into a differential heat flow rate ($\delta\Phi$) gathered at regular intervals with the applied temperature.

DSCs allows for the quick measurement of reaction heats and heats of transition, or heat flow rates and their changes at characteristic temperatures on small sample masses, in wide temperature ranges and with high accuracy (e.g. up to 1-2% accuracy for the measurement of specific heat capacities through adiabatic calorimeters). This features make it a powerful tool for materials characterisation, stability investigation, evaluation of phase diagrams, purity determination, etc. Furthermore, DSC is often coupled with Differential Thermal Analysis (DTA), which measure the change of the ΔT between the sample and the reference, while they are subjected to a controlled temperature program. With respect to DSC, DTA are more flexible in regards to the volume and shape of crucibles, can be used up to very high temperatures (circa 2400 °C) and are highly sensitive [227].

DSC and DTA can be joined together with other methods of thermal analysis. Thermogravimetry (TG) is of particular interest for materials characterisation, since its signal provides information on whether volatile components are involved, and which changes in mass are to be attributed to a transition.

Calorimeters are classified in groups according to various classification systems, depending on the following criteria:

1. Measurement principle
   (a) Heat-compensating calorimeters;
   (b) Heat-accumulating calorimeters;
   (c) Heat exchanging calorimeters.
2. Mode of operation[3]
   - ⋆ Isothermal;
   - ⋆ Isoperibol;
   - ⋆ Adiabatic;
   - ⁕ Scanning of surroundings;

[3]Static (⋆) or dynamic (⁕) modes.

- ⁕ Isoperibol scanning;
- ⁕ Adiabatic scanning;
- ⁕ Temperature modulated.

3. Construction principle
   (a) Single calorimeter;
   (b) Twin or differential calorimeter.

The heat flux DSC used for the current work is a twin calorimeter, a design which allows disturbance from the surroundings. This effect on the system can be eliminated by taking only the difference between the individual measurement signals into account. In calorimeters such as this one, which measure the temperature change of the calorimeter substance, the heat exchange with the isoperibol surroundings is kept low to make the measured signal ΔT as great as possible. The measured signal which describes the intensity of the exchange is proportional to a heat flow rate (Φ) and not to a heat. As a consequence, time dependences of a transition can be observed on the basis of the Φ(t) curve [227].

As previously mentioned, DSCs are usually operated by a control program changing temperature as a function of time. Measurements can thus be performed in a constant or variable (modulated) heating rates.

Constant heating rates include isothermal and scanning modes. In the first, the temperature is kept constant - thus if a reaction or a transition takes place in the sample at that temperature, it is possible to determine its latent heat. On the other hand, if no transitions or reactions occur, the heat flow rate should read zero (as there is no heat exchanged with the specimen). In reality, this is often not the case, as DSCs are not perfectly symmetric and the heat exchange between the sample and environment and the reference and its surrounding are always somewhat different. In scanning mode, temperature changes linearly with time. This is the most widely used DSC mode of operation [227].

All DSC instruments measure a temperature difference (ΔT), which is internally converted into a differential heat flow rate (Φ_m). The relation between the two variables is approximately described by the following system of equations [228]:

$$\begin{cases} \Phi_(t) = -\frac{\Delta T(t)}{R} - \beta(C_S - C_R) - \frac{\tau}{R}\frac{d\Delta T(t)}{dt} \\ \tau = C_R \cdot R \end{cases} \tag{2.11}$$

Where C_S and C_R are the sample and reference heat capacity respectively, R is the thermal resistance between furnace and sample, β is the heating rate. An example of the measured curve for a heat flux DSC displaying exothermic effect is reported in Figure 2.9.

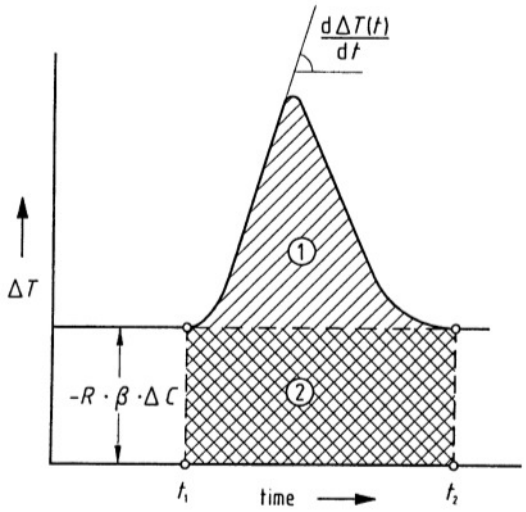

Figure 2.9: Schematic of a DSC exothermic signal. ΔT is the measured signal as function of time, ΔC is the difference between the heat capacities of sample and reference. The area identified as 1 is a measure of the heat released between t_1 and t_2, area 2 identify the baseline, a measure of the heat required to heat the sample between t_1 and t_2 [227].

The established DSC curve is characterised by a baseline (corresponding to steady state conditions) and peaks arising from it. As previously mentioned, peaks appear when the steady state is disturbed by thermally active processes, such as reactions and transitions: endothermal processes give rise to positive peaks, and *vice versa*. Transitions which are not accompanied by heat transfer do not produce peaks, but rather step-like changes in the measured curve's shape.

From the measured heat flow rate it is possible to calculate the specific heat capacity through the following relationship:

$$c_P = \frac{C_P}{m} = \frac{\frac{dQ_S}{dt}}{m\frac{dT}{dt}} = \frac{\Phi_S}{m\beta} = \frac{\Phi_m - \Phi_0}{m\beta} \tag{2.12}$$

Where dQ_S is the heat flow of the sample, m is its mass; Φ_m is the sample heat flow rate, Φ_m is the measured heat flow rate, Φ_0 is the initial heat flow rate, and β the sample heating rate [227].

However, the position of the peak maximum changes with the heating rate, with the thermal conductance of the sample and with its mass. Moreover, due to the instrument's geometry, the point of temperature measurement is not the point where the sample is located - therefore a systematic error will always occur in scanning operation which depends on instrument and experimental parameters. Careful calibration is thus pivotal to acquire trustworthy data.

2.4.2 Thermal expansion

Most crystalline materials undergo dimensional changes in response to temperature variations. Thermal expansion of crystals can be investigate by means of XRD, but macroscopic specimens often present pores, residual stresses or cracks that modify the response of the material to the temperature variation with respect to XRD results. It is thus common laboratory practice to measure thermal expansion with a dilatometer.

Pushrod dilatometers uses a Linear Differential Variable Transformer (LDVT) to convert a pushrod displacement into a voltage. The voltage is therefore converted into a recordable signal by a software. At the same time, the temperature at the free end of the sample is monitored with a thermocouple, making it possible to refer the pushrod displacement to a temperature value (Figure 2.10) [229, 230].

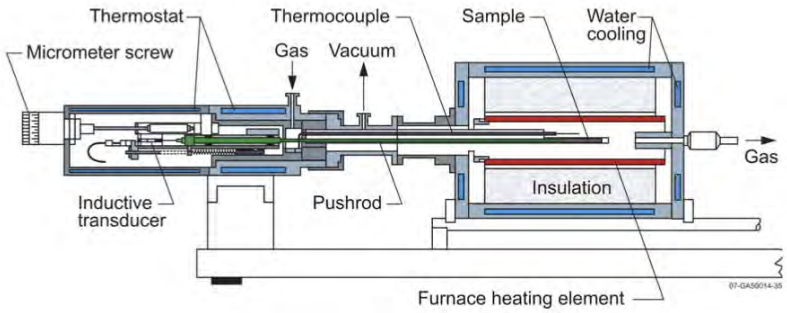

Figure 2.10: Schematics of a pushrod dilatometer in horizontal configuration. This setup minimises convection effects and thus thermal expansion of the equipment's components [229].

It is possible to define a coefficient of thermal expansion (also referred to as thermal expansivity, α_T) as the slope of the tangent to the curve reporting dimensional change as function of temperature, or as the incremental ratio as a function of temperature (average thermal expansion coefficient $\alpha_{T,m}$):

$$\begin{aligned} \alpha_T &= \frac{1}{L}\frac{\mathrm{d}L}{\mathrm{d}T} \\ \alpha_{T,m} &= \frac{1}{L}\frac{\Delta L}{\Delta T} \end{aligned} \tag{2.13}$$

An alternative method in quantifying thermal expansion is in terms of the fractional increase in volume per unit rise in temperature:

$$\beta_T = \frac{1}{V}\left(\frac{\delta V}{\delta T}\right)_P \tag{2.14}$$

In XRD datasets, the thermal expansion curve generally shows an exponential growth. The expansion coefficient can thus be obtained by fitting the lattice parameters values as function of temperature to the following equation [231]:

$$a(T) = a_{T_0} \exp\left[A(T - T_0) + \frac{B}{2}(T^2 - T_0^2)\right] \tag{2.15}$$

where a_{T_0} is the cell parameters a at a reference temperature T_0, whereas A, B are fitting parameters.

Most specimens follow the exponential trend outlined in Eq. 2.15 in a limited temperature range. In fact, first-order transformations might occur in single-phase systems : they are characterised by a discontinuous change in volume at constant temperature and pressure. This might be due to a phase transition, such as the one occurring in iron at 1184 K (from *bcc* to *fcc* structure). The change in volume may be large or very small and positive or negative. In multi-phase systems, the transition may occur over an appreciable temperature range and at generally higher temperatures on heating than on cooling, with hysteresis as the result.

Second-order transformations might also occur. They are generally characterised by the disappearance of ordered structures (i.e. chemical compounds in alloy systems, magnetic moments as in ferromagnetic materials, electron energy states in superconductors), resulting in a discontinuous change in the coefficient of thermal expansion at constant temperature and pressure [232].

As far as common laboratory practice goes, thermal expansion curves for macroscopic specimens can be fitted with a polynomial equation of the type:

$$\frac{\Delta L}{L_0} = a + b(T - T_0) + c(T - T_0)^2 + d(T - T_0)^3 + e(T - T_0)^4 \tag{2.16}$$

Where L is the sample length, L_0 the sample length at the starting temperature T_0 and T is the absolute temperature. The resulting equation is specific for the analysed sample, but can still be used as a guideline for engineering necessities.

2.4.3 Thermal and electrical conductivity

Several different carriers are responsible for heat transfer in solids: electrons, lattice waves (phonons), magnetic excitations and, in some cases, electromagnetic radiation. The measured thermal conductivity (k_{tot}) is therefore the sum of each of these contributions (κ_{ph} and κ_e). In pure metals, the principal heat carriers are phonons and electrons. At low temperatures, the phononic contribution is low due to phonon-electron interactions, but it becomes comparable with the electronic contribution at high temperature. Multi-principal components alloys, however, are characterised by a smaller carrier concentration, decreasing with temperature, as well as by lattice distortions. Consequently, their sensitivity to phonon concentration with temperature is lower and, unlike pure metals, the mean path of electrons increases with temperature [174].

Electrical conductivity is a measure of the ability of a material to conduct an electric current. Since both modes of transport involve free electrons in the metal, thermal and

electrical conductivity are linked by the Wiedemann–Franz equation:

$$k_{tot} = \kappa_{ph} + \kappa_e = \kappa_{ph} + L\sigma T \tag{2.17}$$

where L is the Lorentz number ($2.44 \cdot 10^{-8}$ WK^{-2}), σ is the electrical conductivity and T the absolute temperature.

Laser Flash Analysis

The laser flash analysis method (LFA) is a well-developed technique for measuring the thermophysical properties of solid materials (*i.e.* thermal diffusion, conductivity and specific heat) [233]. The technique entails heating the front side of a plane-parallel, disk-shaped sample by a short laser pulse and measuring the temperature rise on the rear surface *versus* time using an infrared detector. Since modern devices enable the direct calculation of the specific heat c_P and of the thermal diffusivity K, knowing the bulk density of the material ρ it is possible to directly calculate thermal conductivity:

$$k_{tot}(T) = \rho(T)C_P(T)K(T) \tag{2.18}$$

Specific heat capacity for thermal conductivity calculation is determined by the software using the Pyroceram reference according to the following relation:

$$C_P^{sample} = \frac{T_\infty^{ref} Q^{sample} V^{sample} \rho^{sample} D^{sample} d_{sample}^2 C_P^{ref}}{T_\infty^{sample} Q^{ref} V^{ref} \rho^{ref} D^{ref} d_{ref}^2} \tag{2.19}$$

where T_∞^{ref} and T_∞^{sample} correspond to the heat loss corrected voltage increase of detector signal at infinite time for the reference and the sample respectively; Q^{ref} and Q^{sample} are the energy (integral of the laser pulse) on the reference and sample respectively; V^{ref} and V^{sample} are the reference (or sample) amplification factor; ρ^{ref} and ρ^{sample} are the density of the reference and the sample respectively; D^{ref} and D^{sample} are the reference and sample respective thicknesses; d_{ref}^2 and d_{sample}^2 are the orifices area of reference and sample; C_P^{ref} is the tabulated value of specific heat capacity for the reference material [234]. The change in density following heating is taken into consideration by using the thermal expansion data from the dilatometry experiment.

More about the experimental setup is reported in Section 2.6.4.

Seebeck coefficient

Thermoelectricity is the conversion of heat into electricity (or vice versa) and is caused by the coupling of the flow of heat and charge carriers in a material. In particular, semiconductors show the largest coupling between these two forms of energy, and are therefore the materials of election for use in thermoelectric waste heat harvesting and refrigeration [235]. The efficiency of a material is typically defined using the thermoelectric figure of merit:

$$ZT = \frac{S^2\sigma}{k_{tot}}T \tag{2.20}$$

where T is the absolute temperature; the Seebeck coefficient S is the voltage response to a temperature gradient; σ is the electrical conductivity and k_{tot} ($\kappa_{ph} + \kappa_e$) is the thermal conductivity. Three thermoelectric parameters (S, σ and κ_e) are linked through the electronic structure, and cannot be optimised independently. As a consequence, ZT is limited to ≤ 1 for most thermoelectric materials.

According to the phonon-glass electron-crystal (PGEC) guiding principle, the ideal thermoelectric material should possess the electronic properties of an appropriate crystalline solid (*i.e.* large S and σ) and the thermal properties of glass (*i.e.* low κ_e). By combining low thermal conductivity values (< 1 Wm^{-1} K^{-1}) with modest power factors ($S^2\sigma$ = 1-3 $mWm^{-1}K^{-2}$) large ZT values can be obtained.

2.5 Mechanical characterisation

2.5.1 Hardness

Hardness is referred to as the resistance with which a body counters the penetration of another (little deformable) body. Following from this definition, hardness can be defined as the ratio between test force (F) and indentation surface (A):

$$H = \frac{F}{A} \tag{2.21}$$

The deformation of a specimen during indentation consists of two parts, namely elastic strain (reversible) and plastic deformation (permanent). If we imagine pressing a hard sphere against a surface, at the instant of contact there is no strain in the specimen, but the sphere is flattened by the surface traction. The surface traction, consisting of hydrostatic compression as well as shear, produce strain in both the sphere and the sample. The maximum shear is located at a point along the axis of contact; when it reaches a critical value the following phenomena might occur: plastic flow, twinning or phase transformation. These phenomena comprise an inelastic response which continue upon pressing until the increasing indentation area causes the maximum shear stress to drop [236].

However, hardness indentations are a result of plastic, rather than elastic, deformation. Indeed, they result from a transport process in which element of displacement are irreversibly moved from one position to the other by shear stress. The plastic deformation patterns observed during indentation are mediated by the motion of dislocations. In fact, all three inelastic processes (flow, twinning and phase change) require the shearing of neighbouring atoms: in metals, the barrier to dislocations is a balance between the energy required for shearing and the energy barrier opposing it. However, the inelastic processes tend to occur at the same critical elastic strain. By interfering with each other, they decrease the stress needed for further deformation. Assuming that there might be more than one glide system,

that dislocation lines might not be straight, and that they might move at different velocities, the three-dimensional shear deformation rate ($\frac{d\delta}{dt}$) can be defined as follows [236]:

$$\frac{d\delta}{dt} = b \oint (\vec{v} \cdot \vec{n})\, dl \tag{2.22}$$

Where b is the transport entity, n is the density of dislocations and v their velocities. The line integral refers to all of the dislocation lines in the material.

The source of the high plastic resistance of most engineering materials relies on the introduction of extrinsic barriers to dislocation. In other words, dislocations can move freely between these barriers, but require extra stress to overcome them. These sources of plastic resistance are the following [236]:

- Deformation hardening. Since screw dislocations are nearly cylindrically symmetric, they can easily move from one glide plane to the next and back. This motion causes them to leave behind edge dislocation dipoles, which slow further screw motion. This process is the most general determinant of hardness for metals.

- Impurity atoms (alloying). When normal sites in a crystal structure are replaced by different atoms, vacancies or interstitial atoms, the local electronic structure is disturbed and local electronic states are introduced. If a dislocation kink moves into such a site, its energy changes significantly and further motion is opposed.

- Precipitates. A moving dislocation line encountering a precipitate harder than the surrounding matrix can either pass through it or around it. In the latter case, the precipitates can repel the dislocation until a critical energy is reached. At that point, the dislocation line envelops the precipitate and moves onward - however, the loops located around the precipitates exert shearing stresses in addition to the applied stress.

- Grain boundaries. In a polycrystalline material, only few grain boundaries are symmetric in a way that, when one crystal plastically deforms, its boundaries maintain continuity. Rather, mismatches are created, which generate elastic strain on the mutual boundary.

- Surface films. Since surface layers interfere with the motion of dislocations near surfaces, they cause local strain-hardening. In turn, this creates a growing harder surface region which thickens upon further deformation.

- Twin boundaries. Twin boundaries, a common occurrence in all types of crystals, can be coherent or incoherent. Unlike the first, the latter are not symmetric and may resist dislocation motion considerably.

It is worth noting that hardness depends on which face of a non-cubic crystal is being indented. For example, a crystal owning trigonal symmetry will respond differently upon

indentation on a face normal to its c-axis or to its a-axis (anisotropy). Furthermore, the symmetries of crystal surfaces and indenters rarely match, or are rotationally misaligned. As such, crystals cannot be fully characterised by single hardness numbers [236].

Static methods for hardness measurement

Most of the hardness measuring methods standardised today were established before 1930 and have, in principle, remained unchanged. In these procedures, the test force is applied to the test piece without shocks during a prescribed minimum time. These tests are generally identified as 'static methods', to distinguish from the dynamic methods' in which impact force is applied to a sample, and are briefly reviewed in the following pages [237].

In indentation tests such as Brinell, Rockwell, Vickers and Knoop, a set force is applied to an indenter in order to determine the resistance of the material to penetration. A hard material will result in a small or shallow indentation, whereas a soft one in a relatively large and deep one. While hardness is not a fundamental property of the material, it can nevertheless aid the prediction of other structural properties when combined with additional information. In particular, by combining Vicker's hardness results with compositional information, it is possible to qualitatively evaluate resistance to plastic deformation, ductility and fracture strength [238]. An example is provided in Section 2.6.1.

Rockwell Hardness (HR) The indenter is either a right circular cone with a rounded diamond tip or a sphere made of hard metal. The indenter penetrates the sample under a preliminary test force F_0, down to a depth which will be used as reference plane. An additional test force (F_1) is applied until the maximum penetration depth is reached. Afterwards, F_1 is withdrawn so that only F_0 is still acting. At the same time, the indenter moves back by the elastic fraction of the depth of penetration during the total test force; the indentation persists at the remaining depth of penetration, h. The Rockwell hardness is thus defined as:

$$HR = K - \frac{h}{S} \tag{2.23}$$

Where K is a numerical constant and S is the scale division (in mm) [237].

Vickers Hardness (HV) In this procedure the indenter is a straight diamond pyramid with an angle between opposite faces of 136°. Thanks to its shape, the law of proportional resistances applies: as a result, test force and indentation surface are proportional to each other. While, in principle, hardness values obtained with this methods should be independent from the applied load, surface tension create some interdependence between the two quantities.

Following from the definition of hardness reported in Eq. 2.21, in the Vickers method the surface of the indentation remaining on the sample surface after the load has been removed can be calculated from the mean value of two diagonals ($d = (d_1 + d_2)/2$). Assuming that the

Method	Indenter type	Advantages	Disadvantages
Rockwell	Right circular cone with rounded diamond tip. or Hard metal sphere.	Short sample preparation and testing time. Inexpensive equipment. Automated procedure.	Unknown influence of the indenter on the test result. Poor materials differentiation with increasing hardness.
Vickers	Straight diamond pyramid.	Only slight damage of the surface. No limitations in terms of sample's size and hardness. Applicable to very small loads.	Time consuming test preparation and measurement. Sensitivity to impact and vibrations.
Brinell	Sphere of hard metal.	Test inhomogeneous materials. Low cost Suitable for large sample in rough workshop operation.	Unsuitable for thin samples and very high hardnesses. Measurement errors (depending on the the lens system used due to pile-up around the indentations).

Table 2.4: Advantages and disadvantages of Rockwell, Vickers and Brinell hardness testing methods, [237].

permanent indentation is a geometrically true image of the indenter:

$$\begin{aligned} HR &= \frac{0.102 \cdot F}{A} \\ A &= \frac{d^2}{2\sin 68} = \frac{d^2}{1.854} \\ HR &= \frac{0.102 \cdot 1.854 \cdot F}{d^2} \end{aligned} \tag{2.24}$$

From Eq. 2.24 it is clear that the sensitivity of a Vickers measurement depends on the chosen load, since the developing diagonal is roughly proportional to the test piece hardness: $d \simeq \frac{1}{\sqrt{HV}}$. The applied load ranges from 1.961 N to 49.03 N. Furthermore, the minimum test piece thickness must lie between 0.085 and 6.5 mm and the duration of the test amount to 10 to 15 s (unless otherwise indicated), with the force being increased from zero to its final value in 2 to 8 seconds [237].

Brinell Hardness (HBW) Method giving results comparable with Vickers hardness. A sphere of hard metal penetrates vertically under a defined force F. The surface A of the permanent indentation remaining on the surface once the load is removed is calculated from the mean value of two conjugated diameters ($d = \frac{d_1+d_2}{2}$, measured to the projection of the indentation on the sample surface). For calculation of the indentation surface area, it is assumed that the sphere is ideally rigid. Brinell hardness can thus be defined as follows [237]:

$$HBW = \frac{0.102 \cdot F}{A} = \frac{0.102 \cdot 2 \cdot F}{\pi D(D - \sqrt{D^2 - d^2})} \tag{2.25}$$

Advantages and disadvantages of each mode of operations are summarised in Table 2.4.

2.5.2 Small Punch test

The Small Punch (SP) test was first developed in the ‘80s in the U.S. and in Japan as a miniature testing technique for the investigation of irradiated materials from fission and fusion programs. Circa thirty years later, a European Code of Practice (EUCoP) was developed for SP tensile, fracture and creep testing. This rigid methodology made the SP technique suitable for the assessment of new materials, thanks to its low cost and for the small amount of specimen required [239].

In a SP test, a small hemispherical tip (*i.e.* generally a solid punch in a single piece, as recommended in the current CEN Workshop Agreement) is pushed through a disc-shaped specimen (of 0.25 or 0.5 mm thickness) along its axis of symmetry. The test can be performed either at constant load, or at constant displacement rate. In the first case, displacement is measured as a function of time; in the latter the change in force is determined as a function of time [239]. The SP apparatus is reported in Figure 2.11.

Figure 2.11: Schematics of disc retention and SP technique application [240].

To this day, SP has mostly been used to characterise ductile alloys; but since it would be theoretically possible to test small sample volumes in tandem, the technique has attracted some interest for high-throughput assessment of additive-manufactured components [240]. However, the evaluation of SP tests is still a topic of research, because even basic mechanical properties determined through this technique are strongly dependant on the triaxial, time dependent stress state in the specimen and on the test geometry [239]. Furthermore, the test results are dependent on sample orientation and thickness. For this reason, standardised data are sometimes normalised to a specimen thickness of 0.5 mm: this approximation is valid under the assumption that the relationship which links force and displacement is a square function, and offers acceptable results in the first part of the deformation curve [241].

Typically, force-displacement curves obtained after SP comprise five distinct regions [242]:

1. Elastic bending. Produced when the punch contacts the disk, causing a bending stress.
2. Yield. Caused by the bending action in the highest stressed regions, produces plastic deformation and strain hardening.
3. Plastic bending. The strain hardening results in the transfer of the load to adjacent non-yielded sections within the specimen, thus effectively expanding the yield front until it spreads through the entire disk thickness.
4. Membrane stretching. Since bending continues after yield, the amount of plastic strain in the yielded sections is subject to an increase. Eventually the yield front extends beyond the limits of the region of contact between punch and disc, placing a large annular section of the disc in tension (in fact, this area is subjected to both a longitudinal stress and a lateral stress).
5. Necking to failure. Necking occurs in the membrane stretching area once the ductility of the material is exhausted, ultimately leading to failure.

To normalise the results for the standard 0.5 mm thickness and obtain quantitative estimates, the following equation(s) are used:

Ultimate tensile strength for brittle materials [242]:

$$\begin{gathered} Cl = A - (D + 2t) = 8 - (4 + 2t) \\ UTS = \frac{F_m}{t(0.14D - 0.82Cl + 2.17u_m + 0.6)} \end{gathered} \tag{2.26}$$

Where F_m is the maximum load during the test, t is the disk thickness (in mm), D is the punch diameter, Cl is the die clearance (in mm) and u_m is the displacement at failure. In the first equation, A is the diameter of the lower die.

Punch test results obtained after normalising thickness to 0.5 mm [243]:

a. For $P_{test} < P_{inflexion}$ (the pressure at which the inflexion occurs in the load-displacement curve, in the plastic bending region):

$$P_{0.5} = 0.5^2\Big(\frac{P_{test}}{t^2}\Big) \tag{2.27}$$

b. For $P_{test} > P_{inflexion}$:

$$P_{0.5} = 0.5\Big(\frac{P_{test}}{t}\Big) + 0.5P_{inflexion}\Big(\frac{0.5 - t}{t^2}\Big) \tag{2.28}$$

The results of the SP tests are reported and briefly discussed in Section 3.2.1.

2.5.3 Density

Density was measured using flotation in water, also commonly referred to as Archimedes principle, in the ATTENSION equipment (Biolin Scientific, Stockholm, Sweden).

The density of a multi-principal component alloy can be estimated using the following equation:

$$\rho_{est} = \frac{\sum c_i A - i}{\sum \frac{c_i A_i}{\rho_i}} \tag{2.29}$$

where c_i, A_i and ρ_i are respectively concentration, atomic weight and density of the element i. Density values for pure metals were taken from reference [244].

It is also possible to calculate density from X-ray data. Once the XRD profile has been refined and the cell parameters (a, b and c; α, β and γ) are known, it is possible to calculate the volume of the cell. Knowing the content of each unit cell and its chemical structure (*i.e.* knowing the molecular weight), theoretical density can be estimated as follows [212]:

$$\rho_{est} = \frac{MW \cdot n}{V \cdot N_A} \tag{2.30}$$

Where MW is the molecular weight, n the number of molecules per unit cell, V the unit cell volume and N_A Avogadro's number ($6.022 \cdot 10^{23}$).

Lastly, for composite materials, density can be estimated from the Rule of Mixture, as highlighted in Section 1.3.5.

2.6 Experimental details

2.6.1 The AlCrCuScTi alloy

The target alloy has been prepared using induction melting in a BN crucible. Al, Cr, Cu, and Ti were taken as fine powders or grains (Goodfellows, Huntingdon, UK) and mixed with 1 mm Sc grains; metals were used in equiatomic proportions. Complete melting of the sample was achieved above 1600 °C. After 5 min at the melting temperature, the sample was cooled down naturally to room temperature. The as-cast material was thermally annealed in a dynamic vacuum (10^{-2} Pa) at 1000 °C for 4 h, followed by natural cooling to room temperature. Annealing temperature was chosen as a compromise between the very different melting point of elements; a short time was selected to avoid Al evaporation. Part of the annealed sample was fast-heated (1–2 min) to melting using an induction coil in a glove-box and quenched in high purity hydrostatic oil. The three samples are referred to in the text as 'as-cast', 'annealed' and 'quenched'.

All samples were mounted in carbonised resin, polished and etched according to the procedure reported in section 2.2.1. For microstructure and elemental analysis, all samples were mounted in carbonised resin, ground and polished using MetaDiTM Supreme Polycrystalline Diamond Suspension (1 µm). Specimens were etched with a Buehler solution (5 % solution of HNO_3 in ethanol) prior characterisation. Morphology and elemental compositions were analysed using a Hitachi S-4800 Field Emission scanning-electron microscope (SEM) equipped with energy dispersive X-ray (EDX) analyser. The average elemental composition was obtained from 2.5 ×1.5 mm maps.

Vickers hardness was measured on a WilsonR VH3100 Automatic Knoop/Vickers Hardness tester; 50–60 individual points under a 9.81 N (1 kg) testing load were measured to get statistically significant results. It has been demonstrated that the crack length forming in a material during Vickers indentation can be used to characterise ductile-brittle transitions in hard and soft materials. Indentation at various forces produces pyramid-shaped traces linked to material ductility, as well as symmetrical cracks related to the brittleness of the specimen [245]. This methodology gives a good estimation of the ductile–brittle transition, especially if mechanical tests cannot be performed. Thus, in order to investigate cracking phenomena, various forces of 2.94, 9.81, 19.62, 29.43, 49.04 and 98.10 N were applied. Lengths of indentation and cracks were measured using x50 magnification with 0.2 μm accuracy. Since the indenter is bigger than the individual domains characteristic for the sample, no significant differences in hardness values were detected among different areas of indention. Plotting the logarithmic pressure load ($\log_{10} P$) *versus* the logarithm of indentation length ($\log_{10} d$), and *versus* the total length of crack, $\log_{10}(2c)$, gives a straight line, whose slope is close to 2 and to 3/2 respectively. The intersection of the two lines identifies the critical load P_{crit}. For $P > P_{crit}$ brittle cracks appear, whereas for $P < P_{crit}$ only plastic deformation is observed. The crack formation is displayed in Figure 2.12 and discussed in the corresponding Section 3.1.1.

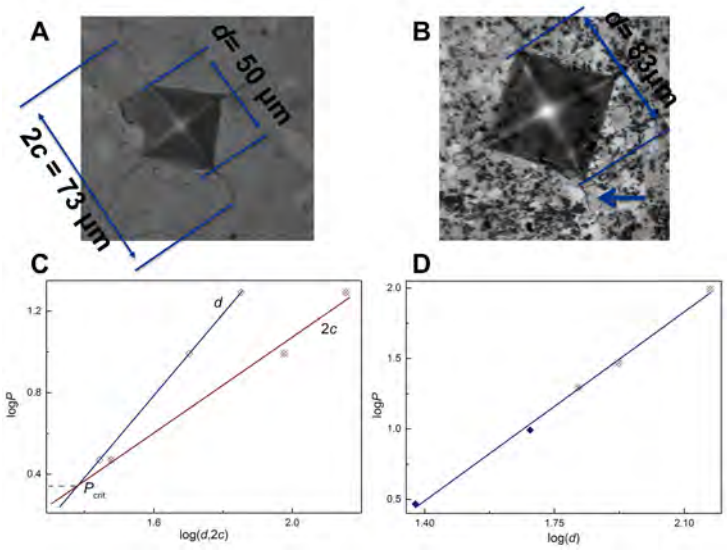

Figure 2.12: (*A*) Optical microscope image of the indentation of the as-cast AlCrCuScTi upon 9.81 N load and (*B*) of the annealed alloy upon 29.43 N load. The arrow shows the formation and prolongation of a single crack. (*C*) $\log_{10} P$ *vs* $\log_{10} d$ and $\log_{10}(2c)$ plots for as-cast alloy; (*D*) $\log_{10} P$ *vs* $\log_{10} d$ plot for annealed alloy (two points at low loadings show no cracks formation, tree data-points at high load pressure display moderate crack formation) [251].

Atomic-force microscope equipped with scanning Kelvin probe (AFM/SKP) measurements were performed in AC mode on the annealed alloy using a JPK NanoWizard3 Instrument (JPK, Berlin, Germany), equipped with a FM-50 Pointprobe® tip. The SKP scanning was performed at 10 $\mathrm{nm \cdot s^{-1}}$ with 5 $\mu \mathrm{m \cdot s^{-1}}$ speeds.

Powder X-ray diffraction profiles for the as-cast and annealed powdered samples were collected at room temperature at the ID-09A beam-line at the ESRF (λ = 0.4145 Å, MAR 555 flat panel detector (marXperts GmbH, Norderstedt, Germany) company, city, country, beam size 10 x 15 $\mu \mathrm{m}^2$). LaB_6 was used as external standard for calibration. For data analysis, two-dimensional images were first integrated to one-dimensional intensity counts as a function of diffraction angle using the FIT2D software (Version 18, ESRF, Grenoble, France, 2016). Phase identification was performed using the Crystallography Open Database and the Inorganic Crystal Structure Database [246].

2.6.2 A library of five- and six-components alloys based on the Co–Gd–Sc–Ti–Y–Zr phase diagram

The target alloys were prepared using induction melting in BN crucibles. Co, Ti and Zr were taken as powders or rods, while Gd, Sc and Y as pieces. All metals were purchased from Goodfellows at ⩾99% purity. In all cases, complete melting was achieved above 1600 °C. After 5 minutes at the melting temperature the samples were cooled down naturally to room temperature (2 minutes). All as-cast materials were annealed in a dynamic vacuum (10^{-2} Pa) at 900 °C for 12 h, followed by 2 hours of natural cooling to room temperature. Annealing

temperature was chosen as being 3/4 of the average melting temperature of elements.

For characterisation, all samples were mounted, polished and etched according to the protocol described in section 2.2.1. For microstructure and elemental analysis, all samples were mounted in carbonised resin, ground and polished using MetaDiTM Supreme Polycrystalline Diamond Suspension (1 µm). Morphology and elemental compositions were analysed using a Hitachi S-4800 Field Emission scanning-electron microscope (SEM) equipped with energy dispersive X-ray (EDX) analyser. The average elemental composition was obtained from 2.5 ×1.5 mm maps.

Vickers hardness was measured on a WilsonR VH3100 Automatic Knoop/Vickers Hardness tester; 25 individual points under a 9.81 N (1 kg) testing load were measured to get statistically significant results.

Powder X-ray diffraction patterns were collected from the powdered samples. Powders were fixed between two Kapton foils and measured at room temperature in transmission mode at the ID06A beam-line at the European Synchrotron Radiation Facility (position sensitive detector, $\lambda = 0.22542$ Å). Phase identification was performed via automated and manual search-match through the Inorganic Crystal Structure Database [246].

2.6.3 The $Al_2CoCrFeNi$, $Al_{0.5}CoCrCuFeNi$ and $AlCoCrCu_{0.5}FeNi$ HEAs with or without scandium

The target alloys were prepared using induction melting from pure metallic powders, in a BN crucible in an Ar-filled glove-box. Complete melting of the samples was achieved above 1300 °C. After 5 minutes at the melting temperature, the sample was cooled down naturally to room temperature. The samples were re-melted three times to assure homogeneity. A brief rationale of the synthesised specimens and their performed analysis is reported in Table 2.5.

Differential scanning calorimetry (DSC) measurements were performed on small pieces of sintered samples (50 mg) placed in an Al_2O_3 crucible and heated in a Netzsch STA 449 *F1 Jupiter*. Heating and cooling were performed in flowing Ar gas with a temperature ramp of 10 K/min from 35 to 1300 °C.

The transition temperatures highlighted by DSC where used to decide annealing conditions. Samples were heat-treated above their first reversible or irreversible transition temperature with the following specifics: $Al_2CoCrFeNi$, $Al_{0.5}CoCrCuFeNi$ and $AlCoCrCu_{0.5}FeNi$ at 850°C, 12 hours; $Al_2CoCrFeNi$+3 wt.% Sc at 900 °C, 12 hours, $Al_{0.5}CoCrCuFeNi$+3 wt.% Sc and $AlCoCrCu_{0.5}FeNi$+3 wt.% Sc at 930 °C for 6 hours. During annealing, pellets of each sample were sealed in a quartz tube under high-vacuum (10^{-7} Pa) and heated in a furnace After annealing, the tubes were quenched in ice water.

For microstructure and elemental analysis, all samples were mounted in carbonised resin, ground and polished using MetaDiTM Supreme Polycrystalline Diamond Suspension (1 μm).

Alloy	Form	Analysis
$Al_2CoCrFeNi$	As-cast pellet	SEM-EDX, Density, Vicker's hardness, DSC, Disc punch test
	Annealed pellet (850°C, 12h)	SEM-EDX, RT PXRD
	Powder from as-cast pellet	RT PXRD, HT PXRD, LT PXRD, HP-HT PXRD
	After sintering	SEM-EDX, Vicker's hardness
$Al_2CoCrFeNi$+0.5wt.% Sc	As-cast pellet	SEM-EDX, Vicker's hardness, Disk punch test
$Al_2CoCrFeNi$+2wt.% Sc	As-cast pellet	SEM-EDX, Vicker's hardness, Disk punch test
$Al_2CoCrFeNi$+3wt.% Sc	As-cast pellet	SEM-EDX, Density, Vicker's hardness, DSC
	Annealed pellet (900°C, 12h)	SEM-EDX, RT PXRD
	Powder from as-cast pellet	RT PXRD, HT PXRD, LT PXRD, HP-HT PXRD
	After sintering	SEM-EDX, Vicker's hardness
$Al_{0.5}CoCrCuFeNi$	As-cast pellet	SEM-EDX, Vicker's hardness, DSC
	Annealed pellet (850°C, 12h)	SEM-EDX
	Powder from as-cast pellet	RT PXRD, HT PXRD
$Al_{0.5}CoCrCuFeNi$+0.5wt.% Sc	As-cast pellet	SEM-EDX, Vicker's hardness
$Al_{0.5}CoCrCuFeNi$+2wt.% Sc	As-cast pellet	SEM-EDX, Vicker's hardness
$Al_{0.5}CoCrCuFeNi$+3wt.% Sc	As-cast pellet	SEM-EDX, Vicker's hardness, DSC
	Annealed pellet (930°C, 6h)	SEM-EDX
	Powder from as-cast pellet	RT PXRD, HT PXRD
$AlCoCrCu_{0.5}FeNi$	As-cast pellet	SEM-EDX, Density, Vicker's hardness, DSC, Disc punch test
	Annealed pellet (850°C, 12h)	SEM-EDX
$AlCoCrCu_{0.5}FeNi$	Powder from as-cast pellet	RT PXRD
$AlCoCrCu_{0.5}FeNi$+0.5wt.% Sc	As-cast pellet	SEM-EDX, Vicker's hardness
$AlCoCrCu_{0.5}FeNi$+2wt.% Sc	As-cast pellet	SEM-EDX, Vicker's hardness
$AlCoCrCu_{0.5}FeNi$+3wt.% Sc	As-cast pellet	SEM-EDX, Vicker's hardness, DSC, Disc punch test
	Annealed pellet (930°C, 6h)	SEM-EDX
	Powder from as-cast pellet	RT PXRD

Table 2.5: Rationale of the alloys presented in Section 3.2, with the corresponding characterisation. The acronyms *RT*, *HT* and *LT* refer to synchrtron PXRD experiments performed at room temperature, high-temperature and low-temperature respectively. *After sintering* refers to the high pressure (HP) experiments performed (*via* SPS, multi-anvil press or piston cylinder).

Morphology and elemental compositions were analysed using a Hitachi S-4800 Field Emission scanning-electron microscope (SEM) equipped with energy dispersive X-ray (EDX) analyser. The average elemental composition was obtained from 2.5 ×1.5 mm maps.

Vickers hardness was measured on a WilsonR VH3100 Automatic Knoop/Vickers Hardness tester; 25 individual points under a 9.81 N (1 kg) testing load were measured to get statistically significant results.

Density was measured using flotation in water, also commonly referred to as Archimedes principle, in the ATTENSION equipment (Biolin Scientific, Stockholm, Sweden). Six measurements were taken for each sample to obtain statistically relevant results.

Small punch tests were performed on discs of diameter 12.5 mm and thickness circa 0.8 mm. Measurements were performed with a properly modified Tinius Olsen H25KS Benchtop Tester equipped with Horizon Software. The setup included a lower die (diameter of 8 mm) and a punch (4 mm diameter). Each experiment was reproduced twice for statistic significance; however, since each specimen had slightly different thickness, the final results were normalised for the standard 0.5 mm thickness as described in Section 2.5.2.

For PXRD study, samples were powdered using a Fritsch mini-mill Pulverisette 23 (steel vial and ball, 10 minutes at 50 r.p.m.). Powder X-Ray diffraction data for the annealed powdered samples were collected at ID06B-LVP beam-line at the ESRF (room temperature, $\lambda = 0.22542$ Å) using position sensitive detector. LaB_6 (NIST SRM 660c) was used as external standard for calibration.

In situ high- and low-temperature powder X-ray diffraction experiments were performed at the DIAMOND light source and PETRA III synchrotron respectively, according to the procedure reported in 2.3.4. Temperature was directly measured with a thermocouple during the experiment; the error arising from the distance between sensor and capillary was estimated to be below 5%.

High pressure experiments

Circa 5 g of the previously synthesised $Al_2CoCrFeNi$ and $Al_2CoCrFeNi$+ 3wt.% Sc were mechanically milled to powders using a Fritsch Planetary Mill PULVERISETTE 5/2 (10 mm steel balls and vials, ball-to-powder ratio 10:1, 36 h, 250 r.p.m.) for the pristine HEA and a Fritsch Mini-Mill Pulverisette 23 (steel vial and ball, 10 minutes at 50 r.p.m.) for the HEA+Sc. These samples are referred as as-cast in the corresponding section, whereas 'annealed' refers to the previously described $Al_2CoCrFeNi$ and $Al_2CoCrFeNi$+ 3wt.% Sc annealed at 850 °C, 12 hours and at 900 °C, 12 hours respectively.

$Al_2CoCrFeNi$ powder was sintered using a FCT Systeme GmbH **Spark Plasma Sintering** Furnace type H-HP D 250 located at Kennametal Manufacturing (UK) Ltd. The tooling consisted of graphite punch and ring elements and carbon-fibre resistance heating elements. 0.35 mm graphite foil was used for lining the graphite elements. The powder under investigation was loaded into the mould. Only the graphite foil was in contact with the powder. To

enable a DC current to pass through the tooling, water cooled rams are used, which clamp the tooling and apply force during sintering and conduct current through the tool and powder. The load provided to the tool from the rams was increased during the processing cycle (see Section 2.1.3). The sample was heated up to 1123 ±10 K and pressed up to 50.0 ±0.2 MPa.

The **high-pressure experiments at 2.1 GPa** were performed in an end-loaded piston cylinder apparatus installed at the Institut fur Mineralogie, WWU Münster [247]. $Al_2CoCrFeNi$ and $Al_2CoCrFeNi$+3 wt.% Sc powders were enclosed in a 2 mm alumina crucible. An alumina disk separated the samples. The pressure assembly consisted of a 1/2 inch talc-Pyrex assembly, which contained 6 mm diameter graphite heater in inner parts of crushable alumina. Temperature was monitored and controlled with a W97Re3–W75Re25 thermocouple. Temperature uncertainties are estimated to be less than ±10 K at lower temperatures, increasing to about ±15 K at 1773 K. The quoted pressure is estimated to be accurate within 0.1 GPa, based on the pressure calibration reported in [248]. The assembly was pressed and heated simultaneously to 2.1 GPa and 850 °C (1173 K), annealed for 60 minutes and finally quenched to room temperature.

Experiments at 9.5 GPa were performed on the large-volume press installed at the beam-line ID06-LVP, ESRF, according to the protocol described in Section 2.3.4. The error on applied pressure and temperature was estimated to be 7% and 18% respectively.

***In situ* high-temperature X-ray diffraction data** for the powdered samples were collected at I-11 beam-line at the Diamond light source (λ = 0.494984 Å) in the experiment underlined in Section 2.3.4. Temperature was directly measured with a thermocouple during the experiment; the error arising from the distance between sensor and capillary was estimated to be below 5%.

For microstructure and elemental analysis, all samples were mounted in carbonised resin, ground and polished using MetaDiTM Supreme Polycrystalline Diamond Suspension (1 μm). Morphology and elemental compositions were analysed using a Hitachi S-4800 Field Emission scanning-electron microscope (SEM) equipped with energy dispersive X-ray (EDX) analyser. The average elemental composition was obtained from 2.5 ×1.5 mm maps.

Vickers hardness was measured on a WilsonR VH3100 Automatic Knoop/Vickers Hardness tester; 5 individual points under a 9.81 N (1 kg) testing load were measured to get statistically significant results.

2.6.4 $Al_2CoCrFeNi$–based composite materials

Two specimens of $Al_2CoCrFeNi$+ 0.2 wt.% Sc were prepared via induction melting from metal powders of $\leqslant$ 99% purity. In the first, scandium was added to the powders as metal pieces prior melting; in the latter scandium was provided from a piece of the Al–2Sc Scalmalloy®

(provided by ESA). After 1-2 minutes at the melting temperature, the sample was cooled down naturally to room temperature.

For microstructure and elemental analysis, the two samples were mounted in carbonised resin, ground and polished using MetaDiTM Supreme Polycrystalline Diamond Suspension (1 μm). Morphology and elemental compositions were analysed using a Hitachi S-4800 Field Emission scanning-electron microscope (SEM) equipped with energy dispersive X-ray (EDX) analyser. The average elemental composition was obtained from 2.5 $\times$1.5 mm maps.

$Al_2CoCrFeNi$ was prepared using induction melting from powders of pure metals. Complete melting of the samples was achieved above 1300 °C. After 1-2 minutes at the melting temperature, the sample was cooled down naturally to room temperature. The sample was re-melted three times to ensure homogeneity. It was then mechanically milled to powder using a Fritsch Planetary Mill PULVERISETTE 5/2 (10 mm steel balls, ball-to-powder ratio 10:1, 36 h, 250 r.p.m.).

Samples of the obtained HEA powder were mixed with hexagonal boron nitride (h-BN, 3 wt.%, Sigma Aldrich), cubic boron nitride (c-BN, 2 wt.%, Kennametal Manufacturing), nanodiamonds (2, wt.%, Sigma Aldrich), silicon carbide (SiC, 2 wt.%, Sigma Aldrich), plasma functionalized multi-welled carbon nanotubes (CN, 1.5 wt.%, Haydale HDPlas®MWCN) or scandium oxide (Sc_2O_3, 0.5 wt.%, Fisher Scientific), using a Fritsch Planetary Mill PULVERISETTE 5/2 (10 mm steel balls, ball-to-powder ratio 5:1, 5 minutes, 250 r.p.m.). With respect to the standard 2 wt.% addition, h-BN was used in higher quantity than c-BN to study the effect of crystal structure as well as different concentration of additive on the HEA matrix. On the other hand, part of the originally weighted CN amount was lost during the loading process of the powder due to its volatility, giving a lower addition than originally planned. Finally, the low amount of Sc_2O_3 was due to its high cost and to the relatively low amount of aluminium which will be necessary to reduce it to scandium metal.

All powders were sintered using a FCT System GmbH Spark Plasma Sintering Furnace type H-HP D 250 located at Kennametal Manufacturing (UK) Ltd (the protocol has been reported in section 2.1.3) [249]. Each specimen was heated up to 1123 $\pm$10 K and pressed up to 50.0 $\pm$0.2 MPa.

For microstructure and elemental analysis, all samples were mounted in carbonised resin, ground and polished using MetaDiTM Supreme Polycrystalline Diamond Suspension (1 μm). Morphology and elemental compositions were analysed using a Hitachi S-4800 Field Emission scanning-electron microscope (SEM) equipped with energy dispersive X-ray (EDX) analyser. The average elemental composition was obtained from 2.5 $\times$1.5 mm maps.

Powder X-ray diffraction patterns were collected from the pristine and nanodiamond-containing samples. Powders were fixed between two Kapton foils and measured at room temperature in transmission mode at the ID06A beam-line at the European Synchrotron Radiation Facility (position sensitive detector, $\lambda = 0.22542$ Å). Phase identification was performed via automated and manual search-match through the Inorganic Crystal Structure

Database [246].

Vickers hardness was measured on a WilsonR VH3100 Automatic Knoop/Vickers Hardness tester; 5 individual points under a 9.81 N (1 kg) testing load were measured to get statistically significant results.

Density was measured using flotation in water, also commonly referred to as Archimedes principle, in the ATTENSION equipment (Biolin Scientific, Stockholm, Sweden). Six measurements were taken for each sample to obtain statistically relevant results.

Furthermore, the following measurements were performed on specimens of the spark-plasma sintered $Al_2CoCrFeNi$ and $Al_2CoCrFeNi$ +2 wt.% nanodiamonds: LFA, Electrical resistivity and Seebeck coefficient, Dilatometry.

In our in-house LFA experiments, 10 x 10 x 3 mm square samples were tested for thermal diffusivity using a NETZSCH LFA 457 laser flash analyzer [250]. Samples were measured for thickness and then coated with graphite to increase absorption of laser energy and reduce reflection. A three positions sample holder was used; two samples were placed in the instrument along with a Pyroceram 9606 reference standard. All measurements were performed in Ar atmosphere.

Temperature dependent electrical resistivity and Seebeck coefficients were measurements on a Seebeck coefficient/Electrical resistance measuring ZEM-3 system (Advanced RIKO, Inc.) equipped with a SDC35 temperature controller (Yamatake), a 2010 multimeter (Keithley®) and a R6146 programmable DC voltage/current generator (ADVANTEST). Electrical resistivity was measured with a 4-points probe method by sending current through the sample and simultaneously measuring the voltage difference along the specimen's length with a type R thermocouple (Pt-13 % Rh *vs* Pt). The Seebeck coefficient was obtained by heating one end of the sample and simultaneously measuring the voltage generated between probes.

During our experiments, linear thermal expansion $\frac{\Delta L}{L_0}$ (accuracy 0.003 %) as function of temperature was determined using a pushrod Netzsch 402 dilatometer. Each 4x4x20 mm rectangular sample was heated in an Al_2O_3 sample holder at a rate of 10 °C/min in Ar atmosphere.

Ashby maps to compare the prepared specimens with commercial products were prepared with the CES EduPack Software (Granta Design Limited, 2017) and the Level 3 Aerospace Materials Database herein contained, as licensed by Swansea University.

Chapter 3

Results and discussion

3.1 Scandium as active alloying element in multi-principal components alloys

So far, the use of scandium has been limited by its high prices and low availability in the market. However, the development of more multi-principal components alloys such as HEAs could open the door to new applications of scandium as active alloying element.

We herein report a set of pioneer studies in the development of new scandium-containing multi-principal components alloys [251, 252]. The section consists of two investigations; in the first scandium is alloyed with first raw metals, in the latter with *hcp*-structured elements. The resulting implications for scandium metallurgy are discussed in section 3.1.3.

3.1.1 Results: The AlCrCuScTi alloy

The composition of the target alloy, AlCrCuScTi, was chosen according to the following rationale:

- Focus on first-raw metals and aluminium, to exploit the low density of scandium.
- Titanium, as it has complete miscibility with scandium in liquid.
- Chromium, which forms an eutectic with scandium, to lower the latter's melting temperature.
- Copper, to form a stable intermetallic with scandium and, ideally, aluminium (*W*-phase).

The data related to the average composition, density and hardness of the AlCrCuScTi alloy are summarised in Table 3.1. The amount of Al in the sample is sensibly reduced during heat treatment (as per EDS semi-quantitative analysis): the high temperatures required by the synthetic route leads to the partial evaporation of Al. The alloy should therefore be considered *quasi*-equimolar.

AlCrCuScTi	Average Composition (±0.5 at.%) from 2.5 mm x 1.5 mm EDX maps					Density ± 0.02 g · cm^{-3}	Hardness	
	Al	Cr	Cu	Sc	Ti		HV	MPa
Nominal	20	20	20	20	20	4.71 (estimated)		
As-cast	21.7	20.0	21.6	17.4	19.3	4.84	636±27	6237±267
Annealed	16.7	19.1	19.5	23.3	23.3	4.83	890±20	8728±196
Quenched	18.1	22.3	20.2	20.5	20.8		797±10	7816±98

Table 3.1: Properties of as-cast, annealed and quenched AlCrCuScTi alloy.

Both the as-cast and annealed alloys show high brittleness and can be easily ground to a fine powder. Because of the easy formation of cracks during indentation, Vickers hardness of the quenched material can only be roughly estimated. Annealing results in a drastic increase of hardness and decrease in the brittleness of the alloy. To compare the brittleness of the as-cast and annealed samples, indentations with various testing forces were performed (see Section 2.6.1 and Figure 2.12) .

The as-cast alloy displays cracks at the lowest load (2.94 N), and P_{crit} can be estimated as 2.26 N. Since the material has a fairly uniform element distribution and microstructure, as typical of as-cast HEAs, brittle cracks propagate in the volume over large distances. The annealed sample, on the other hand, has a more resilient grain structure due to scandium segregation, which inhibits crack propagation in the matrix: the annealed alloy does not show crack formation at moderate loads (below 10 N) and above 10 N only small asymmetric cracks can be detected. Therefore, P_{crit} can be estimated as 10 N approximately. Higher hardness (1.5 times greater) and critical load (at least 4 times greater), combined with suppressed crack propagation, make the annealed alloy more mechanically stable in comparison with the as-cast alloy.

The as-cast, annealed and quenched AlCrCuScTi alloy microstructures are presented in Figure 3.1, 3.4 and 3.2 respectively.

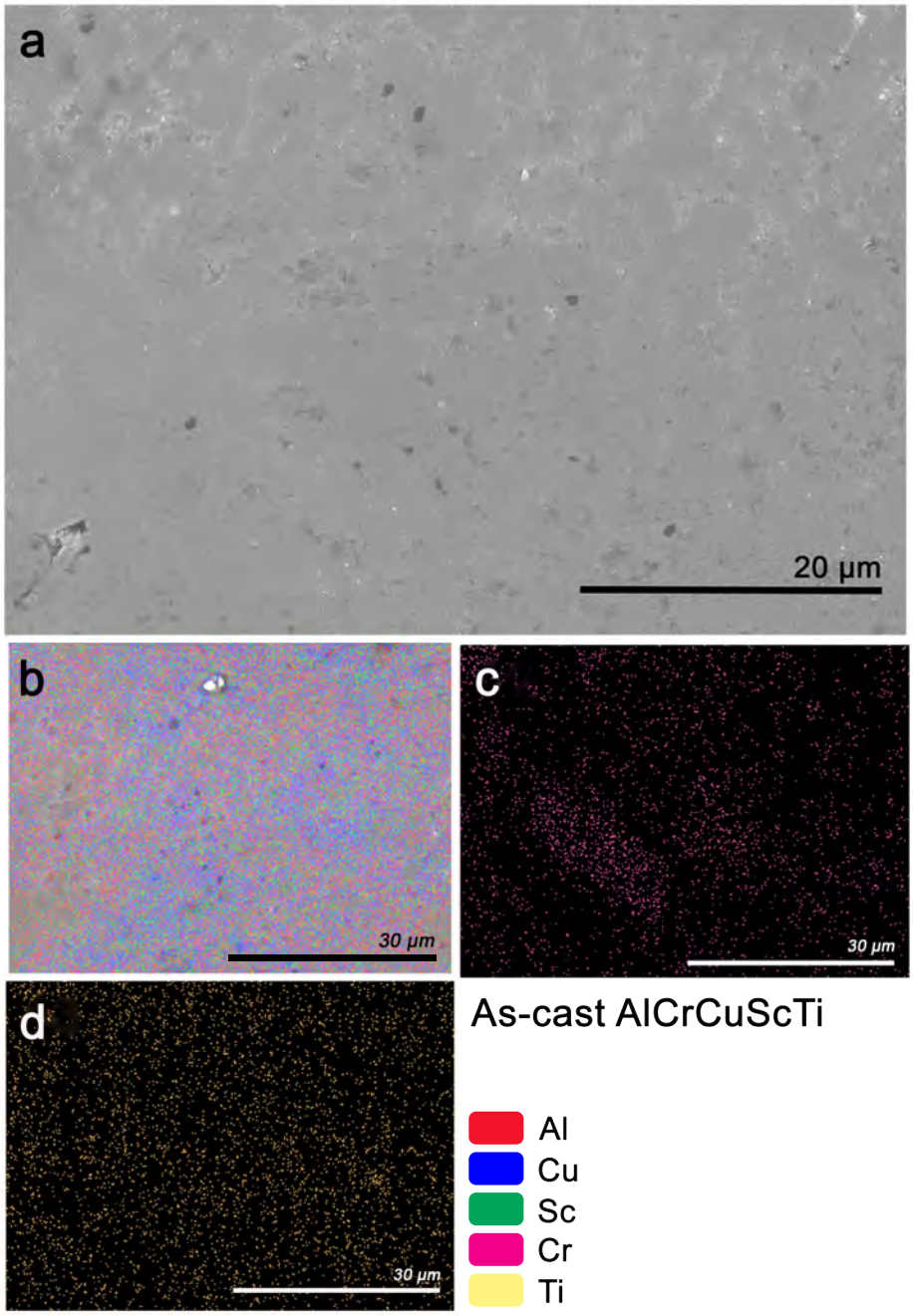

Figure 3.1: SEM images (a) of as-cast AlCrCuScTi alloy. Al, Cu and Sc distributions from EDS maps are highlighted in red, blue and green respectively in (b). The distribution of Cr (c) and Ti (d) are reported in pink and orange respectively [251].

The as-cast alloy presents a flat fairly homogeneous matrix with small precipitates in the upper part of the image (Figure 3.1, a). The features highlighted by SEM do not have an immediate correspondence in the EDX maps, whose element distribution appear homogeneous (Figure 3.1 b, c and d). The absence of obvious micro-structural features is typical for as-cast HEAs [82].

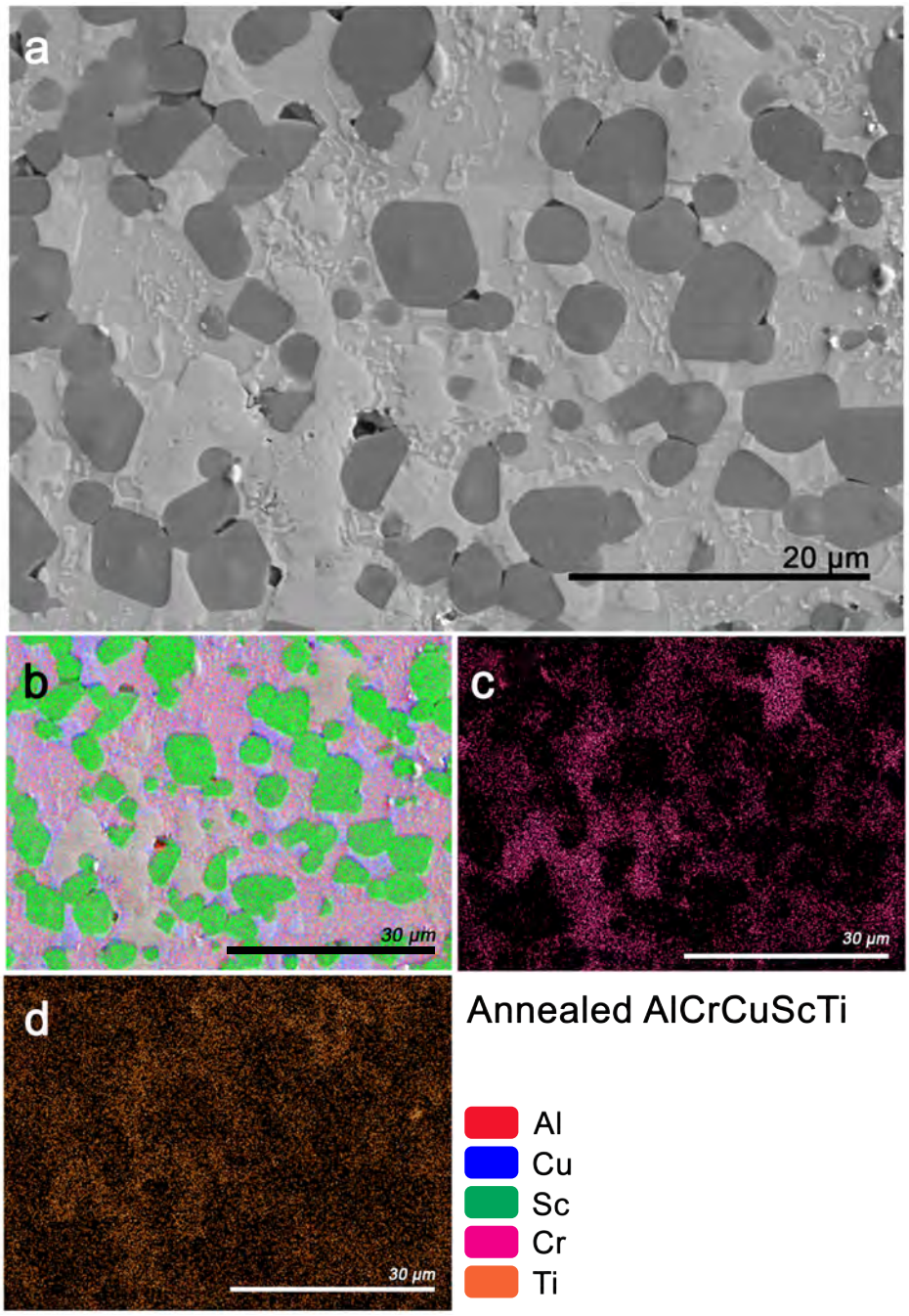

Figure 3.2: SEM images (*a*) of annealed AlCrCuScTi alloy. Al, Cu and Sc distributions from EDS maps are highlighted in red, blue and green respectively in (*b*). The distribution of Cr (*c*) and Ti (*d*) are reported in pink and orange respectively [251].

After annealing, the alloy consists of at least three phases. Square-elliptical dark precipitates rise from a matrix containing a bright and a slightly darker phase (Figure 3.2, *a*). EDX analysis identifies the dark inclusions as being rich in scandium and clearly separated from a bright matrix of chromium and titanium. Aluminium and copper distribute quite evenly in the matrix (Figure 3.2 *b, c,* and *d*).

Indeed, atomic-force microscope equipped with scanning Kelvin probe (AFM-SKP) measurements performed between inclusions reveal the existence of a fine structure: a phase characterised by a different electrical potential grows along grain boundaries and over bigger grains (Figure 3.3).

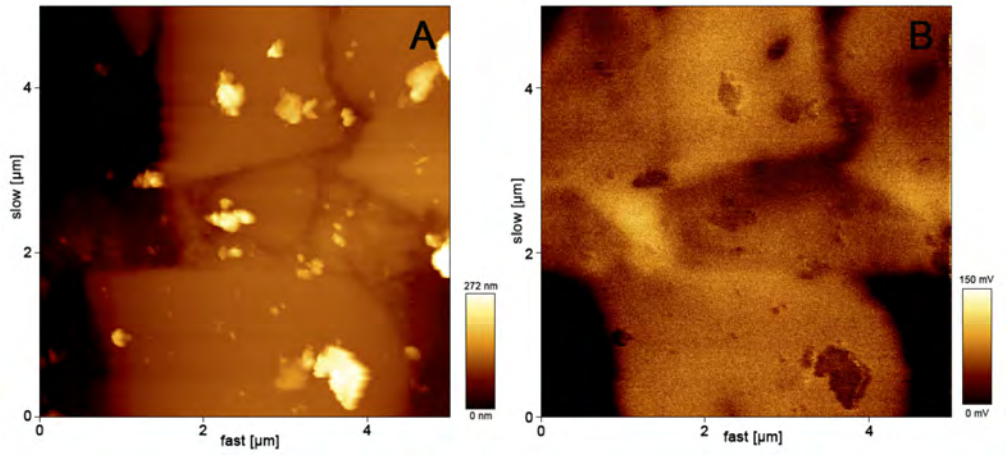

Figure 3.3: Annealed AlCrCuScTi alloy: AFM (A) and SKP (B) images [251].

In fact, few raised regions of maximum 0.7 μm in size protrude slightly from the matrix, probably due to their higher hardness and resistance to polishing. Quite interestingly, the same areas are identified in the Volta potential map as having 150 mV lower potential values.

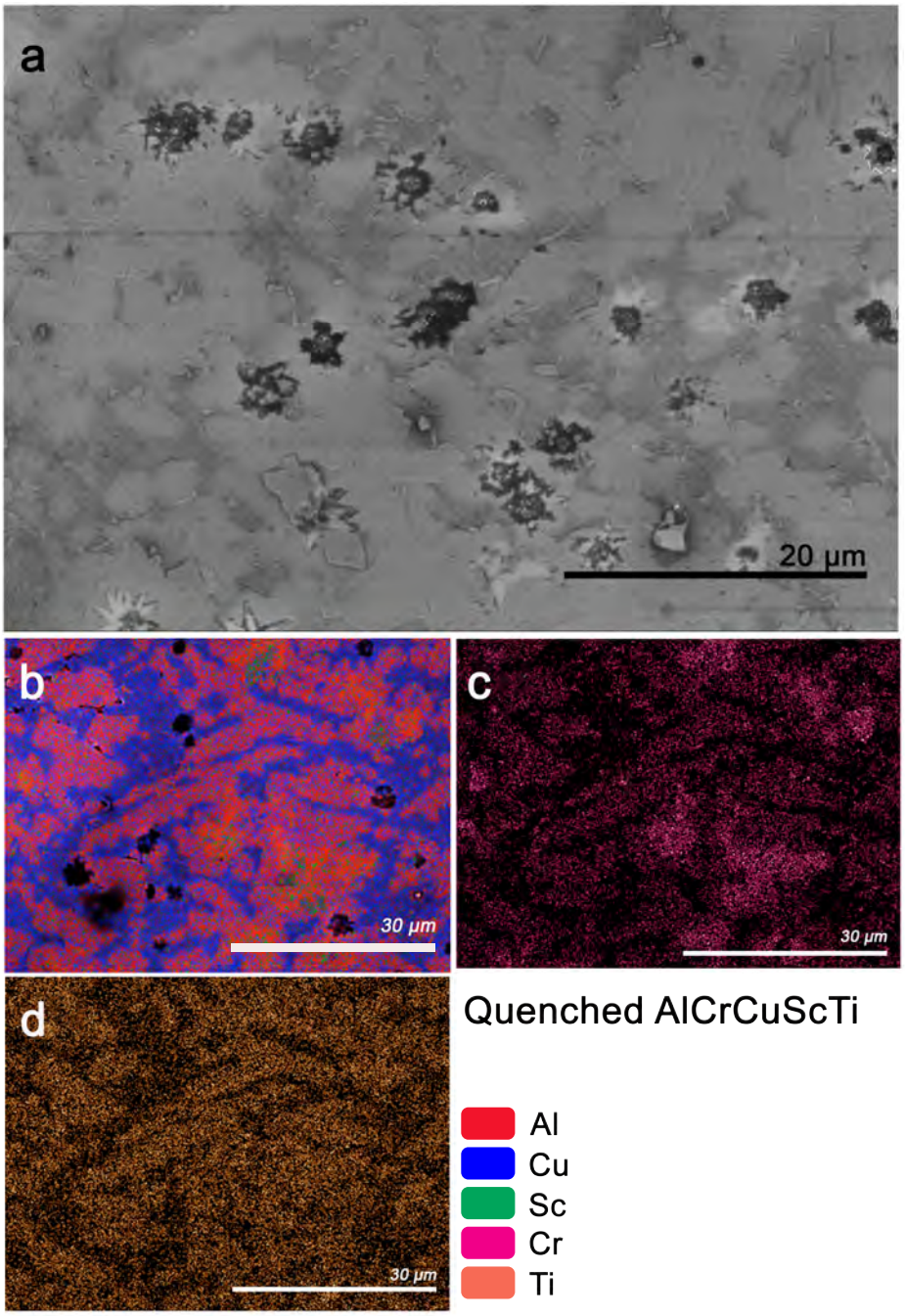

Figure 3.4: SEM images (a) of quenched AlCrCuScTi alloy. Al, Cu and Sc distributions from EDS maps are highlighted in red, blue and green respectively in (b). The distribution of Cr (c) and Ti (d) are reported in pink and orange respectively [251].

The quenched alloy shows a matrix dominated by dendrite-like structures in which numerous holes are present, probably due to the presence of brittle precipitates that were pulled out of the sample during polishing (Figure 3.4, a). EDX maps highlight the presence of two phases in the light matrix: copper segregates from titanium and chromium (Figure 3.4, c and d), whereas aluminium is found in combination with chromium and scandium (Figure 3.4, b).

It has been shown for a number of Al-based alloys containing minor Sc and Cu additions that a noticeable microstructural feature is the appearance of a ternary phase having $ThMn_{12}$-type crystal structure with lattice parameters estimated as $a = 8.63$ Å, $c = 5.10$ Å (see Section 1.1.3) [17]. Its formation and disruption after thermal annealing is responsible for the change in mechanical properties of the alloy. At the Al-rich corner of the Al–Cu–Sc ternary phase diagram, the *W*-phase forms by the combination of the Al-Cu phase (θ-phase, Al_2Cu) and the Al-Sc phase (Al_3Sc) (see Section 1.1.4) [17]. However, no studies have been performed in other regions of the Al-Cu-Sc phase diagram.

As such, the as-cast AlCrCuScTi alloy herein reported is the first example of *W*-phase formation in an over-saturated Sc alloy. The crystallisation of the AlCrCuScTi alloy from a homogeneous melt can be driven by entropy with the formation of a high-entropy alloy or by the enthalpy of formation of binary and ternary compounds, with subsequent formation of a multiphase system. The formation of the *W*-phase as a main component of AlCrCuScTi alloy suggest an enthalpy driven pathway, which can be associated with the relatively high thermodynamic stability of Al–Cu–Sc ternary phases.

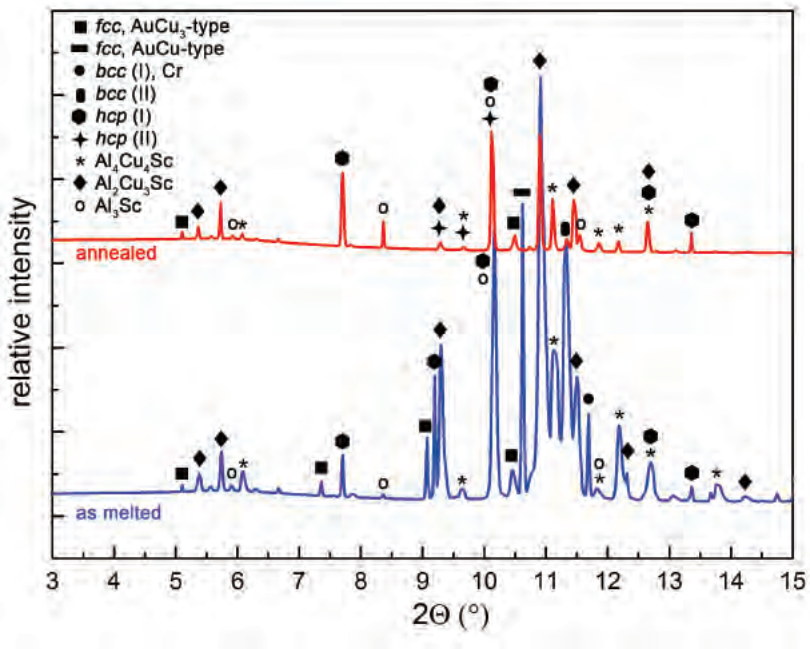

Figure 3.5: A comparison of PXRD profiles for the as-cast (*blue*) and annealed (*red*) AlCrCuScTi alloy ($\lambda = 0.4145$ Å). [251].

The XRD profile (Figure 3.5) of the as-cast alloy is dominated by cubic phases (*fcc*- and *bcc*-based alloys and partially ordered intermetallics, characterised by various cell parameters, ordering type and occupancies) and intermetallic compounds (Al_3Sc, Al_4Cu_4Sc (*W*-phase) and Al_2Cu_3Sc - a ternary phase formed in Sc excess). The existing phases are summarised in Table 3.2: despite its extremely low formation enthalpy, Sc_2O_3 is not present. The inherent

complexity of the alloy makes proper indexing impossible.

Phase	**As-cast alloy**	**Annealed alloy**
Fcc $AuCu_3$-type	Yes	Traces
Fcc AuCu-type	Yes	No
Bcc (I) Cr	Yes	No
Bcc (II)	Yes	Traces
Hcp (I)	Yes	Yes
Hcp (II)	No	Yes
Al_4Cu_4Sc	Yes	Traces
Al_2Cu_3Sc	Yes	Traces
Al_3Sc	Traces	Traces

Table 3.2: Phases in the as-cast and annealed AlCrCuScTi alloy, according to PXRD profiles [251].

The W-phase appears disrupted in the quenched sample (Figure 3.4). Al and Sc segregate in the form of dendrite-like structures from the Cu matrix. Ultimately, the annealing process leads to the coalescence of Sc from these structures. The XRD profile of the annealed alloy (Figure 3.5) shows traces of the pre-existing Sc-containing ternary phases, and the formation of *hcp* alloys (a combination of Sc and Ti in different ratios).

The comparison between as-cast, annealed and quenched alloys highlights the major role played by temperature in the formation of different intermetallics. The instability of the *W*-phase is related to the high content of scandium in the sample: while Sc drives the formation of the *W*-phase in a kinetically determined reaction, its segregation pushes the disaggregation of the very same phase when the sample approaches thermodynamic equilibrium.

The formation of ternary Al–Cu–Sc phases in an equiatomic five-component system shows an important limitation in the design of single- or nearly single-phase high-entropy alloys. The crystallisation of ternary compounds with relatively high thermodynamic stability causes the formation of multiphase composites. It would seem that the formation of stable ternary compounds is preferable and cannot be suppressed by configurational entropy.

The implications of these findings for the use of scandium as alloying element in HEAs will be combined from those presented in the following pages and discussed in depth in Section 3.1.3.

3.1.2 Results: Equi-molar alloys springing from the Co–Gd–Sc–Ti–Y–Zr phase diagram

The aim of this work has been to prepare a combinatorial library of multi-principal component alloys containing only high-temperature melting *hcp*-structured metals through induction melting and then identify hexagonally-structured single-phase solid solutions. Though structurally similar, *fcc* elements were not included [127]. The chosen metals, combined in equal

atomic concentrations, were Co, Gd, Sc, Ti, Y and Zr.

Seven High-Entropy Alloys containing 5 or 6 *hcp*-structured elements were prepared by induction melting (Table 3.3). All samples are multiphase and contain at least one *hcp* phase (Figure 3.16). Due to the large difference in atomic radius and electronegativity among the elements, only a few of them form solid solutions while several form stable intermetallic compounds.

Element	Atomic number	Atomic radius	Lattice constant, Å		Pauling electronegativity	T_m, °C
			a	c		
Cobalt	27	1.25	2.5061	4.0695	1.7	1495
Gadolinium	64	1.79	3.6330	5.7739	1.2	1312
Scandium	21	1.64	3.2899	5.2529	1.3	1539
Titanium	22	1.46	2.9509	4.6826	1.5	1670
Yttrium	39	1.81	3.6474	5.3706	1.2	1526
Zirconium	40	1.60	3.2312	5.1477	1.4	1850

Table 3.3: Parameters of elements adopting *hcp*-structure used to produce the HEA library.

To examine temperature-induced effects in melted compositions and equilibrated systems, as-cast and thermally annealed samples (900 °C, 12 hours in dynamic vacuum 10^{-2} Pa) were investigated. All samples appear to be multi-phase both before and after annealing, with annealing affecting microstructure and mechanical properties of the alloys, but having relatively low impact on element distributions.

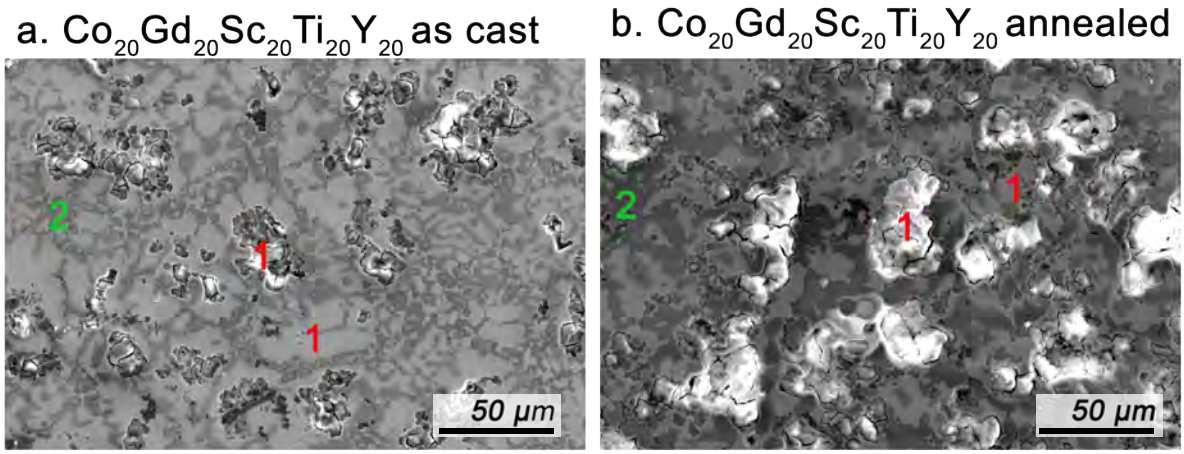

Figure 3.6: SEM images of the as-cast (*left*) and annealed (*right*) $Co_{20}Gd_{20}Sc_{20}Ti_{20}Y_{20}$ alloy. Numbers highlight the regions of sensibly different composition according to EDX maps, and reported in Table 3.4.

The $Co_{20}Gd_{20}Sc_{20}Ti_{20}Y_{20}$ alloy consist of a two-phase matrix from which Gd-Y–rich brittle islands emerge. Gd and Y also make the lighter areas of the matrix, whereas the

darker one (named 2 in Figure 3.6) consists of Co, Sc and Ti. Annealing seem to cause the growth of the Gd-Y islands as they segregate further from the first-raw elements.

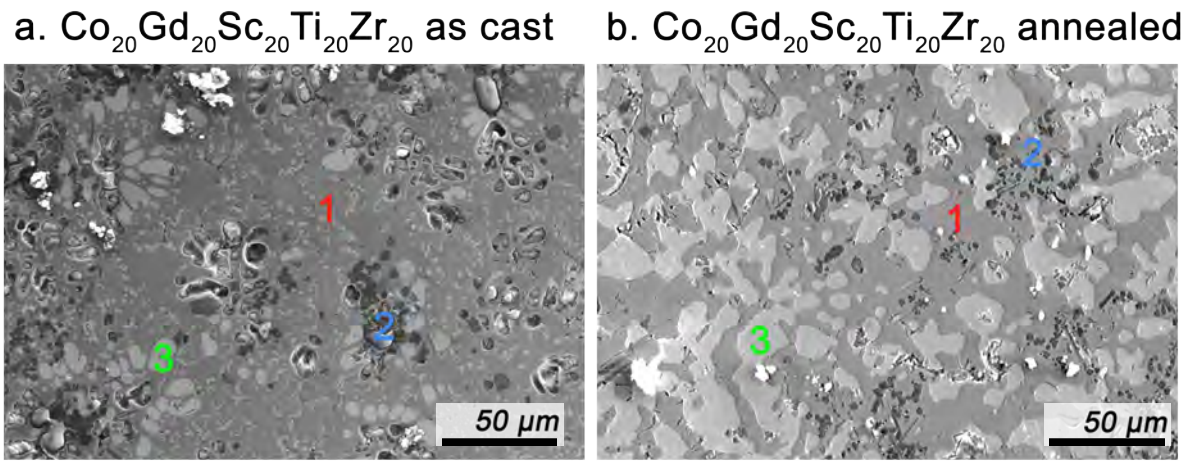

Figure 3.7: SEM images of the as-cast (*left*) and annealed (*right*) $Co_{20}Gd_{20}Sc_{20}Ti_{20}Zr_{20}$ alloy. Numbers highlight the regions of sensibly different composition according to EDX maps, and reported in Table 3.4.

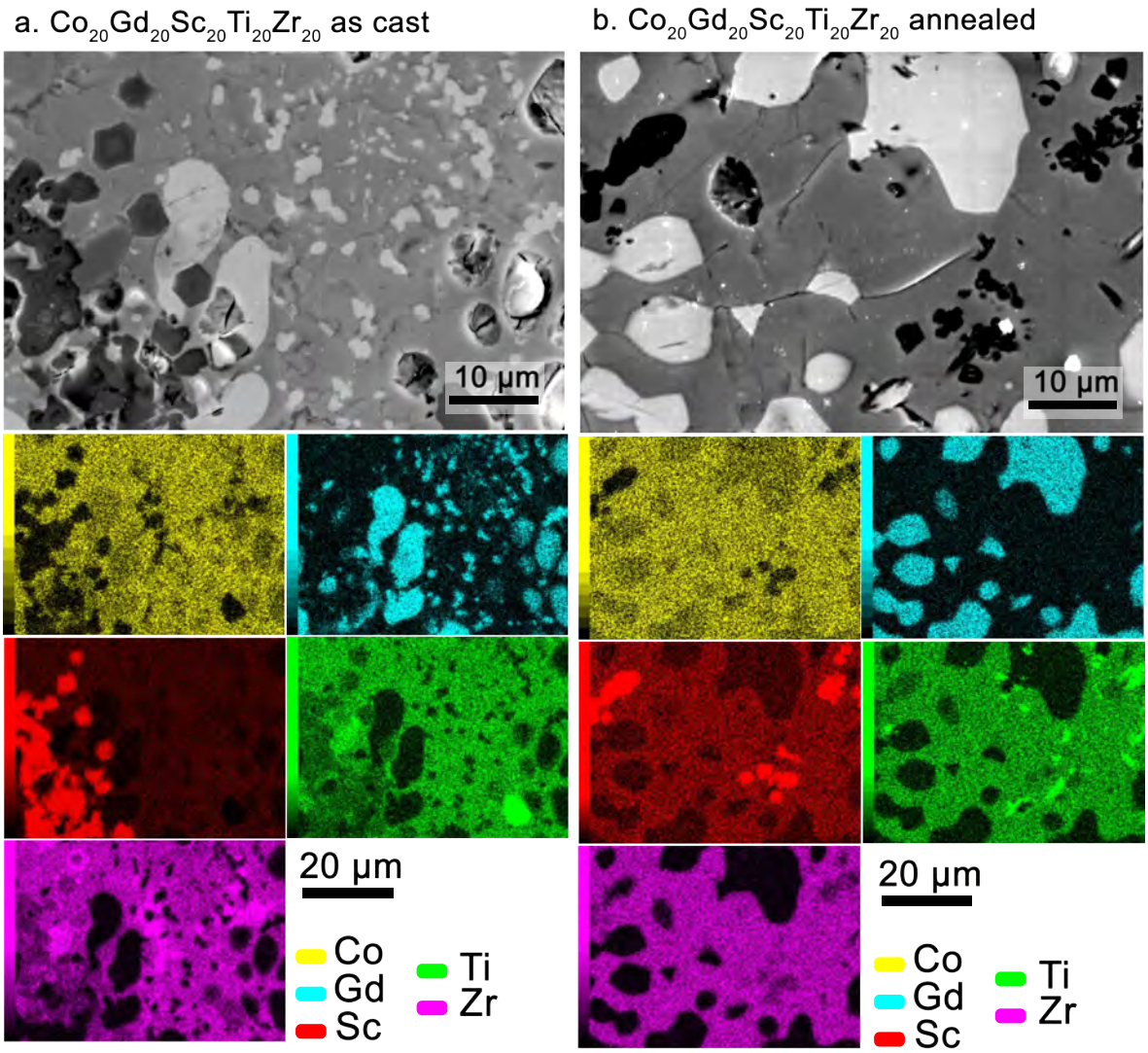

Figure 3.8: SEM and element distribution maps images of the as-cast (*left*) and annealed (*right*) $Co_{20}Gd_{20}Sc_{20}Ti_{20}Zr_{20}$ alloy.

$Co_{20}Gd_{20}Sc_{20}Ti_{20}Zr_{20}$ consists of at least three phases. Numbered as 1 in Figure 3.7 is a light gray matrix consisting of Co, Ti and Zr; the light round areas identified with number 3 are made almost entirely of Gd. Scandium is dispersed in the matrix, but also present as hexagonal dark precipitates (2). Element distribution as per EDX maps and details of the SEM structure are reported in Figure 3.8.

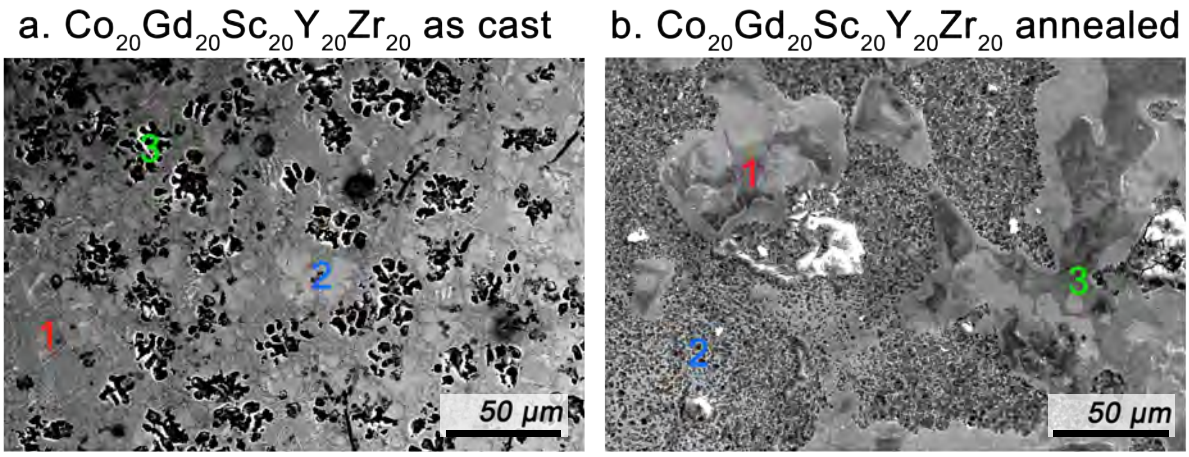

Figure 3.9: SEM images of the as-cast (*left*) and annealed (*right*) $Co_{20}Gd_{20}Sc_{20}Y_{20}Zr_{20}$ alloy. Numbers highlight the regions of sensibly different composition according to EDX maps, and reported in Table 3.4.

The $Co_{20}Gd_{20}Sc_{20}Y_{20}Zr_{20}$ alloy present significant differences both in microstructure and element distribution between before and after annealing (Figure 3.9). The as cast alloy shows a lamellae-structured matrix (1), globular light precipitates (2) and irregular black precipitates (3). The three main features correspond to sensibly different element distributions: Co-Y-Zr for the first; Gd for the second, and Sc-Y for the third. Microstructure changes drastically after annealing. The lamellae-structured areas (1) lose Y to the nano-structured matrix (2); scandium dissolves in elongated gray regions.

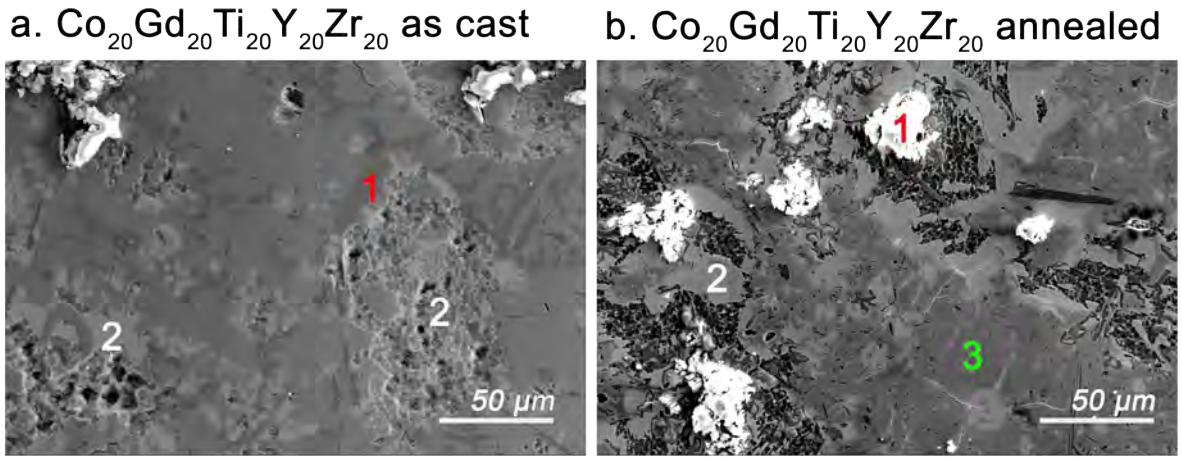

Figure 3.10: SEM images of the as-cast (*left*) and annealed (*right*) $Co_{20}Gd_{20}Ti_{20}Y_{20}Zr_{20}$ alloy. Numbers highlight the regions of sensibly different composition according to EDX maps, and reported in Table 3.4.

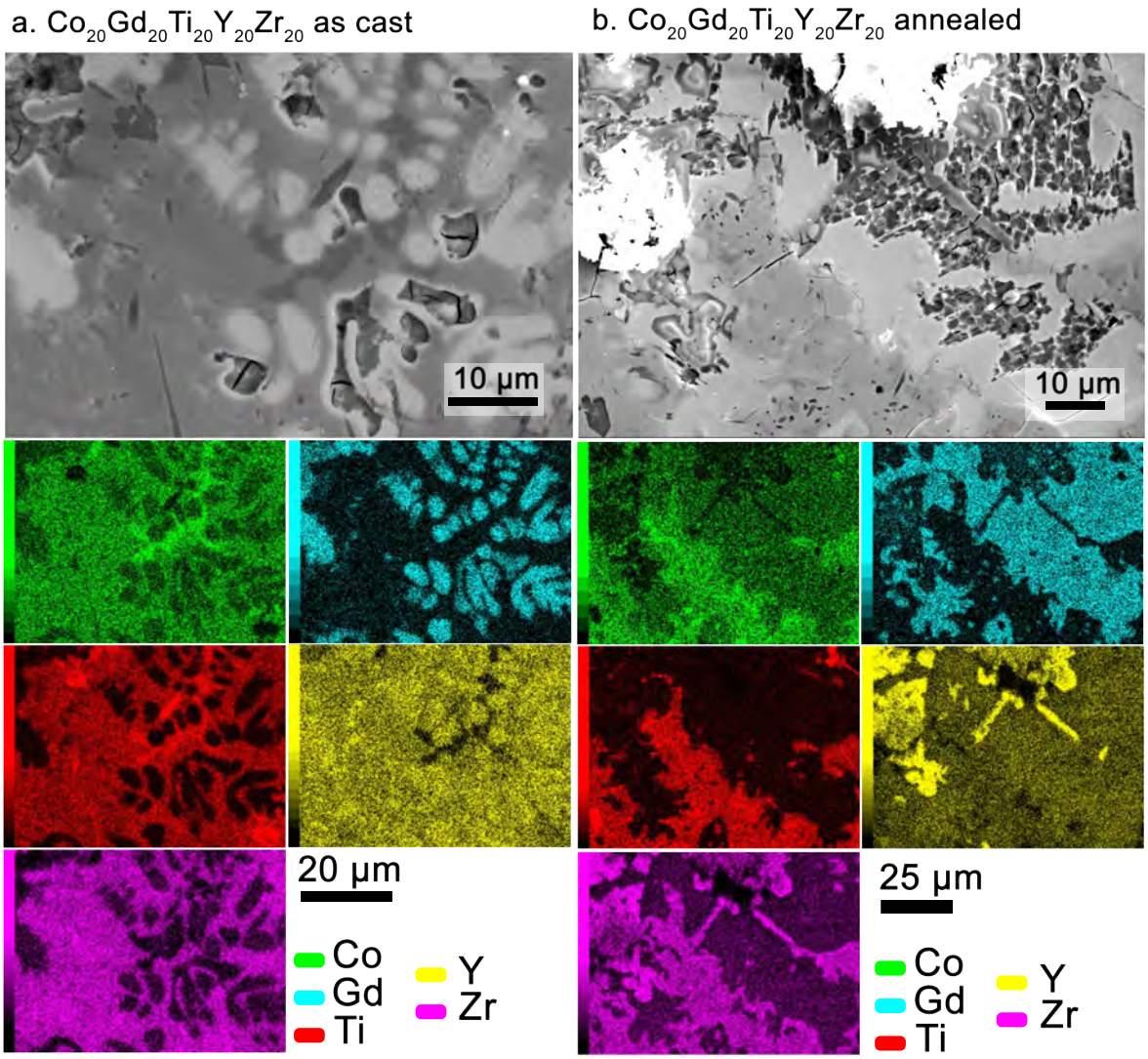

Figure 3.11: SEM and element distribution maps images of the as-cast (*left*) and annealed (*right*) $Co_{20}Gd_{20}Ti_{20}Y_{20}Zr_{20}$ alloy.

Some obvious differences also emerge between the as cast and annealed $Co_{20}Gd_{20}Ti_{20}Y_{20}Zr_{20}$ alloy (Figure 3.10). In the first, two phases are present: an elongated, dark gray one (1), and a light, circular one (2). They are rich in Co, Ti and Zr; and Gd-Y, respectively. After annealing, the microstructure become very incoherent. As Gd segregates in light-gray islands (2), Zr diffuse in the rest of the matrix with Y (3) and with Co-Ti (1).

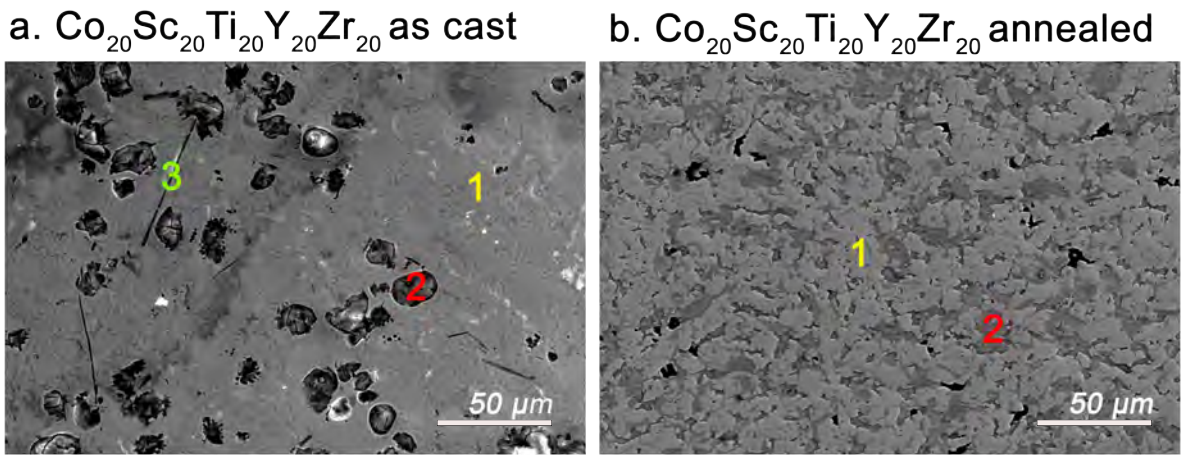

Figure 3.12: SEM images of the as-cast (*left*) and annealed (*right*) $Co_{20}Sc_{20}Ti_{20}Y_{20}Zr_{20}$ alloy. Numbers highlight the regions of sensibly different composition according to EDX maps, and reported in Table 3.4.

On the contrary, annealing of the $Co_{20}Sc_{20}Ti_{20}Y_{20}Zr_{20}$ leads to a simpler and more coherent microstructure, consisting of two intercalated phases (Figure 3.12). The as cast alloy displays a Co-Ti-Sc matrix (1) surrounding dark circular precipitates (Y-Zr). These precipitates (2) appear to be have been partly broken during polishing, leaving round valleys behind. Scandium is present in the as cast alloy as needle-like precipitates (3); which dissolve during annealing to join Y and Zr in (2).

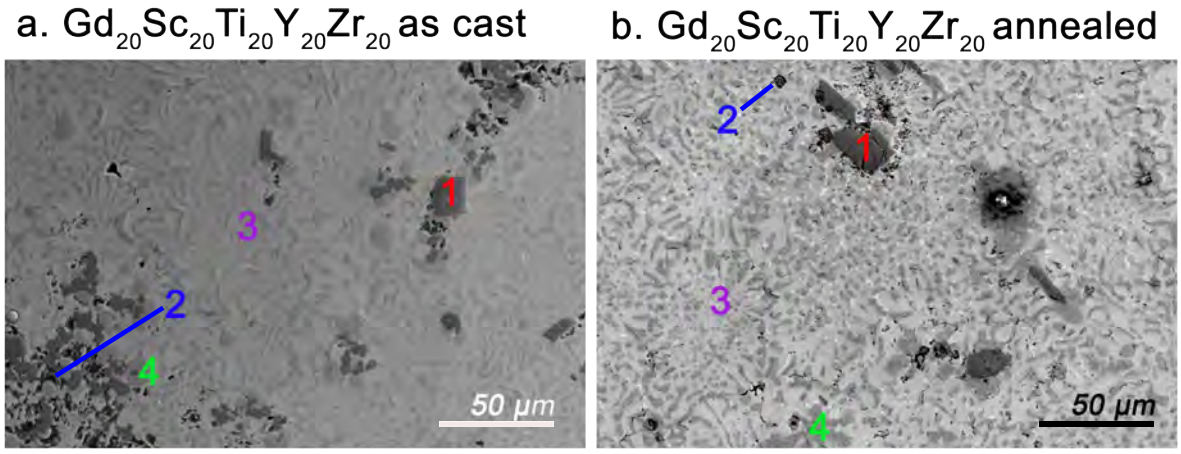

Figure 3.13: SEM images of the as-cast (*left*) and annealed (*right*) $Gd_{20}Sc_{20}Ti_{20}Y_{20}Zr_{20}$ alloy. Numbers highlight the regions of sensibly different composition according to EDX maps, and reported in Table 3.4.

The microstructure of the $Gd_{20}Sc_{20}Ti_{20}Y_{20}Zr_{20}$ alloy appears very heterogeneous (Figure 3.13). The as cast specimen consists of a coral-like fibrous matrix in which two phases are intertwined: a light one (3), consisting of Gd and Y; and a gray one (4), rich in Zr. Square precipitates identified as (1) and hexagonal precipitates numbered as (2) consist almost en-

tirely of Ti and Sc respectively. Annealing causes the dark matrix phase (4) to grow slightly and refine the microstructure, by removing part of the titanium from the precipitates (1).

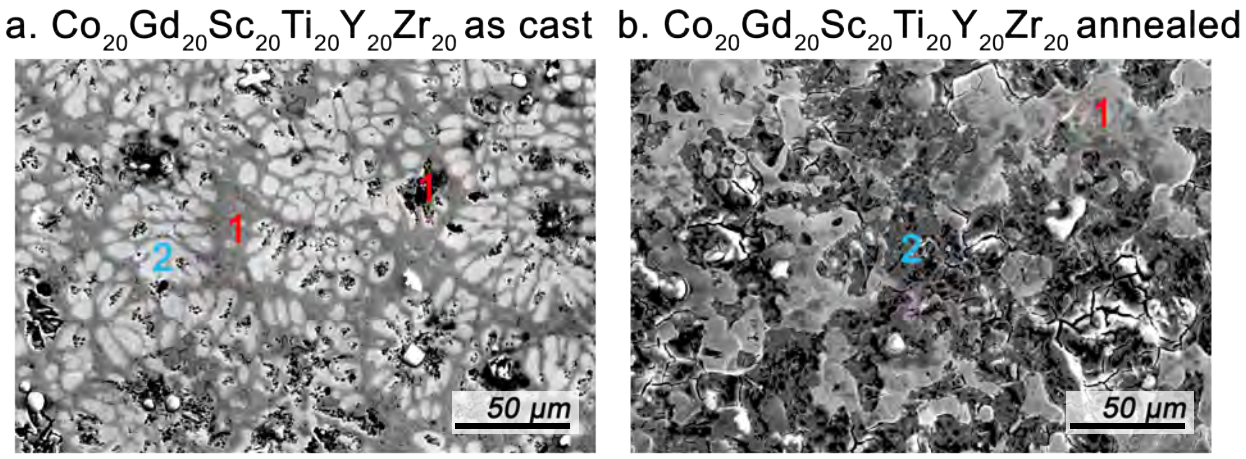

Figure 3.14: SEM images of the as-cast (*left*) and annealed (*right*) $Co_{20}Gd_{20}Sc_{20}Ti_{20}Y_{20}Zr_{20}$ alloy. Numbers highlight the regions of sensibly different composition according to EDX maps, and reported in Table 3.4.

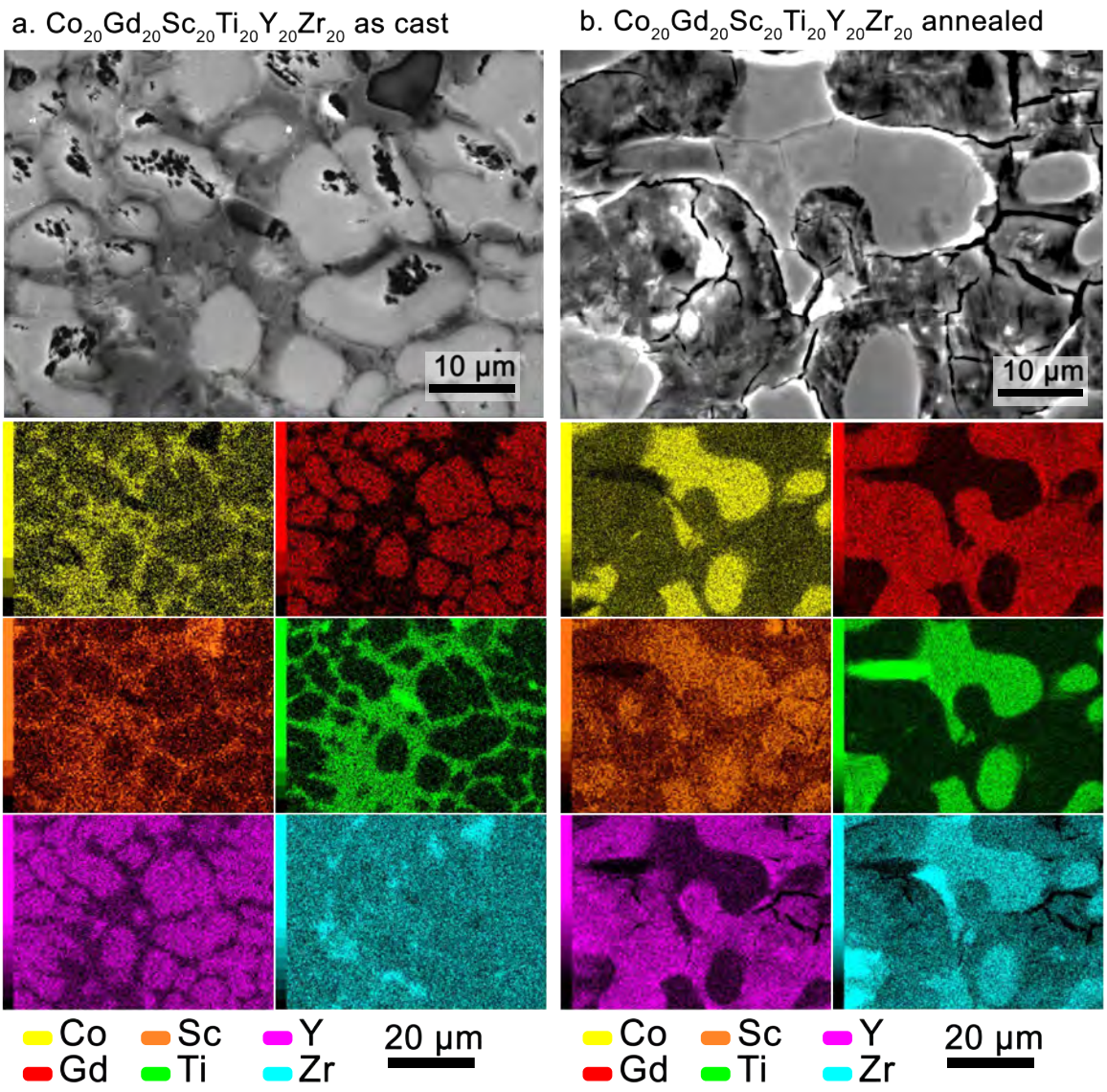

Figure 3.15: SEM and element distribution maps images of the as-cast (*left*) and annealed (*right*) $Co_{20}Gd_{20}Sc_{20}Ti_{20}Y_{20}Zr_{20}$ alloy.

The six-component as cast alloy shows a relatively simple microstructure, consisting of two phases rich in Co, Sc and Ti (1) and in Gd-Y (2) respectively (Figure 3.14). Zr is homogeneously dispersed. Annealing results in a loss of coherence in the alloy, due to the depletion of Zr from the Gd-Y region. On the contrary, Sc diffuses towards the depleted area (2). Element segregation is clearly visible in Figure 3.15.

The distribution of constituent elements as per EDX maps in the various alloys is briefly reviewed in Table 3.4. Numbers refer to the areas highlighted in each SEM figure.

Alloy	**As-cast**	**Annealed**
CoGdScTiY	1. Gd, Y	1. Gd, Y
	2. Co, Sc, Ti	2. Co, Sc, Ti
CoGdScTiZr	1. Co, Ti, Sc, Zr	1. Co, Ti, Sc, Zr
	2. Sc	2. Sc (dots)
	3. Gd	3. Gd
CoGdScYZr	1. Co, Y, Zr	1. Co, Zr
	2. Gd	2. Gd, Y
	3. Sc, Y	3. Sc
CoGdTiYZr	1. Co, Ti	1. Co, Ti, Zr (some Y)
	2. Gd, Y	2. Gd (some Y)
		3. Y, Zr
CoScTiYZr	1. Co, Sc, Ti	1. Co, Ti
	2. Y, Zr	2. Sc, Y, Zr
	3. Sc (lines)	
GdScTiYZr	1. Ti	1. Ti
	2. Sc (dots)	2. Sc (squares)
	3. Gd, Y	3. Gd, Y
	4. Zr	4. Ti, Zr
CoGdScTiYZr	1. Co, Sc, Ti, Zr	1. Co, Sc, Ti, Zr
	2. Gd, Y, Zr	2. Gd, Y, Sc

Table 3.4: Distribution of elements as per EDX maps. Numbers refer to the areas highlighted in each figure.

In the six-component alloy the two phases Co–Sc–Ti–Zr and Gd–Y–Sc co-exist and scandium is homogeneously dispersed in the matrix. We can therefore deduce that the formation of a scandium-containing single-phase solid solution is deeply affected by the balance between atomic size and chemical similarity. If the former prevails, scandium mixes preferably with Ti and Zr. If chemical similarity between scandium and rare-earth metals dominates, Sc dissolves in Y and Gd. The formation of the Sc–Ti–Zr solid solution is consistent to the reported HfScTiZr single-phase *hcp* alloy [163], whereas, to the authors' knowledge, the Gd–Y–Sc solid solution has never been used as the starting point for the development of a multi-component single-phase system. Indeed, even knowledge about *hcp*-metals ternary phase diagrams is still fragmented: the intrinsic complexity of some of these binary phase diagrams, which contain a huge variety of intermetallic compounds, poses a challenge to the exploration of the hyper-dimensional composition space. In fact, out of all possible combinations with Co, Gd, Sc, Ti, Y and Zr, only an isothermal section (T =773 K) of the Co–Gd–Ti phase diagram has been investigated [253].

Yttrium disperses in the matrix homogeneously only in the absence of scandium (Figure 3.10). This result might appear unexpected, as yttrium and scandium are often considered

chemically interchangeable and because the binary Sc–Y phase diagram displays complete miscibility in both solid and liquid states. However, it is just a confirmation of the fact that HEAs present a new type of metallurgy, and simple binary and ternary phase diagrams are not enough to construct a 5-6 elements phase diagram [254]. Indeed, this result suggests that the addition of Y to Sc–Ti–Zr would not lead to a single-phase four-component alloy, but rather to the segregation of Sc–Y-rich areas in a Sc–Ti–Zr matrix.

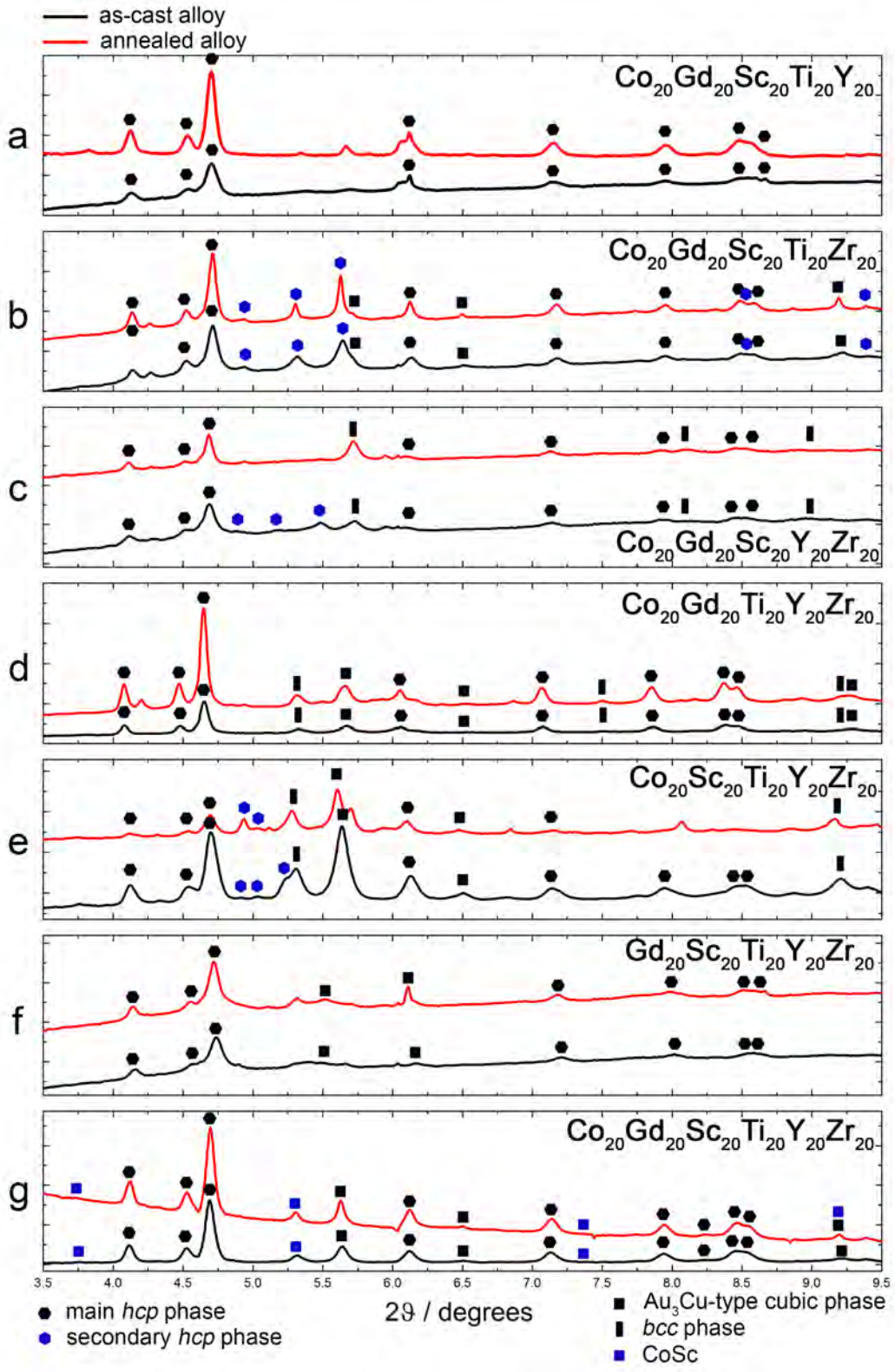

Figure 3.16: Powder X-Ray Diffraction patterns ($\lambda = 0.22542$ Å) of the as-cast (*black*) and annealed (*red*) alloys. Lines corresponding to primary and secondary phases are marked.

Alloy composition	Main phase ($P6_3/mmc$) cell parameters, Å	Secondary phase(s) cell parameters, Å	Vicker's Hardness, HV	
			As-cast	Annealed
CoGdScTiY	a=3.62(2); c=5.70(3)	unindexed phase(s)	218(28)	186(29)
CoGdScTiZr	a=3.61(2); c=5.71(3)	$P6_3/mmc$ (a=3.03(2); c=4.80(3))	345(35)	318(145)
		$Pm\bar{3}m$ (a= 3.96(2))		
CoGdScYZr	a=3.62(3); c=5.71(1)	$Im\bar{3}m$ (a=3.20(1))	257(15)	233(41)
		$P6_3/mmc$ (a=3.05(2); c=5.00(3))		
CoGdTiYZr	a=3.65(7); c=5.76(4)	$Pm\bar{3}m$ (a=3.94(5))	251(72)	429(85)
		$Im\bar{3}m$ (a=3.44(3))		
CoScTiYZr	a=3.62(9); c=5.71(2)	$P6_3/mmc$ (a=3.02(2); c=4.90(3))	358(23)	825(47)
		$Pm\bar{3}m$ (a=3.97(1))		
		$Im\bar{3}m$ (a=3.44(3))		
GdScTiYZr	a=3.59(3); c=5.66(3)	$Pm\bar{3}m$ (a=4.15(3))	289(22)	174(22)
CoGdScTiYZr	a=3.62(2); c=5.70(3)	$Pm\bar{3}m$ (a=3.97)	269(31)1	188(38)
		CoSc $Pm\bar{3}m$ (a=3.435(1))		

Table 3.5: Phase composition from synchrotron PXRD profiles and Vicker's hardness values (1 HV load) before and after annealing.

The PXRD patterns of the as-cast and annealed alloys are very complex and show several crystalline phases (Figure 3.16 and Table 3.5). The broad diffraction lines characteristic for *hcp*-structured alloys might mask several phases with close cell parameters. In all cases an *hcp*-structured alloy has been detected as the main phase, with two or more cubic phases (Au_3Cu and *B2* structure types) as minor admixtures. The PXRD profile for CoGdScTiYZr (Figure 3.16, *g*) also shows lines corresponding to the CoSc intermetallic phase ($Pm\overline{3}m$, a= 3.435 Å). For CoGdScYZr, heat treatment results in the dissolution of the secondary *hcp* phase (probably pure Gd, which goes to enrich the Gd–Y–Sc phase), which could explain its low decrease in hardness in comparison with other alloys. Other lines in the profiles are too broad to be indexed.

As far as mechanical properties are concerned (Table 3.5), Vicker's hardness values refer to the alloys overall compositions and microstructures. Such values are lower than those found in the literature for known HEAs, and generally drop after heat treatment. Exceptions are the CoScTiYZr alloy, which shows remarkably high Vicker's hardness after annealing (825(47) HV), and the CoGdTiYZr alloy, which displays a 50% hardness enhancement. The increase in hardness might be due to the presence of the same intermetallic, of crystal structure $Im\overline{3}m$ (a = 3.44(3) Å). All alloys present high brittleness and crack formation under relatively low load.

3.1.3 Discussion

The results reported in Sections 3.1.1 and 3.1.2 highlight the importance of scandium as compound-forming element.

In the AlCrCuScTi alloy, three Sc-containing phases precipitate upon cooling; that is Al_4Cu_4Sc, Al_2Cu_3Sc and Al_3Sc. Their stability is temperature-dependent. Quenching of the alloy from the melt and annealing of the as-cast specimen both show segregation of the constituent elements of the phases, hinting to the Al–Cu–Sc phases formation being a kinetically-driven process (as opposed to the thermodynamic equilibrium reached after annealing). The relatively low stability of the ternary phase might correspond to a relative minimum in the free energy of the system; in other words, it represents a metastable state. If we assume that the alloy system is in internal equilibrium at an energy state higher than its absolute minimum (the stable state), the high temperature used during the annealing step is necessary to overcome the energy barrier of the relative minimum and eventually reach the stable state.

The formation of intermetallic phases in the equiatomic five-component system shows an important limitation in the design of single- or nearly single-phase high-entropy alloys. The cooling rate is pivotal in favouring or inhibiting the formation of metastable phases, and any annealing process should be properly tuned in order to disrupt unwanted phases. Unfortunately, as clearly showed by the AlCrCuScTi case study, the disruption of intermetallics does not necessarily coincide with the formation of a solid solution. For example, the Sc–Ti phase diagram shows complete miscibility in liquid state, which would suggest high mixing entropy - but the annealed specimen clearly displays scandium segregation from the matrix.

Similarly, high-entropy effect and high mixing enthalpy of scandium with titanium and yttrium in the investigated *hcp* systems cannot effectively inhibit the formation of intermetallic compounds (e.g. CoSc in the CoGdScTiYZr alloy). Conversely, their formation is favoured by the difference in atomic size and electronegativity between the elements. They also display higher thermal stability with respect to the Al–Cu–Sc phase: while annealing affects microstructure and mechanical properties, it has low impact on elemental distribution and phases' nature.

As mentioned in Section 1.1.1, scandium is grouped with RE elements, but often presents strong similarities with lighter metals (especially beryllium). Its peculiar features are generally ascribed to the presence of a single electron in its *d*-orbitals - a somewhat unsatisfying explanation [11]. The dual nature of scandium - first-raw *d*-metal and RE element - is clearly shown by the CoGdScTiYZr alloy.

In the six-component alloy the two phases Sc–Ti–Zr and Gd–Y–Sc co-exist and scandium is homogeneously dispersed in the matrix. If atomic size affinity prevails, scandium mixes preferably with Ti and Zr. If chemical similarity between scandium and rare-earth metals dominates, Sc dissolves in Y and Gd. Moreover, yttrium and scandium are often considered chemically interchangeable and the binary Sc–Y phase diagram displays complete miscibility in both solid and liquid states. However, Y is homogeneously dispersed in the matrix only in absence of scandium. This result suggests that the addition of Y to Sc–Ti–Zr would not lead to a single-phase four-component alloy, but rather to the segregation of Sc–Y-rich areas in a Sc–Ti–Zr matrix.

The body of findings supports the hypothesis of scandium as a compound-forming element even in multi-principal components alloy. Its formation of stable ternary compounds is favoured by enthalpy and cannot be suppressed by configurational entropy.

As such, scandium is unlikely to form single-phase solid solutions with other metals and is thus unsuitable for the development of single-phase HEAs through the traditional casting routes. Nevertheless, different synthetic pathways, such as mechanical alloying, might inhibit precipitation of intermetallics and other diffusion-driven side-reactions and eventually lead to a single-phase metastable alloy [66].

3.2 Scandium additions to High-Entropy Alloys

In the previous section we highlighted the role of scandium as active alloying element for multi-principal components alloy, and reported the formation of stable intermetallics in spite of the high configurational entropy of such alloys.

In this section we investigate the effect of small scandium additions to model HEAs, namely $Al_2CoCrFeNi$, $Al_{0.5}CoCrCuFeNi$ and $AlCoCrCu_{0.5}FeNi$. After a detail characterisation of these alloy, we will move on to study the consequences of scandium additions to microstructure, mechanical properties and phase stability. In particular, we will focus on phase transformations occurring upon pressure and temperature.

The implications of these findings will be discussed in Section 3.2.3.

3.2.1 The scandium effect in aluminium-containing High-Entropy Alloys

Characterisation of the $Al_2CoCrFeNi$, $Al_{0.5}CoCrCuFeNi$ and $AlCoCrCu_{0.5}FeNi$ HEAs

The $Al_2CoCrFeNi$, $Al_{0.5}CoCrCuFeNi$ and $AlCoCrCu_{0.5}FeNi$ HEAs were synthesized via induction melting in the atomic compositions reported in Table 3.6 (as per EDX analysis).

	$Al_2CoCrFeNi$ at.%		$Al_{0.5}CoCrCuFeNi$ at.%		$AlCoCrCu_{0.5}FeNi$ at.%	
	As cast	Anneal.	As cast	Anneal.	As cast	Anneal.
Al	44.4(3)	39.5(1)	13.2(2)	6.6(3)	22.8(2)	27.5(7)
Co	14.7(2)	15.7(7)	17.9(4)	19.8(3)	17.2(5)	16.8(0)
Cr	13.6(2)	13.8(2)	16.6(6)	18.0(6)	17.6(0)	16.0(6)
Cu			16.9(4)	11.1(9)	8.6(7)	6.9(7)
Fe	14.3(4)	15.1(4)	18.5(1)	20.1(4)	17.8(4)	16.8(9)
Ni	12.8(9)	15.7(7)	17.5(2)	17.6(8)	15.8(1)	15.7(1)

Table 3.6: Atomic composition of the synthesised samples according to EDX map (x500, x2000).

Refinements of PXRD performed with synchrotron radiation highlight the presence of a secondary *fcc* phase in the *bcc*-structured $AlCoCrCu_{0.5}FeNi$ alloy (Figure 3.17) and of a very small secondary *bcc* phase in the mainly *fcc*-structured $Al_{0.5}CoCrCuFeNi$ (Figure 3.18). Unlike $Al_{0.5}CoCrCuFeNi$ and $AlCoCrCu_{0.5}FeNi$, $Al_2CoCrFeNi$ appears to be a B2-structured solid solution (Figure 3.19). The presence of the (1 0 0) super lattice peaks in the alloy profile indicates the presence of the ordered sub-lattice, generally attributed to Al and Ni [175, 255, 256].

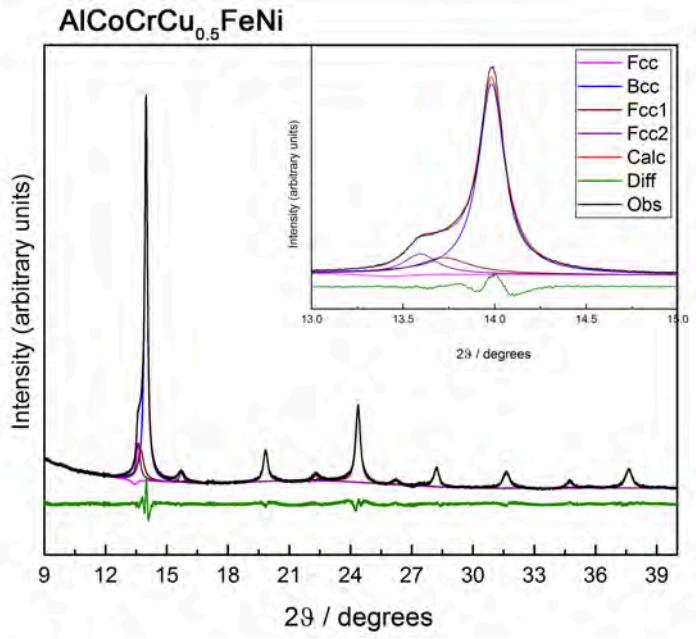

Figure 3.17: PXRD refinement performed at the DIAMOND light source (I11, $\lambda = 0.494984$ Å) of the $AlCoCrCu_{0.5}FeNi$ HEA. The section between 13 and 15 degrees is highlighted to show the asymmetry of the first peak, which can only be fitted by adding an *fcc* phase.

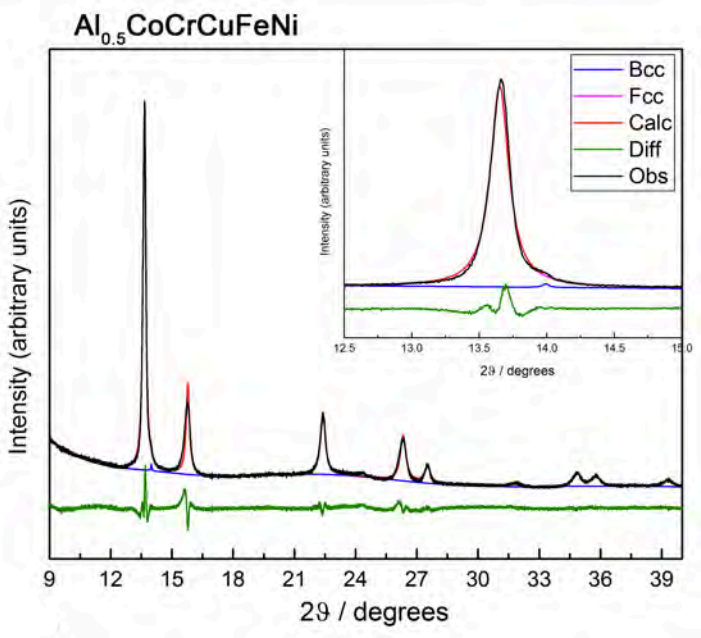

Figure 3.18: PXRD refinement performed at the DIAMOND light source (I11, $\lambda = 0.494984$ Å) of the $Al_{0.5}CoCrCuFeNi$ HEA. The section between 12.5 and 15 degrees is highlighted to show the asymmetry of the first peak, which can only be fitted by adding a small *bcc* phase.

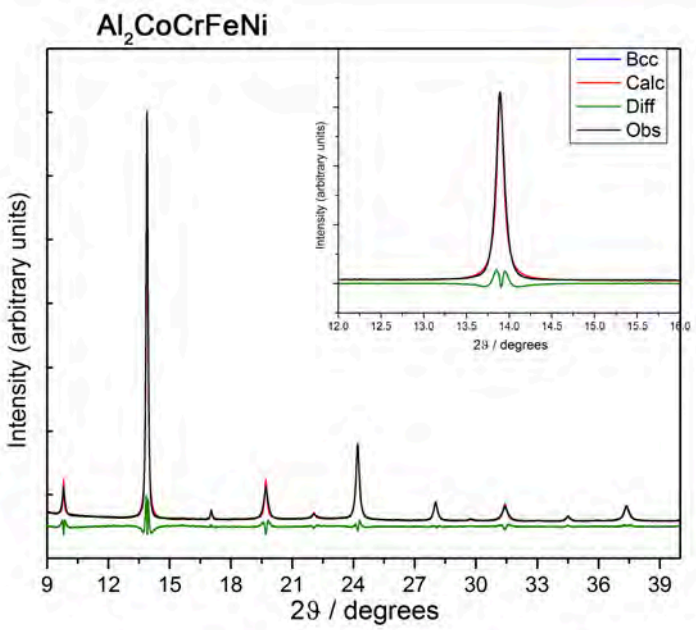

Figure 3.19: PXRD refinement performed at the DIAMOND light source (I11, $\lambda = 0.494984$ Å) of the $Al_2CoCrFeNi$ HEA. The section between 12 and 16 degrees in highlighted to show the symmetry of the first peak.

Lattice parameters of the as-cast alloys are the following:

a_{B2}: 2.877(2) Å for $Al_2CoCrFeNi$;

a_{fcc}: 3.601(1) Å for $Al_{0.5}CoCrCuFeNi$;

a_{bcc}: 2.891(3) Å for $AlCoCrCu_{0.5}FeNi$.

All values are consistent with the literature within experimental error [175, 169, 257, 258]. Small divergences among reported results arise from the high sensitivity of the HEA to synthetic pathway and to very small compositional variations. Nominally equivalent starting materials can thus lead to profoundly different crystal structures, microstructures and phase transitions.

The microstructures and elemental distributions of as-cast and annealed $Al_2CoCrFeNi$, $Al_{0.5}CoCrCuFeNi$ and $AlCoCrCu_{0.5}FeNi$ are reported in the following pages.

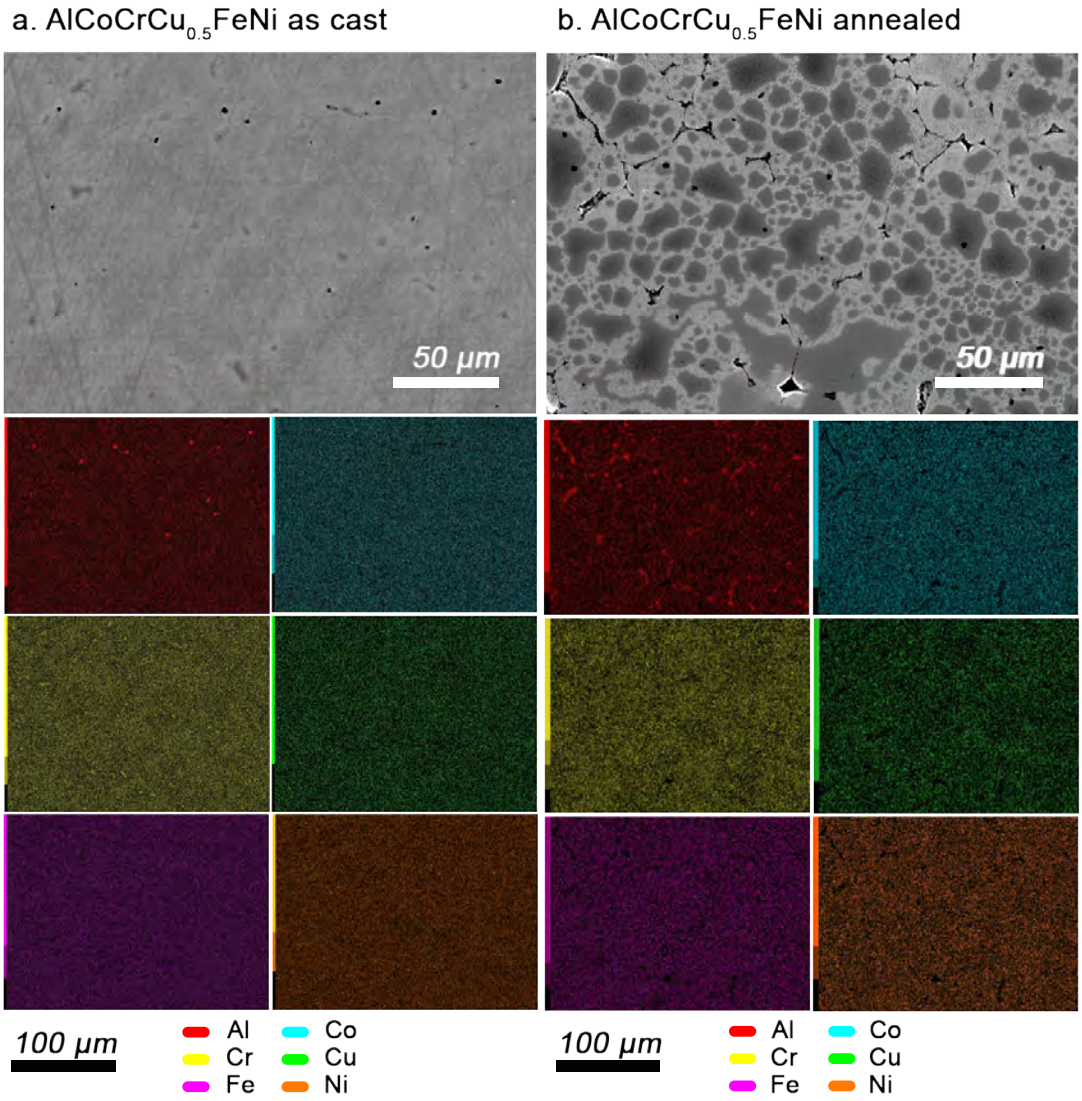

Figure 3.20: Microstructure and element distribution maps of the as-cast and annealed $AlCoCrCu_{0.5}FeNi$ alloy.

Two phases are shown by as cast the $AlCoCrCu_{0.5}FeNi$ alloy, whose microstructure is characterised by a matrix and a circular secondary phase of darker colour. Elemental distributions appear completely homogeneous (Figure 3.20). Annealing results in the growth of a sensibly darker secondary phase and the slight segregation of Al from the rest of elements.

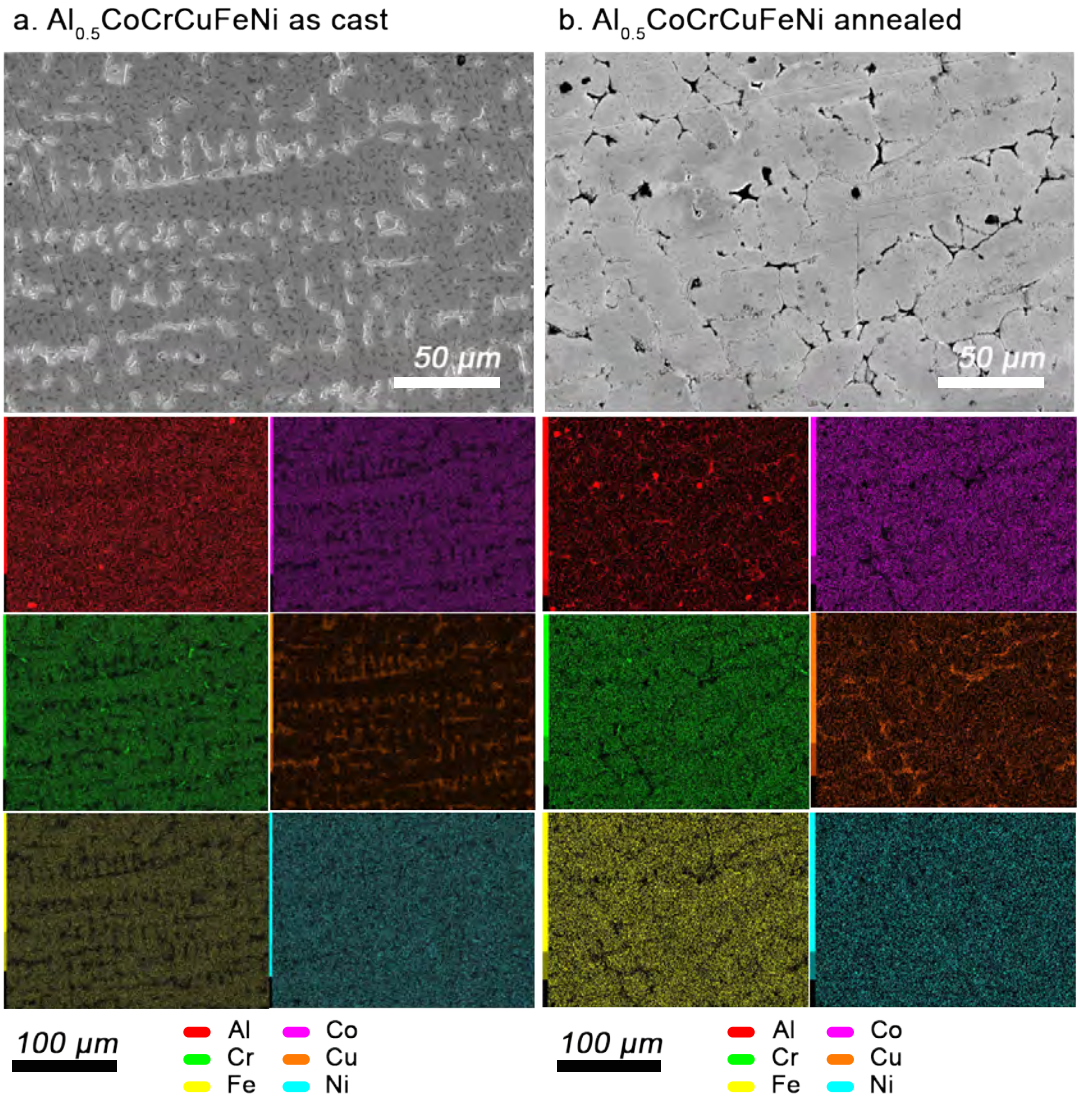

Figure 3.21: Microstructure and element distribution maps of the as-cast and annealed $Al_{0.5}CoCrCuFeNi$ alloy.

The as cast $Al_{0.5}CoCrCuFeNi$ HEA consists of dendritic-like and interdendritic-like regions, the first being richer in Co, Cr and Fe; and the latter Cu-rich (Figure 3.21). Both the dendrite and interdendrite have been previously associated to a simple *fcc* phase, and copper segregation has been explained through its high mixing enthalpy with cobalt, chromium, iron and nickel [169]. The microstructure changes drastically after annealing, as the two phases cannot be easily distinguished. Nevertheless, elements segregation persist, with Cu and Al separating from Co, Cr, Fe and Ni.

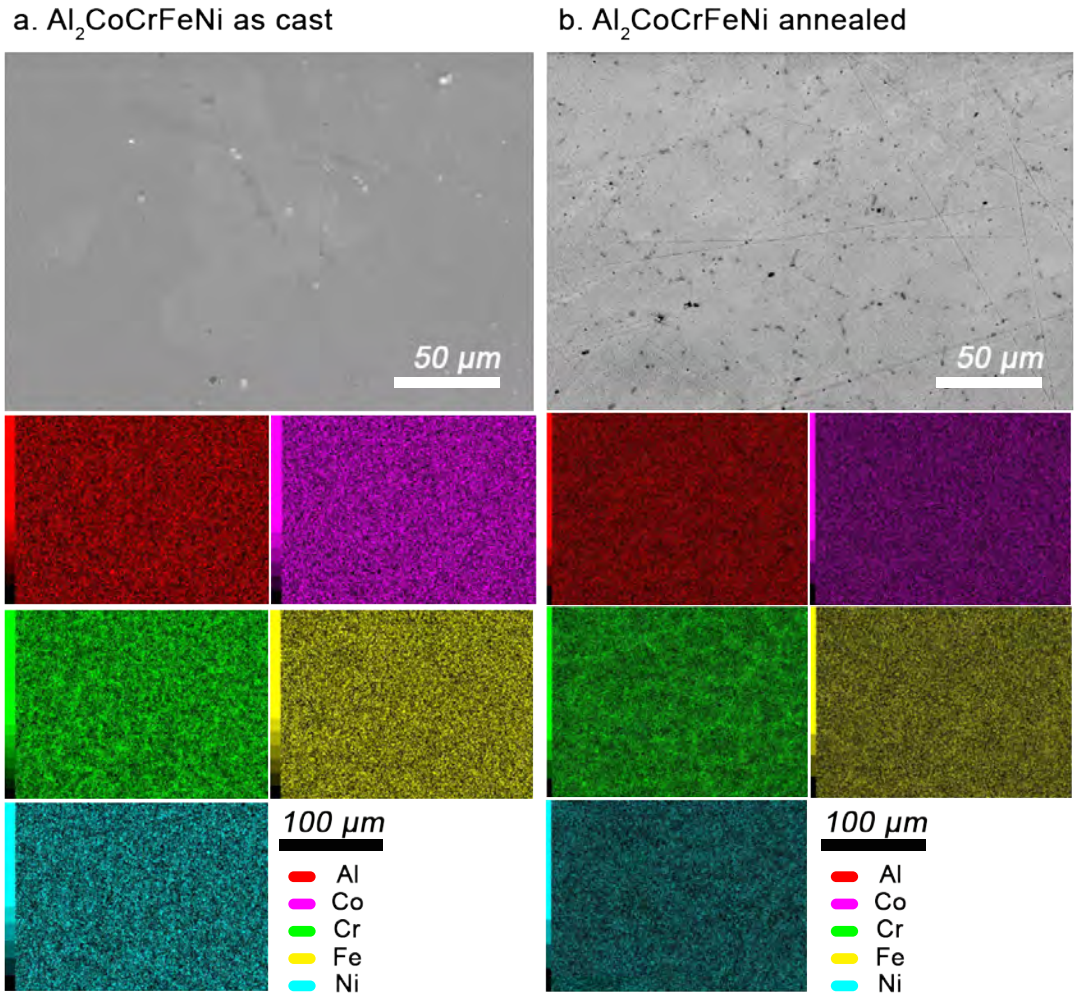

Figure 3.22: Microstructure and element distribution maps of the as-cast and annealed alloy $Al_2CoCrFeNi$.

The as cast $Al_2CoCrFeNi$ microstructure is dominated by large ($\sim$100 μm) unstructured grains which, unlike previous studies, shows no trace of non-equiaxed dendrites [176, 259]. With respect to other elements, chromium segregation is clearly visible, though it can be reduced by annealing (see Figure 3.22). On the other hand, annealing causes the formation of a homogeneously dispersed secondary phase, which appear as black dots within our instrument's resolution.

The metal's ordering and disordering has been identified by high-temperature magnetic data. The magnetisation value strongly depends on chromium, as the only antiferromagnetic element in the system. Since the ordering of a metal in medium and high entropy alloys is spin-driven, chromium ordering can be considered a way to eliminate the magnetic frustration of the antiferromagnetic-ferromagnetic interactions between nearest neighbours and thus to reduce free energy [260, 261, 255]. Annealing increases the magnetisation and makes the ferromagnetic transition more defined [262].

The scandium effect on microstructure and selected mechanical properties

The microstructure of all alloys is strongly affected by even a 3 wt.% addition of scandium (Figure 3.23).

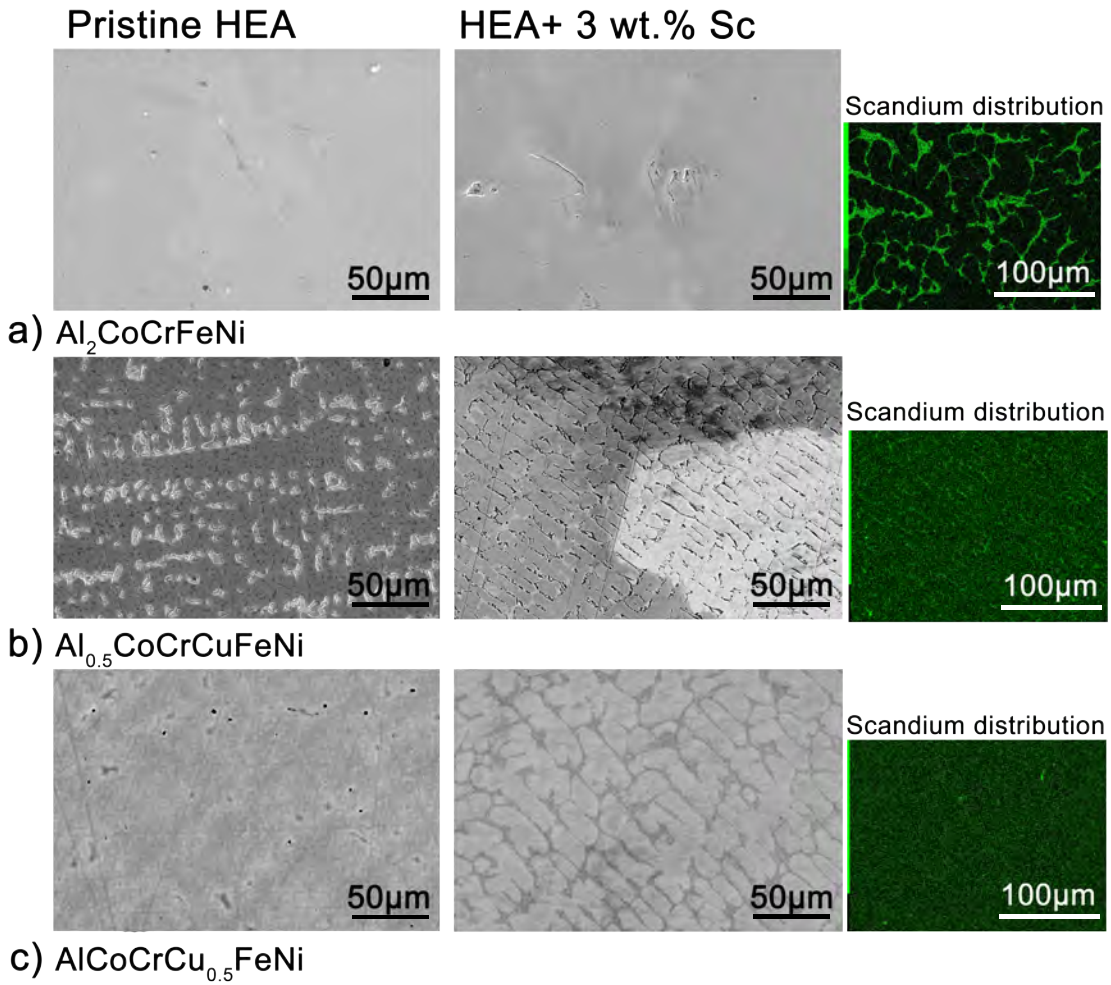

Figure 3.23: Overview of the effect of scandium addition on the microstructure of the three systems. Microstructure of the as-cast (*a*) $Al_2CoCrFeNi$, (*b*) $Al_{0.5}CoCrCuFeNi$ and (*c*) $AlCoCrCu_{0.5}FeNi$ pristine HEA and the same systems after 3 wt.% scandium addition. Scandium distribution is highlighted in the corresponding EDX maps.

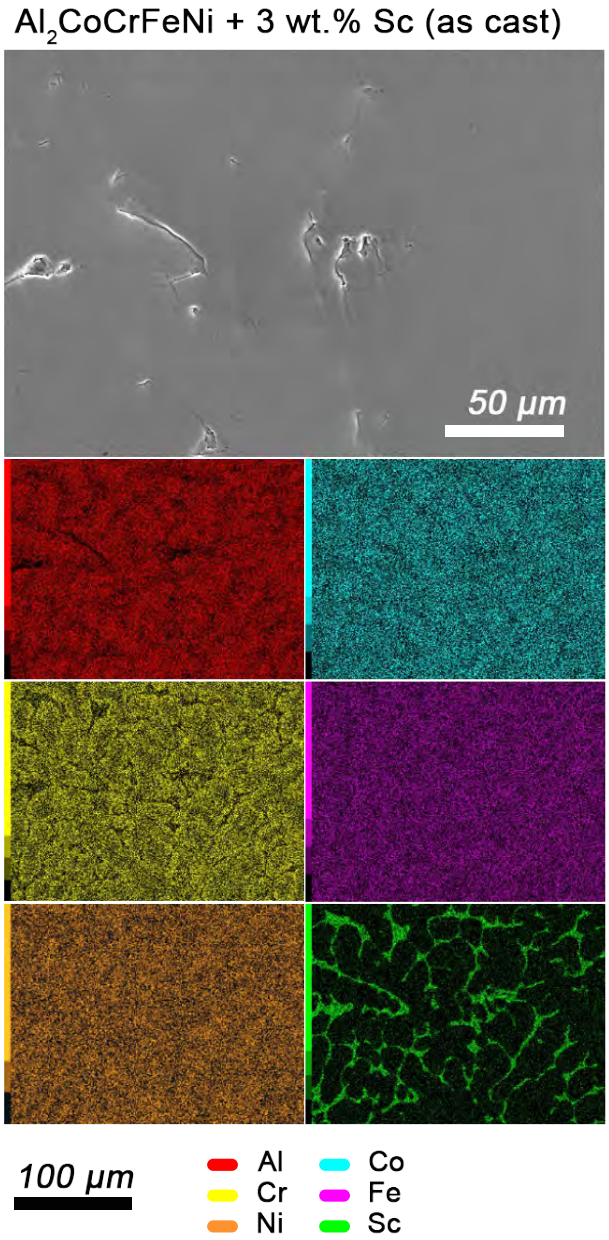

Figure 3.24: Element distributions in the as-cast $Al_2CoCrFeNi$ alloy containing 3 wt.% Sc.

In the case of $Al_2CoCrFeNi$ (Figure 3.24), the large grains of homogeneous compositions are refined and scandium segregates along the grain boundaries. Elemental distribution is mostly unchanged due to scandium addition, because the scandium-based intermetallic which forms along grain boundaries appears to contain all elements in stoichiometric quantities - with the notable exception of chromium (Table 3.7).

	$Al_2CoCrFeNi$ + Sc		$Al_{0.5}CoCrCuFeNi$ + Sc		$AlCoCrCu_{0.5}FeNi$ + Sc	
	Grain at.%	Inter-grain at.%	Grain at.%	Inter-grain at.%	Grain at.%	Inter-grain at.%
Al	29.2(6)	18.4(2)	7.2(6)	2.8(5)	10.7(1)	8.8(3)
Co	19.6(4)	16.2(8)	20.4(0)	3.2(3)	21.3(3)	10.6(0)
Cr	14.1(8)	11.1(1)	17.3(2)	1.6(5)	29.9(3)	6.3(2)
Cu			16.2(7)	75.7(4)	6.0(1)	51.8(6)
Fe	16.5(1)	17.7(1)	20.2(3)	2.4(8)	23.2(5)	8.6(1)
Ni	19.9(9)	19.4(5)	18.2(6)	10.6(5)	14.6(3)	13.0(4)
Sc	0.4(2)	17.0(2)	0.2(2)	3.4(1)	0.1(4)	0.7(5)

Table 3.7: Atomic composition of the prepared samples according to EDX map (x500, x2000).

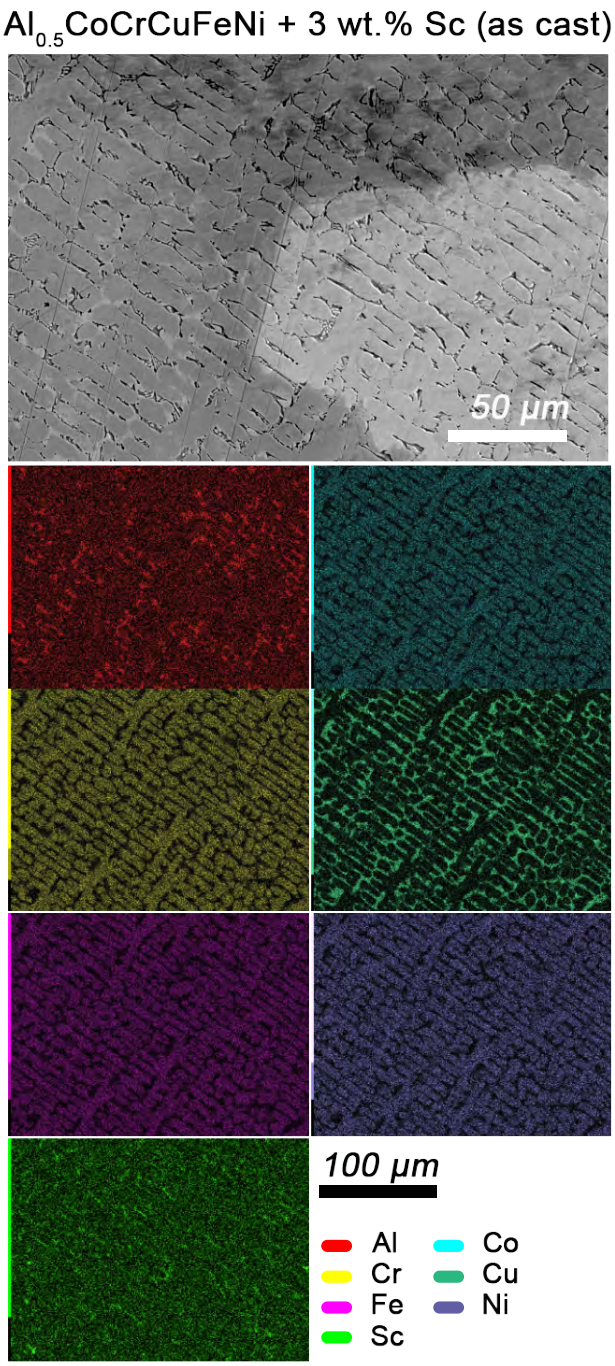

Figure 3.25: Element distributions in the as-cast $Al_{0.5}$CoCrCuFeNi alloy containing 3 wt.% Sc.

In the $Al_{0.5}$CoCrCuFeNi HEA (Figure 3.25), scandium is dispersed homogeneously and aids the formation of a globular microstructure. Nevertheless, most of it segregates along grain boundaries, with copper- and nickel-rich areas.

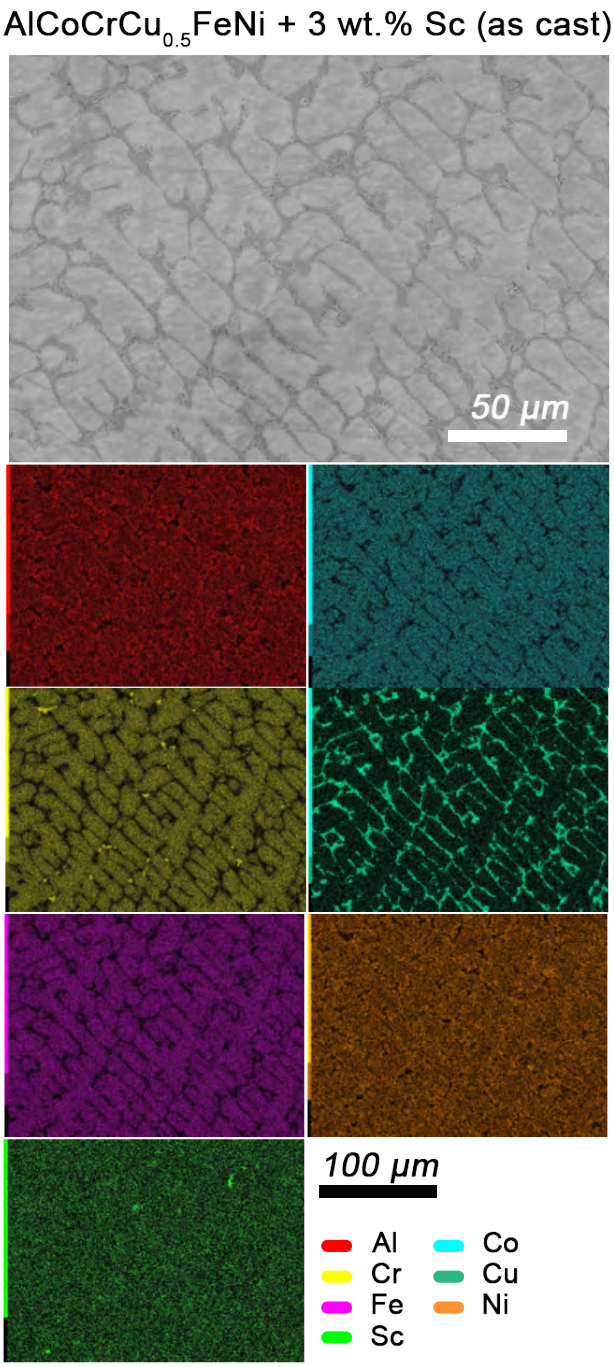

Figure 3.26: Element distributions in the as-cast $AlCoCrCu_{0.5}FeNi$ alloy containing 3 wt.% Sc.

Lastly, following scandium addition the original microstructure of the $AlCoCrCu_{0.5}FeNi$ HEA turns into equiaxed non-dendritic-like grains (Figure 3.26).

The segregation of scandium along grain boundaries appears surprising, considering the strongly negative mixing enthalpy of the metal with iron, nickel, cobalt and aluminium [263, 264, 265]. The driving force of the segregation is thus the formation of the second-

ary phase.

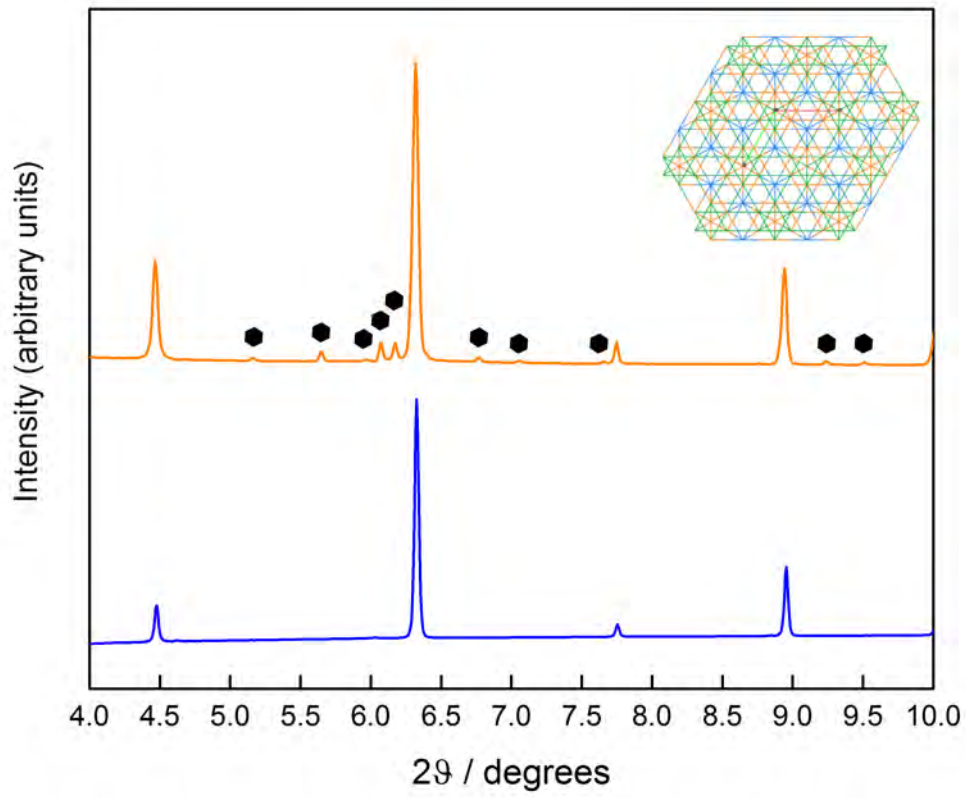

Figure 3.27: PXRD profile (DIAMOND, λ = 0.22542 Å) of the as-cast B2-structured $Al_2CoCrFeNi$ alloy before (*blue*) and after (*orange*) a 3 wt.% Sc addition. The crystal structure of the hexagonal $MgZn_2$-type intermetallic is reported in the insert as its AlCuSc analogue (Al in green, Cu in orange and Sc in blue).

The secondary phase (Figure 3.27) is the same in all systems and consists of a ternary intermetallic of $MgZn_2$-type. Compounds of this structure type have been reported for scandium with several metals, in the compositions AlCuSc, AlCoSc, $Al_{1.06}Cr_{0.94}Sc$, AlFeSc, AlNiSc [17]. As confirmed by elemental composition maps, the ternary phase has thus no preferential composition; but is rather a highly-disordered structure containing all five elements.

Knowledge about scandium-containing ternary compounds is still fragmented. Out of all the cited $MgZn_2$-type intermetallics, only AlCuSc has been thoroughly investigated, due to its effect on the mechanical properties of Al-based alloys, as part of the so-called W-phase. In particular, it was shown that the microhardness of the W-phase is much higher than the one of Al_3Sc (5150-51700 MPa against 3900-4300 MPa) [17].

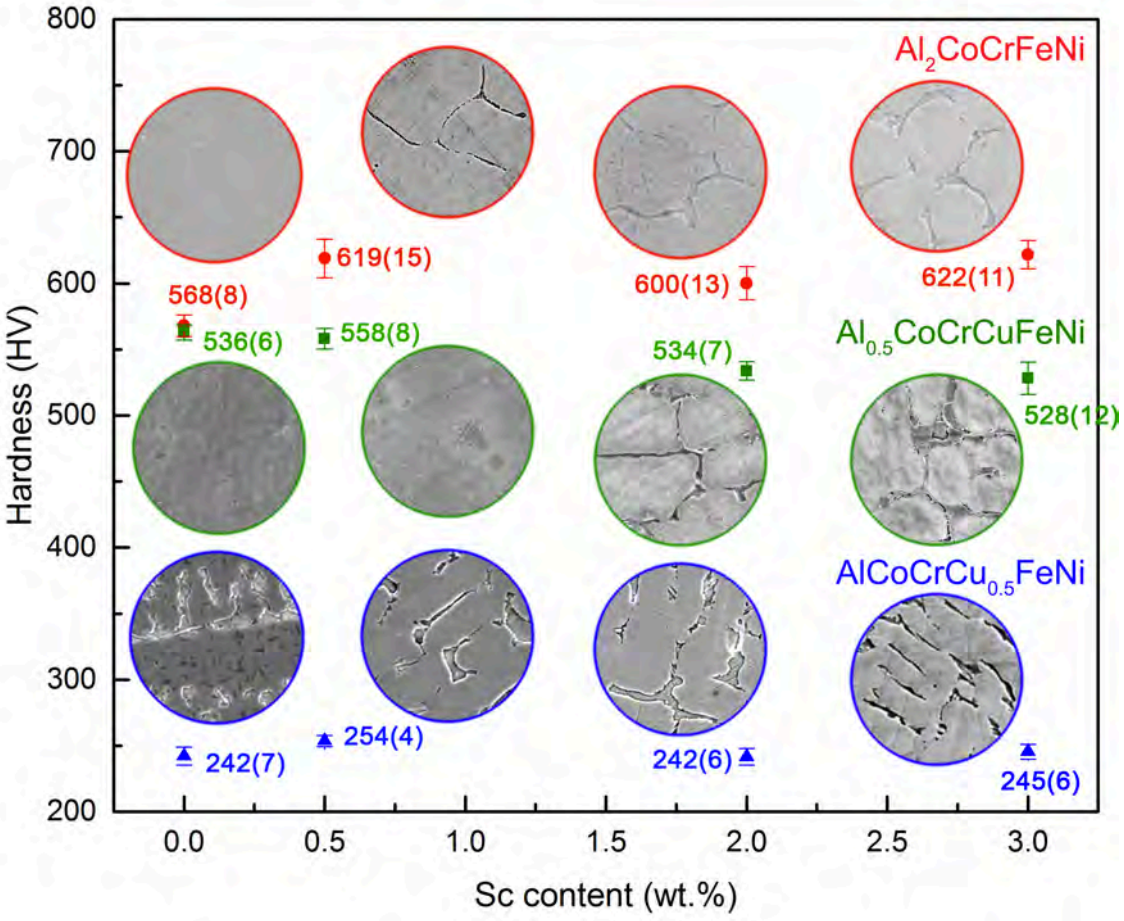

Figure 3.28: Vickers hardness values for $Al_2CoCrFeNi$ (*red*), $Al_{0.5}CoCrCuFeNi$ (*green*) and $AlCoCrCu_{0.5}FeNi$ (*blue*) HEAs with 0, 0.5, 2 and 3 wt.% Sc additions. Values are an average of 25 indentations at 1 HV. SEM microstructures for all alloys are shown in circles of 30 μm diameter.

The formation of a very hard phase in the HEA matrix is bound to affect mechanical properties. As shown in Figure 3.28, single phase *bcc* alloys are harder than duplex-structured and *fcc* alloys. This is hardly surprising, considering the stronger interatomic forces involved in *bcc vs fcc* packing. On the other hand, increasing additions of scandium to $Al_{0.5}CoCrCuFeNi$ does not affect hardness. It is even detrimental to the hardness of the $AlCoCrCu_{0.5}FeNi$ alloy, and is not accompanied by an increase in ductility (as shown by the disk punch tests presented in Figure 3.29) [243, 242].

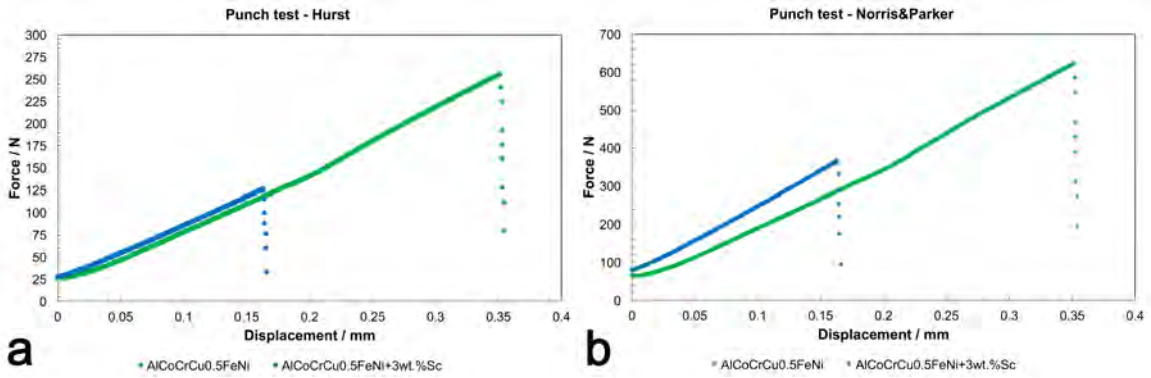

Figure 3.29: Disk punch test for the $AlCoCrCu_{0.5}FeNi$ alloy with 0 and 3 wt.% Sc, data elaborated according to the equations reported by (*a*) Hurst and (*b*) Norris and Parker [243, 242].

Only in the originally hard $Al_2CoCrFeNi$ HEA does the formation of the intermetallic result in an increase in hardness. The addition of 0.5 wt.% Sc causes a 20% hardness enhancement (Figure 3.28), as well as visible grain refinement. Disk punch tests performed on the HEA with 0, 0.5 and 2 wt.% scandium additions show a decisive increment in brittleness, proportional to the concentration of scandium (Figure 3.30).

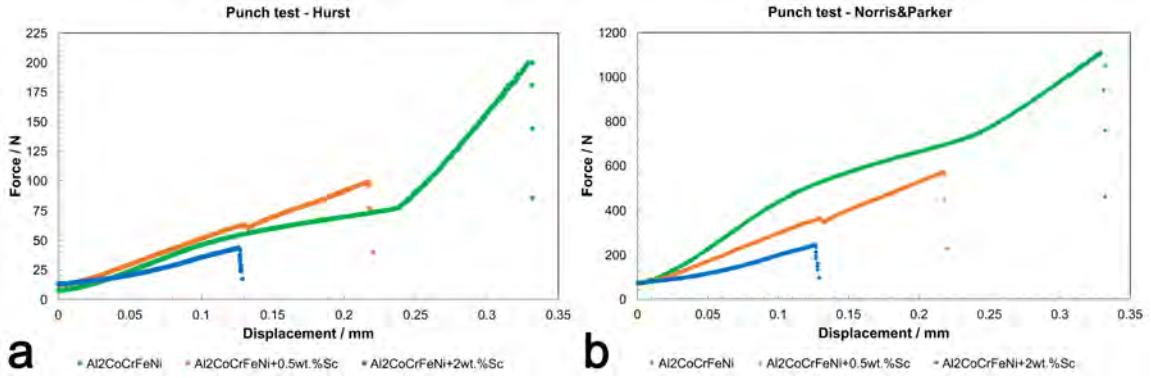

Figure 3.30: Disk punch test for the $Al_2CoCrFeNi$ alloy with 0, 0.5 and 2 wt.% Sc, data elaborated according to the equations reported by (*a*) Hurst and (*b*) Norris and Parker [243, 242].

Effect of heat treatment

Differential scanning calorimetry (DSC) was performed on alloys from room temperature to 1300 °C with a 10 K/min heating rate. The second cycle of heating and cooling (chosen to ignore the effect of the synthetic route on the specimens - *i.e.* internal stress-strain, magnetic ordering, ...) is reported in Figure 3.31.

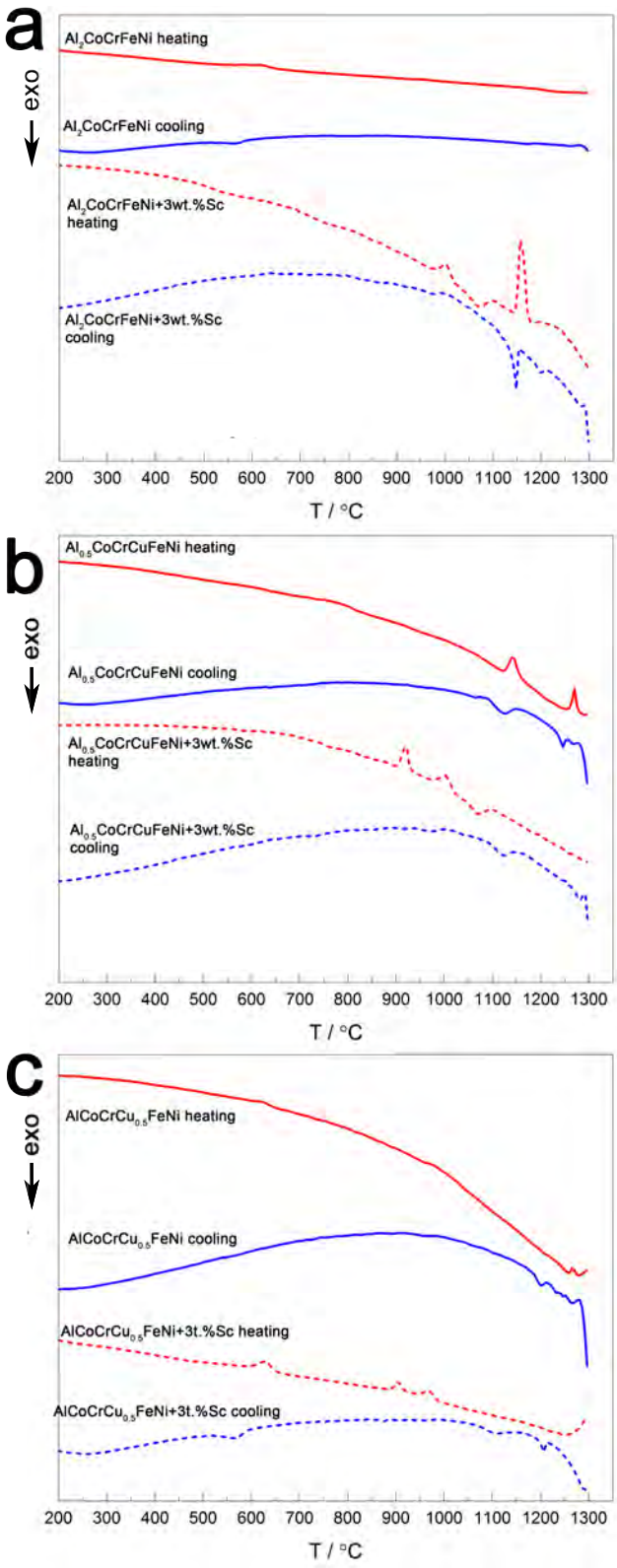

Figure 3.31: Differential scanning calorimetry of (*a*) $Al_2CoCrFeNi$, (*b*) $Al_{0.5}CoCrCuFeNi$ and (*c*) $AlCoCrCu_{0.5}FeNi$ with (*dotted line*) and without (*solid line*) scandium. The second heating/cooling cycle is reported for each specimen, in *red* and *blue* respectively.

The DSC profile of $Al_2CoCrFeNi$ (Figure 3.31, *a*) has a sigmoid-like deviation between 600 and 700 °C. In a theoretical work, Gao associates this feature with the transition $bcc_1 + bcc_2 + B2 \longrightarrow bcc + B2$, but this is incompatible with the crystal structure of the $Al_2CoCrFeNi$ alloy as per Figure 3.19. The divergence between the results reported here and Gao's interpretation might arise from the profound differences in the crystal structure of the nominally equivalent starting material [85]. To unequivocally identify the cause of the transition, a more detailed investigation of the effect of temperature on phase stability is needed. The corresponding Sc-containing sample displays a sharp reversible peak at 1150 °C, probably corresponding to the melting and crystallisation of the intermetallic phase, preceded by irreversible peaks. These two endothermic peaks, located at 906 °C and 966 °C might correspond to phase transitions occurring in the scandium-phase. The sigmoid-like deviation clearly visible in the pristine alloy is hardly distinguishable from the background line in the Sc-containing specimen, but is located at higher temperature (between 700 and 800 °C).

$Al_{0.5}CoCrCuFeNi$ shows a slight reversible peak centred at 760 °C as well as two reversible peaks above 1150 °C (Figure 3.31, *b*). In previously reported DSC curves, the two endothermic peaks of $Al_{0.5}CoCrCuFeNi$ at 1140 and 1270 °C have been associated with melting of interdendritic-like and dendritic-like material respectively. The results of Jones et al. highlight a third reversible peak, appearing at 850 °C and related to the dissolution and recrystallisation of the $L1_2$ phase, which might form during prolonged heat treatment below 850 °C and is dependent from the sample cooling rate [266]. Its absence is indicative of the purity of the as-cast *fcc* sample, which is confirmed by high-resolution PXRD data (Figure 3.18) [267]. The scandium containing specimen shows three irreversible peaks upon heating (the first two, endothermic, at 921 and 1000 °C; the latter, exothermic, at 1073 °C). Interestingly, upon cooling the Sc-containing specimen behaves very similarly to its corresponding pristine alloy. The irreversible transitions occurring in the sample might thus relate solely to the intermetallic, and have little impact on the matrix.

Finally, $AlCoCrCu_{0.5}FeNi$ displays a reversible transition at circa 624 °C, which is maintained in the Sc-containing sample (Figure 3.31, *c*). Irreversible phenomena occur in the pristine alloy above 1150 °C, as in the previous sample. The scandium-containing alloy presents two irreversible endothermic peaks (at 906 and 966 °C) upon heating and two exothermic peaks upon cooling (at 1102 and 1206 °C), which were deemed to be too far from the heating ones to be considered part of the same phenomenon.

Reversible phenomena thus occur in all systems above 600 °C; whereas irreversible peaks appear in the scandium-containing alloys at circa 900 °C . To investigate the nature of these transitions, the pristine alloys were annealed above their average first reversible transition temperature; and the scandium-containing specimens at the temperatures of their first irreversible transition. Annealing time was shortened for the samples at the highest temperature (930 °C), so as not to lose aluminium.

$Al_2CoCrFeNi$, $Al_{0.5}CoCrCuFeNi$ and $AlCoCrCu_{0.5}FeNi$ were annealed at 850 °C for 12 hours. $Al_2CoCrFeNi$+3 wt.% Sc was treated at 900 °C for 12 hours, while $Al_{0.5}CoCrCuFeNi$+3 wt.% Sc and $AlCoCrCu_{0.5}FeNi$+3 wt.% Sc at 930 °C for 6 hours. The corresponding element

distribution and microstructures are presented in the following pages.

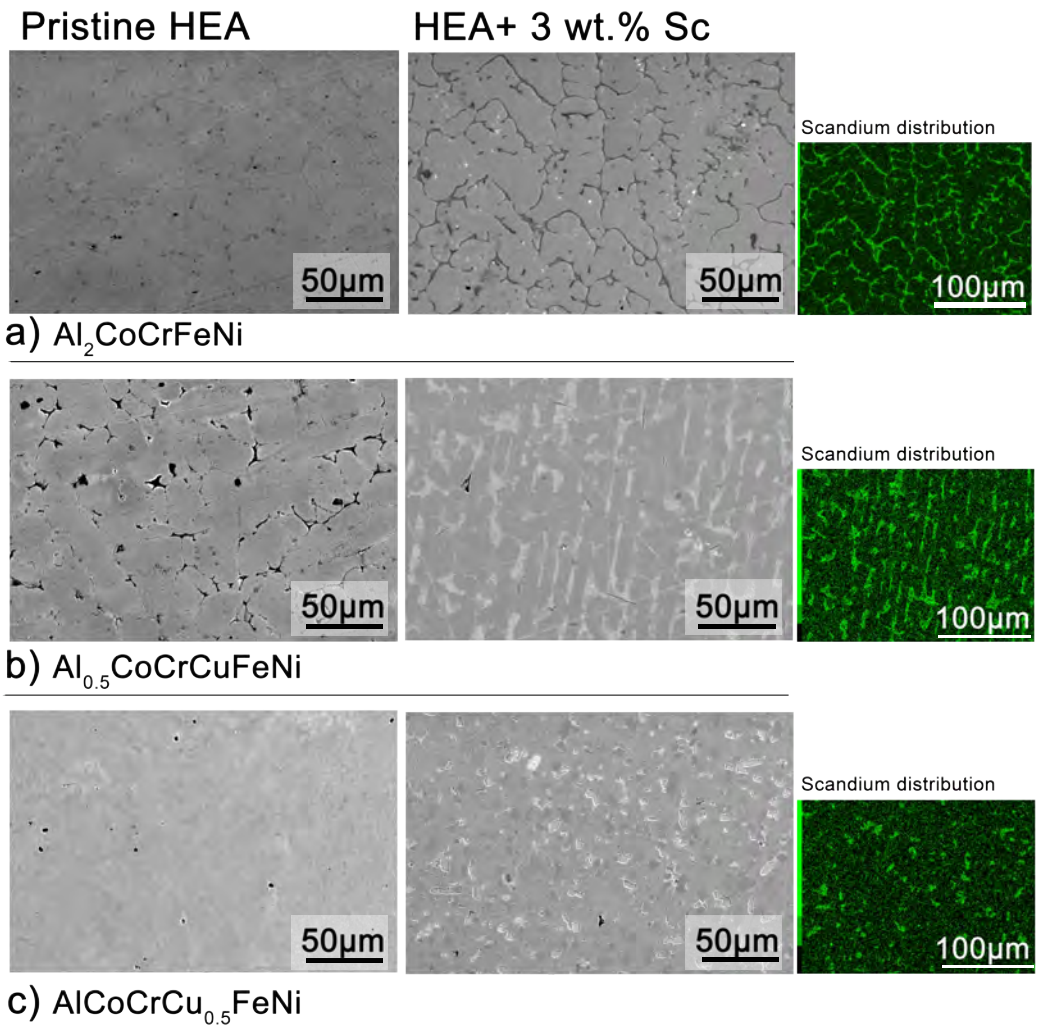

Figure 3.32: Microstructure of annealed $Al_2CoCrFeNi$ (a), $Al_{0.5}CoCrCuFeNi$ (b) and $AlCoCrCu_{0.5}FeNi$ (c) before and after 3 wt.% Sc addition. Blank alloys were annealed at 850 °C for 12h; $Al_2CoCrFeNi$ + 3 wt.% Sc at 900 °C, 12h; $Al_{0.5}CoCrCuFeNi$ and $AlCoCrCu_{0.5}FeNi$ at 930 °C, 6h. In green is shown the scandium element distribution according to EDX maps.

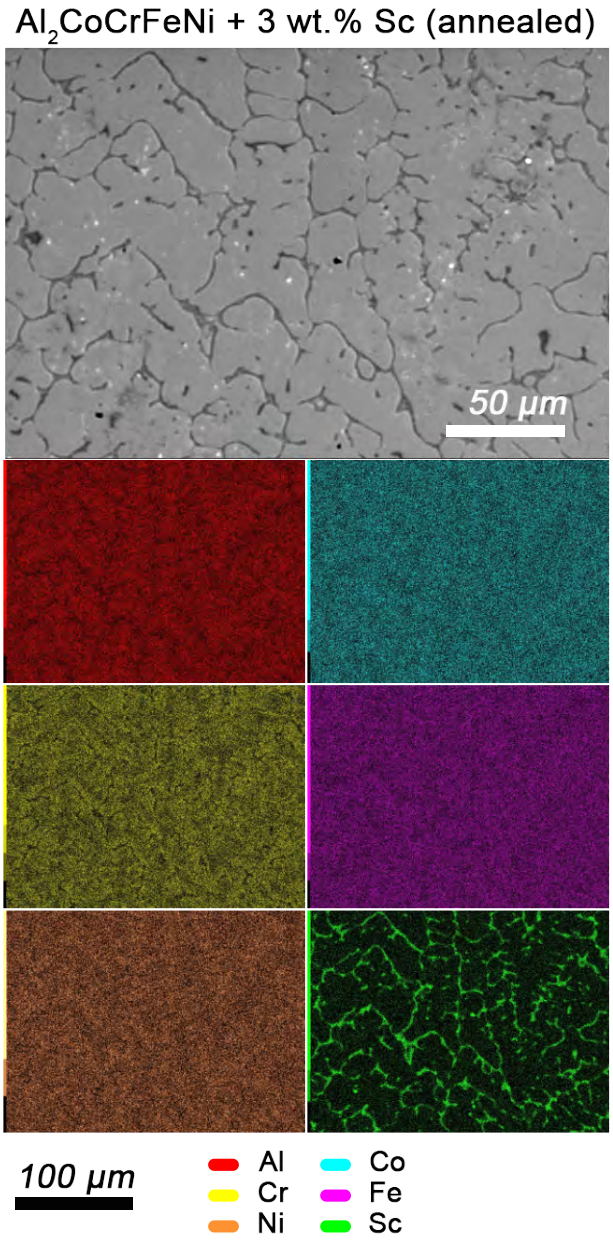

Figure 3.33: Microstructure and element distributions in the annealed $Al_2CoCrFeNi$ + 3wt.% Sc alloy.

Figure 3.33 reports the microstructure and element distribution of the annealed $Al_2CoCrFeNi$ + 3wt.% Sc alloy. With respect to Figure 3.22, *b* (the annealed pristine alloy), microstructure is refined and the intermetallic scandium phase grows in a dendritic-like structure. The secondary phase which would have appeared in the pristine alloy (in the form of black dots) is not displayed in the matrix. A comparison with the scandium-containing alloy prior to annealing (Figure 3.24) shows a more homogeneous distribution of chromium, even though the metal still visibly segregates along grain boundaries.

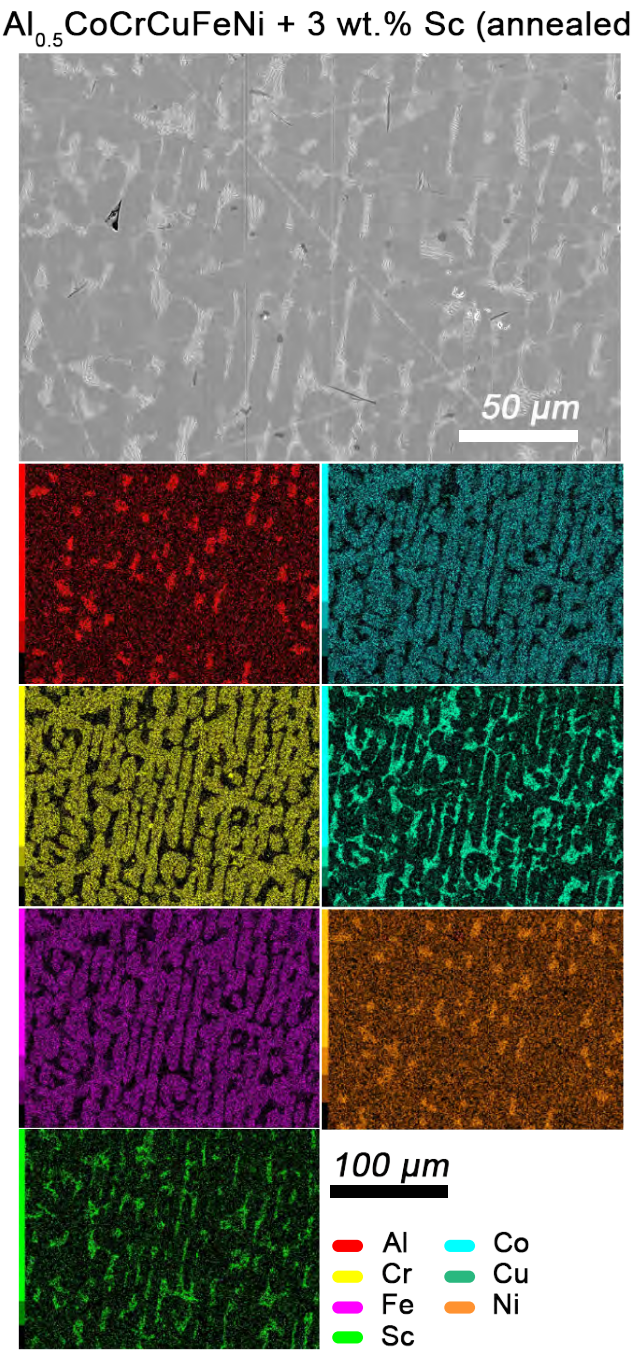

Figure 3.34: Microstructure and element distributions in the annealed $Al_{0.5}CoCrCuFeNi$ + 3wt.% Sc alloy.

The heat treatment of the pristine $Al_{0.5}CoCrCuFeNi$ (Figure 3.21, *b*) causes the disruption of the original dendritic- and interdentritic-like microstructure. Interestingly, however, the microstructure of the scandium-containing alloy after annealing is quite similar to the as cast pristine alloy: a columnar cellular structure displaying strong element segregation (Figure 3.34). The light phase consists mostly of Cu and Sc, and within it regions rich in Al and

Ni. The darker areas are rich in Co, Cr and Fe. It is of interest to note that this element segregation is different from the one prior annealing (Figure 3.25), as Ni is depleted from the matrix.

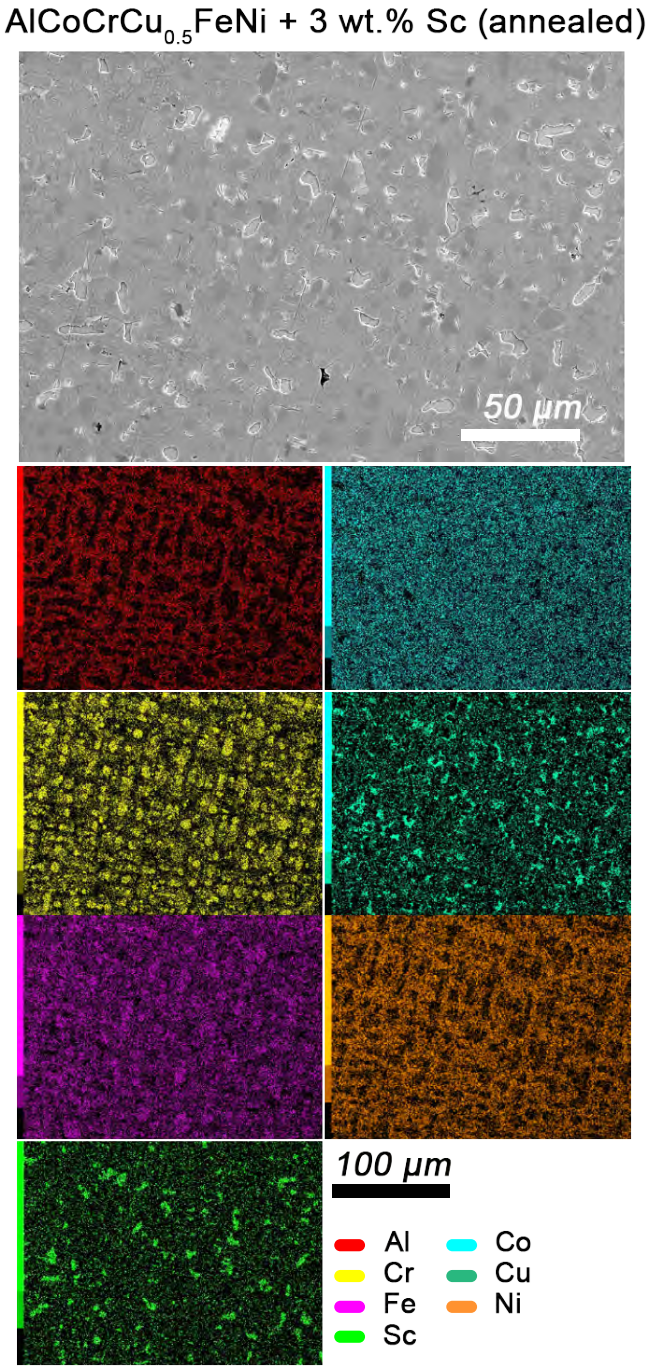

Figure 3.35: Microstructure and element distributions in the annealed $AlCoCrCu_{0.5}FeNi$ + 3wt.% Sc alloy.

The annealed $AlCoCrCu_{0.5}FeNi$ + 3 wt.% Sc has a complex microstructure (Figure 3.35). Acircular particles grow in an unstructured matrix, the bigger of those being easily removed

from the specimen during polishing (and leaving behind elongated valleys). Elemental segregation occurs to form several diverse regions: a Co-rich matrix, areas rich in Al and Ni, Cu-Sc precipitates. Iron clearly segregates from Al and Ni, but does not follow the trend of other elements. Finally, Cr coalesces in circular well-shapes areas. Combining this information we can note that the brittle phase is, as expected, rich in Cu and Sc. It is also interesting to note that the annealed scandium-containing alloy is very different not only from the pristine alloy, but also from the original as cast specimen. Indeed, the annealed pristine alloy shows no clustering of Cr, Fe and Cu (Figure 3.20, *b*); and the scandium-containing as cast alloy clearly highlights the coexistence of Co, Cr and Fe (Figure 3.26).

Phase evolution upon heating

To further investigate the nature of the transitions occurring in the studied HEA systems and how they are affected by the intermetallic, an X-Ray Diffraction (XRD) *in situ* study of the B2-structured $Al_2CoCrFeNi$ and the *fcc*-structured $Al_{0.5}CoCrFeNi$ HEAs with and without 3 wt.% scandium was performed. Quantitative data are available only for the main phases, whose lines had enough intensity to be detected and refined. The development of scandium-rich phases could not be directly observed.

Several works have highlighted that $Al_{0.5}CoCrCuFeNi$ consists of a mixture of two *fcc* phases of similar cell parameters, corresponding to dendritic- and interdendritic-like phase [268, 269, 270]. Chen reported a single *fcc* structure below 500 °C, and a dual *fcc*/*bcc* structure above 600 °C [271]. According to Jones, on the other hand, two *fcc* phases of similar cell parameters co-exist and are stable up until their melting temperatures (1150 °C for the Cu based solid solution and 1350 °C for the multi-component phase) [266]. As shown in Figure 3.18, the system consists of an *fcc* phase (a_{fcc} = 3.601(1) Å) and a small (< 10%) amount of *bcc* phase (a_{bcc} = 2.867(4) Å). As shown in Figure 3.36*a*, heating does not affect the primary phase: diffraction lines become sharper, but their relative intensity is constant. The addition of scandium (Figure 3.36, *b*) has no impact on the *fcc* matrix, but influences the $bcc \longrightarrow fcc_2$ equilibrium by shifting it towards the formation of *bcc*. The second fcc_2 phase (a_{fcc_2} = 3.609(2) Å) reported in Figure 3.36, *a* can thus be considered a minor admixture in an exsolution equilibrium with the *bcc* phase.

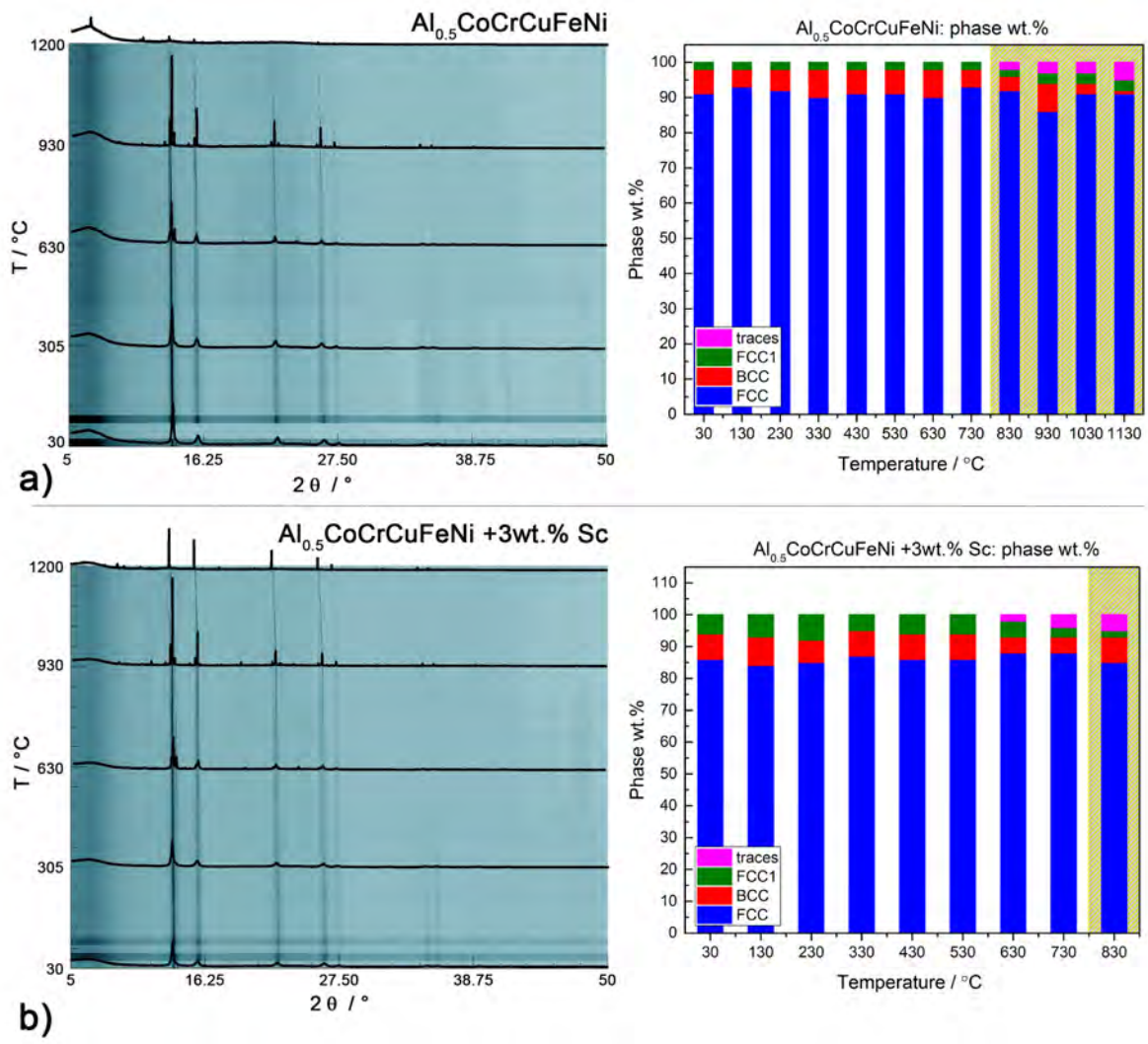

Figure 3.36: High-temperature behaviour of $Al_{0.5}CoCrCuFeNi$ with (*b*) or without (*a*) scandium. The yellow area signals the start of oxidation. In pink are reported the amount of oxides detected. (I11 at DIAMOND, $\lambda = 0.494984$ Å).

The thermal behaviour of the B2-structured $Al_2CoCrFeNi$ sample is displayed in Figure 3.37, *a*. The decomposition of 40 wt.% of the B2 phase above 620 °C and the exsolution of an *fcc* phase ($a_{fcc_1} = 3.635(8)$ Å) is observed. At 750 °C a second fcc_2 phase of lattice parameter $a_{fcc_2} = 3.631(9)$ Å develops from fcc_1 and grows almost linearly with temperature. The continuous presence of the (1 0 0) super-lattice peak in the PXRD profile of the alloy suggests that the Al-rich sub-lattice responsible for the B2 crystal structure might not be involved in the exsolution process.

Results for the Sc-containing $Al_2CoCrFeNi$ alloy are presented in Figure 3.37, *b*. The exsolution of the *fcc* phase from B2 follows a different pathway, with fcc_1 and fcc_2 forming at the same time. The transformation occurs at higher temperatures: a 3 wt.% scandium addition is enough to stabilise the main B2 phase for about 150 °C.

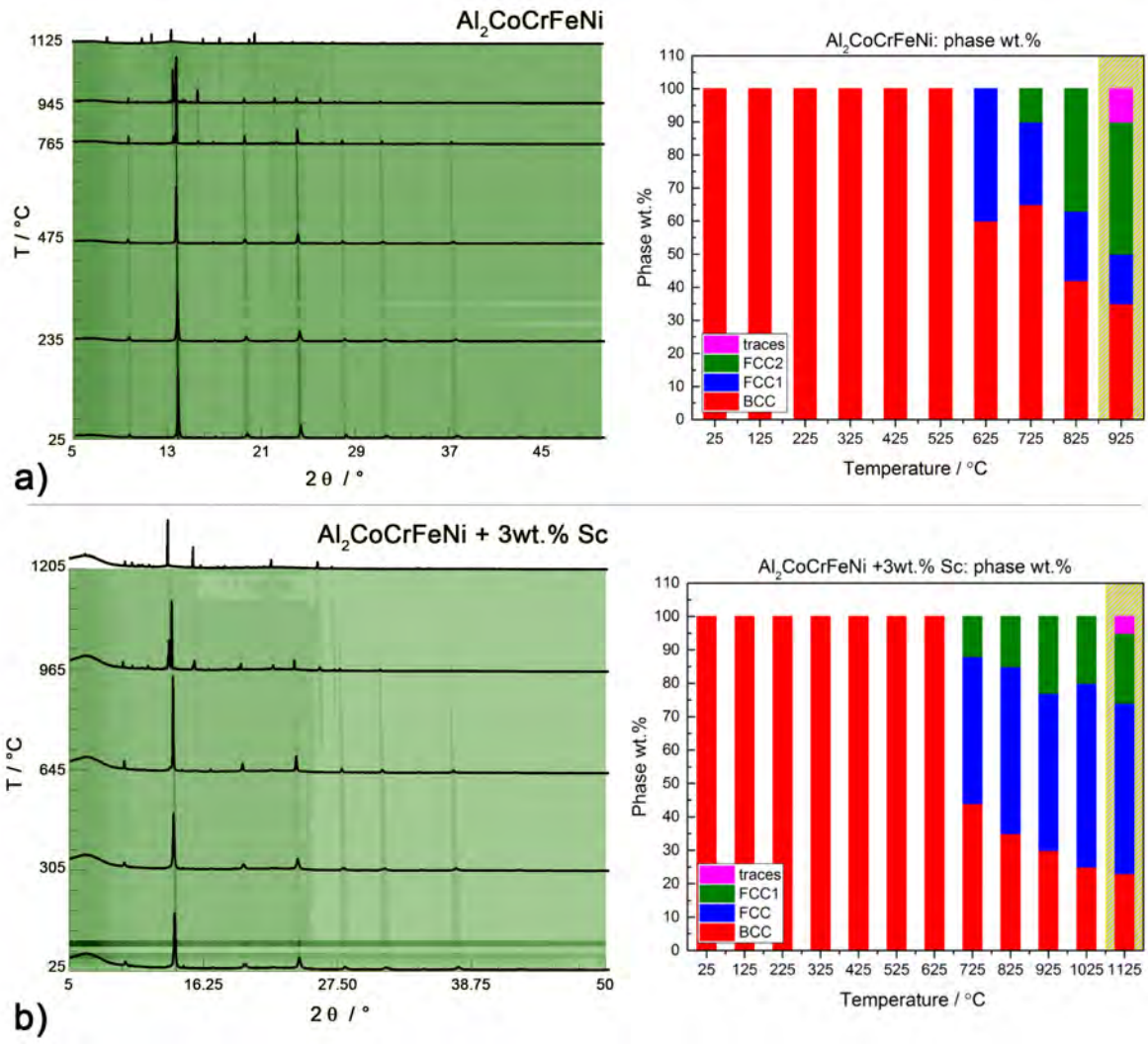

Figure 3.37: High-temperature behaviour of B2 structured $Al_2CoCrFeNi$ with (b) or without (a) scandium. The yellow area signals the start of oxidation. In pink are reported the amount of oxides detected (I11 at DIAMOND, $\lambda = 0.494984$ Å).

The thermal expansion coefficient of $Al_2CoCrFeNi$ and $Al_2CoCrFeNi$ + 3 wt.% Sc can be evaluated by *in situ* high-temperature PXRD measurements by fitting the corresponding dataset to Eq. 2.15 (see Section 2.4.2).

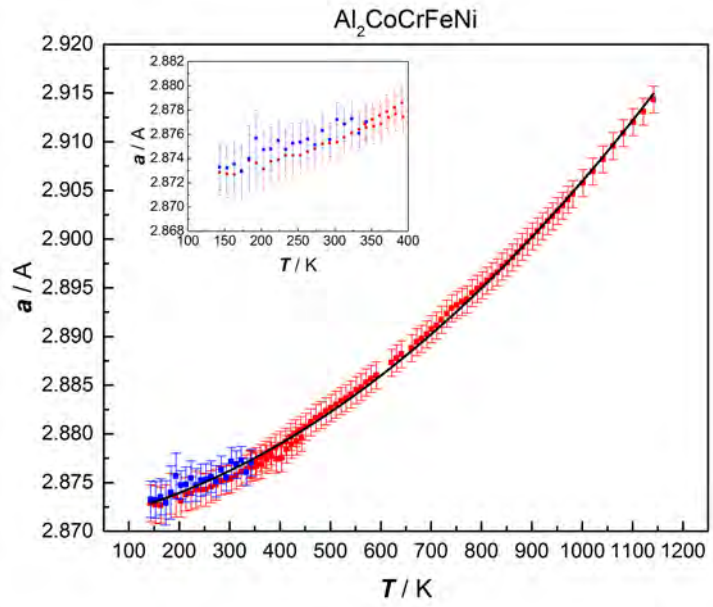

Figure 3.38: Lattice thermal expansion data fitted with Eq. 2.15 for *a*) $Al_2CoCrFeNi$. In *red* are reported data collected upon heating from 100–400 K (PETRAIII, λ = 0.207150 Å) and from 300–1100 K (DIAMOND, λ = 0.494984 Å); in blue are presented data collected upon cooling from 300–100 K (PETRAIII, λ = 0.207150 Å). The low temperature data are highlighted in the inset.

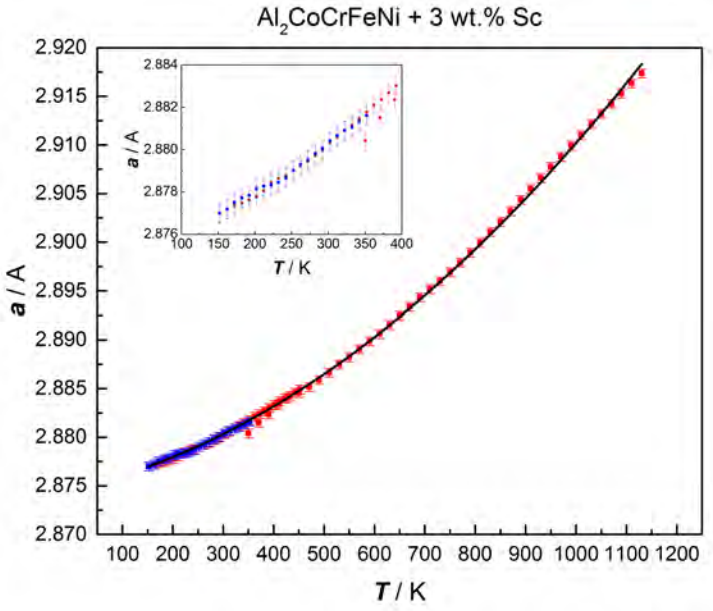

Figure 3.39: Lattice thermal expansion data fitted with Eq. 2.15 for $Al_2CoCrFeNi$ + 3 wt.% Sc. In *red* are reported data collected upon heating from 100–400 K (PETRAIII, λ = 0.207150 Å) and from 300–1100 K (DIAMOND, λ = 0.494984 Å); in blue are presented data collected upon cooling from 300–100 K (PETRAIII, λ = 0.207150 Å). The low temperature data are highlighted in the inset.

Figure 3.38 and 3.39 report the variation of the lattice parameter a_{B2} upon heating and cooling. A satisfactory fitting can be obtained for $Al_2CoCrFeNi$ for the parameters A and B equalling $3.6(2) \cdot 10^{-6}$ K^{-1} and $1.69(3) \cdot 10^{-8}$ K^{-2} respectively; and for $Al_2CoCrFeNi$ + 3 wt.% Sc for A and B equalling $4.2(1) \cdot 10^{-6}$ K^{-1} and $1.62(2) \cdot 10^{-8}$ K^{-2} respectively.

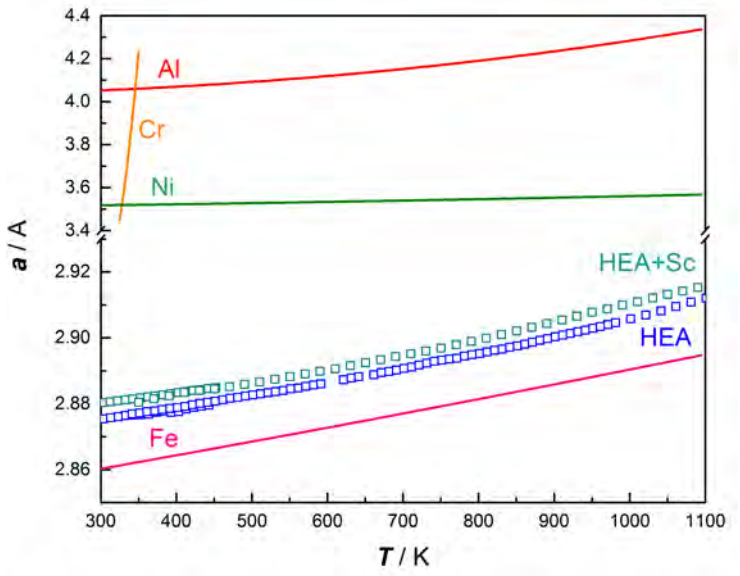

Figure 3.40: Lattice thermal expansion curves for $Al_2CoCrFeNi$ and $Al_2CoCrFeNi$ + 3 wt.% Sc with respect to their constitutive cubic metals [272, 273, 274, 275].

As highlighted in Figure 3.40, the scandium-containing B2 phase has slightly bigger cell parameters than the regular alloy, and follows the same trend with temperature. This trend is consistent to the one of pure iron in the investigated temperature range, but differs strongly from the behaviour of other cubic metals which constitute the alloy (in particular, chromium and nickel) [272, 273, 274, 275].

3.2.2 High-Pressure High-Temperature tailoring of High Entropy Alloys for extreme environments

I herein report a consistent high-pressure high-temperature *in situ* investigation of microstructure evolution and phase transformation in the B2-structured $Al_2CoCrFeNi$ and in the scandium-containing $Al_2CoCrFeNi$, according to the methodology reported in Section 2.6.3.

Rationale behind the choice of specimens and experimental conditions

A palette of samples obtained in different conditions to explore the hyper-metric phase diagram of $Al_2CoCrFeNi$ with and without scandium additions was prepared. Part of the two as cast samples used for the previous experiments (Section 3.2.1) were pulverized and processed further, according to the procedure thoroughly reported in Section 2.6.3.

Since P-T phase diagrams of HEAs are currently unavailable, we first studied *in situ* the effect of pressure on $Al_2CoCrFeNi$ and $Al_2CoCrFeNi$ +3 at.% Sc at room temperature, from ambient pressure to pressures that are well-within the reasonable and readily reproducible limits of high pressure laboratory techniques (from ambient pressure to 9.5 GPa in the multi-anvil press located at ESRF). No phase transition occurred in the specimens when only pressure was applied.

On the other hand, the DSC and *in situ* experiments reported in Section 3.2.1 highlighted a strong temperature effect at constant (ambient) pressure, with several phase transitions occurring above 870 K. To learn more about the nature of this transition, we annealed $Al_2CoCrFeNi$ above its first reversible transition (1123 K) and $Al_2CoCrFeNi$ +Sc at the temperature of its first irreversible transition (1173 K) at ambient pressure.

We thus proceeded to study the combined effect of temperature and pressure on the two samples.

- Pristine $Al_2CoCrFeNi$ was sintered with SPS at 0.05 GPa at its annealing temperature (1123 K) to compare the result obtained with the sintered powder with those of the annealed pellet.

- At the relatively low pressure of 2.1 GPa, we annealed $Al_2CoCrFeNi$ and $Al_2CoCrFeNi$ +Sc just below their corresponding melting temperature at ambient pressure (1253 K, piston cylinder apparatus).

- Finally, we studied *in situ* the effect of temperature at 9.5 GPa from room temperature to 1500 K.

The chosen pressures (0.05 GPa, 2.1 GPa and 9.5 GPa) are convenient for the equipment used as they allow recovery of a specimen with the size needed for further mechanical characterisation. Their corresponding uncertainties are highlighted in Section 2.6.3. Preparation conditions and corresponding phase compositions are reported in Table 3.10. The atomic compositions of the $Al_2CoCrFeNi$ and $Al_2CoCrFeNi$ +Sc alloys according to EDX maps are reported in Table 3.8 and Table 3.9 respectively. Since element distribution is homogeneous

in the pristine alloy, its composition is reported as determined from EDX maps measurements. Where different phases are clearly discernible, such as in the as cast and annealed Sc-containing pellet, the average value obtained from EDX maps is combined with point measurements in the different phases (10 measurements for each phase).

$Al_2CoCrFeNi$					
	Pellet		Sintered powder		
	As-cast	Annealed, 1123 K	SPS, 1123 K	2.1 GPa, 1253 K	9.5 GPa, 1500 K
Al	44.4(3)	39.5(1)	40.7(5)	39.1(1)	38.8(2)
Co	14.7(2)	15.7(7)	14.0(4)	13.9(8)	14.2(4)
Cr	13.6(2)	13.8(2)	14.5(2)	13.8(4)	14.6(0)
Fe	14.3(4)	15.1(4)	16.7(7)	18.5(0)	17.8(9)
Ni	12.8(9)	15.7(7)	13.9(2)	14.5(7)	14.2(0)

Table 3.8: Atomic percent composition of the samples (according to x500 EDX maps). The entries 'as-cast' and 'annealed' correspond to the as-cast and annealed pellets respectively. All other entries refer to the powder sample composition after high-pressure high-temperature sintering.

$Al_2CoCrFeNi$ + 3 wt.% Sc

	Pellet						Sintered powder		
		As-cast			Annealed, 1173 K		2.1 GPa, 1253 K	9.5 GPa, 1000 K	9.5 GPa, 1500 K
	Grain	Intergrain	Average	Grain	Intergrain	Average	Average	Average	Average
Al	46.4(3)	30.5(1)	41.9(0)	45.1(4)	34.0(5)	41.3(0)	43.1(0)	41.4(8)	41.8(0)
Co	14.2(6)	14.0(2)	13.3(7)	15.0(8)	14.0(7)	14.4(8)	14.1(1)	14.1(4)	14.4(5)
Cr	11.6(8)	9.5(5)	13.5(8)	12.0(7)	9.8(8)	14.0(2)	13.5(3)	13.8(5)	13.9(5)
Fe	12.6(5)	14.1(8)	14.2(2)	13.2(0)	16.0(9)	14.7(2)	14.2(1)	14.8(8)	14.7(1)
Ni	14.5(8)	14.8(1)	13.7(8)	14.2(1)	13.4(6)	13.2(7)	13.0(7)	13.0(8)	13.4(1)
Sc	0.4(2)	16.9(2)	2.7(9)	0.2(9)	12.4(5)	2.2(0)	2.0(1)	2.7(5)	1.6(9)

Table 3.9: Atomic percent composition of the samples (according to x500 EDX maps). The entries 'as-cast' and 'annealed' correspond to the as-cast and annealed pellets respectively. All other entries refer to the powder sample composition after high-pressure high-temperature sintering.

Preparation technique/ Pressure / Temperature / Time	PXRD Measurement condition conditions	Main B2 phase a, Å/ V, Å^3	Minor phase(s)
	$Al_2CoCrFeNi$		
As cast	Ambient / Diamond	2.877(2) / 23.833(5)	
Ambient pressure / 1580 K / 5 min			
Annealed	Ambient / ESRF	2.863(2) / 23.463(5)	
Ambient pressure / 1123 K / 12 h			
Spark Plasma Sintering	Ambient / CuKα_1	2.866(2) / 23.541(5)	
0.05 GPa / 1123 K / min			
Multi-anvil press	Ambient / ESRF	B2" 2.885(3) / 24.125(5)	6 wt.% $fcc_1 : a = 3.623(7)$Å
9.5 GPa / 1500 K / 30 min			$\frac{1}{2}V = 23.799(5)$Å^3
	$Al_2CoCrFeNi$ + 3wt.% Sc		
As cast	Ambient / Diamond	2.882(2) / 23.926(5)	$MgZn_2$-type phase
Ambient pressure / 1580 K / 5 min			
Annealed	Ambient / CuKα_1	2.882(2) / 23.904(5)	$MgZn_2$-type phase
Ambient pressure / 1123 K / 12 h			
Piston cylinder press	Ambient / CuKα_1	2.881(2) / 23.915(5)	$MgZn_2$-type phase
2.1. GPa / 1253 K / 60 min			
Multi-anvil press	Ambient / ESRF	2.864(2) / 23.481(5)	$MgZn_2$-type phase
9.5 GPa / 1000 K / 30 min			$\frac{1}{2}V = 23.799(5)$Å^3
Multi-anvil press	Ambient / ESRF	2.869(2) / 23.617(5)	
9.5 GPa / 1500 K / 30 min			$\frac{1}{2}V = 23.799(5)$Å^3

Table 3.10: Preparatory conditions and phase composition in as-cast, annealed and sintered $Al_2CoCrFeNi$ and $Al_2CoCrFeNi$+Sc alloys.

Opening the door to $p - T$ space

The structure of as-cast and annealed $Al_2CoCrFeNi$ and $Al_2CoCrFeNi$ + 3wt.% Sc has been widely discussed in Section 3.2.1 and is herein only briefly summarised for clarity.

As-cast $Al_2CoCrFeNi$ is B2-structured. The presence of (1 0 0) super-lattice peaks in the PXRD profile of the alloy indicates the presence of the widely reported Al-rich sublattice, responsible for the B2 crystal structure. The lattice parameter of the as-cast alloy (a = 2.877(2) Å) is consistent with the values from the literature. The $Al_2CoCrFeNi$ microstructure is dominated by large (100 μm) grains and, unlike previous studies, does not show non-equiaxed dendrites. Chromium segregation is clearly visible in the as-cast material, but is reduced by heat treatment. The microstructural features of the $Al_2CoCrFeNi$ pristine and Sc-containing alloy are reported in Figure 3.42.

At ambient pressure, DSC results for $Al_2CoCrFeNi$ display a sigmoid-like reversible transition at 890 K (Figure 3.31, *a*). From *in situ* PXRD data (Figure 3.37) we observe the decomposition of 40 wt.% of the B2 phase above 890 K and the exsolution of a *fcc* phase (a_{fcc_1} = 3.636(8) Å). A second fcc_2 phase of lattice parameter a_{fcc_2} = 3.630(6) Å develops from the first *fcc* phase at 1023 K (65 wt.% *bcc*, 25 wt.% fcc_1, 10 wt.% fcc_2). From 1023 to 1273 K, fcc_2 grows almost linearly.

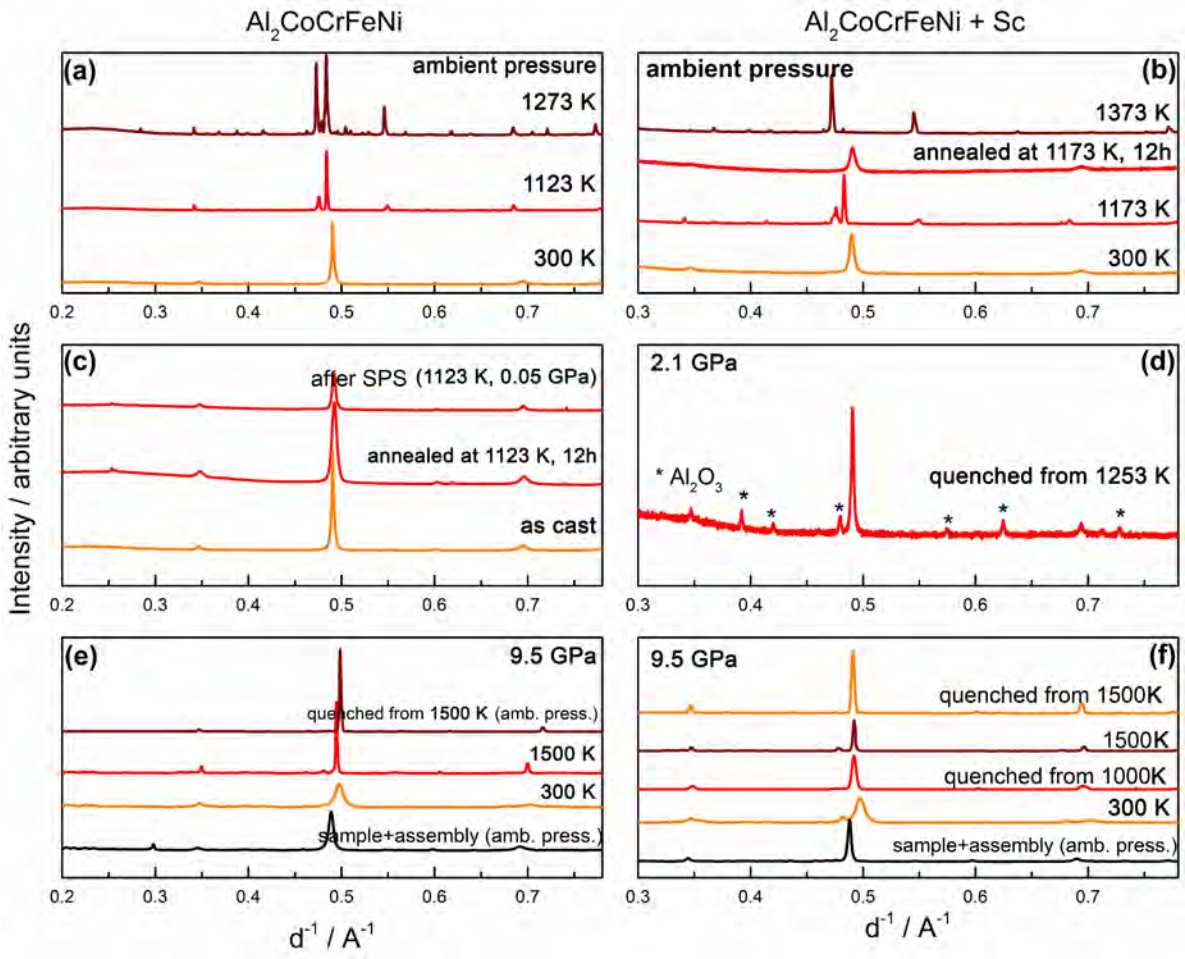

Figure 3.41: Resume of PXRD profiles obtained for $Al_2CoCrFeNi$ (a) during *in situ* ambient pressure heating, (c) measured after ambient pressure annealing and SPS, (e) before, during and after *in situ* 9.5 GPa heating. PXRD profiles of $Al_2CoCrFeNi$+Sc (b) during *in situ* ambient pressure heating, (d) measured after ambient pressure sintering at 2.1 GPa, (f) before, during and after *in sit*u 9.5 GPa heating. PXRD profiles are plotted as function of $1/d$ to compare data obtained from DIAMOND (I11, $\lambda = 0.494984$ Å), ESRF (ID06, $\lambda = 0.22542$ Å) and in house instrument (CuKα_1, $\lambda = 1.54059$ Å).

The $Al_2CoCrFeNi$ sample annealed or sintered above the temperature of the reversible transition (*i.e.* 1123 K) should therefore display all three phases. However, neither the annealed nor the spark-plasma sintered sample's PXRD profiles reflect any change from the as-cast alloy (Figure 3.41). Where the annealed pellet is concerned, the microstructure is dominated by nano-scale spherical particles, with features strikingly similar to those reported by Kao for annealing at 1173 and at 1373 K (Figure 3.42, b) [175].

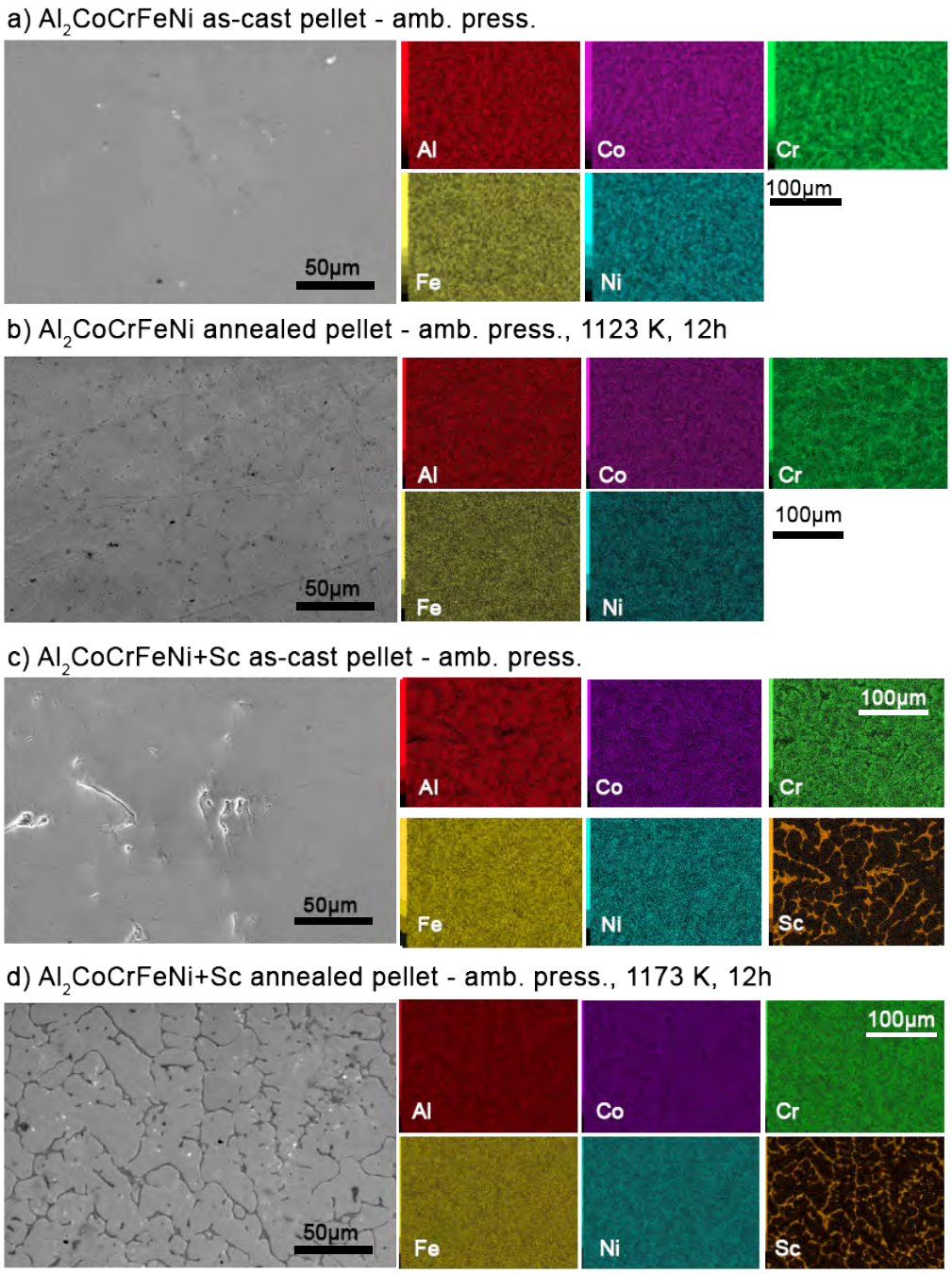

Figure 3.42: Microstructure and element distribution maps of as cast and annealed $Al_2CoCrFeNi$ and $Al_2CoCrFeNi$ + 3 wt.% Sc at ambient pressure.

Analogously, spark-plasma sintering of $Al_2CoCrFeNi$ powder of 5-20 μm particle size results in homogeneous element distributions (Figure 3.43, *a*). Despite intergranular porosity, grain growth has occurred with respect to the original particle size (see Section 2.1.3). Nevertheless, cracks and cavitations cause the macroscopic density of the spark-plasma sintered sample to be only 92.5% of the density of the thermally annealed sample prepared at the same temperature ($\rho_{f,ann} = 6.4(1)$ g $\cdot$ cm^{-3} and $\rho_{f,SPS} = 5.92(7)$ g $\cdot$ cm^{-3} as established from

flotation; $\rho_{d_{XRD},ann} = 6.33(1)\ \mathrm{g \cdot cm^{-3}}$ and $\rho_{d_{XRD},SPS} = 6.24(1)\ \mathrm{g \cdot cm^{-3}}$ as estimated from PXRD data). Combining DSC and PXRD results we can thus deduce that the reversible transition occurring at 890 K in this as-cast alloy is faster than the corresponding annealing time, and shorter than our *in situ* heating rate.

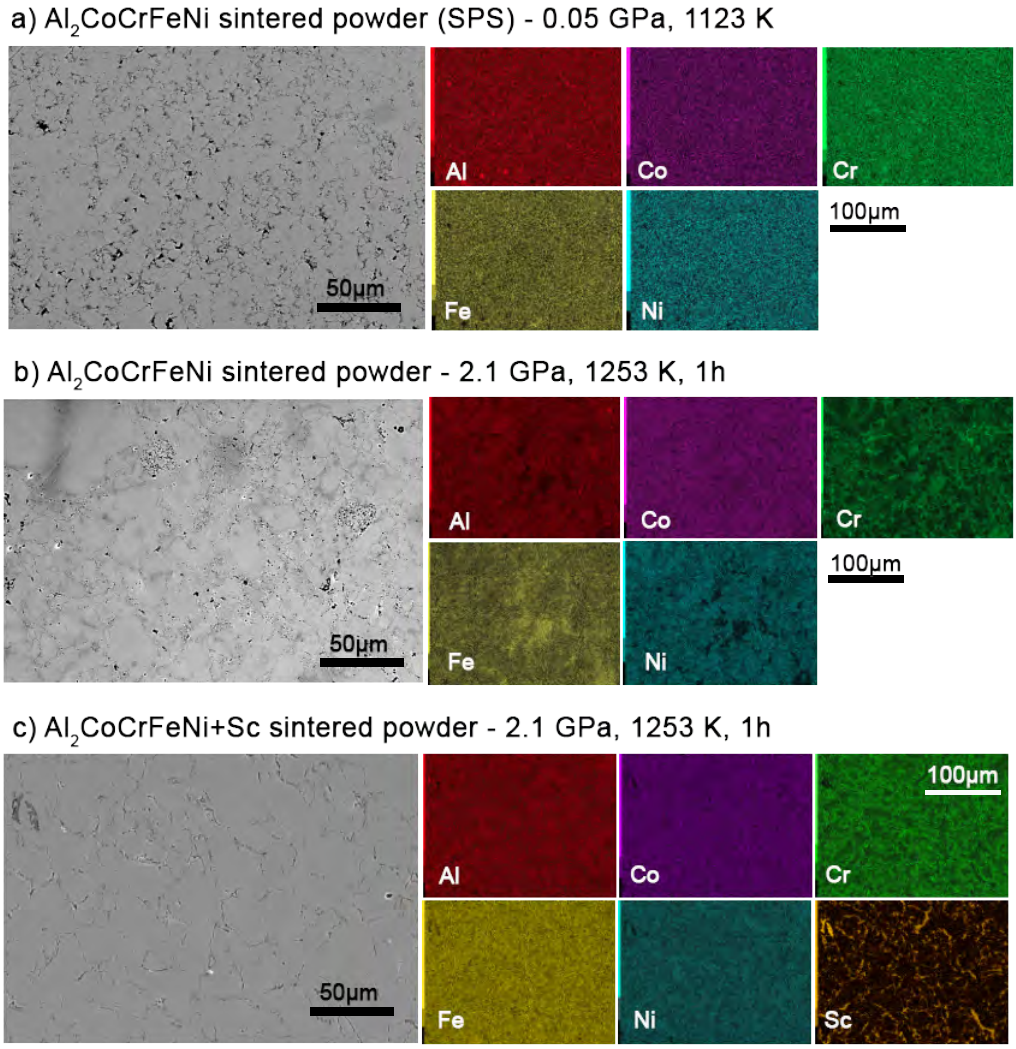

Figure 3.43: Microstructure and element distribution maps of sintered $Al_2CoCrFeNi$ (*a*, SPS at 0.05 GPa; *b* at 2.1 GPa) and $Al_2CoCrFeNi$ + 3 wt.% Sc (*c*, 2.1 GPa).

Low densification is still relevant with the high-pressure high-temperature treatment of $Al_2CoCrFeNi$ at 2.1 GPa and 1253 K. It results in inhomogeneity in the element distributions of Fe, Ni and Cr and the appearance of a fine lamellar microstructure along grain boundaries, similar to what was previously reported for spinodal decomposition in analogous systems (Figure 3.43, *b* and *c*) [160].

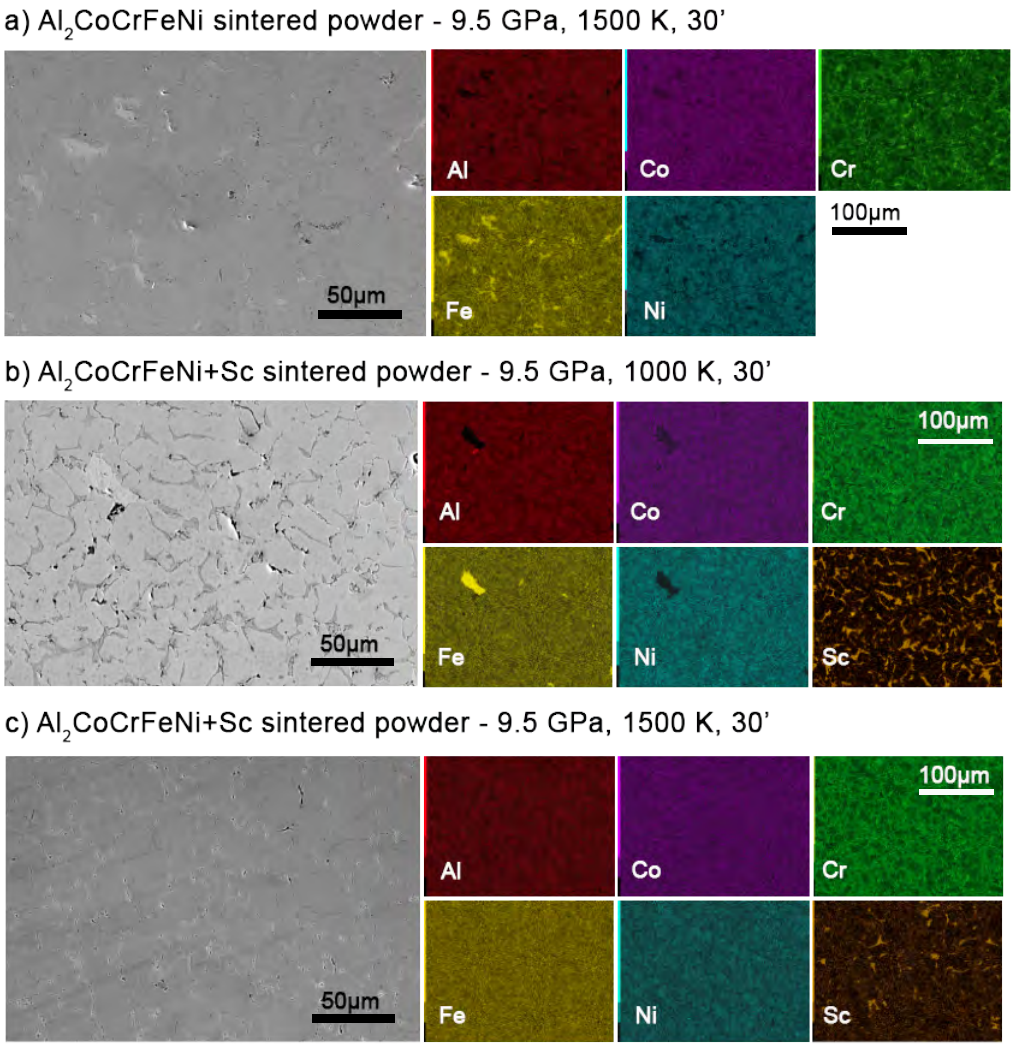

Figure 3.44: Microstructure and element distribution maps of sintered $Al_2CoCrFeNi$ (*a*, 1500 K) and $Al_2CoCrFeNi$ + 3 wt.% Sc (*b*, 1000 K; *c*, 1500 K) at 9.5 GPa.

Complete densification is achieved only with the sample treated at 9.5 GPa (Figure 3.44). During the *in situ* PXRD experiments of room-temperature compression, B2 diffraction lines broaden. This is indicative for anisotropic compression.

The rapid exsolution of a secondary *fcc* phase (a = 3.623(7) Å) from the original B2 phase occurs at circa 740 K and can be followed from its (1 1 1), (2 0 0) and (1 1 0) diffraction lines. A second event occurs at 800 K, corresponding to the formation of a second unknown phase (possibly a primitive cubic phase). The *fcc* (1 1 1) diffraction line partly overlaps with the (2 0 0) MgO diffraction line, but the (2 0 0) *fcc* line can be clearly followed. At 1500 K, the sample consists of B2 phase and 6 wt.% *fcc* phase. Upon quenching, at 450 K the first *fcc* phase undergoes exsolution of a second fcc_2 phase, whereas the B2 high-temperature high-pressure phase can be recovered (Figure 3.45, *a* and *c*).

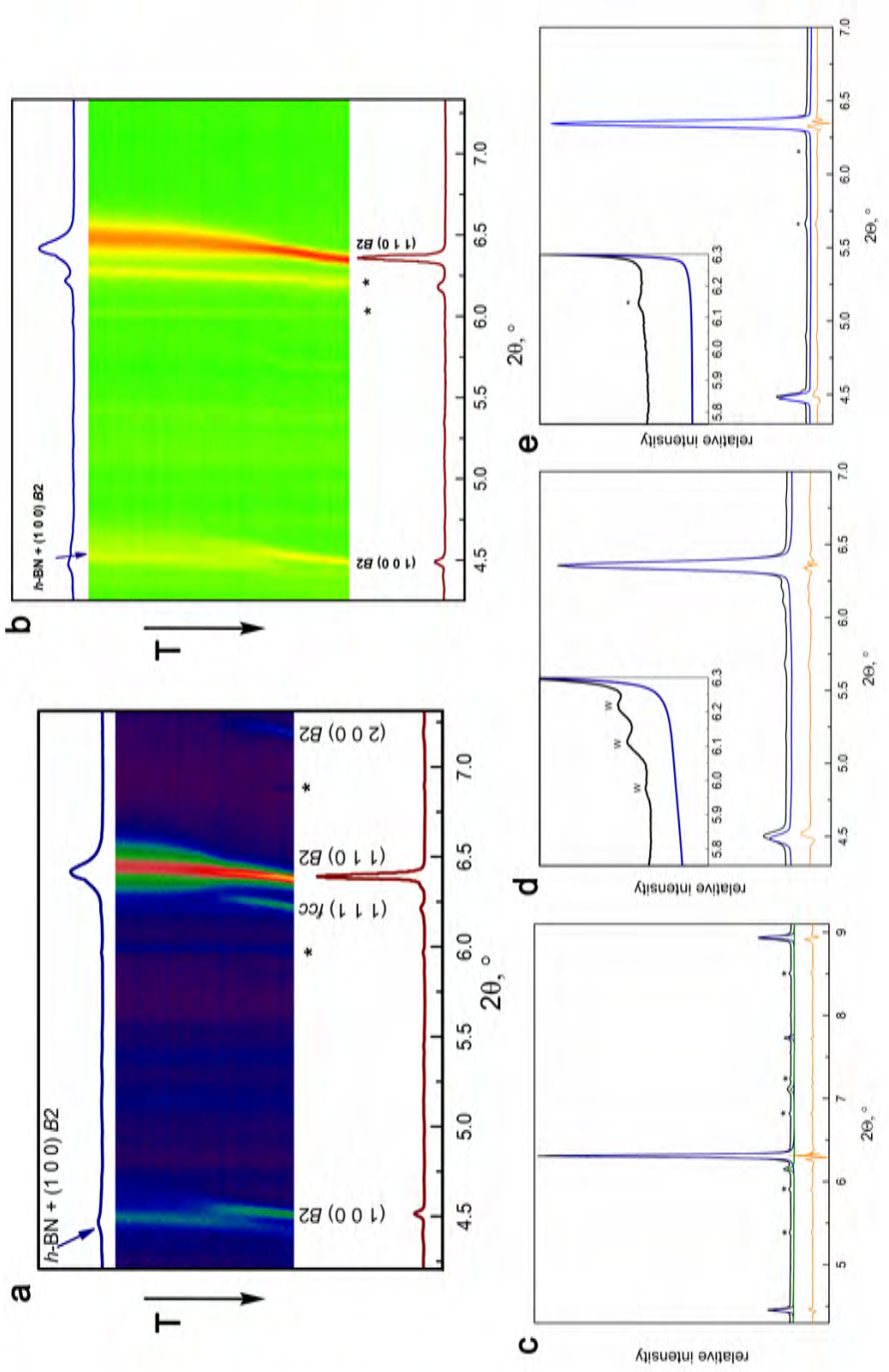

Figure 3.45: PXRD patterns collected at the ESRF ID06-LVP ($\lambda = 0.22542$ Å). Temperature dependent (from room temperature to 1500 K, 9.5 GPa) PXRD patterns for (a) $Al_2CoCrFeNi$ and (b) $Al_2CoCrFeNi$ +Sc. The appearance of the secondary *fcc* phase at circa 740 K is clearly visible in (a). (c) $Al_2CoCrFeNi$ sample recovered after 9.5 GPa compression, quenched from 1500 K. The calculated profile (*blue line*) is shifted down from experimental data (*black line*) for clarity, difference is shown below. The profile can be fitted with a B2 and an *fcc* phase. (d) $Al_2CoCrFeNi$ +Sc sample recovered after 9.5 GPa compression, quenched from 1000 K. The $MgZn_2$-type W-phase is highlighted. (e) $Al_2CoCrFeNi$ +Sc sample recovered after 9.5 GPa compression, quenched from 1500 K. All lines marked with star in the figure correspond to the assembly.

The quenched sample can be recovered and characterised further. Its microstructure is comparable with the original as cast alloy, but does not exhibit nano-structuring (Figure 3.44, *c*).

Vicker's hardness tests performed on the different $Al_2CoCrFeNi$ samples establish a direct dependence of hardness on the applied pressure (Figure 3.46).

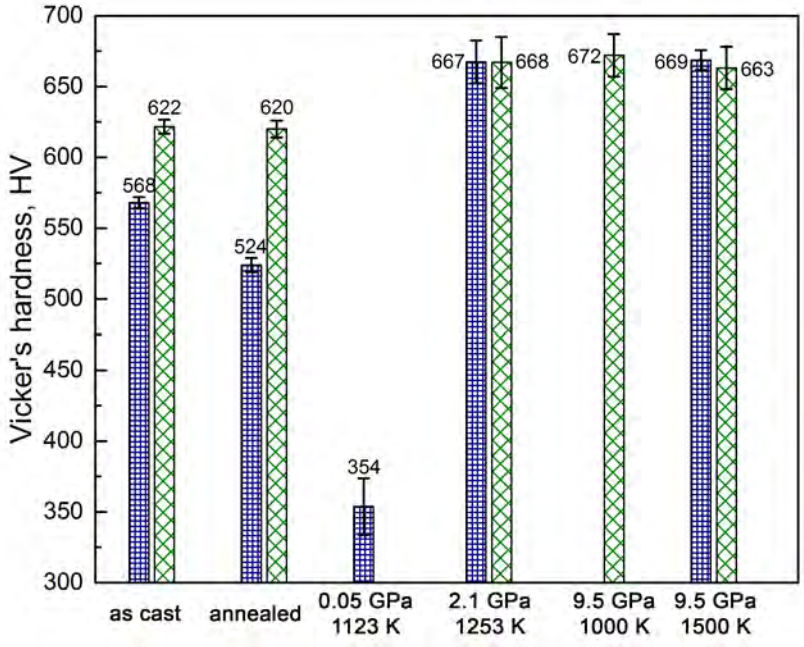

Figure 3.46: Vicker's hardness values for the $Al_2CoCrFeNi$ (*blue*) and $Al_2CoCrFeNi$ + 3 wt.% Sc (*green*) alloys. Reported values are average of 25 indentations, performed with a load of HV 1 (as-cast and annealed samples) or HV 0.2 (sintered samples). Two trends occur: hardness enhancement due to scandium addition (clearly visible at ambient pressure) and enhancement following pressure treatment and densification.

The as-cast material loses part of its internal stress during annealing, causing a decrease in hardness. The spark-plasma sintered powder, having low densification between individual particles, displays less than half the original hardness. Surprisingly, however, high-temperature treatments at 2.1 GPa and 9.5 GPa show an increase in hardness of almost 20 % compared to the original as-cast alloy (comparable to the increase obtained when 0.5 wt.% Sc was added to the pristine as cast alloy at ambient pressure, Figure 3.28).

In the light of the above results we have established the importance of pressure for the tuning of mechanical properties in HEAs. The combined influence of pressure and temperature treatments extends from B2 phase stabilisation to high-temperature resistance, microstructure refinement and hardness enhancement.

Increase complexity to achieve simplicity: The scandium effect

At room temperature and pressure, the as-cast $Al_2CoCrFeNi$+Sc alloy consists of a mixture of B2-structured alloy (a = 2.88(2) Å) and a ternary hexagonal intermetallic (detected as three diffraction lines between 5.9° – 6.3°). From element distributions and PXRD we deduce the presence of the W-phase analogue AlCuSc ($MgZn_2$ structural type) in which Al and Cu sites are occupied by either Al, Co, Fe or Ni. The ternary compound precipitates along grain boundaries causing grain refinement, whereas the B2 matrix contains only a barely detectable amount of scandium ($\leqslant$ 0.42 wt.%, corresponding to an average of 0.4 at.% in Table 3.9, Figure 3.42, *c* and *d*).

The scandium-containing alloy undergoes a reversible transition between 1023 and 1073 K and displays a set of endothermic peaks at 1179 and 1239 K. The latter correspond to phase transition and melting/crystallisation of the W-phase. From *in situ* high-temperature PXRD we link the first DSC peak to the same B2 to fcc_1+fcc_2 exsolution (a_{fcc_1} = 3.635(8) Å; a_{fcc_2} = 3.631(9) Å) occurring in the original $Al_2CoCrFeNi$ alloy (Figure 3.37, *a*). It is worth noting that the decomposition of the B2 phase at ambient pressure occurs at a significantly higher temperature in the intermetallic-containing HEA (Figure 3.37, b).

The main microstructural features of $Al_2CoCrFeNi$+Sc are maintained upon sintering at 2.1 GPa (Figure 3.43, *c*). The sample shows a homogeneous elemental distribution, probably due to the higher stability of the intermetallic phase, acting as barrier to diffusion between grains. Spinodal decomposition does not occur and the hexagonal intermetallic fills the space between grains of the main phase. The number of cavities in the scandium containing sample is noticeably less than in the scandium-free sample. PXRD shows only the main B2 phase, as the W-phase diffraction lines are masked by Al_2O_3 from the assembly (Figure 3.41, *d*).

Sintering at 9.5 GPa results in complete densification of the sample (Figure 3.44, *b* and *c*). Two events occur at 1020 K and 1330 K, probably related to a change of ordering in the B2 phase and the dissolution of the intermetallic (Figure 3.45, *b*). The diffraction lines corresponding to fcc_1, cP and fcc_2 are not present. The recovered alloy treated at 9.5 GPa and 1500 K displays a strikingly different microstructure compared with both as-cast and low-pressure materials. Not only is Cr homogeneously dispersed in the matrix, the scandium phase has partially dissolved in the matrix as well (Figure 3.44, *c*). The result is confirmed by the disappearance of the diffraction lines characteristic for the W-phase in the 9.5 GPa, 1500 K sample (Figure 3.45, *d* and Figure 3.45, *e*). Only the diffraction line belonging to MgO from the assembly can be detected in the region of interest (Figure 3.41, *f*). The recovered B2 phase has cell parameter a = 2.869(2) Å.

3.2.3 Discussion

The present work provides a wide characterisation of three common HEA systems and of the effect brought upon them by the addition of a small scandium concentration. We report $Al_2CoCrFeNi$, $Al_{0.5}CoCrCuFeNi$ and $AlCoCrCu_{0.5}FeNi$ to be B2-, *fcc*- (with a minor amount of *bcc* phase) and *bcc*+*fcc*-structured respectively. While the reported cell parameters are in agreement with the literature, the presence of ordered sub-lattices or of different secondary phases is still under debate. The structural differences of $Al_2CoCrFeNi$, $Al_{0.5}CoCrCuFeNi$ and $AlCoCrCu_{0.5}FeNi$ corresponding to nominally equal composition can be ascribed to the extreme sensitivity of the phase to synthetic pathway and compositional variations. However, *in situ* and *ex situ* investigation of alloy behaviour upon heating also points out to the existence of reversible exsolution equilibria having deep impact on phase stability. The occurrence of such phenomena at relatively low temperatures represents a concern for the actual industrial application of HEA systems.

The addition of scandium to the Al-containing HEAs results in the precipitation of a ternary intermetallic of $MgZn_2$-type along grain boundaries. The matrix coherence following the formation of the secondary phase is maintained and Vicker's hardness increases up to 20 % due to precipitation hardening (for 0.5 wt.% Sc addition to $Al_2CoCrFeNi$). The intermetallic has high thermal stability and affects the *bcc* $\longrightarrow$ *fcc* exsolution equilibrium by stabilising the body-centred cubic phase with respect to the face-centered cubic one. This effect is likely related to the segregation of part of the *fcc*-stabilising elements (*i.e.* Ni and Co) in the ternary compound. Out of *bcc*-stabilisers, aluminium segregates in the $MgZn_2$-type phase, but chromium has much lower affinity for the secondary phase and coalesces in the matrix (as highlighted by EDX results).

Lattice thermal expansion data of the B2-structured alloy with or without scandium show that both systems follow the same trend upon heating. However, the B2-phase in the scandium-containing HEA has slightly bigger cell parameters: this is further indication of compositional difference between the matrix of the two systems.

The second part of the work provides a wide investigation of the parameters which influence phase formation and stability in HEAs. We first highlight the role of HEAs powders processing route in achieving dense samples, by comparing as-cast and annealed specimens to samples obtained after spark plasma sintering and hot pressing (in either multi-anvil cell or piston cylinder press). The relatively mild experimental conditions used during SPS and in multi-anvil cell are not enough to obtain a material of density comparable with the as-cast alloy. In fact, while densification by SPS is promoted by the current flow between particles, HEAs have been reported as having higher electrical resistivity values in comparison with conventional alloys [262]. The results obtained at 2.1 GPa (1253 K) and 9.5 GPa (1000 K) with respect to the one at 9.5 GPa and 1500 K highlight the prominent role of temperature over pressure in the densification of the $Al_2CoCrFeNi$ powders. Plastic deformation and ultimately densification can only occur after appreciable interparticle bonding has taken place. This step requires

overcoming a high energetic barrier through high temperature. It is thus quite likely that densification would be aided by the occurrence of an exothermal reaction, such as the one leading to the formation of the $Al_2CoCrFeNi$ HEA from elemental powders.

The role of pressure and temperature is pivotal in every step of sample processing, because it deeply affects not only sintering but also phase stability. An in-depth study of the P-T space of a HEA system has never been attempted before. The body of experiments points out the exceptional stability of the B2 phase from ambient pressure to 9.5 GPa, as the alloy does not undergo any pressure-driven phase transitions at room temperature. Conversely, as reported in the first part of this section, heating the alloy at ambient pressure results in the exsolution of 40% of the B2 phase in two *fcc* phases (over 893 K). The behaviour of the alloy is very different when heating is performed at 9.5 GPa. The transformation occurring in the $Al_2CoCrFeNi$ HEA can be summarised as follows:

Heating at 9.5 GPa:

$$B2 \xrightarrow{740\ \mathrm{K}} B2' + fcc_1 \xrightarrow{800\ \mathrm{K}} B2'' + fcc_1 + cP \tag{3.1}$$

Quenching at 9.5 GPa:

$$B2'' + fcc_1 + cP \xrightarrow{450\ \mathrm{K}} B2'' + fcc_1 + cP + fcc_2 \tag{3.2}$$

The sample recovered after quenching consists of the B2" phase and 6 wt.% of other phases. The secondary phase, though minor, could contribute to the hardness enhancement via sintering effect with grain boundary pinning.

Finally, the effect of a homogeneous precipitate to the high-temperature high-pressure stability of the primary HEA phase is presented.

The Sc-containing $MgZn_2$-type secondary phase has previously been reported for Al-Cu-based alloys as detrimental to mechanical properties, since it inhibits the formation of the Al_3Sc intermetallic. To study its interaction with a complex matrix can thus prove useful for further tuning of functional alloys. At ambient pressure, the intermetallic leads to a 10% hardness increase and delays the B2 to *fcc* transition by an extra 150 K. The stabilisation effect could be related to the higher thermal stability of the secondary phase, acting as barrier to diffusion through grain boundaries. While either pressure or compound precipitation can singularly delay the transition from B2 to *fcc*, together they display a synergistic effect. In fact, the specimen containing 3 wt.% scandium and pressed under a load of 9.5 GPa shows no traces of *fcc* phase and can be recovered as a pure B2 phase. It displays a microstructure comparable to the original as-cast HEA, with a 20% hardness increase.

The dissolution of the intermetallic phase in the matrix at 9.5 GPa and 1500 K represents one of the unique aspects of this system. The Sc-containing $MgZn_2$-type phase is exceptionally stable, and its formation cannot be prevented by the high-entropy effect in multicomponent alloys. Nevertheless, high-pressure high-temperature treatment results in its dissolution in the HEA matrix with the formation of a single-phase Sc-doped alloy. Furthermore, this is

achieved by maintaining, and enhancing, the hardness increase. An adequate high-pressure high-temperature treatment could thus be functional in dissolving the analogous AlCuSc *W*-phase in Al-Cu alloys, while retaining the benefits of scandium additions upon quenching.

3.3 New scandium sources for materials development.

The previous sections have highlighted the role of different amounts of scandium in multi-principal components alloys. Nevertheless, further investigations of scandium metallurgy and eventually industrial applications are inevitably linked to the relatively low availability and high price of metal ingots on the market.

In order to overcome this problem, it is of the utmost importance to find new, cheaper, scandium sources. This includes scandium compounds, such as Sc_2O_3 and ScF_3, or commercially available scandium-containing alloys, such as Scalmalloy®. Both approaches have advantages and limits:

- The aluminothermical reduction of scandium oxide to form aluminium-scandium alloys is a well-known process [276]. The use of scandium compounds as scandium sources grants the additions of higher scandium concentrations, but in turn relies on the reduction of scandium by means of a second metal (generally aluminium). Therefore, every newly-developed alloy aiming to exploit this reaction should contain considerable quantities of reducing agent. Moreover, the low thermal conductivity of scandium oxide makes it unsuitable for some synthetic routes, such as induction melting.

- Scandium in its Scalmalloy®form has been successfully added to commercial alloys (*i.e.* A356), but it low concentration often falls below the detection limit of commonly used characterisation techniques [277].

In Figure 3.47 we present the first example of a scandium-doped HEA obtained by induction melting of element powder and scandium master alloy ($Al_2CoCrFeNi$ + 0.2 wt.% Sc). The alloy obtained using scandium ingots is shown as comparison.

Unfortunately, further characterisation is impossible: the lines of the $MgZn_2$-type phase, if present, could not be detected by in-house PXRD equipment.

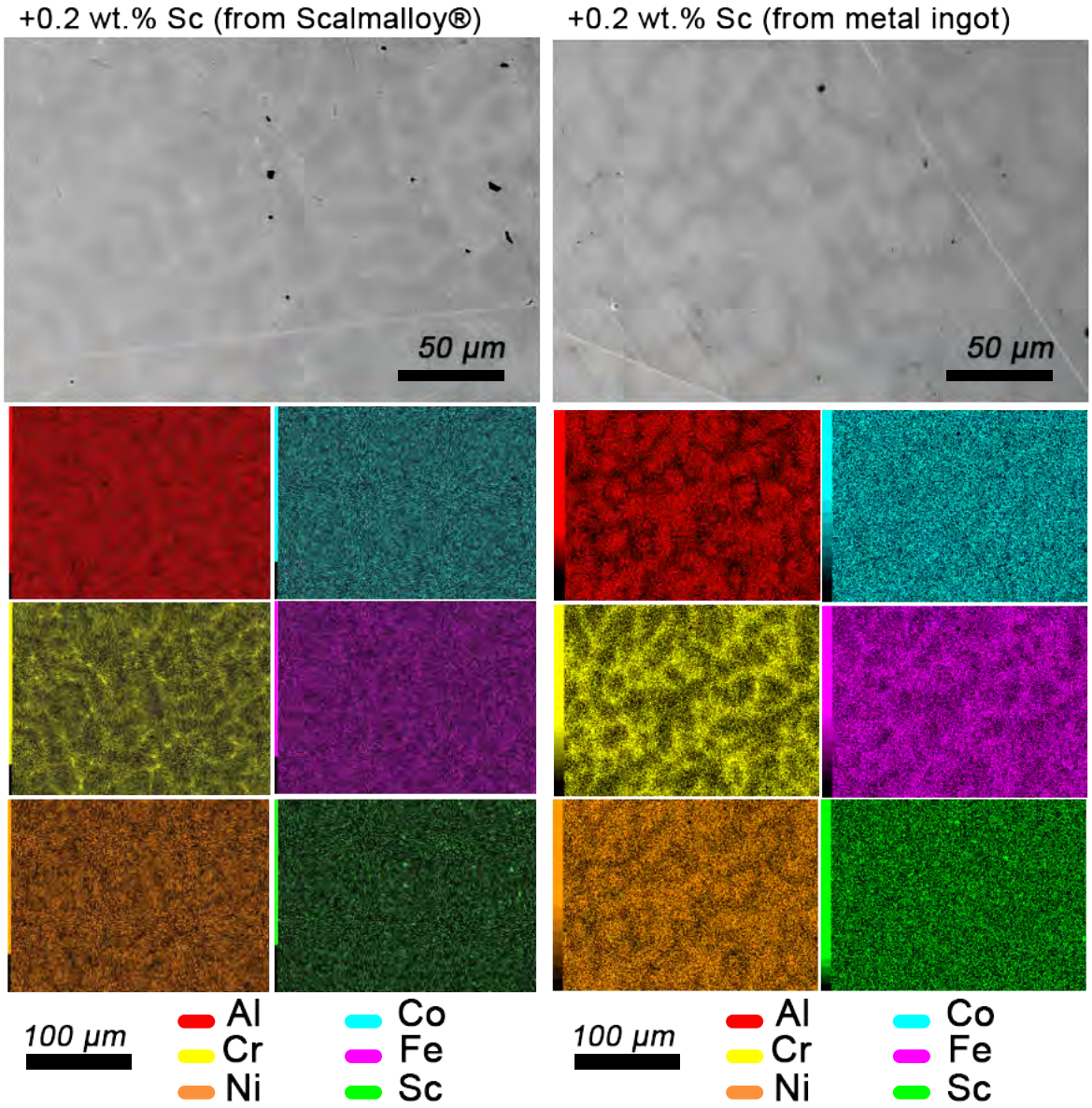

Figure 3.47: Microstructure and element distribution of the $Al_2CoCrFeNi$ HEA + 0.2 wt.% Sc (*left*) prepared from Scalmalloy®; (*right*) prepared from scandium ingots.

On the other hand, since its low thermal and electrical conductivity make Sc_2O_3 incompatible with induction melting equipment, we decided to develop a scandia-doped HEA specimen through Spark-Plasma Sintering. The $Al_2CoCrFeNi$+0.5 wt.% Sc_2O_3 sample was then compared with equally prepared samples containing diverse additives traditionally used for the development of Metal Matrix Composites. The results of this investigation are reported in the following section, and discussed in 3.3.2.

Sample code	Compositions according to EDX Maps (at. %)					Nominal material addition	Density ($g \cdot cm^{-3}$)
	Al	Co	Cr	Fe	Ni		
HEA	40.7(4)	14.0(3)	14.5(2)	16.7(2)	13.9(3)	NA	6.12(6)
HEA +nano-diamonds	41.6(3)	13.7(3)	14.7(2)	16.2(2)	13.6(3)	2 wt.%	6.12(2)
HEA +SiC	36.9(5)	14.5(3)	26.4(5)	10.5(2)	11.5(1)	2 wt.%	5.03(7)
HEA +Sc_2O_3	49.4(7)	5.9(5)	10.6(4)	10.1(2)	23.7(1)	0.5 wt.%	5.26(7)
HEA +*h*-BN	36.2(3)	15.6(2)	16.2(2)	16.9(2)	14.8(2)	3 wt.%	5.26(8)
HEA +*c*-BN	45.8(4)	14.7(4)	11.9(2)	15.8(3)	11.6(3)	2 wt.%	5.63(6)
HEA +CN	31.4(6)	17.6(6)	19.3(4)	19.2(4)	12.7(2)	1.5 wt.%	

Table 3.11: Overview of the sintered samples. The acronym 'HEA' stands for the $Al_2CoCrFeNi$ High-Entropy Alloy

3.3.1 Scandium oxide and the first generation of HEA-based Metal Matrix Composites

The current study presents preliminary results obtained while investigating the $Al_2CoCrFeNi$ HEA as a potential metal matrix for composite materials. The effect of different reinforcing agents (*i.e.* nano-diamonds, SiC, Sc_2O_3, h-BN, *c*-BN and CN) on the sintering process was evaluated to select a candidate for further characterisation and development. The blank B2-structured $Al_2CoCrFeNi$ underwent the same sintering process as its composites, whose compositions are reported in Table 3.11.

Composites created to achieve high-performance thermal management materials traditionally employ diamonds, silicon carbide or carbon nanotubes as additives [278]. Diamond is selected as a high quantity filler because it is an isotropic material with record thermal conductivity (up to 2200 $W \cdot m^{-1}K^{-1}$ for pure monocrystals) and due to its thermal expansion coefficient in metal matrix composites (MMCs), which is comparable to the one of semiconductor elements [279]. Equally high thermal conductivity is realised in silicon carbide particle reinforced aluminium [280]. Finally, carbon nanotubes have attracted much attention as promising reinforcements for MMCs due to their high strength and electrical/thermal conductivities [281, 282]. As previously mentioned, the addition of Sc_2O_3 to the HEA was justified from the need to find a cheaper route to achieve the addition of scandium in the HEA system, which is known to enhance phase stability and mechanical properties. Lastly, boron nitride is characterised by low dielectric coefficient and extreme thermal shock resistance, which make it an attractive addition to composite ceramics or to metal alloys [283, 284, 285].

All samples were spark plasma sintered into disks of 8 cm diameter and 5 mm thickness; but none of the specimens except the HEA and HEA +2 wt.% nano-diamonds retained their shape. The poor sintering of SiC-, Sc_2O_3-, BN-containing samples was confirmed by density measurements (Table 3.11), displaying up to a 20% density decrease in comparison with the HEA sample. Density measurement of the HEA +1.5 wt.% CN sample was impossible due to its extreme fragility.

More indications of samples densification can be extracted by SEM and EDX images (Figure 3.48).

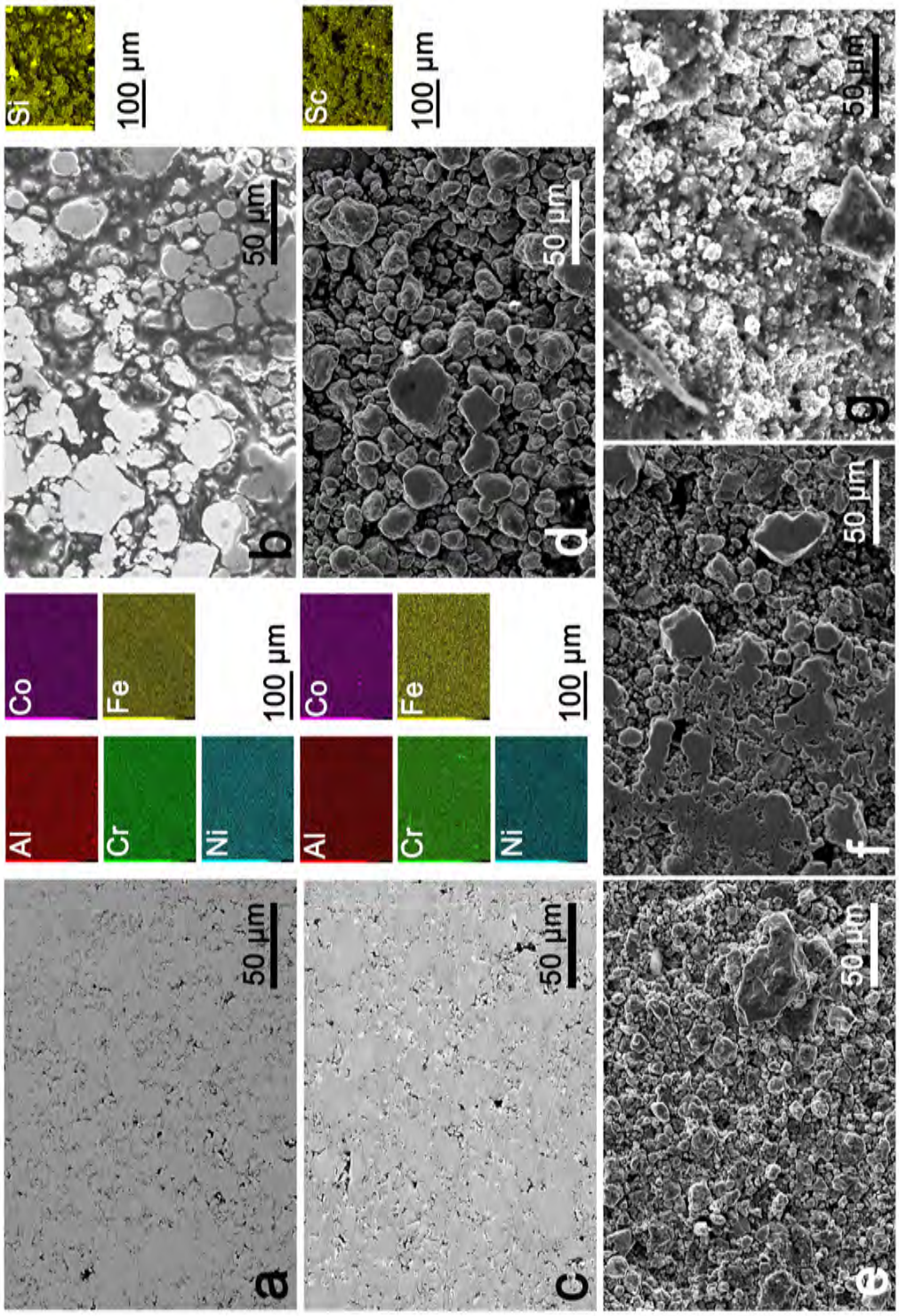

Figure 3.48: SEM and selected EDX micrographs of (*a*) $Al_2CoCrFeNi$ HEA with element distribution maps; (*b*) $Al_2CoCrFeNi$ + 2 wt.% SiC with a distribution map of Si in the sample; (*c*) $Al_2CoCrFeNi$ +2 wt.% nano-diamonds with element distribution maps of the HEA matrix; (*d*) $Al_2CoCrFeNi$ +0.5 wt.% Sc_2O_3 with a distribution map of Sc in the sample; (*e*) $Al_2CoCrFeNi$ +3 wt.% *h*-BN; (*f*) $Al_2CoCrFeNi$ +2 wt.% *c*-BN; (*g*) $Al_2CoCrFeNi$ +1.5 wt.% CN.

Spark-plasma sintering of HEA powder of 5-20 μm particle size results in homogeneous element distributions (Figure 3.48, *a*). Despite intergranular porosity, grain growth has occurred with respect to the original particle size [286]. Nevertheless, due to porosity the density of the spark-plasma sintered sample is only 92.5 % of the density of the thermally annealed sample prepared at the same temperature (see Section 3.2.2). An equally homogeneous element distribution is displayed by the nano-diamond-containing HEA (Figure 3.48, *c*). Nanodiamonds are not identifiable from composition maps, but SEM highlights the presence of a dark-coloured phase along grain boundaries. Unfortunately, the nanodiamonds dimensions fall below the detection limit of our instrument, thus the identification cannot by confirmed by morphology. We can only hypothesize that nano-diamonds are not subsumed by the matrix, but appear as inclusions; a result consistent with the previously reported absence of chemical bonding between diamonds and Al metal matrix in composites [287, 288]. This conclusion is confirmed by the XRD results reported in Figure 3.49.

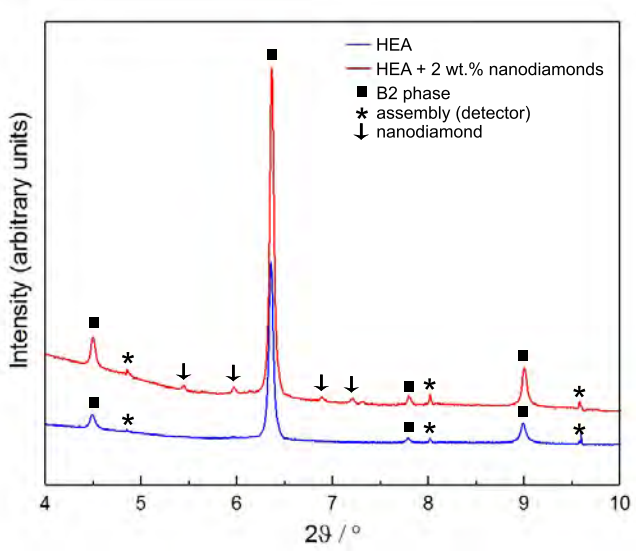

Figure 3.49: PXRD profiles obtained for $Al_2CoCrFeNi$ (*blue*) and $Al_2CoCrFeNi$ + 2 wt.% nanodiamonds (*red*) at ESRF (ID06, $\lambda = 0.22542$ Å). The lines corresponding to nanodiamond inclusions are identified with an arrow. Asterisks signal lines created during signal integration (due to the nature of the detector), squares highlight the original B2 phase.

In the case of the SiC-containing sample (Figure 3.48; *b*), the HEA demonstrates minimal capacity to penetrate the silicon clusters. It has been postulated that the incomplete densification of large elemental clusters is a result of entrapped gases and/or localised increases in electrical resistivity [249, 289]. Higher temperature and pressure might force the matrix into these features and encapsulate the SiC particles.

The traditional route to produce the commercially available Al-Sc master alloy makes use of the cheaper Sc_2O_3 as scandium source and exploits the reduction of the precursor with Al to form Al_2O_3 as by-product [276]. Nevertheless, while the studied HEA contains over 30% Al, the conditions of temperature and pressure used are not enough to achieve the dissolution

of the oxide in the HEA matrix following the formation of metallic scandium, or sample densification (Figure 3.48, *d*).

BN and CN-reinforced materials (Figure 3.48, *e*, Figure 3.48, *f* and Figure 3.48, *g*) show exceptionally poor densification behaviour even for very small additions. The poor performance of BN-bearing systems is likely connected to the high dielectric strength of BN (374 $kV \cdot mm^{-1}$), but hexagonal and cubic BN (respectively added as 3 wt.% and 2 wt.%) show quite different densification, quantifiable as a 6% density difference [192].

Out of the seven evaluated composites, only HEA +2 wt.% nano-diamonds exhibited the desired response to SPS in terms of density and elemental distribution. As such, this sample and the blank HEA were the subject of further thermal, electrical and mechanical characterisation.

Thermoelectric properties

Differential scanning calorimetry performed on the as-cast $Al_2CoCrFeNi$ alloy, on $Al_2CoCrFeNi$ powder after sintering and on the $Al_2CoCrFeNi$ +2 wt.% nano-diamonds composites are remarkably different (Figure 3.50). While the as-cast alloy presents a sigmoid-like reversible transition between 850 and 950 K, corresponding to the B2 to *fcc* phase transformation, the signal is not present in either of the sintered samples. The absence of phase transition in the interval make the system promising for further thermal and electrical characterisation.

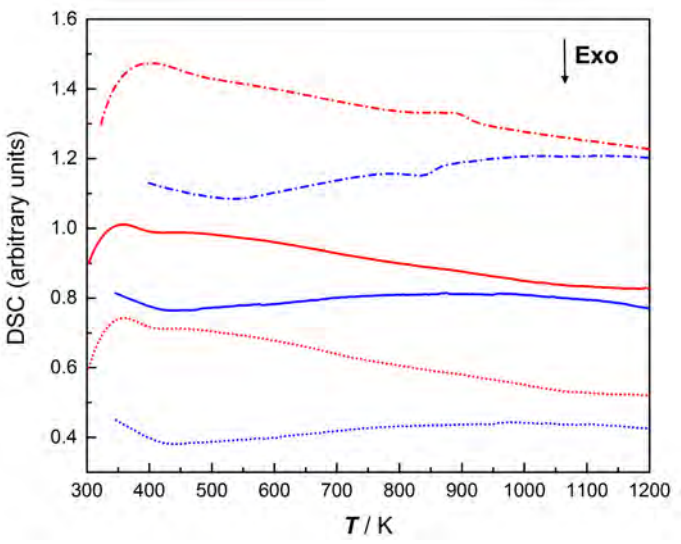

Figure 3.50: Differential scanning calorimetry (300-1200 K, 10 K/min) of as-cast $Al_2CoCrFeNi$ (*short dash*), spark-plasma sintered $Al_2CoCrFeNi$ powder (solid line) and $Al_2CoCrFeNi$ composite material containing 2 wt.% nano-diamonds (*dotted line*). Heating and cooling cycles are reported in *red* and *blue* respectively.

Diamond-reinforced aluminium composites have been proposed as promising materials for the thermal management of electronic components, due to their ideal combination of high thermal (k_{tot}) and electrical (σ) conductivity and low coefficient of thermal expansion (α_T).

Thermal conductivity values as high as 600 $W \cdot m^{-1}K^{-1}$ and 552 $W \cdot m^{-1}K^{-1}$, combined with very low α_T (7-7.5 $\cdot 10^{-5}$ K^{-1}) were reported for coated diamond particles and composites containing 50 vol.% diamond particles [288, 290, 291].

On the other hand, as cast high-entropy alloys typically have electrical resistivity between 100 and 220 $\mu\Omega \cdot$ cm, which are values much higher than conventional alloys and comparable with bulk metallic glasses [292].

Figure 3.51 reports an overview of the thermal and electrical properties of the two specimens. The sintered $Al_2CoCrFeNi$ HEA shows an electric resistivity of 225.84 $\mu\Omega \cdot$ cm at 300 K, in good agreement with the value of 211.29 $\mu\Omega \cdot$ cm at 300 K previously reported for the same as-cast alloy in pellet form (Figure 3.51, *b*) [262]. The corresponding electrical conductivity is thus slightly lower than that previously reported for the $Al_2CoCrFeNi$ HEA [293]. Electrical resistivity is constant below 850 K - a feature which might arise from electron scattering from a complex microstructure and magnetic clusters , while it increases linearly with temperature above 850 K.

The low carriers' concentration (10^{19}-10^{21} cm^{-3} between 4-300 K), decreasing with temperature, and the high lattice distortion typical for HEAs support the hypothesis of electrical resistivity being affected by phonon scattering above the Debye temperature of the alloy. Electrical resistivity of the nano-diamond composite shows the opposite trend and decreases very steeply between 300 and 400 K [294]. The specimen behaves like a semiconductor, a feature which has not been observed for diamond-containing MMCs before. Resistivity is much higher in comparison with the standard HEA as is expected considering the loss of mean free path following the introduction of the additive.

Lattice distortion and low carrier concentration are also the main reason for the increase of thermal conductivity with temperature in HEAs. This behaviour is opposite to the one shown by most pure metals in which the increase in lattice vibrations following heating result in electron scattering whose decreased mobility causes the decrease in thermal conductivity [292]. High-entropy alloys of the $Al_xCoCrFeNi$ series have been found to have low but diverse thermal conductivity (from 0.47 $W \cdot m^{-1}K^{-1}$ to 17.5 $W \cdot m^{-1}K^{-1}$ at 400 K), and the sintered HEA and the HEA nano-diamonds composite display thermal conductivity in this same range (6.9 and 7.9 $W \cdot m^{-1}K^{-1}$ at 400 K respectively, Figure 3.51, *a*) [174].

The average Seebeck coefficient values for the two systems are reported in Figure 3.51, *c*. Both composition appear to be *n*-type. While the absolute value of the Seebeck coefficient is almost constant for the HEA, it increases over a wide temperature range for the composite, reaching a maximum at 940 K ($\sim$20 μVK^{-1}).

As shown in Figure 3.51, *d*, the phononic contribution is higher for the composite than for the pure alloy on the whole temperature range. This result can be ascribed to the presence of lattice scattering points on the interface between alloy and diamonds as well as to the sintering technique.

From the power factors (σS^2) and thermoelectric figure of merit ZT ($\frac{\sigma S^2 T}{k_{tot}}$) reported in Figures 3.51, *e* and *d*, it is clear that the higher absolute Seebeck coefficient value of the

composite specimen cannot overcome its very low electrical conductivity, making it unsuitable as thermoelectric material.

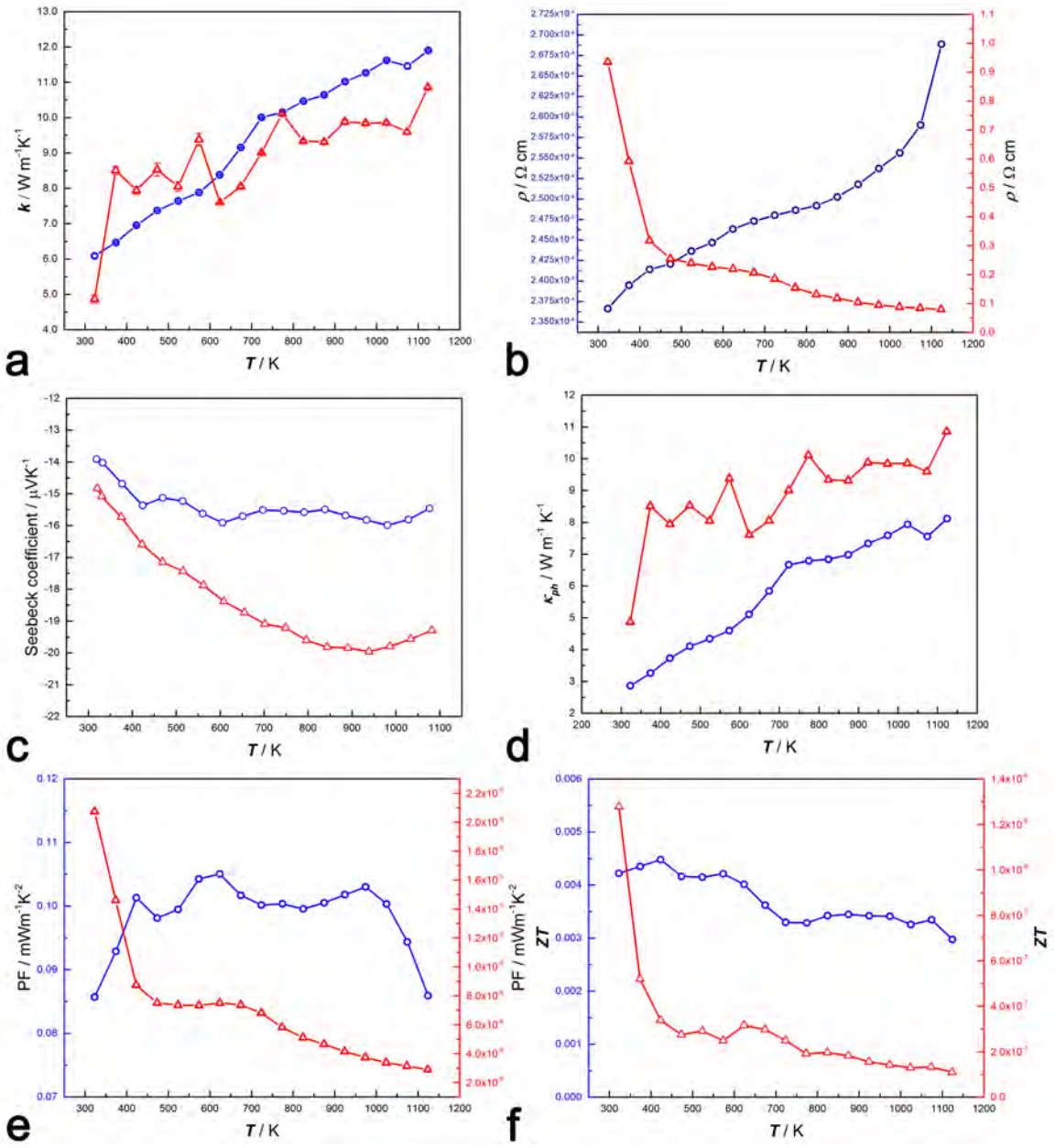

Figure 3.51: Variation of average thermoelectric figures results for $Al_2CoCrFeNi$ (*blue*) and of its composite material containing 2 wt.% nano-diamonds (*red*) with temperature (300-1150 K): (*a*) thermal conductivity (error for each measurement is shown as error bar); (*b*) electrical resistivity; (*c*) Seebeck coefficient; (*d*) calculated phononic contribution to the global thermal conductivity; (*e*) calculated power factor; (*f*) thermoelectric figure of merit ZT.

Thermal expansion

The experimental data shown in Figure 3.52, *a* clearly show that the relative length changes $\frac{\Delta L}{L_0}$ are not linearly dependent with temperature over the studied range.

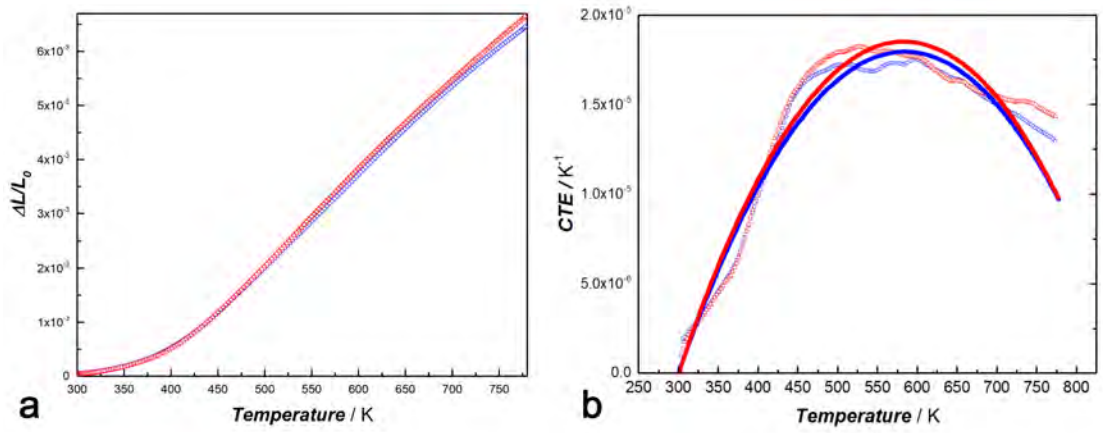

Figure 3.52: (*Left*) Thermal expansion of the $Al_2CoCrFeNi$ HEA (*blue*) and of its composite material containing 2 wt.% nano-diamonds (*red*) after spark-plasma sintering. *Right*: thermal expansion coefficient from 300 to 770 K, (*circles*) obtained as $\alpha_{T,m}$ and (*line*) obtained as thermal expansivity α_T .

Thermal expansion curves for the two materials can be fitted over the range 300 to 770 K with a polynomial equation (see Eq. 2.16). Using the fitted data for $\frac{\Delta L}{L_0}$, values of thermal expansion coefficient (α_T) and average thermal expansion coefficient $\alpha_{T,m}$) can be calculated [230]. They are reported in Figure 3.52, *b* in the range 300 to 770 K.

The expansion coefficient evaluated for $Al_2CoCrFeNi$ by *in situ* high-temperature PXRD measurements (Figure 3.38), can be obtained by fitting the corresponding dataset to Eq. 2.15. Experimental data obtained through dilatometry deviate from the PXRD values below 650 K; the effect of porosity is prominent at low temperature, and only above 650 K do the specimens behave as bulk materials. Subsequent cycles of heating and cooling reduce the hysteresis between the two curves and lead to thermal expansion values closer to lattice values above 400 K.

The exceptional behaviour of the nanodiamond composite with respect to the pristine HEA is highlighted when the experimental results are compared with the theoretical values obtained applying the Rule of Mixture (Table 3.12). Experimental values of Vicker's hardness fall short with respect to the estimated lower and upper bounds. This might be an effect of low densification of the composite material. The small difference between experimental and estimated density (calculated as per Eq 1.13) can also be ascribed to the low densification of the sample; but it is difficult to imagine that densification could have such a broad impact on thermoelectric properties. Indeed, the coefficient of thermal expansion and electrical conductivity (both estimated at 300 K according to Eq. 1.15 and 1.18) differ from the corresponding theoretical value by orders of magnitude. We can thus conclude that the used ROM fail in

	Volume fraction	Density (gcm^{-3})	$\alpha_{T,m}$, 300 K (K^{-1})	σ, 300 K (Sm^{-1})	HV
$Al_2CoCrFeNi$	0.9640	6.41(4) (bulk alloy)	$1.76(2) \cdot 10^{-6}$	$4.42(3) \cdot 10^5$	354(44)
Diamonds	0.036	3.50	$1 \cdot 10^{-6}$	$1 \cdot 10^{-17}$	10 000
Composite (ROM)		6.31	$1.79 \cdot 10^{-6}$	$4.15 \cdot 10^5$	$366 \leq \text{HV} \leq 701$
Composite (Exp)		6.12(2)	$1.39(5) \cdot 10^{-7}$	$1.08(7) \cdot 10^2$	337(30)

Table 3.12: Rule of Mixture applied to the HEA composite for the calculation of theoretical density, thermal expansion coefficient, electrical conductivity and Vicker's hardness. Tabulated values for diamond are taken from [13].

predicting the properties of the system, probably due to the poor description of the matrix and its interaction with the additive, and due to the presence of pores.

3.3.2 Discussion

In the current work the formation of composites based on the $Al_2CoCrFeNi$ HEA was investigated. Trials performed via spark-plasma sintering using hexagonal or cubic boron nitride, carbon nanotubes, silicon carbide and scandium oxide as additives failed due to their low affinity with the matrix. The addition of 2 wt.% nano-diamonds, on the other hand, resulted in a compact composite with good machinability. However, the presence of residual porosity in the sintered $Al_2CoCrFeNi$ and its nano-diamonds composite (highlighted by microscopy, density and thermal expansion results) emphasises the unsuitability of spark plasma sintering for the densification of HEA powders.

In fact, densification by SPS is promoted by the flow of current between metallic particles, and HEAs have been reported as having higher electrical resistivity values in comparison with conventional alloys. Electrical resistivity is even higher for the nano-diamond composite, and it is thus not surprising that in both samples only limited grain growth occurs with respect to the original particle size. Plastic deformation and ultimately densification require appreciable inter-particle bonding which, in the case of the investigated system, is strongly dependent on heating conditions, rather than the applied pressure. Considering that no phase transition appears between room temperature and 1200 K, complete densification might occur at higher temperature. This is also suggested by the comparison between macroscopic thermal expansion curves of the composites and lattice thermal expansion of the as-cast material: subsequent cycles of heating and cooling reduce the hysteresis between the two curves, and ultimately both composite behave as the original bulk material. In the first heating cycle, on the other hand, values obtained for the composite specimen are much lower than those for lattice expansion; consistent with the presence of porosity and localised non-homogeneities.

Even though the sintered $Al_2CoCrFeNi$ HEA and its nano-diamond composite have similar thermal behaviour, they strongly differ in terms of electrical properties. Both samples display high electrical resistance due to the high lattice distortion typical of multi-principal component alloys and by the loss of mean free path following the introduction of the additive. The phononic contribution to scattering is thus higher for the composite than for the sintered alloy. However, while in the alloy electrical resistivity increases with temperature, the opposite holds true for the nano-diamond composite.

While promising as forefather of a new class of materials (HEA Composites), the properties of the reported composite are still far from ideal. If we compare it with the commercially-available Dymalloy® (an alloy of 80% Ag and 20% Cu containing up to 55 wt.% diamonds, used to dissipate heat in microelectronic components because of its extremely high thermal conductivity, [295]), the $Al_2CoCrFeNi$ + 2 wt.% nanodiamonds HEAC proves to be sensibly cheaper, but cannot compete in term of thermal conductivity. The comparison between our specimens and commercial systems for some thermal and electric properties are reported in the following pages.

Figure 3.53 highlights that our specimens have density higher than the target Dymalloy®,

but lower than any commercial alloy comprising the same elements. While this low density can be ascribed to the uncomplete densification of the sample during SPS, it is interesting to note that the trend is maintained for the bulk Al_2CoCrFeNi and CoCrFeNi multi-principal component alloys. Even with a thermal conductivity comparable to the one of commercial bulk alloys (Co-based superalloys, Ni-Cr-Fe alloys, Ni-Fe INVAR alloys), our specimens are still very far from the performances required to substitute Dymalloy®.

The same conclusions can be drawn from the Ashby map reported as Figure 3.54. The thermal properties of our specimens make them closer to commercial bulk alloys than to Dymalloy®. It is possible that, by changing the relative percentages of elements in the alloy, the CTE can be lowered; whereas, in order to enhance thermal conductivity, different additives should be considered, to maintain the economic advantage of using cheap, widely available elements.

Finally, the comparison of thermoelectrical properties (Figure 3.55) between our HEA systems and commercial bulk alloys highlights the good similarity between Al_2CoCrFeNi and Ni-Cr-Co alloys. They show comparable electrical resistivity and thermal conductivity, slightly higher thermal expansion coefficient and sensibly lower density. However, as these alloys are generally used for high-temperature applications, even a small difference in CTE can prove to be disruptive.

The relative similarity between HEAs and Ni-Cr-Co alloys make the behaviour of the diamond composite even more striking. In fact, its electrical resistivity is several orders of magnitude higher than any of the considered metal and alloy system (Figure 3.55).

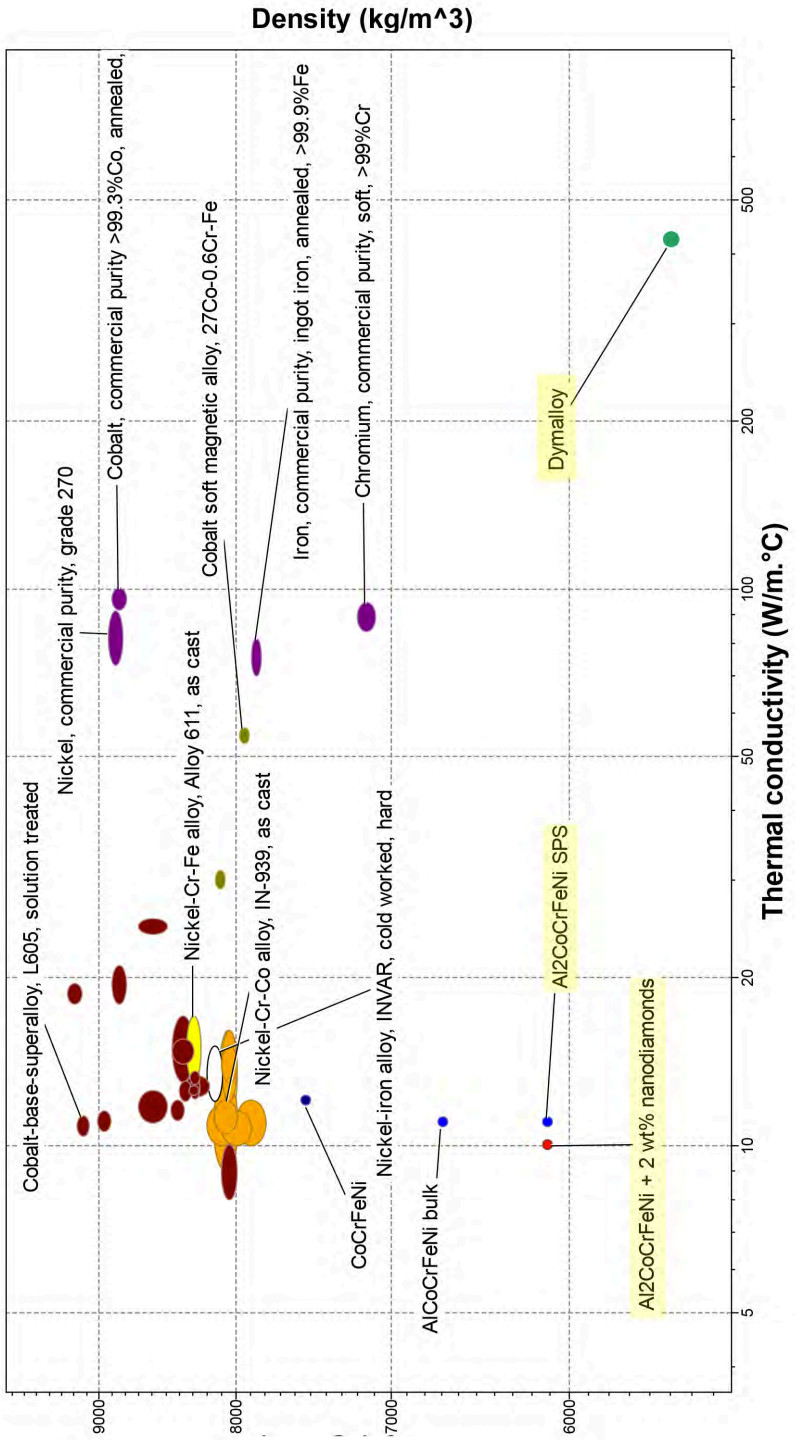

Figure 3.53: Ashby map of density *vs* thermal conductivity prepared with the CES Edupack2017 Software and corresponding database. Only bulk materials were considered, and of those only the elements constituting the HEA and their commercial alloys. They are reported as families with the following colour codes: elements of commercial purity (*purple*), Co soft magnetic alloys (*olive*), Co-based superalloy (*burgundy*), Ni-Cr-Fe alloys (*yellow*), Ni-Co-Cr alloys (*orange*), Ni-Fe INVAR alloy (*white*), first-raw metal HEAs (*blue*), $Al_2CoCrFeNi$ + 2 wt.% nanodiamonds (*red*), Dymalloy® (*green*).

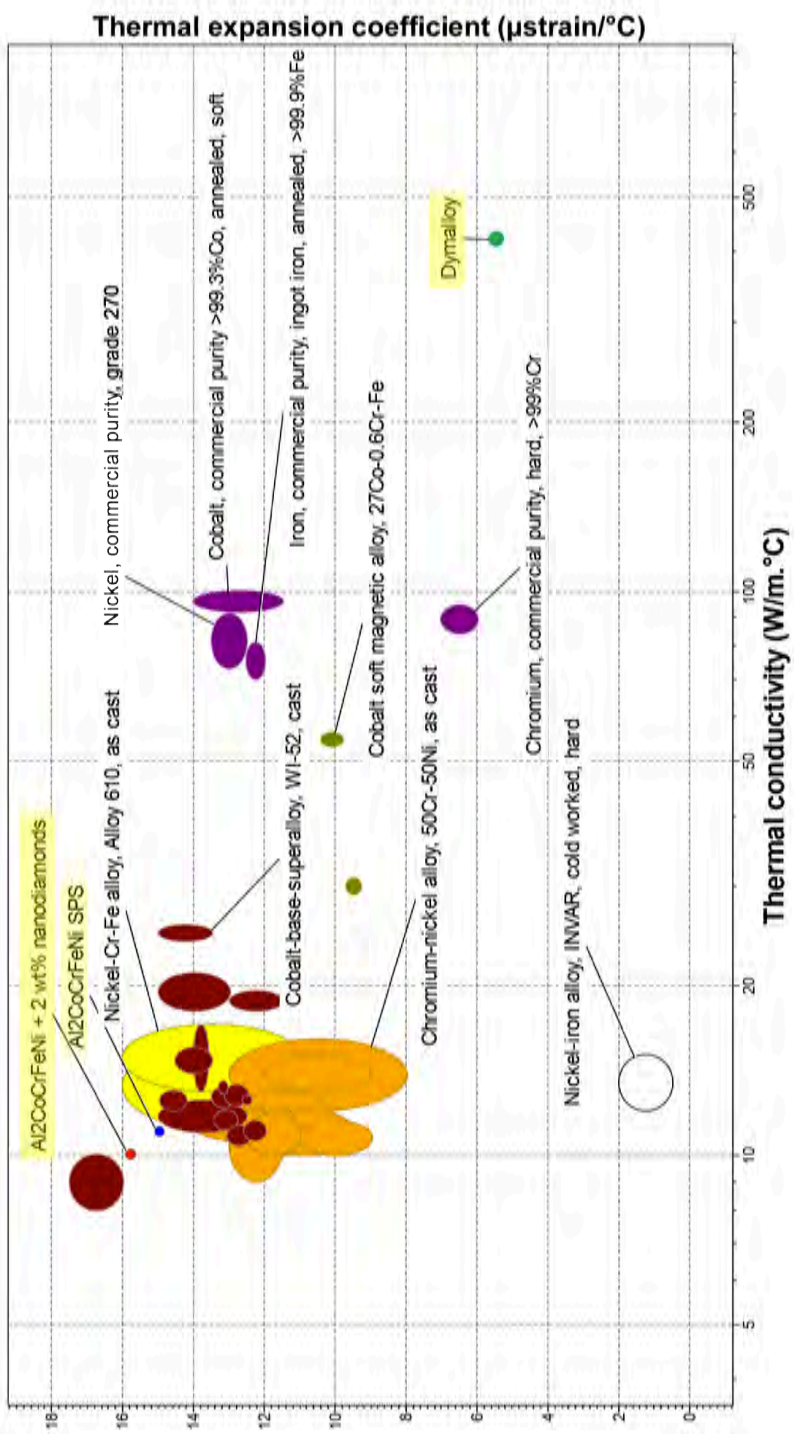

Figure 3.54: Ashby map of CTE *vs* thermal conductivity prepared with the CES Edupack2017 Software and corresponding database. Only bulk materials were considered, and of those only the elements constituting the HEA and their commercial alloys; materials with density $\leq 3000 Kgm^3$ were excluded. The results are reported as families with the following colour codes: elements of commercial purity (*purple*), Co soft magnetic alloys (*olive*), Co-based superalloy (*burgundy*), Ni-Cr-Fe alloys (*yellow*), Ni-Co-Cr alloys (*orange*), Ni-Fe INVAR alloy (*white*), first-raw metal HEAs (*blue*), $Al_2CoCrFeNi$ + 2 wt.% nanodiamonds (*red*), Dymalloy® (*green*).

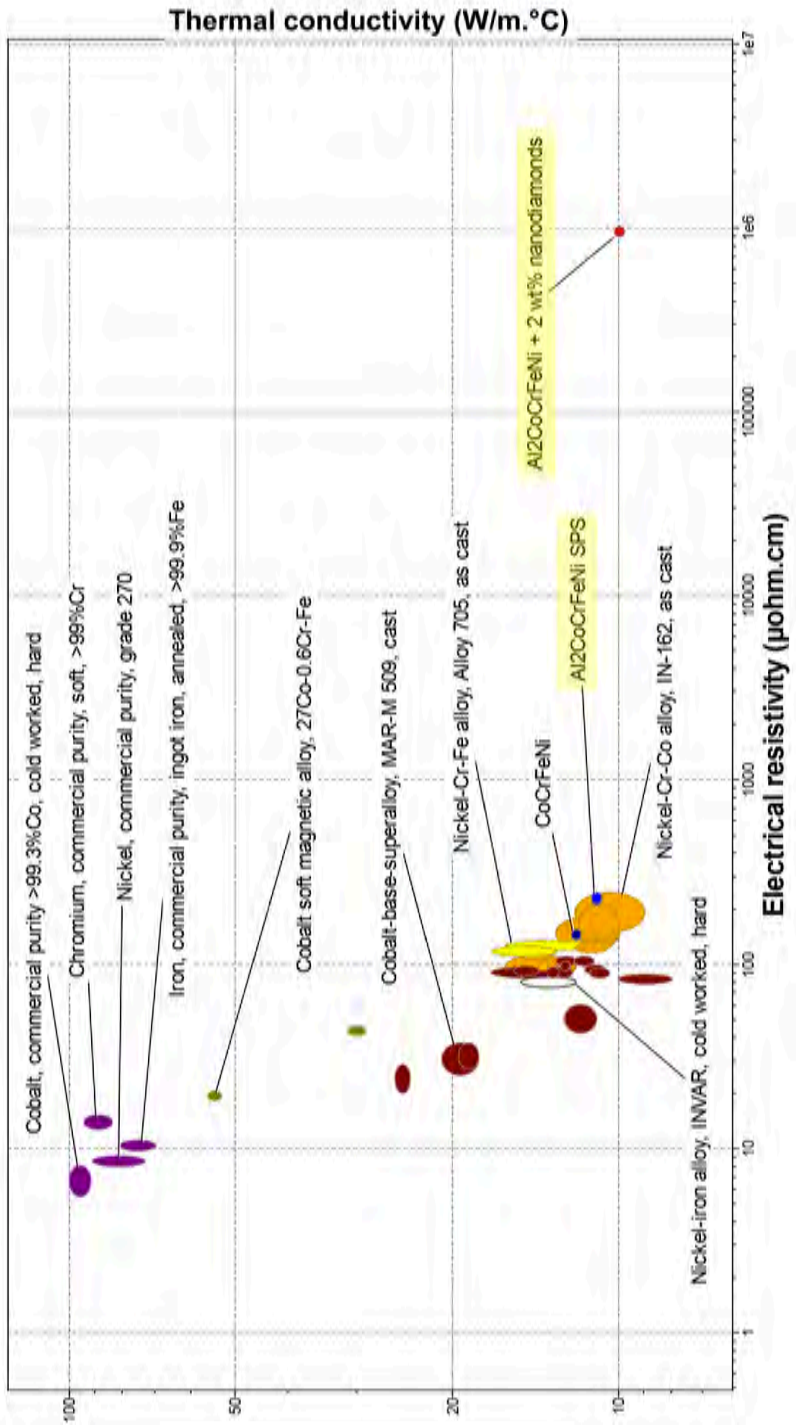

Figure 3.55: Ashby map of thermal conductivity *vs* electrical conductivity prepared with the CES Edupack2017 Software and corresponding database. Only bulk materials were considered, and of those only the elements constituting the HEA and their commercial alloys; materials with density $\leq 3000 Kgm^3$ were excluded. The results are reported as families with the following colour codes: elements of commercial purity (*purple*), Co soft magnetic alloys (*olive*), Co-based superalloy (*burgundy*), Ni-Cr-Fe alloys (*yellow*), Ni-Co-Cr alloys (*orange*), Ni-Fe INVAR alloy (*white*), first-raw metal HEAs (*blue*), $Al_2CoCrFeNi$ + 2 wt.% nanodiamonds (*red*).

Chapter 4

Conclusion and future perspectives

Despite its excellent elemental properties, lightweight nature and good alloying potential, scandium has received relatively little attention in the manufacturing community. The use of scandium is conventionally restricted to minor additions to alloys in structural applications. In this frame the role of scandium is that of a compound-forming elements, whose intermetallics deeply affects the properties of the matrix. The term 'scandium effect' came thus to indicate the positive influence of small scandium additions to multicomponent alloys.
The development of a new class of alloys displaying formidable compositional complexity and microstructural variation opened the doors for new scandium applications. High-Entropy Alloys (HEAs) are multi-principal components alloys displaying simple structures – solid solution(s), intermetallic compounds, or both – in a limited number of crystalline phases. These effects have been often ascribed to the predominance of mixing entropy with respect to the enthalpy of formation of compounds.

Scandium appeared to be a suitable candidate for new alloy's systems. Since it displays physic-chemical similarities both with first raw metals and with rare-earth elements, we studied two separate equimolar systems which took advantage of its affinities. The synthesis and investigation of the AlCrCuScTi alloy led to the identification of the so-called W-phase, previously reported only in Al-based Cu-containing alloys. Conversely, scandium formed complex multi-phase systems with other *hcp*-structured metals (namely Co, Gd, Ti, Y and Zr). In both cases mixing entropy did not succeeded in hindering the formation of numerous intermetallic compounds.

Even when scandium was added in small amounts to HEA compositions, it caused the segregation of a secondary phase. Addition of 0.5-5 wt.% Sc to $Al_2CoCrFeNi$, $Al_{0.5}CoCrCuFeNi$ and $AlCoCrCu_{0.5}FeNi$ brought about the formation of a hexagonal Laves phase, in which each site could be occupied by each metal with equal probability. This is not surprising, considering that AlCoSc, $Al_{1.06}Cr_{0.94}Sc$, AlCuSc, AlFeSc and AlNiSc all crystallise in the $MgZn_2$-type structure.

The B2-structured $Al_2CoCrFeNi$ HEA proved to be the most interesting system, since as

little as a 0.5 wt. % scandium addition could enhance hardness by 20 %. Further investigations on the phase stability of the doped alloy also highlighted the postponement of the $B2 \longrightarrow fcc_1 + fcc_2$ exsolution by roughly 150 °C, with respect to the original HEA.

A subsequent in-depth investigation of the P–T space of the $Al_2CoCrFeNi$ and $Al_2CoCrFeNi$ + 5 wt.% Sc systems highlighted the exceptional stability of the B2 phase from ambient pressure to 9.5 GPa at room temperature. At 9.5 GPa and 1500 K, however, the original $Al_2CoCrFeNi$ transformed into a recoverable high-pressure phase and underwent exsolution of a face-centred and a primitive cubic phase. While either pressure or compound precipitation can singularly delay the exsolution, together they display a synergistic effect. In fact, after the Sc-containing HEA has been heated at 9.5 GPa, no traces of secondary phases can be found: the original $MgZn_2$-type intermetallic has dissolved in the matrix. The resulting sample can thus be considered as a single-phase scandium-doped HEA.

Since further development of scandium metallurgy relies heavily on its availability on the market, and in the light of the successful results obtained for small scandium addition in HEAs, we deemed it pivotal to look for alternative scandium sources. Preliminary tests performed using Scalmalloy® as scandium metal source for a 0.2 wt.% addition in $Al_2CoCrFeNi$ proved possible, but an in-depth characterisation of the material was prevented by the detection limit of our in-house techniques. On the other hand, Sc_2O_3 required an entirely different approach, since its low thermal and electrical conductivity made it incompatible with traditional melting routes. By mixing Sc_2O_3 with $Al_2CoCrFeNi$ alloyed powder and spark-plasma sinter it, we hoped to exploit the redox reaction occurring between the oxide and aluminium. While this trial proved unsuccessful, from the diverse additives used in the same conditions sprang a material which can be rightfully considered the first example of a HEA-based Matrix Composite. This is the $Al_2CoCrFeNi$ + 2 wt.% nanodiamonds specimen, which was thoroughly characterised as per its thermal and electrical properties.

The challenges to overcome in order to elevate scandium from a laboratory-based curiosity to the status of mainstream alloying element are not limited to its high cost. Scandium has a relatively high melting point and is practically impossible to mill, features which make it difficult to exploit its low density in the creation of new alloys (for example, with lithium or magnesium). In this context, the development of new scandium sources is essential: our pioneering investigations should be extended further and more compounds should be taken into consideration as potential scandium metal wells.

Meanwhile, the dissolution of a highly-stable scandium intermetallic in a multi-principal component matrix and the consequent formation of a Sc-doped single-phase HEA could be the basis for a new type of alloy's treatment. We suggest that an adequate P–T treatment could dissolve the detrimental W-phase in Al-based Cu-containing commercial alloys.

In the Introduction chapter, it was highlighted that the knowledge about scandium is quite fragmented. This work gave some answers and raised many more questions. The

author strongly believes that, for scandium to be effectively used in functional and structural materials, more detailed investigation are needed. The role of its single *d*-electron, which is often ascribed as the cause of its unpredictable behaviour, should be better understood and modelled.

Only then will it be possible to explore more of this uncharted territory.

Bibliography

[1] R. K. Smith, The quest for excellence. Milestones of aviation, New York: Crescent Books, 1991.

[2] E. A. Starke and J. T. Staley, Application of modern aluminum alloys to aircraft Progress in Aerospace Sciences, vol. 32, no. 2, pp. 131–172, 1996.

[3] A. G. Malikov, A. A. Golyshev, and M. Y. Ivanova, Influence of scandium on the microstructure and strength properties of the welded joint at the laser welding of aluminum-lithium alloys in XXV Conference on High-Energy Processes in Condensed Matter, vol. 1893, p. 030005, AIP Publishing, 2017.

[4] J. C. Williams and E. A. Starke Jr, Progress in structural materials for aerospace systems Acta Mat., vol. 51, no. 19, pp. 5775–5799, 2003.

[5] I. N. Fridlyander, Aluminium alloys in aircraft in the periods of 1970-2000 and 2001-2015 Met. Sci. Heat Treat., vol. 43, no. 1-2, pp. 6–10, 2001.

[6] I. N. Fridlyander, Russian aluminium alloys for aerospace and transport applications Mat. Sci. Forum, vol. 331-337, pp. 921–926, 2000.

[7] Z. Ahmad, The properties and application of scandium-reinforced aluminum JOM, vol. 55, no. 2, pp. 35–39, 2003.

[8] W. T. Tack, Aluminium-scandium alloys US Patent 5597529, 1997.

[9] F. T. A. Panel, FTAP First Cycle, Final Report tech. rep., 2012.

[10] D. Hunn, Lockheed Martin armor developments Adv. Mater. Process., vol. 164, no. 10, p. 23, 2006.

[11] C. T. Horovitz, K. A. Gschneidner Jr, G. A. Melson, D. H. Youngblood, and H. H. Schock, Scandium: Its occurrence, chemistry, physics, metallurgy, biology and technology. London, UK: Academic Press Inc. Ltd., 1975.

[12] S. A. Wood and I. M. Samson, The aqueous geochemistry of gallium, germanium, indium and scandium Ore Geo. Rev., vol. 28, no. 1, pp. 57–102, 2006.

[13] G. V. Samsonov, Handbook of the physicochemical properties of the elements. New York: IFI / Plenum, 1968.

[14] D. R. Kammler, M. A. Rodriguez, R. G. Tissot, D. W. Brown, B. Clausen, and T. A. Sisneros, In-situ time-of-flight neutron diffraction study of high-temperature α-to-β-phase transition in elemental scandium Met. Mater. Trans. A, vol. 39, no. 12, pp. 2815–2819, 2008.

[15] M. Debessai, J. J. Hamlin, and J. S. Schilling, Comparison of the pressure dependences of T_c in the trivalent d-electron superconductors Sc, Y, La, and Lu up to megabar pressures Phys. Rev. B, vol. 78, p. 064519, 2008.

[16] C. Buzea and K. Robbie, Assembling the puzzle of superconducting elements: A review Supercond. Sci. Technol., vol. 18, 2005.

[17] S. Riva, K. V. Yusenko, N. P. Lavery, D. J. Jarvis, and S. G. R. Brown, The scandium effect in multicomponent alloys Int. Mat. Rev., vol. 61, no. 3, pp. 1–26, 2016.

[18] D. Seipler, B. Bremicker, U. Goebel, H. Happel, H. Hoenig, and B. Perrin, Electronic structure of intermetallic compounds with CsCl structure J. Phys. F: Met. Phys., vol. 7, no. 4, p. 599, 1977.

[19] V. G. Khoruzhaya and K. E. Kornienko, Metal chemistry of scandium in binary systems formed with platinum-group metals as the basis for construction multicomponent systems based on those metals Pow. Metall. Met. Ceram., vol. 40, no. 7-8, pp. 362–373, 2001.

[20] N. Yurchenko, N. Stepanov, and G. Salishchev, Laves-phase formation criterion for hih-entropy alloys Mat. Sci. Tec., vol. 11, no. 1, pp. 17–22, 2016.

[21] B. Y. Kotur, Crystal chemistry of ternary intermetallic compounds of scandium with transition metals and carbon, silicon or germanium J. All. Compd., vol. 219, no. 1–2, pp. 88–92, 1995.

[22] A. F. Reid and A. E. Ringwood, High-pressure scandium oxide and its place in the molar volume relationships of dense structures of M_2X_3 and ABX_3 type Journal of Geophysical Research, vol. 74, no. 12, pp. 3238–3252, 1969.

[23] S. M. Sharma and N. Garg, Chapter 1 - Material Studies at High Pressure, pp. 1–47. Amsterdam: Elsevier, 2017.

[24] E. Y. Tonkov, Compounds and alloys under high pressure: A handbook. Amsterdam, The Netherlands: Gordon and Breach Science Publishers, 1998.

[25] X. Liu, R. Ehrl, and K.-J. Range, High pressure synthesis and structures of scandium-zinc intermetallic compounds $ScZn_2$, Sc_3Zn_{17} and $Sc_{13}Zn_{58}$ Rev. High Pressure Sci. Technol., vol. 7, pp. 1016–1018, 1998.

[26] J. Grewe, J. S. Schilling, K. Ikeda, and K. A. Gschneidner, Anomalous behavior of the weak itinerant ferromagnet Sc_3In under hydrostatic pressure Physical Review B, vol. 40, no. 13, pp. 9017–9024, 1989. PRB.

[27] B. Y. Kotur, Scandium binary and ternary alloy systems and intermetallic compounds Croatica Chem. Acta, vol. 71, no. 3, pp. 635–658, 1998.

[28] J. T. Staley and W. Haupin, Aluminum and aluminum alloys. John Wiley & Sons, Inc., 2000.

[29] J. Røyset and N. Ryum, Scandium in aluminium alloys Int. Mat. Rev., vol. 50, no. 1, pp. 19–44, 2005.

[30] V. V. Zakharov and T. D. Rostova, On the possibility of scandium alloying of copper-containing aluminum alloys Metal Science and Heat Treatment, vol. 37, no. 2, pp. 65–69, 1995.

[31] M. L. Kharakterova, Phase composition of Al–Cu–Sc alloys at temperatures of 450 °C and 500 °C Russ. Metall., vol. 4, pp. 195–199, 1991.

[32] M. Y. Teslyuk and W. M. Protasov, Crystal structures of ternary phases in the Al–Cu–Sc system Crystal. Rep., vol. 10, no. 4, pp. 561–562, 1965.

[33] M. Jia, Z. Zheng, and Z. Gong, Microstructure evolution of the 1469 Al–Cu–Li–Sc alloy during homogenization J. All. Compd., vol. 614, pp. 131–139, 2014.

[34] M. Gazizov, V. Teleshov, V. Zakharov, and R. Kaibyshev, Solidification behaviour and the effects of homogenisation on the structure of an Al–Cu–Mg–Ag–Sc alloy J. All. Compd., vol. 509, no. 39, pp. 9497–9507, 2011.

[35] S. He, Y. Liu, Z. Li, H. Wu, and B. Huang, Thermal stability and crystallization behaviour in Y–based metallic glasses Metall. Mat. Trans. A, vol. 39, no. 8, pp. 1797–1803, 2008.

[36] N. G. Bukhanko, E. F. Kazakova, and E. M. Sokolovskaya, Interaction of aluminium with cobalt and scandium Russ. Metall., vol. 4, pp. 425–431, 2001.

[37] V. Raghavan, Al–Co–Sc (aluminium-cobalt-scandium) J. Phase Equilib. Diff., vol. 30, no. 2, pp. 179–180, 2009.

[38] P. Villars, K. Cenzual, and R. Gladyshevskii, Handbook of inorganic substances 2015. Berlin: De Gruyter, 2015.

[39] P. Nandi, S. Suwas, S. Kumar, and K. Chattopadhyay, The effect of minor addition of Ni on the microstructural evolution and mechanical properties of suction cast Al-0.14 at.% Sc Binary Alloy Metall. Mat. Trans. A, vol. 44, no. 6, pp. 2591–2603, 2013.

[40] M. Očko, E. Babic, R. Krsmik, E. Girt, and B. Leontic, Some properties of AlSc solid solutions Journal of Physics F: Metal Physics, vol. 6, no. 5, p. 703, 1976.

[41] Y. A. Bazin, P. S. Popel, B. P. Domashnikov, V. M. Zamyatin, and B. A. Baum, Possible causes of the modification and hardening of aluminum by scandium. Izv. Vyssh. Uchebn. Zaved., Tsvet. Met., vol. 5, no. 101, 1984.

[42] I. G. Brodova, P. S. Popel, and G. I. Eskin, Liquid metal processing: Applications to Aluminium alloy production. London: Taylor & Francis, 2002.

[43] V. V. Zakharov, Stability of the solid solution of scandium in aluminum Metal Science and Heat Treatment, vol. 39, no. 2, pp. 61–66, 1997.

[44] I. G. Brodova, I. V. Polents, and P. S. Popel, The effect of master alloy structure upon grain refinement of aluminium alloys with zirconium Phys. Met. Metall., vol. 76, no. 5, p. 508, 1993.

[45] S. Komura, P. B. Berbon, M. Furukawa, Z. Horita, M. Nemoto, and T. G. Langdon, High strain rate superelasticity in an Al-Mg alloy containing scandium Scripta Mat., vol. 38, no. 12, pp. 1851–1856, 1998.

[46] T. D. Rostova, V. G. Davydov, V. I. Yelagin, and V. V. Zakharov, Effect of scandium on recrystallization of aluminium and its alloys Mat. Sci. Forum, vol. 331-337, pp. 793–798, 2000.

[47] S. Lee, A. Utsunomiya, H. Akamatsu, K. Neishi, M. Furukawa, Z. Horita, and T. G. Langdon, Influence of scandium and zirconium on grain stability and superplastic ductilities in ultrafine-grained Al–Mg alloys Acta Materialia, vol. 50, no. 3, pp. 553–564, 2002.

[48] V. V. Zakharov, Industrial aluminum alloys with scandium additive Metal Science and Heat Treatment, vol. 37, no. 7, pp. 283–285, 1995.

[49] I. G. Brodova, I. G. Shirinkina, O. V. Antonova, A. V. Chirkova, S. V. Dobatkin, and V. V. Zakharov, Evolution of the structure and phase composition of rapidly solidified Al-Mg-Mn-Sc-Zr alloys during deformation in a bridgman anvil Russian Metallurgy (Metally), vol. 2010, no. 4, pp. 328–334, 2010.

[50] H. Fujii, M. Sugamata, J. Kaneko, and M. Kubota, Effect of scandium addition on rapidly solidified Al-transition metals alloys Mat. Sci. Forum, vol. 396-402, pp. 245–250, 2002.

[51] V. G. Davydov, V. I. Elagin, V. V. Zakharov, and D. Rostoval, Alloying aluminum alloys with scandium and zirconium additives Metal Science and Heat Treatment, vol. 38, no. 8, pp. 347–352, 1996.

[52] V. I. Elagin, V. V. Zakharov, and T. D. Rostova, Scandium-alloyed aluminum alloys Metal Science and Heat Treatment, vol. 34, no. 1, pp. 37–45, 1992.

[53] E. Clouet, L. Lae, T. Epicier, W. Lefebvre, M. Nastar, and A. Deschamps, Complex precipitation pathways in multicomponent alloys Nat. Mat., vol. 5, no. 6, pp. 482–488, 2006. 10.1038/nmat1652.

[54] Y. V. Milman, D. V. Lotsko, and O. I. Sirko, 'Sc effect' of improving mechanical properties in aluminium alloys Mat. Sci. Forum, vol. 331-337, no. 1-3, pp. 1107–1112, 2000.

[55] Y. V. Milman, Scandium effect on increasing mechanical properties of aluminium alloys High Temp. Mat. Pr.-ISR, vol. 25, pp. 1–10, 2006.

[56] T. Svistunova, O. Bobkova, and B. Belyasov, Effect of scandium on structure and properties of corrosion-resistant steel Metal Science and Heat Treatment, vol. 50, no. 5-6, pp. 214–219, 2008.

[57] I. N. Igoshin, Y. A. Bazin, B. A. Baum, B. D. Raspopova, and B. P. Domashnikov, Effect of scandium on properties of 35KHGSL steel in liquid and solid state Steel in the USSR, vol. 18, no. 1, pp. 39–40, 1988.

[58] B. A. Parker, Z. F. Zhou, and P. Nolle, The effect of small additions of scandium on the properties of aluminium alloys Journal of Materials Science, vol. 30, no. 2, pp. 452–458, 1995.

[59] W. Wang and C. Y. Cheng, Separation and purification of scandium by solvent extraction and related technologies: a review Journal of Chemical Technology & Biotechnology, vol. 86, no. 10, pp. 1237–1246, 2011.

[60] S. Jaireth, D. M. Hoatson, and Y. Miezitis, Geological setting and resources of the major rare-earth-element deposits in Australia Ore Geology Reviews, vol. 62, no. 0, pp. 72–128, 2014.

[61] T. Zingg, T. Richmond, and H. J. Guntherodt, Electronic transport properties of glassy Fe–Sc alloys Mat. Sci. Eng. A, vol. 99, pp. 179–182, 1988.

[62] M. F. Braun, K. P. Scheltz, E. F. Wassermann, and M. Ghafari, Relaxation studies of the remnant magnetization in the spin glass-like state of amorphous $Fe_{90}(Zr_xSc_y)_{10}$ alloys J. Phys. Coll., vol. 49, no. C-8, pp. 1165–1166, 1988.

[63] D. R. Vujic, D. A. Lohemeier, and S. H. Whang, Occurrence of glassy phases in Sc–Co and Sc–Ni systems Int. J. Rapid Solid., vol. 5, no. 277-298, 1990.

[64] X. L. Wang, F. Jiang, H. Hahn, J. C. Li, H. Gleiter, J. Sun, and J. X. Fang, Plasticity of scandium-based nanoglass Scripta Mat., vol. 98, pp. 40–43, 2015.

[65] X. K. Xi, S. Li, R. J. Wang, D. Q. Zhao, M. X. Pan, and W. H. Wang, Bulk scandium–based metallic glasses J. Mat. Res., vol. 20, no. 9, pp. 2243–2247, 2005.

[66] K. M. Youssef, A. J. Zaddach, C. Niu, D. L. Irving, and C. C. Koch, A novel low-density, high-hardness, high-entropy alloy with close-packed single-phase nanocrystalline structures Mat. Res. Lett., vol. 3, no. 2, pp. 95–99, 2014.

[67] J. W. Yeh, S. K. Chen, S. J. Lin, J. Y. Gan, T. S. Chin, T. T. Shun, C. H. Tsau, and S. Y. Chang, Nanostructured high-entropy alloys with multiple principal elements: novel alloy design concepts and outcomes Adv. Eng. Mat., vol. 6, no. 5, pp. 299–303, 2004.

[68] B. Cantor, I. T. H. Chang, P. Knight, and A. J. B. Vincent, Microstructural development in equiatomic multicomponent alloys Mat. Sci. Eng. A, vol. 375-377, pp. 213–218, 2004.

[69] O. N. Senkov, J. M. Scott, S. V. Senkova, D. B. Miracle, and C. F. Woodward, Microstructure and room temperature properties of a high-entropy TaNbHfZrTi alloy J. All. Compd., vol. 509, no. 20, pp. 6043–6048, 2011.

[70] Y. Zhang, X. Yang, and P. K. Liaw, Alloy design and properties optimization of high-entropy alloys JOM, vol. 64, no. 7, pp. 830–838, 2012.

[71] G. Laplanche, A. Kostka, O. M. Horst, G. Eggeler, and E. P. George, Microstructure evolution and critical stress for twinning in the CrMnFeCoNi high-entropy alloy Acta Mat., vol. 118, pp. 152–163, 2016.

[72] H. Chen, A. Kauffmann, B. Gorr, D. Schliephake, C. Seemüller, J. N. Wagner, H. J. Christ, and M. Heilmaier, Microstructure and mechanical properties at elevated temperatures of a new Al-containing refractory high-entropy alloy Nb-Mo-Cr-Ti-Al J. All. Compd., vol. 661, pp. 206–215, 2016.

[73] D.-Y. Yu and Y. Zhang, The ultrahigh charpy impact toughness of forged Al_xCoCrFeNi high entropy alloys at room and cryogenic temperatures Intermetall., vol. 70, pp. 24–28, 2016.

[74] B. Gludovatz, A. Hohenwarter, K. V. S. Thurston, H. Bei, Z. Wu, E. P. George, and R. O. Ritchie, Exceptional damage-tolerance of a medium-entropy alloy CrCoNi at cryogenic temperatures Nat. Comm., vol. 7, p. 10602, 2016.

[75] C.-H. Tsau and P.-Y. Lee, Microstructures of $Al_{7.5}Cr_{22.5}Fe_{35}Mn_{20}Ni_{15}$ high-entropy alloy and its polarization behaviours in sulfuric acid, nitric acid and hydrochloric acid solutions Entropy, vol. 18, p. 288, 2016.

[76] Z. Y. Zheng, X. C. Li, C. Zhang, and J. C. Li, Microstructure and corrosion behaviour of the FeCoNiCuSn_x high entropy alloys. Mat. Sci. Tec., vol. 31, no. 10, pp. 1148–1152, 2015.

[77] A. Poulia, E. Georgatis, A. Lekatou, and A. E. Karantzalis, Microstructure and wear behavior of a refractory high entropy alloy Int. J. Refrac. Met. Hard Mat., vol. 57, pp. 50–63, 2016.

[78] M. A. Hemphill, T. Yuan, G. Y. Wang, J. W. Yeh, C. W. Tsai, A. Chuang, and P. K. Liaw, Fatigue behavior of $Al_{0.5}$CoCrCuFeNi high entropy alloys Acta Mat., vol. 60, no. 16, pp. 5723–5734, 2012.

[79] A. T. Samaei, M. M. Mirsayar, and M. R. M. Aliha, The microstructure and mechanical behavior of modern high temperature alloys Eng. Sol. Mech., vol. 3, pp. 1–20, 2015.

[80] J. Antonaglia, X. Xie, Z. Tang, C. W. Tsai, J. W. Qiao, Y. Zhang, M. O. Laktionova, E. D. Tabachnikova, J. W. Yeh, O. N. Senkov, M. C. Gao, J. T. Uhl, P. K. Liaw, and K. A. Dahmen, Temperature effect on deformation and serration behavior of high-entropy alloys (HEAs) JOM, vol. 66, pp. 2002–2008, 2014.

[81] A. M. Manzoni, S. Singh, H. M. Daoud, R. Popp, R. Vö lkl, U. Glatzel, and N. Wanderka, On the path to optimizing the Al-Co-Cr-Co-Fe-Ni-Ti high entropy alloy family for high temperature applications Entropy, vol. 18, p. 104, 2016.

[82] D. B. Miracle and O. N. Senkov, A critical review of high entropy alloys and related concepts Acta Mat., vol. 122, pp. 448–511, 2017.

[83] U. Dahlborg, J. Cornide, M. Calvo-Dahlborg, T. C. Hansen, A. Fitch, Z. Leong, S. Chambreland, and R. Goodall, Structure of some CoCrFeNi and CoCrFeNiPd multicomponent HEA alloys by diffraction techniques J. All. Compd., vol. 681, pp. 330–341, 2016.

[84] L. J. Santodonato, Y. Zhang, M. Feygenson, C. M. Parish, M. C. Gao, R. J. K. Weber, J. C. Neuefeind, Z. Tang, and P. K. Liaw, Deviation from high-entropy configurations in the atomic distributions of a multi-principal-element alloy Nat. Comm., vol. 6, 2015.

[85] M. C. Gao, J. W. Yeh, P. K. Liaw, and Y. Zhang, High-entropy alloys: Fundamentals and applications. Switzerland: Springer, 2016.

[86] Y.-L. Chen, C.-W. Tsai, C.-C. Juan, M.-H. Chuang, J.-W. Yeh, T.-S. Chin, and S.-K. Chen, Amorphization of equimolar alloys with HCP elements during mechanical alloying J. All. Compd., vol. 506, pp. 210–215, 2010.

[87] A. Takeuchi, K. Amiya, T. Wada, K. Yubuta, and W. Zhang, High-entropy alloys with a hexagonal close-packed structure designed by equi-atomic alloy strategy and binary phase diagrams JOM, vol. 66, no. 10, pp. 1984–1992, 2014.

[88] A. Takeuchi, K. Amiya, T. Wada, and K. Yubuta, Dual HCP structures formed in senary ScYLaTiZrHf multi-principal-element alloy Intermetallics, vol. 69, pp. 103–109, 2016.

[89] R. Li, J. Gao, and K. Fan, Study to microstructure and mechanical properties of Mg containing high entropy alloys Mater. Sci. Forum, vol. 650, pp. 265–271, 2010.

[90] K. V. Yusenko, S. Riva, P. A. Carvalho, M. V. Yusenko, S. Arnaboldi, A. S. Sukhikh, M. Hanfland, and S. A. Gromilov, First hexagonal close packed high-entropy alloy with outstanding stability under extreme conditions and electrocatalytic activity for methanol oxidation Scripta Mat., vol. 138, pp. 22–27, 2017.

[91] J. W. Yeh, Physical metallurgy of high-entropy alloys JOM, vol. 67, no. 10, pp. 2254–2261, 2005.

[92] A. Takeuchi and A. Inoue, Mixing enthalpy of liquid phase calculated by Miedema's scheme and approximated with sub-regular solution model for assessing forming ability of amorphous and glassy alloys Intermetall., vol. 18, no. 9, pp. 1779–1789, 2010.

[93] A. Sharma, P. Singh, D. D. Johnson, P. K. Liaw, and G. Balasubramaniana, Atomistic clustering-ordering and high-strain deformation of an $Al_{0.1}$CrCoFeNi high-entropy alloy Sci. Rep., vol. 6, p. 31028, 2016.

[94] D. A. Porter and K. E. Easterling, Phase Transformations in Metals and Alloys. Wokingham, England: Van Nostrand Reinhold Co Ltd., 1984.

[95] E. P. Gyftopoulos and G. P. Beretta, Thermodynamics: Foundations and applications. New York, USA: Dover Publications, INC, 2005.

[96] B. S. Murty, J. W. Yeh, and S. Ranganathan, High-entropy alloys. Oxford, UK: Elsevier Inc., 2014.

[97] C.-J. Tong, M.-R. Chen, S.-K. Chen, J.-W. Yeh, T.-T. Shun, S.-J. Lin, and S.-Y. Chang, Mechanical performance of the Al_xCoCrCuFeNi high-entropy alloy system with multiprincipal elements Metall. Mater. Trans. A, vol. 36 A, pp. 1263–1271, 2005.

[98] J. M. Zhu, H. M. Fu, H. F. Zhang, A. M. Wang, H. Li, and Z. Q. Hu, Synthesis and properties of multiprincipal component AlCoCrFeNiSi_x alloys Mat. Sci. Eng. A, vol. 527, no. 27–28, pp. 7210–7214, 2010.

[99] J. M. Zhu, H. M. Fu, H. F. Zhang, A. M. Wang, H. Li, and Z. Q. Hu, Microstructures and compressive properties of multicomponent AlCoCrFeNiMo_x alloys Mater. Sci. Eng. A, vol. 527, pp. 6975–6979, 2010.

[100] Y. F. Ye, Q. Wang, J. Lu, C. T. Liu, and Y. Yang, High-entropy alloy: challenges and prospects Mat. Today, vol. 19, no. 6, pp. 349–362, 2016.

[101] Z. Wang, W. Qiu, Y. Yang, and C. T. Liu, Atomic-size and lattice-distortion effects in newly developed high-entropy alloys with multiple principal elements Intermetall., vol. 64, pp. 63–69, 2015.

[102] M. Calvo-Dahlborg, J. Cornide, J. Tobola, D. Nguyen-Manh, J. S. Wróbel, J. Juraszek, S. Jouen, and U. Dahlborg, Interplay of electronic, structural and magnetic properties

as the driving feature of high-entropy CoCrFeNiPd alloys J. Phys. D: Applied Phys., vol. 50, no. 18, p. 185002, 2017.

[103] K.-Y. Tsai, M.-H. Tsai, and J. W. Yeh, Sluggish diffusion in Co–Cr–Fe–Mn–Ni high-entropy alloys Acta Mat., vol. 61, no. 13, pp. 4887–4897, 2013.

[104] M.-H. Tsai and J.-W. Yeh, High-entropy alloys: a critical review Mater. Res. Lett., vol. 2, pp. 107–123, 2014.

[105] O. N. Senkov, J. D. Miller, D. B. Miracle, and C. Woodward, Accelerated exploration of multi-principal element alloys with solid solution phases Nat. Comm., vol. 6, p. 6529, 2015.

[106] R. Kozak, A. S. Sologubenko, and W. Steurer, Single-phase high-entropy alloys – an overview Z. Kristallog., 2014.

[107] W. Hume-Rothery, G. W. Mabbott, and K. M. Channel-Evans, The freezing points, melting points, and solid solubility limits of the alloys of silver and copper with the elements of the B Sub-Groups. Philos. Trans., R. Soc. London, 1934.

[108] W. Hume-Rothery, Factors affecting the stability of metallic phases. Phase Stability in Metals and Alloys, New York, USA: McGraw-Hill, 1967.

[109] Y. Quéré, Physics of materials. Amsterdam, The Netherlands: Gordon and Breach Science Publishers, 1998.

[110] U. Mizutani, H. Sato, M. Inukai, M. Nishino, and E. S. Zijlstra, Electrons per atom ratio determination and Hume-Rothery electron concentration rule for P-based polar compounds studied by FLAPW-Fourier calculations Inorg. Chem., vol. 54, pp. 930–946, 2015.

[111] J. M. Zhang, R. G. Evans, and S. Yang, The prediction of solid solubility of alloys: developments and applications of Hume-Rothery's rules, J. Crystalliz. Phys. Chem., vol. 1, pp. 103–119, 2010.

[112] G. P. Tiwari and R. V. Ramanujan, The relation between the electron to atom ratio and some properties of metallic systems J. Mat. Sci., vol. 36, pp. 271–183, 2001.

[113] M. Calvo-Dahlborg and S. G. R. Brown, Hume-Rothery for HEA classification and self-organizing map for phases and properties prediction J. All. Compd., vol. 724, pp. 353–364, 2017.

[114] T. B. Massalski, Comments Concerning Some Features of Phase Diagrams and Phase Transformations Mat. Trans., vol. 51, pp. 583–596, 2010.

[115] S. Guo, Phase selection rules for cast high entropy alloys: an overview Mater. Sci. Technol., vol. 31, pp. 1223–1230, 2015.

[116] A. Takeuchi and A. Inoue, Classification of bulk metallic glasses by atomic size difference, heat of mixing and period of constituent elements and its application to characterization of the main alloying element Mater. Trans. JIM, no. 2817-2829, 2005.

[117] X. Yang and Y. Zhang, Prediction of high-entropy stabilized solid-solution in multi-component alloys Mater. Chem. Phys., vol. 132, pp. 233–238, 2012.

[118] Y. Zhang, Y. J. Zhou, J. P. Lin, G. L. Chen, and P. K. Liaw, Solid-solution phase formation rules for multi-component alloys Adv. Eng. Mat., vol. 10, pp. 534–538, 2008.

[119] M. G. Poletti and L. Battezzati, Electronic and thermodynamic criteria for the occurrence of high entropy alloys in metallic systems Acta Mat., vol. 75, pp. 297–306, 2014.

[120] Z.-S. Nong, J.-C. Zhu, Y. Cao, X.-W. Yang, Z. H. Lai, and Y. Liu, Stability and structure prediction of cubic phase in as cast high entropy alloys Mater. Sci. Technol., vol. 30, pp. 363–369, 2014.

[121] M.-X. Ren, B.-X. Li, and H.-Z. Fu, Formation condition of solid solution type high-entropy alloy Trans. Nonferrous Metals Soc. China (English Edition), vol. 23, pp. 991–995, 2013.

[122] I. Toda-Caraballo and P. E. J. Rivera-Díaz-del Castillo, A criterion for the formation of high entropy alloys based on lattice distortion Intermetall., vol. 71, pp. 76–87, 2016.

[123] J. W. Yeh, Alloy design strategies and future trends in high-entropy alloys JOM, vol. 65, pp. 1759–1771, 2013.

[124] C. J. Tong, Y. L. Chen, S. K. Chen, J. W. Yeh, T. T. Shun, C. H. Tsau, S. J. Lin, and S. Y. Chang, Microstructure characterization of Al_xCoCrCuFeNi high-entropy alloy system with multi-principal elements Metall. Mater. Trans. A, vol. 36A, pp. 881–893, 2005.

[125] F. Zhang, C. Zhang, S. L. Chen, J. Zhu, W. S. Cao, and U. R. Kattner, An understanding of high entropy alloys from phase diagram calculations Calphad, vol. 45, pp. 1–10, 2014.

[126] C. Y. Hsu, C. C. Juan, S. T. Chen, T. S. Sheu, S. T. Chen, J. W. Yeh, and S. K. Chen, Phase diagrams of high-entropy alloy system Al–Co–Cr–Fe–Mo–Ni J. Appl. Meteorol., vol. 65, no. 1829–1839, 2013.

[127] C. L. Tracy, S. Park, R. D. R., S. J. ZInkle, H. Bei, M. Lang, R. C. Ewing, and W. L. Mao, High pressure synthesis of a hexagonal close-packed phase of the high-entropy alloy CrMnFeCoNi Nat. Comm., vol. 8, p. 15634, 2017.

[128] Y. L. Chen, Y. H. Hu, C. W. Tsai, J. W. Yeh, S. K. Chen, and S. Y. Chang, Structural evolutions during mechanical milling and subsequent annealing of Cu–Ni–Al–Co–Cr–Fe–Ti alloys Mater. Chem. Phys., vol. 118, pp. 354–361, 2009.

[129] Q. Hu, S. Guo, J. M. Wang, Y. H. Yan, S. S. Chen, D. P. Lu, K. M. Liu, J. Z. Zou, and X. R. Zeng, Parametric study of amorphous high-entropy alloys formation from two new perspectives: atomic radius modification and crystalline structure of alloying elements Sci. Rep., vol. 7, p. 39917, 2017.

[130] H. W. Chang, P. K. Huang, A. Davison, J. W. Yeh, C. H. Tsau, and C. C. Yang, Nitride films deposited from an equimolar Al–Cr–Mo–Si–Ti alloy target by reactive DC magnetron sputtering Thin Solid Films, vol. 516, pp. 6402–6408, 2008.

[131] M. H. Tsai, J. W. Yeh, and J. Y. Gan, Diffusion barrier properties of AlMoNbSiTaTiVZr high-entropy alloy layer between copper and silicon Thin Solid Films, vol. 516, pp. 5527–5530, 2008.

[132] L. Liu, J. B. Zhu, C. Hou, J. C. Li, and Q. Jiang, Dense and smooth amorphous films of multicomponent FeCoNiCuVZrAl high-entropy alloy deposited by direct current magnetron sputtering Mat. Design, vol. 46, pp. 675–679, 2013.

[133] P. F. Yu, L. J. Zhang, J. L. Ning, M. Z. Ma, X. Y. Zhang, Y. C. Li, P. K. Liaw, G. Li, and R. P. Liu, Pressure-induced phase transitions in HoDyYGdTb high-entropy alloy Mat. Lett., vol. 196, pp. 137–140, 2017.

[134] G. Li, D. Xiao, P. Yu, L. Zhang, P. Liaw, Y. Li, and R. Liu, Equation of State of an AlCoCrCuFeNi High-Entropy Alloy JOM, vol. 67, no. 10, pp. 2310–2313, 2015.

[135] Y. Dong, Y. Lu, J. Kong, J. Zhang, and T. Li, Microstructure and mechanical properties of multi-component AlCrFeNiMo$_x$ high-entropy alloys J. All. Compd., vol. 537, pp. 96–101, 2013.

[136] M.-H. Chuang, M.-H. Tsai, C.-W. Tsai, N.-H. Yang, S.-Y. Chang, J.-W. Yeh, S.-K. Chen, and S.-J. Lin, Intrinsic surface hardening and precipitation kinetics of $Al_{0.3}CrFe_{1.5}MnNi_{0.5}$ multi-component alloy J. All. Compd., vol. 551, no. 0, pp. 12–18, 2013.

[137] S. T. Chen, W. Y. Tang, Y. F. Kuo, S.-Y. Chen, C.-H. Tsau, T.-T. Shun, and J.-W. Yeh, Microstructure and properties of age-hardenable $Al_xCrFe_{1.5}MnNi_{0.5}$ alloys. Mater. Sci. Eng. A, vol. 527, pp. 5818–5825, 2010.

[138] W. H. Liu, Z. P. Lu, J. Y. He, J. H. Luan, Z. J. Wang, B. Liu, Y. Liu, M. W. Chen, and C. T. Liu, Ductile CoCrFeNiMo$_x$ high entropy alloys strengthened by hard intermetallic phases Acta Mat., vol. 116, pp. 332–342, 2016.

[139] S. Niu, H. Kou, T. Guo, Y. Zhang, J. Wang, and J. Li, Strengthening of nanoprecipitations in an annealed $Al_{0.5}$CoCrFeNi high entropy alloy Mat. Sci. Eng. A, vol. 671, pp. 82–86, 2016.

[140] F. He, Z. Wang, S. Niu, Q. Wu, J. Li, J. Wang, C. T. Liu, and Y. Dang, Strengthening the $CoCrFeNiNb_{0.25}$ high entropy alloy by FCC precipitate J. All. Compd., vol. 667, pp. 53–57, 2016.

[141] B. S. Li, Y. P. Wang, M. X. Ren, C. Yang, and H. Z. Fu, Effects of Mn, Ti and V on the microstructure and properties of AlCrFeCoNiCu high entropy alloys Mat. Sci. Eng. A, vol. 498, pp. 482–486, 2008.

[142] U. S. Hsu, U. D. Hung, J. W. Yeh, S. K. Chen, Y. S. Huang, and C. C. Yang, Alloying behavior of iron, gold and silver in AlCoCrCuNi-based equimolar high-entropy alloys Mat. Sci. Eng. A, vol. 460-461, pp. 403–408, 2007.

[143] M.-H. Tsai, A.-C. Fan, and H.-A. Wang, Effect of atomic size difference on the type of major intermetallic phase in arc-melted CoCrFeNiX high-entropy alloys J. All. Compd., vol. 695, p. 1479–1487, 2017.

[144] I. A. Ibrahim, F. A. Mohamed, and E. J. Lavernia, Particulate reinforced metal matrix composites – a review Journal of Materials Science, vol. 26, no. 5, pp. 1137–1156, 1991.

[145] H. Prasad, S. Singh, and B. B. Panigrahi, Mechanical activated synthesis of alumina dispersed FeNiCoCrAlMn high entropy alloy J. All. Compd., vol. 692, pp. 720–726, 2017.

[146] L. Rogal, D. Kalita, A. Tarasek, P. Bobrowski, and F. Czerwinski, Effect of SiC nanoparticles on microstructure and mechanical properties of the CoCrFeMnNi high entropy alloy J. All. Compd., vol. 708, pp. 344–352, 2017.

[147] S. Riva, A. Tudball, S. Mehraban, N. P. Lavery, S. G. R. Brown, and K. Y. Yusenko, A novel high-entropy alloy-based composite material J. All. Compd., submitted.

[148] W. D. Callister Jr., Materials science and engineering: An introduction. New York, USA: Wiley & Sons, 1985.

[149] H. S. Kim, On the rule of mixtures for the hardness of particle reinforced composites Materials Science and Engineering: A, vol. 289, no. 1, pp. 30–33, 2000.

[150] A. L. Geiger and J. A. Walker, The processing and properties of discontinuously reinforced aluminum composites JOM, vol. 43, no. 8, pp. 8–15, 1991.

[151] K. Pietrak and T. S. Wiśniewski, A review of models for effective thermal conductivity of composite materials J. Power Techn., vol. 95, no. 1, pp. 14–24, 2015.

[152] E. H. Kerner, The elastic and thermo-elastic properties of composite media Proceedings of the Physical Society. Section B, vol. 69, no. 8, p. 808, 1956.

[153] H. A. Bruck and B. H. Rabin, Evaluation of Rule-of-Mixtures prediction of thermal expansion in powder-processed Ni-Al_2O_3 composites J. Am. Ceram. Soc., vol. 82, no. 10, pp. 2927–2930, 1999.

[154] P. S. Turner, Thermal-expansion stresses in reinforced plastics J. Res. NBS, vol. 37, pp. 239–246, 1946.

[155] R. A. Schapery, Thermal expansion coefficients of composite materials based on energy principles Journal of Composite Materials, vol. 2, no. 3, pp. 380–404, 1968.

[156] R. Lord Rayleigh Sec., On the influence of obstacles arranged in rectangular order upon the properties of a medium Philosophical Magazine Series 5, vol. 34, no. 211, pp. 481–502, 1892.

[157] R. Hill, The elastic behaviour of a crystalline aggregate Proceedings of the Physical Society. Section A, vol. 65, no. 5, p. 349, 1952.

[158] L. Li, L. Huang, X. Song, F. Ye, J. Lin, and G. Cheng, Microstructure and performance of TiAlBeSc alloys with low density Rare Met. Mater. Eng., vol. 5, pp. 826–829, 2012.

[159] Y. C. Lin and Y. H. Cho, Elucidating the microstructural and tribological characteristics of NiCrAlCoCu and NiCrAlCoMo multicomponent alloy cladlayers synthesized in situ. Surf. Coat. Technol., vol. 203, pp. 1694–1701, 2009.

[160] Y. Zhang, T. T. Zuo, Z. Tang, M. C. Gao, K. A. Dahmen, P. K. Liaw, and Z. P. Lu, Microstructures and properties of high-entropy alloys Progress in Materials Science, vol. 61, pp. 1–93, 2014.

[161] O. N. Senkov, G. B. Wilks, D. B. Miracle, C. P. Chuang, and P. K. Liaw, Microstructures and properties of high-entropy alloys Prog. Mater. Sci., vol. 61, pp. 1–93, 2010.

[162] K. G. Pradeep, N. Wanderka, P. Choi, J. Banhart, B. S. Murty, and D. Raabe, Atomic-scale compositonal characterization of a nanocrystalline AlCrCuFeNiZn high-entropy alloy using atom probe tomography Acta Mat., vol. 61, p. 4696–4706, 2013.

[163] L. Rogal, J. Morgiel, Z. Swiatek, and F. Czerwinski, Microstructure and mechanical properties of the new Nb25Sc25Ti25Zr25 eutectic high entropy alloy Materials Science and Engineering: A, vol. 651, pp. 590–597, 2016.

[164] C.-H. Tsau, Phase transformation and mechanical behaviour of TiFeCoNi alloy during annealing Mat. Sci. Eng. A, vol. 501, pp. 81–86, 2009.

[165] M. C. Gao and D. E. Alman, Searching for Next Single-Phase High-Entropy Alloy Compositions Entropy, vol. 15, pp. 4504–4519, 2013.

[166] M. Feuerbacher, M. Heidelmann, and C. Thomas, Hexagonal High-Entropy Alloys Mat. Res. Lett., vol. 3, pp. 1–6, 2015.

[167] J. O. A. Paschoal, H. Kleykamp, and F. Thummler, Phase equilibria in the quaternary molybdenum-ruthenium-rhodium-palladium system Z. Metallkd., vol. 74, p. 652, 1983.

[168] S. S. Ghazi and K. R. Ravi, Phase-evolution in high entropy alloys: role of synthesis route Intermetall., vol. 73, pp. 40–42, 2016.

[169] C.-C. Tung, J.-W. Yeh, T.-T. Shun, S.-K. Chen, Y.-S. Huang, and H.-C. Chen, On the elemental effect of AlCoCrCuFeNi high-entropy alloy system Mat. Lett., vol. 61, no. 1, pp. 1–5, 2007.

[170] Z. Tang, M. Gao, H. Diao, T. Yang, J. Liu, T. Zuo, Y. Zhang, Z. Lu, Y. Cheng, Y. Zhang, K. Dahmen, P. Liaw, and T. Egami, Aluminum alloying effects on lattice types, microstructures, and mechanical behavior of high-entropy alloys systems JOM, vol. 65, no. 12, pp. 1848–1858, 2013.

[171] S. Singh, N. Wanderka, B. S. Murty, U. Glatzel, and J. Banhart, Decomposition in multi-component AlCoCrCuFeNi high-entropy alloy Acta Mat., vol. 59, no. 1, pp. 182–190, 2011.

[172] S. Singh, N. Wanderka, K. Kiefer, K. Siemensmeyer, and J. Banhart, Effect of decomposition of the Cr-Fe-Co rich phase of AlCoCrCuFeNi high entropy alloy on magnetic properties Ultramicroscopy, vol. 111, no. 6, pp. 619–622, 2011.

[173] C. J. Tong, Y. L. Chen, S. K. Chen, J. W. Yeh, T. T. Shun, C. H. Tsau, S. J. Lin, and S. Y. Chang, Microstructure characterization of Al_xCoCrCuFeNi high-entropy alloy system with multiprincipal elements Metall. Mat. Trans. A, vol. 36A, no. 4, pp. 881–893, 2005.

[174] H.-P. Chou, Y.-S. Chang, S.-K. Chen, and J.-W. Yeh, Microstructure, thermophysical and electrical properties in Al_xCoCrFeNi ($0 \leqslant x \leqslant 2$) high-entropy alloys Materials Science and Engineering: B, vol. 163, no. 3, pp. 184–189, 2009.

[175] Y.-F. Kao, T.-J. Chen, S.-K. Chen, and J.-W. Yeh, Microstructure and mechanical property of as-cast, -homogenized, and -deformed Al_xCoCrFeNi ($0 \leqslant x \leqslant 2$) high-entropy alloys Journal of Alloys and Compounds, vol. 488, no. 1, pp. 57–64, 2009.

[176] C. Li, J. C. Li, M. Zhao, and Q. Jiang, Effect of aluminum contents on microstructure and properties of Al_xCoCrFeNi alloys Journal of Alloys and Compounds, vol. 504, Supplement 1, pp. S515–S518, 2010.

[177] C. Li, J. C. Li, M. Zhao, and Q. Jiang, Effect of alloying elements on microstructure and properties of multiprincipal elements high-entropy alloys J. All. Compd., vol. 475, pp. 752–757, 2009.

[178] Y. Lu, Y. Dong, S. Guo, L. Jiang, H. Kang, T. Wang, B. Wen, Z. Wang, J. Jie, Z. Cao, H. Ruan, and T. Li, A Promising New Class of High-Temperature Alloys: Eutectic High-Entropy Alloys Scientific Reports, vol. 4, p. 6200, 2014.

[179] M. Park and C. A. Schuh, Accelerated sintering in phase-separating nanostructured alloys Nat. Comm., vol. 6, p. 6858, 2015.

[180] P. F. Yu, L. J. Zhang, H. Cheng, H. Zhang, M. Z. Ma, Y. C. Li, G. Li, P. K. Liaw, and R. P. Liu, The high-entropy alloys with high hardness and soft magnetic property prepared by mechanical alloying and high-pressure sintering Intermetall., vol. 70, pp. 82–87, 2016.

[181] Z. J. Jiang, J. Y. He, H. Y. Wang, H. S. Zhang, Z. P. Lu, and L. H. Dai, Shock compression response of high entropy alloys Mat. Res. Lett., vol. 4, no. 4, pp. 226–232, 2016.

[182] N. S. Weston, F. Derguti, A. Tudball, and M. Jackson, Spark plasma sintering of commercial and development titanium alloy powders J. Mat. Sci., vol. 50, no. 14, pp. 4860–4878, 2015.

[183] H.-L. Wang, T.-X. Gao, J.-Z. Niu, P.-J. Shi, J. Xu, and Y. Wang, Microstructure, thermal properties, and corrosion behaviour of FeSiBAlNi alloy fabricated by mechanical alloying and spark plasma sintering Int. J. Miner. Metall. Mat., vol. 23, no. 1, pp. 77–82, 2016.

[184] S. Mohanty, N. P. Gurao, and K. Biswas, Sinter ageing of equiatomic $Al_{20}Co_{20}Cu_{20}Zn_{20}Ni_{20}$ high entropy alloy via mechanical alloying Mat. Sci. Eng. A, vol. 617, pp. 211–218, 2014.

[185] A. Zhang, J. Han, J. Meng, B. Su, and P. Li, Rapid preparation of AlCoCrFeNi high entropy alloy by spark plasma sintering from elemental powder mixture Mat. Lett., vol. 181, pp. 82–85, 2016.

[186] X.-H. Qu, L. Zhang, M. Wu, and S.-B. Ren, Review of metal matrix composites with high thermal conductivity for thermal management application Prog. Mater. Sci. Mat. Int., vol. 21, pp. 189–197, 2011.

[187] M. O. Bodundrin, K. K. Alaneme, and L. H. Chown, Aluminium matrix hybrid composites: a review of reinforcement philosophies; mechanical, corrosion and tribological characteristics J. Mat. Res. Tech., vol. 4, pp. 434–445, 2015.

[188] D. K. Das, P. C. Mishra, S. Singh, and S. Pattanaik, Fabrication and heat treatment of ceramic-reinforced aluminium matrix composites – a review Int. J. Mech. Mat. Eng., vol. 1, no. 6, pp. 1–15, 2014.

[189] K. K. Alaneme and A. O. Aluko, Fracture toughness (K_{1C}) and tensile properties of as-cast and age-hardened aluminium (6063)-silicon carbide particulate composites Scientia Iranica, vol. 19, pp. 992–996, 2012.

[190] T. V. Christy, N. Murugan, and N. Kumar, A comparative study on the microstructures nd mechanical properties of Al 6061 alloy and the MMC Al 6061/TiB2/12p J. Miner. Mat. Charact. Eng., vol. 9, pp. 57–65, 2010.

[191] B. Hwu, S. Lin, and M. Jahn, Effect of process parameters on the properties of squeeze cast SiCp-6061 Al metal matrix composite Mat. Sci. Eng. A, vol. 207, pp. 135–141, 1996.

[192] A. Lipp, K. A. Schwetz, and K. Hunold, Hexagonal boron nitride: fabrication, properties and applications J. Europ. Ceramic Soc., vol. 5, pp. 3–9, 1989.

[193] N. P. Lavery, S. Mehraban, C. Pleydell-Pearce, S. G. R. Brown, D. J. Jarvis, W. Voice, and M. Brunnock, Combinatorial development and high throughput materials characterisation of steels Steelmaking, vol. 42, no. 10, pp. 727–733, 2015.

[194] J. Zhao, The diffusion-mutiple approach to designing alloys Ann. Rev. Mat. Res., vol. 35, no. 1, pp. 51–73, 2005.

[195] J. Zhao, X. Zheng, and D. Cahill, High-throughput measurements of material properties JOM, vol. 63, no. 3, pp. 40–44, 2011.

[196] D. L. Zhang, Processing of advanced materials using high-energy mechanical milling Progress in Materials Science, vol. 49, no. 3, pp. 537–560, 2004.

[197] A. W. Weeber, H. Bakker, and F. R. de Boer, The preparation of amorphous Ni-Zr powder by grinding the crystalline alloy EPL (Europhysics Letters), vol. 2, no. 6, p. 445, 1986.

[198] C. Suryanarayana, Mechanical alloying and milling Progress in Materials Science, vol. 46, no. 1, pp. 1–184, 2001.

[199] B. S. Murty and S. Ranganathan, Novel materials synthesis by mechanical alloying/milling International Materials Reviews, vol. 43, no. 3, pp. 101–141, 1998.

[200] M. H. Enayati and F. A. Mohamed, Application of mechanical alloying/milling for synthesis of nanocrystalline and amorphous materials International Materials Reviews, vol. 59, no. 7, pp. 394–416, 2014.

[201] E. Ma, J. H. He, and P. J. Schilling, Mechanical alloying of immiscible elements: Ag-Fe contrasted with Cu-Fe Phys. Rev. B, vol. 55, no. 9, pp. 5542–5545, 1997. PR.

[202] J. Groza, K. R. Anderson, M. Fendorf, and C. J. Echer, Surface oxide debonding in field assisted powder sintering Mat. Sci. Eng. A, vol. 270, no. 2, pp. 278–282, 1999.

[203] H.-L. Wang, T.-X. Gao, J.-Z. Niu, P.-J. Shi, J. Xu, and Y. Wang, Microstructure, thermal properties, and corrosion behaviors of FeSiBAlNi alloy fabricated by mechanical alloying and spark plasma sintering Int. J. Miner. Metall. Mat., vol. 23, no. 1, pp. 77–82, 2016.

[204] W. C. Nixon, Scanning electron microscopy Contemporary Phys., vol. 10, no. 1, pp. 71–96, 1969.

[205] J. Goldstein, D. E. Newbury, D. C. Joy, C. E. Lyman, P. Echlin, E. Lifshin, L. Sawyer, and J. R. Michael, Scanning Electron Microscopy and X-ray Microanalysis. New York: Springer US, third edition ed., 2003.

[206] J. Goldstein, D. E. Newbury, P. Echlin, D. C. Joy, A. D. Romig Jr., C. E. Lyman, C. Fiori, and E. Lifshin, Scanning Electron Microscopy and X-ray Microanalysis: A text for biologists, material scientists and geologists. New York and London: Plenum Press, 1992.

[207] J. C. Russ, Fundamentals of energy dispersive X-ray analysis. Butterworths Monographs in Materials, London: Butterworths, 1984.

[208] P. Echlin, Handbook of sample preparation for Scanning Electron Microscopy and X-ray microanalysis. New York, USA: Springer US, 2009.

[209] P. Eaton and P. West, Atomic Force Microscopy. New York: Oxford University Press, 2010.

[210] G. Haugstad, Atomic Force Microscopy: Understanding basic modes and advanced applications. Hoboken, New Jersey: John Wiley & Sons, 2012.

[211] M. Pitteri and G. Zanzotto, On the definition and classification of Bravais lattices Acta Crystallogr. A, vol. A52, pp. 830–838, 1996.

[212] V. K. Pecharsky and P. Y. Zavalij, Fundamentals of powder diffraction and structural characterization of materials. New York, USA: Springer, 2005.

[213] C. Giacovazzo, H. Monaco, D. Viterbo, F. Scordari, G. Gilli, G. Zanotti, and M. Catti, Fundamentals of crystallography. Oxford: International Union of Crystallography [and] Oxford University Press, 1992.

[214] H. M. Rietveld, A profile refinement method for nuclear and magnetic structures J. Appl. Cryst., vol. 2, pp. 65–71, 1969.

[215] L. B. McCusker, R. B. Von Dreele, D. E. Cox, D. Louer, and P. Scardi, Rietveld refinement guidelines J. Appl. Cryst., vol. 32, pp. 36–50, 1999.

[216] V. Petricek, M. Dusek, and L. Palatinus, Crystallographic computing system JANA2006: General features Z. Kristallogr., vol. 229, no. 5, pp. 345–352, 2014.

[217] J. Perl, J. Shin, J. Schumann, B. Faddegon, and H. Paganetti, TOPAS: an innovative proton Monte Carlo platform for research and clinical applications Med. Phys., vol. 39, no. 11, pp. 6818–6837, 2012.

[218] S. P. Thompson, J. E. Parker, J. Marchal, J. Potter, A. Birt, F. Yuan, R. D. Fearn, A. R. Lennie, S. R. Street, and C. C. Tang, Fast X-ray powder diffraction on I11 at DIAMOND J. Synchrotron Rad., vol. 18, pp. 637–648, 2011.

[219] P. Rajiv, R. Dinnebier, and M. Jansen, Powder 3D Parametric: A program for automated sequential and parametric Rietveld refinement using Topas Mat. Sci. Forum, vol. 651, pp. 97–104, 2010.

[220] J. Guignard and W. Crichton, The large volume press facility at ID06 beamline of the European synchrotron radiation facility as a High Pressure-High Temperature deformation apparatus. Rev. Sci. Instrum., vol. 86, no. 8, p. 085112, 2015.

[221] L. S. Dubrovinsky and S. K. Saxena, Thermal expansion of periclase (MgO) and tungsten (W) to melting temperatures Phys. Chem. Minerals, vol. 24, pp. 547–550, 1997.

[222] R. S. Pease, An X-ray study of boron nitride Acta Cryst., vol. 5, pp. 356–361, 1952.

[223] Y. Zhao, R. B. Von Dreele, D. J. Weidner, and D. Schiferl, P- V- T Data of hexagonal boron nitride h-BN and determination of pressure and temperature using thermoelastic equations of state of multiple phases High Press. Res. Int. J., vol. 15, no. 6, pp. 369–386, 1997.

[224] Y. Le Godec, D. Martinez-Garcia, M. Mezouar, G. Syfosse, J. P. Itié, and J. M. Besson, Thermoelastic behaviour of hexagonal graphite-like boron nitride High Press. Res. Int. J., vol. 17, no. 1, pp. 35–46, 2000.

[225] J. Garai, J. Chen, and G. Telekes, P-V-T Equation of State for Periclase CALPHAD, vol. 33, pp. 737–743, 2009.

[226] W. Crichton and M. Mezouar, Noninvasive pressure and temperature estimation in large-volume apparatus by equation-of-state cross-calibration High Temp. High Press., vol. 34, no. 2, pp. 235–242, 2002.

[227] G. W. H. Hohne, W. F. Hemminger, and H.-J. Flammersheim, Differential Scanning Calorimetry. New York, USA: Springer, 2003.

[228] A. P. Gray, Analytical Calorimetry, vol. 1. New York: Plenum Press, 1968.

[229] J. E. Daw, J. L. Rempe, L. Knudson, K. G. Condie, and J. C. Crepeau, Viability of pushrod dilatometry techniques for high temperature in-pile measurements tech. rep., Idaho National Laboratory, 2008.

[230] J. D. James, J. A. Spittle, S. G. R. Brown, and R. W. Evans, A review of measurement techniques for the thermal expansion coefficient of metals and alloys at elevated temperatures Meas. Sci. Technol., vol. 12, pp. R1–R15, 2001.

[231] C. Ho and R. Taylor, Thermal expansion of solids. Materials Park, Ohio, USA: ASM International, 1998.

[232] Y. S. Touloukian, R. K. Kirby, R. E. Taylor, and P. D. Desai, Thermal expansion of metallic elements and alloys, vol. 12 of Thermophysical properties of matter – The TPRC Data series. New York, USA: IFI/Plenum, 1975.

[233] W. J. Parker, R. Jenkins, C. Butler, and G. L. Abbott, Flash method of determining thermal diffusivity, heat capacity, and thermal conductivity J. App. Phys., vol. 32, no. 1679, 1961.

[234] M. Kover, M. Behulovà, M. Drienovsky, and P. Motycka, Determination of the specific heat using laser flash apparatus J. Therm. Anal. Calorim., vol. 122, no. 1, pp. 151–156, 2015.

[235] D. M. Rowe, CRC Handbook of thermoelectrics. New York, USA: CRC Press, 1995.

[236] J. J. Gilman, Chemistry and physics of mechanical hardness. Hoboken, New Jersey: John Wiley & Sons, 2009.

[237] K. Hermann, Hardness testing: Principles and applications. Materials Park, Ohio: ASM International, 2011.

[238] J. Edwards, Hardness testing. Characterization of materials, John Wiley & Sons, 2012.

[239] M. Bruchhausen, S. Holmstrom, I. Simonovski, T. Austin, J. M. Lapetite, S. Ripplinger, and F. de Haan, Recent developments in small punch testing: Tensile properties and DBTT Theoretical and Applied Fracture Mechanics, vol. 86, pp. 2–10, 2016.

[240] R. C. Hurst, R. J. Lancaster, S. P. Jeffs, and M. R. Bache, The contribution of small punch testing towards the development of materials for aero-engine applications Theoretical and Applied Fracture Mechanics, vol. 86, pp. 69–77, 2016.

[241] R. Lacalle, J. A. Alvarez, and F. Gutiérrez-Solana, Analysis of key factors for the interpretation of small punch test results Fatigue Fract. of Eng. Mat Struct., vol. 31, pp. 841–849, 2008.

[242] S. D. Norris and J. D. Parker, Deformation processes during disc bend loading Mater. Sci. Technol., vol. 12, pp. 163–170, 1996.

[243] R. Hurst, The european code of practice for small punch testing: where do we go from here? Metall. J., vol. 63, pp. 5–11, 2010.

[244] W. M. Haynes, A Ready-Reference Book of Chemical and Physical Data. CRC Handbook of Chemistry and Physics, Boca Raton, FL, USA: CRC Press, 96 ed., 2015.

[245] G. R. Anstis, P. Chantikul, B. R. Lawn, and D. B. Marshall, A critical evaluation of indentation techniques for measuring fracture toughness: I, Direct crack measurements J. Am. Ceram. Soc., vol. 64, pp. 533–538, 1981.

[246] M. Hellenbrandt, The inorganic crystal structure database (ICSD) – present and future Chr. Rev., vol. 10, pp. 17–22, 2004.

[247] F. R. Boyd and J. L. England, Apparatus for phase-equilibrium measurements at pressures up to 50 kilobars and temperatures up to 1750 degrees J. Geophys. Res., vol. 65, pp. 741–748, 1960.

[248] S. Klemme and H. S. O'Neill, The reaction $MgCr_2O_4 + SiO_2 = Cr_2O_3 + MgSiO_3$ and the free energy of formation of magnesiochromite ($MgCr_2O_4$) Contrib. Mineral. Petrol., vol. 130, pp. 59–65, 1997.

[249] G. A. Sweet, M. Brochu, R. L. Hexemer Jr, I. W. Donaldson, and D. P. Bishop, Consolidation of aluminum-based metal matrix composites via spark plasma sintering Materials Science and Engineering: A, vol. 648, pp. 123–133, 2015.

[250] S. Min, J. Blumm, and A. Lindemann, A new laser flash system for measurement of the thermophysical properties Thermochim. Acta, vol. 455, pp. 46–49, 2006.

[251] S. Riva, C. M. Fung, J. R. Searle, R. N. Clark, N. P. Lavery, S. G. R. Brown, and K. V. Yusenko, Formation and disruption of W-Phase in high-entropy alloys Metals, vol. 6, no. 106, 2016.

[252] S. Riva, S. G. R. Brown, N. P. Lavery, and K. V. Yusenko, A library for hexagonally-closed packed multi-component alloys Phys. Met. Metall., submitted.

[253] N. Mattern, M. Zinkevich, J. H. Han, and W. Loser, Experimental and thermodynamic assessment of the Co–Gd–Ti system Calphad, vol. 54, pp. 144–157, 2016.

[254] F. Tancret, I. Toda-Caraballo, E. Menou, and P. E. J. Rivera Díaz-Del-Castillo, Designing high entropy alloys employing thermodynamics and Gaussian process statistical analysis Mat. Design, vol. 115, pp. 486–497, 2017.

[255] M. S. Lucas, L. Mauger, J. A. Munoz, Y. Xiao, A. O. Sheets, S. L. Semiatin, J. Horwath, and Z. Turgut, Magnetic and vibrational properties of high-entropy alloys Journal of Applied Physics, vol. 109, 2011.

[256] C. Li, M. Zhao, J. C. Li, and Q. Jiang, B2 structure of high-entropy alloys with addition of Al Journal of Applied Physics, vol. 104, 2008.

[257] Z. Tang, T. Yuan, C.-W. Tsai, J.-W. Yeh, C. D. Lundin, and P. W. Liaw, Fatigue behavior of a wrought $Al_{0.5}CoCrCuFeNi$ two-phase high-entropy alloy Acta Mat., vol. 99, pp. 247–258, 2015.

[258] T. G. Novak, H. D. Vora, R. S. Mishra, M. L. Young, and N. B. Dahotre, Synthesis of $Al_{0.5}CoCrCuFeNi$ and $Al_{0.5}CoCrFeMnNi$ high-entropy alloys by laser melting Metall. Mat. Trans. B, vol. 45, pp. 1603–1607, 2014.

[259] W.-R. Wang, W.-L. Wang, S.-C. Wang, Y.-C. Tsai, C.-H. Lai, and J.-W. Yeh, Effects of Al addition on the microstructure and mechanical property of $Al_xCoCrFeNi$ high-entropy alloys Intermetallics, vol. 26, pp. 44–51, 2012.

[260] L. Luznik, P. Kozelj, S. Vrtnik, A. Jelen, Z. Jaglicic, A. Meden, M. Feuerbacher, and J. Dolinsek, Complex magnetism of Ho–Dy–Y–Gd–Tb hexagonal high-entropy alloy Phys. Rev. B, vol. 92, p. 224201, 2015.

[261] C. Niu, A. J. Zaddach, A. A. Oni, X. Sang, J. W. Hurt III, J. M. LeBeau, C. C. Koch, and D. L. Irving, Spin-driven ordering of Cr in the equiatomic high entropy alloy NiFeCrCo Appl. Phys. Lett., vol. 106, p. 161906, 2015.

[262] Y. F. Kao, S. K. Chen, T. J. Chen, P. C. Chu, J. W. Yeh, and S. J. Lin, Electrical, magnetic, and Hall properties of $Al_xCoCrFeNi$ high-entropy alloys J. All. Compd., vol. 509, pp. 1607–1614, 2011.

[263] V. Sudavtsova, M. Shevchenko, V. Berezutskii, and M. Ivanov, Thermodynamic properties of liquid Fe-Sc alloys Powder Metallurgy and Metal Ceramics, vol. 52, no. 7-8, pp. 456–464, 2013.

[264] M. A. Shevchenko, M. I. Ivanov, V. V. Berezutskii, V. G. Kudin, and V. S. Sudavtsova, Thermodynamic properties of alloys of the Ni-Sc and Ni-Y systems Russian Journal of Physical Chemistry A, vol. 88, no. 6, pp. 897–902, 2014.

[265] M. A. Shevchenko, V. V. Berezutskii, M. I. Ivanov, V. G. Kudin, and V. S. Sudavtsova, Thermodynamic properties of alloys of the Al-Co and Al-Co-Sc systems Russian Journal of Physical Chemistry A, vol. 88, no. 5, pp. 729–734, 2014.

[266] N. G. Jones, A. Frezza, and H. J. Stone, Phase equilibria in an $Al_{0.5}CrFeCoNiCu$ high entropy alloy Mat. Sci. Eng. A, vol. 615, pp. 214–221, 2014.

[267] N. G. Jones, K. A. Christofidou, and H. J. Stone, Rapid precipitation in an $Al_{0.5}CrFeCoNiCu$ high entropy alloy Mat. Sci. Tec., vol. 31, pp. 1171–1177, 2015.

[268] N. G. Jones, R. Izzo, P. M. Mignanelli, K. A. Christofidou, and H. J. Stone, Phase evolution in an $Al_{0.5}CrFeCoNiCu$ High Entropy Alloy Intermetallics, vol. 71, pp. 43–50, 2016.

[269] N. G. Jones, J. W. Aveson, A. Bhowmik, B. D. Conduit, and H. J. Stone, On the entropic stabilization of an $Al_{0.5}CrFeCoNiCu$ Intermetall., vol. 54, pp. 148–153, 2014.

[270] E. J. Pickering, H. J. Stone, and N. G. Jones, Fine-scale precipitation in the high-entropy alloy $Al_{0.5}CrFeCoNiCu$ Mat. Sci. Eng. A, vol. 645, pp. 65–71, 2015.

[271] S. Chen, X. Xie, B. Chen, J. Qiao, Y. Zhang, Y. Ren, K. A. Dahmen, and P. K. Liaw, Effects of temperature on serrated flows of $Al_{0.5}CoCrCuFeNi$ High-Entropy Alloy JOM, vol. 67, pp. 2314–1320, 2015.

[272] B. F. Figgins, G. O. Jones, and D. P. Riley, LXXVII. The thermal expansion of aluminium at low temperatures as measured by an X-ray diffraction method Philos. Mag., vol. 1, pp. 747–758, 1956.

[273] Z. S. Basinski, W. Hume-Rothery, and A. L. Sutton, The lattice expansion of iron Proc. R. Soc. Lond. A, vol. 229, pp. 459–467, 1955.

[274] E. A. Owen and E. L. Yates, LXVI. X-ray measurement of the thermal expansion of pure nickel The London, Edinburgh, and Dublin Philos. Mag. J. Sci., vol. 21, pp. 809–819, 1936.

[275] R. G. Ross and W. Hume-Rothery, High temperature X-ray metallography: I. A new Debye-Sherrer camera for use at very high temperatures II. A new parafocusing camera III. Applications to the study of chromium, hafnium, molybdenum, rhodium, ruthenium and tungsten J. Less Comm. Met., vol. 5, pp. 258–270, 1963.

[276] G. P. Tarcy and P. A. Foster Jr., Method for making a light metal-rare earth metal alloy US Patent 5037608, 1991.

[277] F. Zupanic, G. Lojen, M. Steinacher, and T. Boncina, Vpliv skandija na mikrostrukturo in lastnosti aluminijeve livne zlitine A356 / Effect of scandium on the microstructure and properties of the aluminium casting alloy A356 Livarski vesnik, vol. 64, no. 1, pp. 28–39, 2017.

[278] I. Firkowska, A. Boden, B. Boerner, and S. Reich, The origin of high thermal conductivity and ultralow thermal expansion in copper-graphite composites Nano Letters, vol. 15, pp. 4745–4751, 2015.

[279] A. M. Abyzov, F. M. Shakhov, A. I. Averkin, and V. I. Nikolaev, Mechanical properties of a diamond-copper composite with high thermal conductivity Mat. Design, vol. 87, pp. 527–539, 2015.

[280] M. Schobel, P. Dobron, J. Bernardi, R. Wimpory, and K. Weidenmann, Elasto-plastic deformation within diamond reinforced metals for thermal management Diamond and Related Mat., vol. 70, pp. 52–58, 2016.

[281] C. Biao and K. Kondoh, Sintering behaviours of carbon nanotubes-aluminium composite powders Metals, vol. 6, no. 9, p. 213, 2016.

[282] B. Boesl, D. Lahiri, S. Behdad, and A. Agarwal, Direct observation of carbon nanotube induced strengthening in aluminium composite via in situ tensile tests Carbon, vol. 69, pp. 79–85, 2014.

[283] X. Duan, Z. Yang, L. Chen, Z. Tian, D. Cai, Y. Wang, D. Jia, and Y. Zhou, Review on the properties of hexagonal boron nitride matrix composite ceramics J. Europ. Ceramic Soc., vol. 36, pp. 3725–3737, 2016.

[284] K. L. Firestein, A. E. Steinman, I. S. Golovin, J. Cifre, E. A. Obraztsova, A. T. Matveev, A. M. Kovalskii, O. I. Lebedev, D. V. Shtansky, and D. Golberg, Fabrication, characterization, and mechanical properties of spark plasma sintered Al-BN nanoparticle composites Materials Science and Engineering: A, vol. 642, pp. 104–112, 2015.

[285] K. L. Firestein, S. Corthay, A. E. Steinman, A. T. Matveev, A. M. Kovalskii, I. V. Sukhorukova, D. Golberg, and D. V. Shtansky, High-strength aluminium-based composites reinforced with BN, AlB_2 and AlN particles fabricated via reactive spark plasma sintering of Al-BN powder mixtures Mat. Sci. Eng. A, vol. 681, pp. 1–9, 2017.

[286] D. Liu, H. Wen, D. Zhang, C. Wang, Y. Lin, Y. Xiong, T. Topping, J. M. Schoenung, and E. J. Lavernia, Stress-enhanced grain growth in a nanostructured aluminium alloy during spark plasma sintering Philosophical Magazine Letters, vol. 94, no. 11, pp. 741–748, 2014.

[287] M. Anisimova, A. Knyazeva, and I. Sevostianov, Effective thermal properties of an aluminum matrix composite with coated diamond inhomogeneities Int. J. Eng. Sci., vol. 106, pp. 142–154, 2016.

[288] K. Mizuuchi, K. Inoue, Y. Agari, Y. Morisada, M. Sugioka, M. Tanaka, T. Takeuchi, J. Tani, M. Kawahara, Y. Makino, and M. Ito, Thermal properties of Al/diamond composites fabricated in continuous solid-liquid co-existent state by SPS Mat. Sci. Forum, vol. 706-709, pp. 1967–1972, 2012.

[289] N. B. Podymova and A. A. Karabutov, Combined effects of reinforcement fraction and porosity on ultrasonic velocity on SiC particulate aluminium alloy matrix composites Composites Part B: Eng., vol. 113, pp. 138–143, 2017.

[290] X. Liang, C. Jia, K. Chu, H. Chen, J. Nie, and W. Gao, Thermal conductivity and microstructure of Al/diamond composites with Ti-coated diamond particles consolidated by spark plasma sintering J. Composite Mat., vol. 46, pp. 1127–1136, 2012.

[291] Y. Zhang, X. Wang, S. Jiang, and J. Wu, Thermo-physical properties of Ti-coated diamond/Al composites prepared by pressure infiltration Mat. Sci. Forum, vol. 654-656, pp. 2572–2575, 2010.

[292] M. H. Tsai, Physical properties of High Entropy Alloys Entropy, vol. 15, pp. 5338–5345, 2013.

[293] S. Shafeie, S. Guo, Q. Hu, H. Fahlquist, P. Erhart, and A. Palmqvist, High-entropy alloys as high-temperature thermoelectric materials J. App. Phys., vol. 118, p. 184905, 2015.

[294] M. V. Novikov, A. L. Maistrenko, V. I. Kushch, and S. A. Ivanov, Evaluation of the quality of composite diamond-containing materials by their electrical and thermal conductivity Mat. Sci., vol. 42, no. 1, pp. 113–120, 2006.

[295] J. A. Kerns, N. J. Colella, D. Makowiecki, and H. L. Davidosn, Dymalloy: A composite substrate for high power density electronic components. Lawrence Livermore National Laboratory, United States: United States Department of Energy, 1995.